Replicons: functional elementary units of genome architecture

Das Replicon, ein elementarer, funktionaler Bestandteil der Genomarchitektur
Vom Fachbereich Biologie der Technischen Universität Darmstadt zur Erlangung des akademischen Grades eines Doctor rerum naturalium
genehmigte Dissertation von Dipl. Biol. Marius Armin Reinhart aus Frankfurt am Main
Tag der Einreichung: 28.09.2016, Tag der Prüfung: 24.11.2016
Darmstadt 2016 — D 17

1. Gutachten: Prof. Dr. M. Cristina Cardoso
2. Gutachten: Prof. Dr. Barbara Drossel

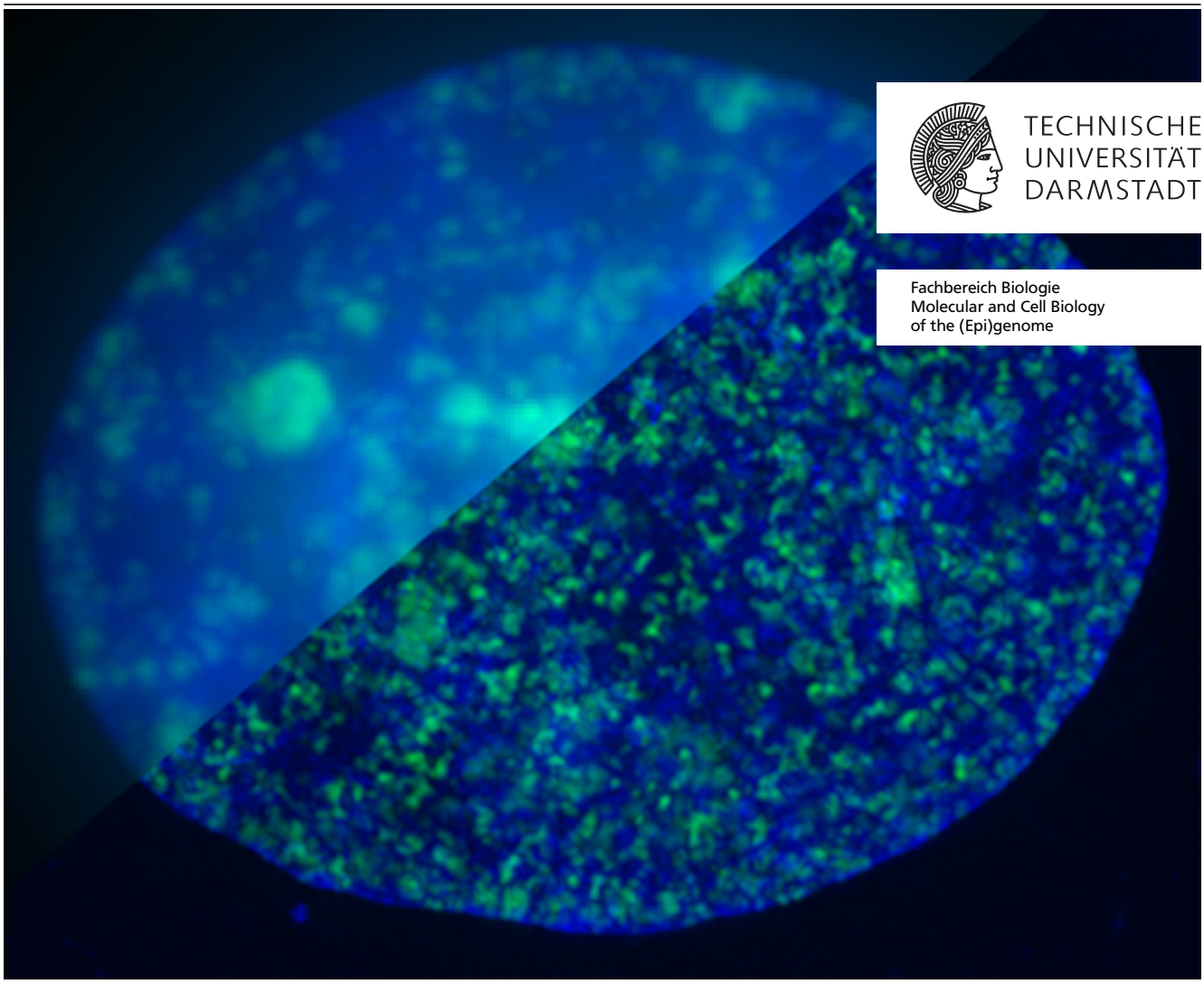

TECHNISCHE UNIVERSITÄT DARMSTADT

Fachbereich Biologie
Molecular and Cell Biology
of the (Epi)genome

Replicons:
functional elementary units of genome architecture
Das Replicon, ein elementarer, funktionaler Bestandteil der Genomarchitektur

Genehmigte Dissertation von Dipl. Biol. Marius Armin Reinhart aus Frankfurt am Main

1. Gutachten: Prof. Dr. M. Cristina Cardoso
2. Gutachten: Prof. Dr. Barbara Drossel

Tag der Einreichung: 28.09.2016
Tag der Prüfung: 24.11.2016

Darmstadt — D 17

Well, you have to know these things when you're a king, you know.

Arthur, King of the Britons
Monty Python and the Holy Grail (1975)

Summary

Only 750 years after Roger Bacon developed the first simple microscope, super-resolution microscopy is in full swing, letting us go where no one has gone before: beyond the Abbe limit. A perfect dance performance is needed as thousands of replisomes dance around the DNA during the Synthesis-Phase, for even a single error could lead to cell death or cancer. To gain an understanding of the choreography and the complex regulations necessary to maintain this highly dynamic process without a misstep, I employed recent advancements in microscopy. Due to improvements made in the last decade, it is now possible to take a closer look at the individual participants of DNA replication, the replisomes. My aim was to dive into the depth of DNA replication dynamics to detect, analyze and quantify DNA replication on the level of single replication machineries (replisomes).

Up until now imaging with high temporal resolution could only be achieved by live cell microscopy, trading spatial resolution against temporal resolution and photobleaching. I laid a solid foundation for my DNA replication studies by refining a cell staining method using "pulse and chase" experiments to gain temporal resolution in single fixed cells. This approach allows the study of highly dynamic DNA synthesis processes with the high spatial resolution achievable in fixed cells. For the statistical evaluation of this multi-label super-resolution data, I designed a computer guided approach to quantify thousands of replication foci in hundred of cells with a minimal amount of operator interaction. This program is a robust tool to quantify DNA replication foci free of observer bias and achieves consistent quantifications during biological and technical replicates.

The application of the newly developed foci recognition toolkit enabled me to resolve and quantify DNA replication foci formerly lost in the mist of wide field or even confocal imaging. The DNA replication foci quantification matched beautifully with the calculated numbers by Mills et al. [113] and Hozák et al. [71], indicating the ability to finally resolve DNA replication on the replisome level. This was further confirmed by DNA fiber measurements of DNA replication fork speed (RFS), inter origin distances (IODs), genome size analysis and DNA replication (S-Phase) timing.

To dig even deeper into the highly dynamic DNA replication processes, a simplistic computer model was created to simulate DNA synthesis *in silico*. Using the aquired biological data, I was able to correlate simulated *in silico* microscopy images from this 1D replication model to live cell microscopy in 4D.

Altogether I was able to answer basic questions regarding the control of DNA replication on the level of individual replisomes. I resolved and quantified individual replisomes and utilized those measurements to cogenerate a theoretical DNA replication simulation model.

Zusammenfassung

Vor 750 Jahren entwickelte Roger Bacon das erste Mikroskop. Heute stehen uns ultrahochauflösende Mikroskope zur Verfügung, die es uns ermöglichen in Welten vorzudringen die nie ein Mensch zuvor gesehen hat. Die technische Entwicklung der Mikroskope erlaubt es die hochgradig dynamischen und komplexen Prozesse der DNA Replikation im Detail zu untersuchen. Alle partizipierenden DNA Replikationsproteine befinden sich in einem stetigen Tanz um die zu verdoppelnde DNA, sie formen Replikationsmaschinen, lesen und verdoppeln das Genom, um im Anschluss zerlegt, abgelöst und an einer neuen Sequenz wieder aufgebaut zu werden. Diese Choreographie muss genauestens reguliert und überwacht werden, da bereits der kleinste Fehler weitreichende Konsequenzen haben kann. Mein Ziel war es, durch die Beobachtung einzelner Replisome (DNA Replikationsmachinen) einen neuen, tieferen Einblick in die Prozesse der DNA Replikation zu erhalten.

Bis jetzt konnten zeitliche und zeitlich-räumliche Abläufe in Zellen nur durch Lebendzellmikroskopie untersucht werden, dabei musste man aber auf die überlegene Auflösung von ultrahochauflösenden Mikroskopen verzichten, da deren exzessives Lichtbedürfnis zum Bleichen der eingesetzten Fluorophore bis hin zum Zelltod durch Phototoxizität geführt hätte. Das von mir entwickelte Verfahren erlaubt es vier aufeinanderfolgende Zeitpunkte in einer Zelle zu markieren, diese im Anschluss mit ultrahochauflösender Mikroskopie zu untersuchen und den zeitlichen Ablauf sichtbar zu machen. Dieser Ansatz ermöglicht es, in fixierten Zellen einen Einblick in den hochdynamischen Prozess der DNA Replikation zu erhalten.

Der Auflösungsgewinn durch ultrahochauflösende Mikroskope geht Hand in Hand mit einem Anwachsen der Rohdaten. Zur beobachterunabhängigen Auswertung dieser Daten habe ich ein computergestütztes Programm entwickelt, dass aufgrund der intrinsischen Bilddaten wichtige Parameter für sensible Variablen der Auswertung vorgibt. Die praktische Anwendung beider Methoden ermöglichte es mir DNA Replikationsorte in mehreren hundert Zellen zu messen, zu separieren und zu zählen. DNA Stranganalysen zur DNA Replikationsgeschwindigkeitsmessung sowie der Distanz zwischen aktivierten DNA Replikationsstartpunkten und die Bestimmung der Genomgröße bestätigen diese Theorie. Die Messungen zu den biologischen Grundlagen der Replikation wurden anschließend genutzt um ein DNA Replikationscomputermodell zu erzeugen. Dieses Modell versetzt uns zum ersten Mal in die Lage, simulierte 1D Replikationsfortschritte und die Aktivierung neuer DNA Replikationsstartpunkte mit ultrahochauflösenden Mikroskopiebildern zu vergleichen.

Diese Arbeit ermöglichte es mir grundlegende Fragen der DNA Replikation zu beantworten, und diese bis hinunter auf das Replisomelevel zu verfolgen.

Contents

1 Introduction: A journey through the microscopic ages of DNA replication

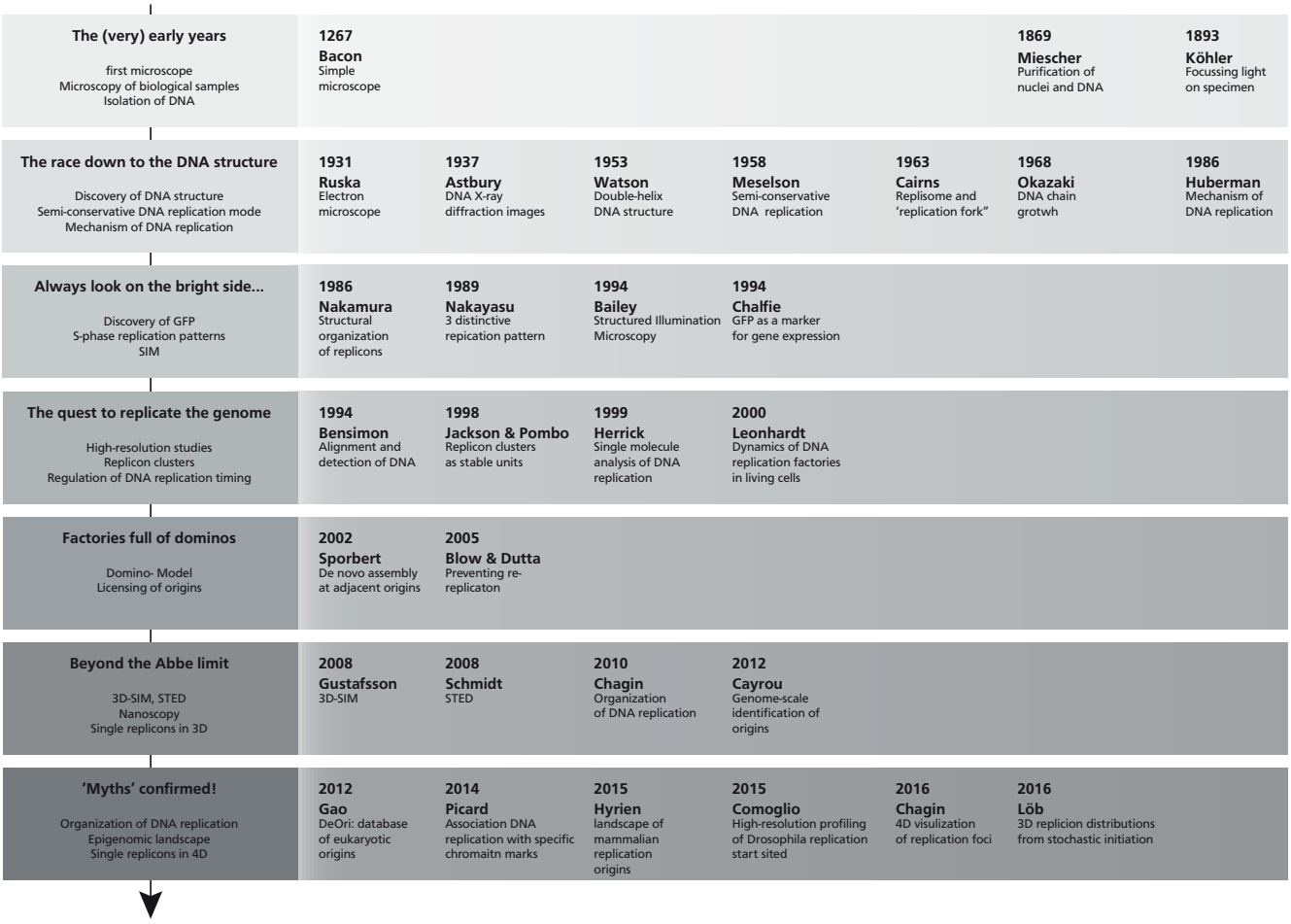

Figure 1.1: Graphical overview of microscopy developments and their impact on DNA replication studies. Milestones for microscopy and DNA replication studies from 1267 to 2016.

1.1 The (very) early years

Long after water filled glass bowls were used to read small letters[150], a simple single lens microscope started the microscopic revolution[3]. Spurred throughout the ages by accidental inventions[174], leaps by Galileo[52] and Hooke (1695), it was not until Carl Zeiss started to mass-produce microscopes in 1847, DNA observation started to take off. Simultaneously Mendel studied 29,000 pea plants (1866) and Haeckel postulated the containment of hereditary traits in the nucleus (1866)[36,64], while Miescher put the microscope to good use and purified the nuclei and observed DNA[112]. Köhler's game-changing illumination technique[86] helped to perfect Zeiss UV-microscope together with Siedentopf in 1908. In 1927, shortly after Levene described the nucleic acid structure (1919), Koltsov postulated the semi-conservative replication idea[154].

1.2 The race down to the DNA structure

Phase contrast microscopy[191] and DNA X-ray defraction images ([1] Franklin, 1952, "Photo 52") lead to fantastic images, new discoveries and the description of the double-helix DNA structure[179]. Meselson and Stahl ingeniously demonstrated

the semi-conservative DNA replication[108]. The first confocal microscope[114] and the Nipkow disc were clear landmarks of the microscopy revolution. Radioactive tagging and autoradiography allowed Cairns to observe DNA unwinding and the replication fork[19], Huberman and Riggs confirmed similar replication structures in mammalian chromosomes[72] and Okazaki described the lagging strand synthesis and "their" fragments[123,124,158,159].

Table 1.1: Microscopy and DNA milesstones

Year	Author	Paper or Landmark	cite
63	Plinius and Seneca	Water filed glass bowls to read small letters	150
1267	Bacon	The first simple microscope	3
1590	Janssen	Accidental discovery of the compound microscope with two (or more) lenses by Zacharias Janssen	174
1610	Galilei	"Microscope" with 1000x magnification	52
1665	Hooke	"Micrographia"	150
1847	Zeiss	First "mass produced" microscopes in 1847	
1866	Mendel	Hereditary traits in 29 000 pea plants	107
1866	Dahm, Haeckel	Hereditary traits contained in the nucleus	36,64
1871	Miescher	Purified nuclei for the first time and observed DNA	112
1893	Köhler	Ein neues Beleuchtungsverfahren für mikrophotographische Zwecke	86
1907	Smith	On the Absorption of Antibodies	
1908	Zeiss, Köhler and Siedentopf	First fluorescence microscopes based on UV-microscopy	
1919	Phoebus Levene	Identification of the nucleic acid structure	
1927	Soyfer	"Replicate in a semi-conservative fashion using each strand as a template"	154
1933	Ruska	Discovery of the electron microscope	139
1947	Astbury	DNA X-ray diffraction images	1
1953	Watson and Crick	X-ray diffraction "Photo 51"	179
1953	Watson and Crick	Discovery of the double-helix DNA structure	179
1955	Zernike	Discovery of phase contrast microscopy	191
1958	Meselson and Stahl	Confirmation of the semi-conservative DNA replication model	108
1961	Minsky	Discovery of the confocal microscope	114
1962	Shimomura et al.	Extraction, Purification and Properties of GFP	147
1963	Cairns	DNA unwinding for replication and "replication fork"	19
1966	Huberman and Riggs	Autoradiography of chromosomal DNA fibers from Chinese hamster cells.	72
1967	Egger and Petran	Discovery of the "Nipkow disk"	48
1966	Huberman and Riggs	On the mechanism of DNA replication in mammalian chromosomes	72
1968	Huberman and Riggs	Mammalian DNA is replicated in a similar manner	73
1968	Okazaki et al.	Mechanism of DNA chain growth. I. Possible discontinuity and unusual secondary structure of newly synthesized chains.	123
1968	Sugimoto et al.	Mechanism of DNA chain growth, II. Accumulation of newly synthesized short chains in E. coli infected with ligase-defective T4 phages.	159
1969	Van Dilla et al.	Duration of the cell cycle	176
1969	Sugimoto et al.	Mechanism of DNA chain growth, III. Equal annealing of T4 nascent short DNA chains with the separated complementary strands of the phage DNA	158
1969	Okazaki and Okazaki	Mechanism of DNA chain growth. IV. Direction of synthesis of T4 short DNA chains as revealed by exonucleolytic degradation.	124
1972	Danna and Nathans	Bidirectional Replication of Simian Virus 40 DNA	38
1974 – 1979		Fork speed, replication speed and replicon sizes	87,165,166,181,187–190
1975	Köhler	Continuous cultures of fused cells secreting antibody of predefined specificity.	
1986	Nakamura et al.	Structural organizations of replicon domains during DNA synthetic phase in the mammalian nucleus	119
1989	Nakayasu	Three distinctive replication patterns	120
1992	O'Keefe	Dynamic organization of DNA replication in mammalian cell nuclei spatially and temporally defined replication of chromosome	125
1992	Rizzoli et al.	Progression of DNA synthesis	138
1993	Bailey et al.	Structured Illumination Microscopy (SIM)	5
1994	Chalfie et al.	Green fluorescent protein as a marker for gene expression	30
1994	Hell, Hell et al.	4pi microscope	66,67
1994	Bensimon et al.	Alignment and sensitive detection of DNA by a moving interface	7
1997	Wu and Gilbert	The replication origin decision point is a mitogen	182
1997	Michalet et al.	Dynamic molecular combing: stretching the whole human genome for high-resolution studies.	111
1998	Jackson and Pombo	Replicon Clusters Are Stable Units of Chromosome Structure Evidence That Nuclear Organization Contributes to the Efficient Activation and Propagation of S Phase in Human Cells	77
1999	Dimitrova and Gilbert	The Spatial Position and Replication Timing of Chromosomal Domains Are Both Established in Early G1 Phase	44
1999	Herrick and Bensimon	Single molecule analysis of DNA replication.	69
2000	Berezney et al.	Heterogeneity of eukaryotic replicons , replicon clusters , and replication foci	8
2000	Leonhardt et al.	Dynamics of DNA Replication Factories in Living Cells	92
2000	Keck and Berger	DNA replication at high resolution	82
2000	Davey and O'Donnell	Mechanisms of DNA replication	39
2001	Gilbert	Eukaryotic origins	
2001	Tada et al.	Repression of origin assembly in metaphase depends on inhibition of RLF-BCdt1 by geminin	160
2001	Norio and Schildkraut	Visualization of DNA Replication on Individual Epstein-Barr Virus Episomes	122
2002	Sporbert et al.	DNA Polymerase Clamp Shows Little Turnover at Established Replication Sites but Sequential De Novo Assembly at Adjacent Origin Clusters	156
2002	Gerbi and Bielinsky	DNA replication and chromatin	56
2002	Gerbi	Initiation of DNA replication in multicellular eukaryotes	55
2003	Vashee	Sequence-independent DNA binding and replication initiation by the human origin recognition complex	177
2003	DePamphilis	The 'ORC cycle': a novel pathway for regulating eukaryotic DNA replication	41
2004	Sadoni	Stable chromosomal units determine the spatial and temporal organization of DNA replication	140
2004	Sancar et al.	DNA replication and DNA repair mechanisms most of the replication machinery is also used in DNA repair.	141
2005	Blow and Dutta	Preventing rereplication	12
2005	Sporbert et al.	PCNA acts as a stationary loading platform for transiently interacting Okazaki fragment maturation proteins	155
2005	Cvetic and Walter	Eukaryotic origins of DNA replication: could you please be more specific?	35
2005	Patel	Origin selection and silent origins	127
2006	DePamphilis et al.	Regulating the licensing of DNA replication origins in metazoa	42
2006	Langston and O'Donnell	DNA replication: keep moving and don't mind the gap.	90
2007	Aljadem	Impact of chromatin structure	
2007	Pomerantz and O'Donnell	Replisome mechanics: insights into a twin DNA polymerase machine.	129
2007	Sasaki and Gilbert	The many faces of the origin recognition complex	143
2007	Lucas et al.	High-throughput mapping of origins of replication in human cells.	98
2007	McInerney et al.	Characterization of a triple DNA polymerase replisome.	106
2007	Hamdan et al.	Dynamic DNA helicase-DNA polymerase interactions assure processive replication fork movement.	65
2007	Lovett	Polymerase switching in DNA replication.	97

Continued on next page

Table 1.1 – continued from previous page

Year	Author	Paper or Landmark	cite
2008	Gustafsson et al.	3D–SIM	63
2008	Nick McElhinny et al.	Division of labor at the eukaryotic replication fork.	121
2008	Stillman	DNA Polymerases at the Replication Fork in Eukaryotes	157
2008	Schmidt et al.	Discovery of stimulated emission depletion (STED)	144
2009	Boye and Grallert	In DNA replication, the early bird catches the worm.	15
2009	Lipps and Rhodes	G-quadruplex structures: in vivo evidence and function.	95
2009	Remus and Diffley	Eukaryotic DNA replication control: lock and load, then fire.	135
2010	Chagin et al.	Organization of DNA Replication	29
2010	Masai et al.	Eukaryotic chromosome DNA replication: where, when, and how?	102
2010	D'Angiolella et al.	SCF (Cyclin F) controls centrosome homeostasis and mitotic fidelity through CP110 degradation.	37
2010	Yardimci et al.	Uncoupling of sister replisomes during eukaryotic DNA replication.	184
2010	Botchan and Berger	DNA replication: making two forks from one prereplication complex.	14
2011	Heller et al.	Eukaryotic origin-dependent DNA replication in vitro reveals sequential action of DDK and S-CDK kinases.	68
2011	Ozeri-Galai et al.	Failure of origin activation in response to fork stalling leads to chromosomal instability at fragile sites.	126
2011	Fu et al.	Selective bypass of a lagging strand roadblock by the eukaryotic replicative DNA helicase.	51
2011	Martin et al.	Genome-wide depletion of replication initiation events in highly transcribed regions.	100
2011	Tanaka et al.	Origin association of Sld3, Sld7, and Cdc45 proteins is a key step for determination of origin-firing timing.	162
2012	Cayrou et al.	Genome-scale identification of active DNA replication origins.	26
2012	Knott et al.	Forkhead transcription factors establish origin timing and long-range clustering in S. cerevisiae	84
2012	Ritson and Moses	A fragment based click chemistry approach towards hybrid G-quadruplex ligands: design, synthesis and biophysical evaluation	137
2011	Casas-Delucchi et al.	Histone hypoacetylation is required to maintain late replication timing of constitutive heterochromatin.	22
2011	Siow et al.	OriDB, the DNA replication origin database updated and extended.	151
2012	Douglas and Diffley	Replication timing: the early bird catches the worm.	45
2012	Siddiqui-Jain et al.	CK2 inhibitor CX-4945 suppresses DNA repair response triggered by DNA-targeted anticancer drugs and augments efficacy: mechanistic rationale for drug combination therapy.	148
2012	Di Antonio et al.	Experimental approaches to identify cellular G-quadruplex structures and functions.	43
2012	Boos et al.	Activation of the replicative DNA helicase: breaking up is hard to do.	13
2012	Bianco et al.	Analysis of DNA replication profiles in budding yeast and mammalian cells using DNA combing.	11
2012	Gao et al.	DeOri: a database of eukaryotic DNA replication origins.	53
2012	Gilbert	Replication origins run (ultra) deep.	58
2012	Besnard et al.	Unraveling cell type-specific and reprogrammable human replication origin signatures associated with G-quadruplex consensus motifs.	10
2012	Casas-Delucchi et al.	Targeted manipulation of heterochromatin rescues MeCP2 Rett mutants and re-establishes higher order chromatin organization.	20
2013	Dellino et al.	Genome-wide mapping of human DNA-replication origins: levels of transcription at ORC1 sites regulate origin selection and replication timing.	40
2013	Cavalli and Misteli	Functional implications of genome topology.	24
2013	Gundersen and Worman	Nuclear positioning.	62
2013	Whitehouse and Smith	Chromatin dynamics at the replication fork: there's more to life than histones.	180
2013	McGuffee et al.	Quantitative, genome-wide analysis of eukaryotic replication initiation and termination.	105
2013	Kubota et al.	The Elg1 replication factor C-like complex functions in PCNA unloading during DNA replication.	88
2013	Yamazaki et al.	Replication timing regulation of eukaryotic replicons: Rif1 as a global regulator of replication timing.	183
2013	Mesner et al.	Bubble-seq analysis of the human genome reveals distinct chromatin-mediated mechanisms for regulating early- and late-firing origins.	109
2013	Masai	A personal reflection on the replicon theory: from R1 plasmid to replication timing regulation in human cells.	101
2013	Hyrien et al.	From simple bacterial and archaeal replicons to replication N/U-domains.	75
2013	Tarsounas and Tijsterman	Genomes and G-quadruplexes: for better or for worse.	163
2013	Ulrich	New insights into replication clamp unloading.	170
2013	Técher et al.	Replication dynamics: biases and robustness of DNA fiber analysis.	167
2013	Mojardín et al.	Specification of DNA replication origins and genomic base composition in fission yeasts.	115
2013	Pope and Gilbert	The replication domain model: regulating replicon firing in the context of large-scale chromosome architecture.	130
2013	Yoshida et al.	Time to be versatile: regulation of the replication timing program in budding yeast.	186
2013	Forterre	Why are there so many diverse replication machineries?	49
2014	Casas-Delucchi and Cardoso	Epigenetic control of DNA replication dynamics in mammals	21
2014	Hori et al.	Lethal effects of short-wavelength visible light on insects.	70
2014	Murat and Balasubramanian	Existence and consequences of G-quadruplex structures in DNA.	118
2014	Volle and Dalal	Histone variants: the tricksters of the chromatin world.	178
2014	Gilbert and Allan	Supercoiling in DNA and chromatin.	59
2014	Valton et al.	G4 motifs affect origin positioning and efficiency in two vertebrate replicators.	173
2014	Picard et al.	The spatiotemporal program of DNA replication is associated with specific combinations of chromatin marks in human cells.	128
2014	Champeris Tsaniras et al.	Licensing of DNA replication, cancer, pluripotency and differentiation: an interlinked world?	31
2014	Renard-Guillet et al.	Temporal and spatial regulation of eukaryotic DNA replication: from regulated initiation to genome-scale timing program.	136
2014	Sansoni et al.	The histone variant H2A.Bbd is enriched at sites of DNA synthesis.	142
2014	Castillo Bosch et al.	FANCJ promotes DNA synthesis through G-quadruplex structures.	23
2015	Urban et al.	The hunt for origins of DNA replication in multicellular eukaryotes.	171
2015	Siler et al.	Measuring the effectiveness of scientific gatekeeping.	149
2015	Hyrien	Peaks cloaked in the mist: the landscape of mammalian replication origins.	74
2015	Song and Brady	Post-translational modifications of tubulin: pathways to functional diversity of microtubules.	153
2015	Yeeles et al.	Regulated eukaryotic DNA replication origin firing with purified proteins.	185
2015	Ticau et al.	Single-molecule studies of origin licensing reveal mechanisms ensuring bidirectional helicase loading.	168
2015	Chistol and Walter	Single-Molecule Visualization of MCM2-7 DNA Loading: Seeing Is Believing.	32
2015	Comoglio et al.	High-resolution profiling of Drosophila replication start sites reveals a DNA shape and chromatin signature of metazoan origins.	33
2015	Duzdevich et al.	The dynamics of eukaryotic replication initiation: origin specificity, licensing, and firing at the single-molecule level.	47
2016	Chagin et al.	4D Visualization of replication foci in mammalian cells corresponding to individual replicons	27
2016	Löb et al.	3D replicon distributions arise from stochastic initiation and domino-like DNA replication progression	96

1.3 Always look on the bright side...

Along came Aequorea victoria[147] and brought light into darkness. Where audioradiography once ruled[72,73,164], immunofluorescence labeling of fixed cells (e.g. refs.[2,77,78,83,99,104,119]) and the labeling of newly synthesized DNA by modified nucleotide incorporation, monoclonal antibodies[61,92,140,152] and fusion proteins[94,169] opened our eyes. Cell cycle duration[176], fork speed, replication speed and replicon sizes[87,165,166,181,187–190] where all unearthed from the dark

along with structural organizations of replicon domains during DNA synthesis[119] and the three distinctive early, mid and late S-Phase replication patterns[120].

Also the first affordable home computers made digital image analysis possible through the help of Rasband who developed THE milestone in image analysis ImageJ (then NHI Image) in 1987[145]. Replication sites where described extensively during the following years. Not only replication origins[16,17] and essential polymerases were also observed[116] but also spatially and temporally dynamic organizations of DNA replication[125,138].

1.4 The quest to replicate the genome

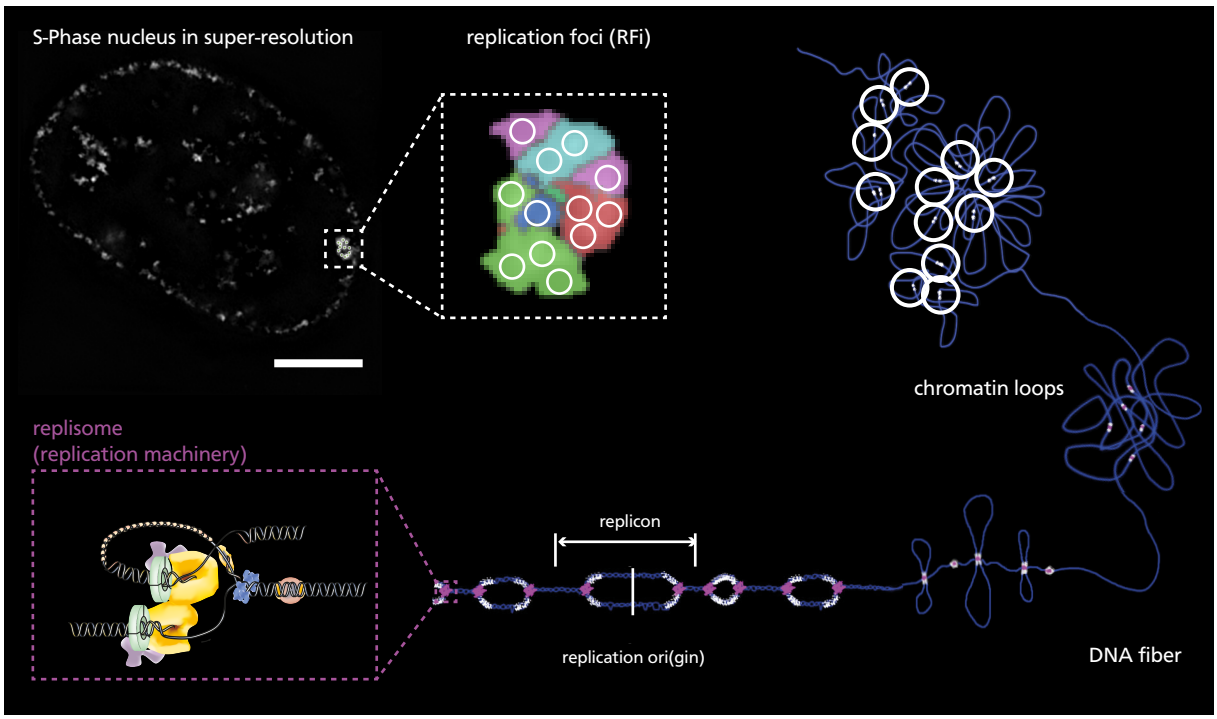

Figure 1.2: DNA replication structures from the nucleus to the replisome.
A fluorescently labeled HeLa Kyoto cell with a typical late S-Phase replication pattern, is presented in the top left corner (Scale bar = 5 μm). Magnified super-resolution replication foci, with white circles representing individual replication sites displayed in the middle of the top row. A scheme of clustered chromatin loops with active replication sites (white), build from a DNA fiber, are shown on the right. Starting point of DNA replication, the replication origin (ori) and the region replicated by a single origin displayed in the bottom row. Each replicon is replicated by two replication machineries (magenta), composed of various replication proteins, a detailed view is displayed in the bottom left corner, adapted from Chagin et al. [27,29].

Chromatin loops and their "functional" attachments to active transcription units were shown as chromatin organizers during mitosis[76] and replication factories were proposed as DNA replication sites clusters organized to the nucleoskeleton[71]. Molecular combing, refined fiber analysis and sensitive detection of DNA[7] opened the door to a whole genome stretch and high-resolution studies[111]. It allowed analysis of single DNA molecules during replication in a much greater resolution[69] than ever before. Stable replicon clusters were also established for effective activation, propagation of the synthesis Phase (S-Phase)[77] and regulation of replication timing[44]. Studies on DNA replication proteins and origin complexes lead to the quantified heterogeneity of eukaryotic replicons, replicon clusters and replication foci[8,39,82], while Leonhardt[92] described the dynamics of replication factories and Gilbert tried to "make sense of eukaryotic DNA replication origins"[57]. Different regulatory levels are necessary to initiate and regulate DNA replication, not only the chromatin structure, nuclear and chromosomal locations but also origin recognition complex (ORC) and a whole bunch of other

factors apparently define start sites of replication[41,55,56,143].

1.5 Factories full of dominos

A cold war followed between representatives of the “factory model”[54,73,77] and “dynamicists” as Sporbert[156] showed little PCNA turnover on established sites but domino-like activation of neighboring origins. While further discoveries lead to stable chromosomal units which determine spatial and temporal organization of DNA replication[140], similarities between DNA replication and repair machineries were also demonstrated[141]. The mechanism for "licensing" DNA replication origins also prevent DNA rereplication and demonstrated why DNA is duplicated once, and only once, during each cell cycle[12,42]. Despite Cvetic wishing for "eukaryotic origins of DNA replication to please be more specific"[35], DNA replication is a very robust mechanism and stalled forks could be reactivated or reactivate neighboring origins to close all gaps and provide us with a perfect copy in $1 : 10^9$ nucleotides[90,127].

1.6 "Peaks cloaked in the mist"[74]

The search for a consensus motif of DNA replication origins continued with high throughput mapping of potential origins and next generation sequencing[10,18,26,40,81,98,100,109,110,117,128,172] but stalled without a conclusive definition of the mammalian origin of replication. Studies into the epigenomic landscape, epigenetic control of DNA replication and higher order chromatin organization[20–22] investigate the link of epigenetics and DNA replication (unpublished data, Heinz et al.) possible replication origins remained elusive. Even Hyrien’s "Peaks cloaked in the mist" all out approach was not able to identify possible origins by similarities in thousands of microarrays and next generation sequencing techniques, suggesting origins form at unspecific DNA sites, but are suppressed by ongoing transcription[74].

1.7 To go where no one has gone before: beyond the Abbe limit

Meanwhile the microscopy(c) arms race to and beyond the diffraction limit calculated by Abbe continued with the Structured Illumination Microscopy (SIM)[5], the 3D-SIM[63] and the retaliatory attack: stimulated emission depletion (STED)[144]. Until now only clusters of DNA replication foci could be imaged[9,50,71,77,99,113,119,120,175]. Dramatic increases in spatial resolution along all three axes enable the visualization and quantification of small replication structures for the first time[29,34,85,93]. An exponential increase form ~100 to >1000 in DNA replication foci numbers correlated with developments in microscopy techniques and computational analysis tools. Further improvements fastforwarded microscopy into the nanoscopy era. It was now possible to resolve structures well below the Abbe limit, down to 30 nm and smaller. Nanoscopy[63,66,67] is in full swing and let us go where no one has gone before: beyond the Abbe limit.

2 Aims of the work

- How to gain spatio-temporal resolution in fixed cells? (see Chapter 3 on page 9)
- How to remove bias from DNA replication foci quantification? (see Chapter 4 on page 23)
- How to quantify DNA replication parameters in super-resolution? (see Chapter 5 on page 47)
- How to simulate and visualize DNA replication models? (see Chapter 6 on page 73)
- How to find the elusive "none existing" DNA replication motif of mammalian origin? (see Chapter 7 on page 95)

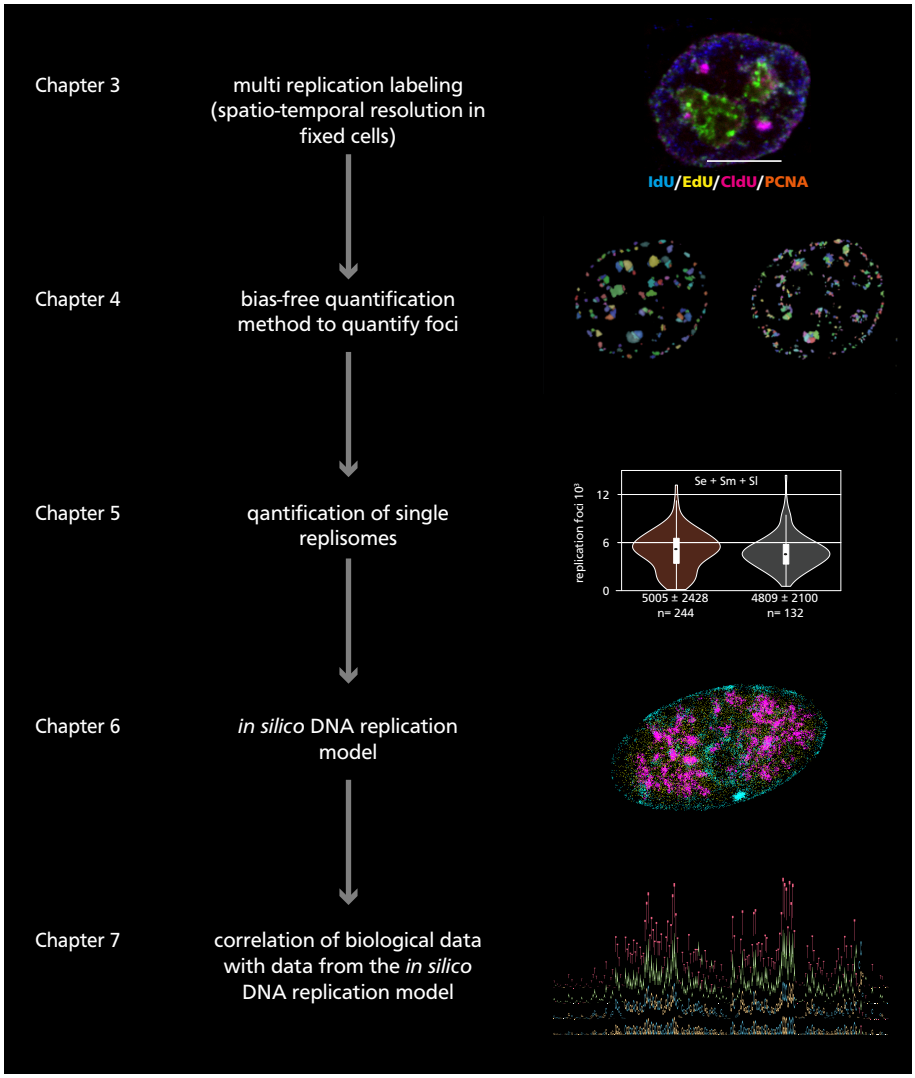

Figure 2.1: Graphical overview of the thesis' aims, from labeling to genomics.
In this step by step guide I give an overview of the key aspects from this thesis and how they work hand in hand in the quest for DNA replication analysis.

3 Spatio-temporal visualization of DNA replication dynamics

3.1 Aims of "Spatio-temporal visualization of DNA replication dynamics"

Until now imaging at high temporal resolution went hand in hand with photobleaching and reduced spatial resolution in live cell microscopy. As a solid foundation for DNA replication studies, I combined selected replication labeling methods in "pulse chase" experiments to visualize consecutive time points of DNA replication *in situ*. The careful combination of modified nucleotides, corresponding antibodies and selected GFP-tagged replication proteins allowed us to visualize up to four different time points during a single S-Phase in one individual cell. Through this multi-replication labeling approach I gained temporal resolution and even improvements in spatial resolution for a spatio-temporal overview of the highly dynamic processes of DNA synthesis in individual fixed cells without the need for live cell imaging.

3.2 Contributions

- M. Reinhart wrote the intro, developed and wrote the protocol for "Polytemporal DNA Replication Staining" and prepared Figure 2.

3.3 Publication

Chapter 15

Spatiotemporal Visualization of DNA Replication Dynamics

Marius Reinhart, Corella S. Casas-Delucchi, and M. Cristina Cardoso

Abstract

The ability of cells to copy their DNA allows them to transmit their genetic information to their progeny. In such, this central biological process preserves the instructions that direct the entire development of a cell. Earlier biochemical analysis in vitro and genetic analysis in yeast laid the basis of our understanding of the highly conserved mechanism of DNA replication. Recent advances on labeling and live-cell microscopy permit now the dissection of this fundamental process in vivo within the context of intact cells. In this chapter, we describe in detail how to perform multiple DNA replication labeling and detection allowing high spatial resolution imaging, as well as how to follow DNA replication in living cells allowing high temporal resolution imaging.

Key words DNA replication, Fluorescent protein, Immunofluorescence staining, Live-cell microscopy, Nucleotide pulse labeling

1 Introduction

The accurate duplication of the genome is the basis for cell proliferation. The process of DNA replication takes place during S-phase and is organized both spatially and temporally [1], so that the activation of single replication origins throughout S-phase results in conserved in situ labeling patterns that change as S-phase progresses [2–4]. Nevertheless, the mechanism by which active replication spreads along a chromosome remains unclear.

First hints about the organization of active replication sites were obtained by pioneering experiments using radioactively labeled nucleotides, which are incorporated during the DNA synthesis process. These studies provided very valuable data on the localization of active replication sites along single stretched DNA fibers and further presented the first in situ data on DNA replication in mammalian cells [5, 6]. However, detailed spatial

Marius Reinhart and Corella S. Casas-Delucchi have contributed equally to this work.

Yaron Shav-Tal (ed.), *Imaging Gene Expression: Methods and Protocols*, Methods in Molecular Biology, vol. 1042,
DOI 10.1007/978-1-62703-526-2_15,

information about the in situ organization of replication sites had to wait for the development of the first specific antibodies against halogenated nucleotides in the 1980s [2, 7]. In situ detection of incorporated nucleotides and later of replication factors [8, 9] provided quite detailed spatial information; however, they represent single snapshots of the dynamic replication process. The combination of two pulses with differently modified nucleotides, on the other hand, for the first time ascertained the organization of DNA replication in situ both spatially and temporally: each snapshot gives detailed spatial information and the correlation between both provides valuable information on the way active sites of DNA replication progress in situ [10, 11]. Later, the sequential use of directly labeled nucleotides made it possible to visualize sites of DNA synthesis in living cells at different time points. However, fluorescent dUTPs are not permeable through the cell membrane and need to be delivered by microinjection of cells or scratch loading ([12] and references therein). However, these elegant methods have the drawback that it is technically difficult to get even one nucleotide into the cell and incorporated into DNA making it not widely used and difficult to extend to multiple labelings. Finally, the development of fluorescent proteins for cell biological applications [13] made the next step possible, namely, the visualization of DNA replication progression in vivo over longer periods of time [14, 15]. Following fluorescently tagged PCNA in vivo, Sporbert et al. showed that new replication foci are always activated adjacently to already active ones [16] and proposed a domino model to explain the propagation of active DNA replication, where active replication results in its own propagation by, for instance, destabilizing chromatin/DNA and thereby facilitating firing of nearby origins [17].

Here, we present in detail two very useful methods, both allowing visualization of DNA replication dynamics in situ using fluorescence microscopy. The first, consisting of time-lapse imaging of living cells expressing fluorescently tagged replication proteins, provides both 3D spatial information and especially extensive temporal information. The second, a further development of pulse and chase experiments using modified nucleotides to label replication in situ [18], allows the visualization of up to four combined snapshots of replication sites active at selected time intervals. While the former approach can be used to visualize replication progression continuously, the latter facilitates the study of the spatial progression throughout chromatin domains thanks to the simultaneous visualization of all four replication time points. Like the Heisenberg uncertainty principle [19], achieving the highest possible spatial resolution is often incompatible with acquiring the most detailed temporal information.

2 Materials

All solutions and materials used for cell culture and live-cell microscopy must be sterile.

2.1 Live-Cell Visualization of DNA Replication Dynamics

1. Cell lines: for live-cell microscopy, cells should grow adherently. While the cell line to be used depends on the interest of the scientist, there are certain considerations simplifying the acquisition of data (*see* **Note 1**). In general, transiently expressed fluorescently tagged replication factors are necessary. However, there are also stable cell lines available [15].
2. Growing medium: use the standard medium required for the cell line to be imaged.
3. Pre-warmed PBS containing 0.5 mM EDTA and 0.05 % trypsin.
4. Plasmids: mammalian expression vectors coding for the replication factor of interest tagged to a fluorescent protein. The fluorescent marker should be chosen according to the wavelengths that can be imaged using the microscope available. It is possible to combine different fluorescent markers, also depending on the microscope setup. The most standard marker, which can typically be imaged in most microscopes, is green fluorescent protein (GFP) [20]. Replication factors most commonly used to label sites of ongoing replication in living cells are PCNA and DNA Ligase 1 [14, 15, 21].
5. Transfection reagents: nucleofection system from Amaxa (Lonza), nucleofection solution V, cuvette, and pipette (*see* **Note 2**).
6. Microscopy dishes: the form and size depends on the optical table inset available in the microscope. The bottom has to be thin enough for higher magnification objectives to be able to image through to the sample. Material can be glass or optical plastic. Glass lids are recommended for optimal contrast images (*see* **Note 3**).
7. Microscope: for high-resolution imaging of living cells, we recommend the use of a spinning disk confocal microscope, characterized by high-speed acquisition and low phototoxicity to cells. The stage should be motorized to allow the acquisition of 3D stacks at several points in one experiment.
8. Incubation chamber: the incubation chamber on the microscope must keep a constant temperature, CO_2, and humidity imitating the normal cell growth conditions (*see* **Note 4**).

2.2 Polytemporal DNA Replication Staining

1. Growth medium.
   Human cervical cancer cells (HeLa) and *M. cabrerae* fibroblasts [22] are cultivated in Dulbecco's Modified Eagle's Medium (DMEM) supplemented with 10 % fetal calf serum (FCS), 2 mM L-glutamine, and 25 mg/l gentamicin.

2. Denaturation.
   (a) Enzymatic denaturation: DNaseI (Roche), 2× DNase buffer: mix 60 mM Tris–HCl pH 8.1, 0.66 mM $MgCl_2$ and 1 mM mercaptoethanol in ddH_2O.
   (b) Acid denaturation: mix 336 µl 12 N HCl with 10 µl Triton X-100 and 654 µl ddH_2O (freshly prepared).
3. PBST wash buffer.

   Mix 1× PBS with Tween 20 to a final concentration of 0.01 %.
4. PBSTE DNAse stop buffer.

   Add 1 mM EDTA to 1× PBST.
5. Blocking buffers.

   4 % bovine serum albumin (BSA) in PBS.

   0.2 % fish skin gelatin (Sigma) in PBS.
6. Primary antibodies/chemical detection.
   (a) Click-iT EdU Alexa Fluor 488 Imaging Kit (Invitrogen).
   (b) Rat anti-bromodeoxyuridine (BrdU), reacts weakly with chlorodeoxyuridine (CldU) (Gentaur Molecular Products, catalog no. OBT0030CX).
   (c) Mouse anti-bromodeoxyuridine (BrdU), reacts also with iododeoxyuridine (IdU) (Becton Dickinson, catalog no. 347580).
   (d) Anti-DNA Ligase 1 rabbit polyclonal antibody [14].
7. Secondary antibodies (*see* **Note 5**).
   (a) CF405M-conjugated goat anti-mouse IgG (H + L) highly cross-adsorbed, 2 mg/mL (Biotium).
   (b) Cy5-conjugated AffiniPure donkey anti-rat IgG (H + L) highly cross-adsorbed, 1.5 mg/mL (Jackson ImmunoResearch Europe).
   (c) Cy3-conjugated AffiniPure donkey anti-rabbit IgG (H + L) highly cross-adsorbed, 1.5 mg/mL (Jackson ImmunoResearch Europe).
8. Mounting.

   Add 8 g Moviol 4-88 (Polyscience) to 40 ml 0.2 M Tris–HCl pH 8.5 and dissolve by heating to 50–60 °C with occasional stirring. After cooling down, add 20 ml glycerol and 1–2.5 % DABCO (anti-fading agent) and spin at 3,800 × *g* for 15 min, aliquot supernatant and store at –20 °C.

   Alternatively, use Vectashield mounting medium (Vector Laboratories, Inc.).

3 Methods

Below, we provide detailed protocols for (1) replication labeling by live-cell microscopy for mouse embryonic fibroblasts and (2) fixed cell polytemporal replication imaging in human cervical cancer cells and cabrera's vole fibroblasts, a rodent species endemic from the Iberian peninsula [22].

3.1 Live-Cell Visualization of DNA Replication Dynamics

Here, we present a detailed protocol to image active sites of DNA replication and, simultaneously, highlight specific nuclear regions, in this case using MaSat-GFP, a polydactyl zinc finger protein that specifically binds the major satellite repeats enriched at mouse constitutive heterochromatin (*see* Fig. 1 and Movie S1).

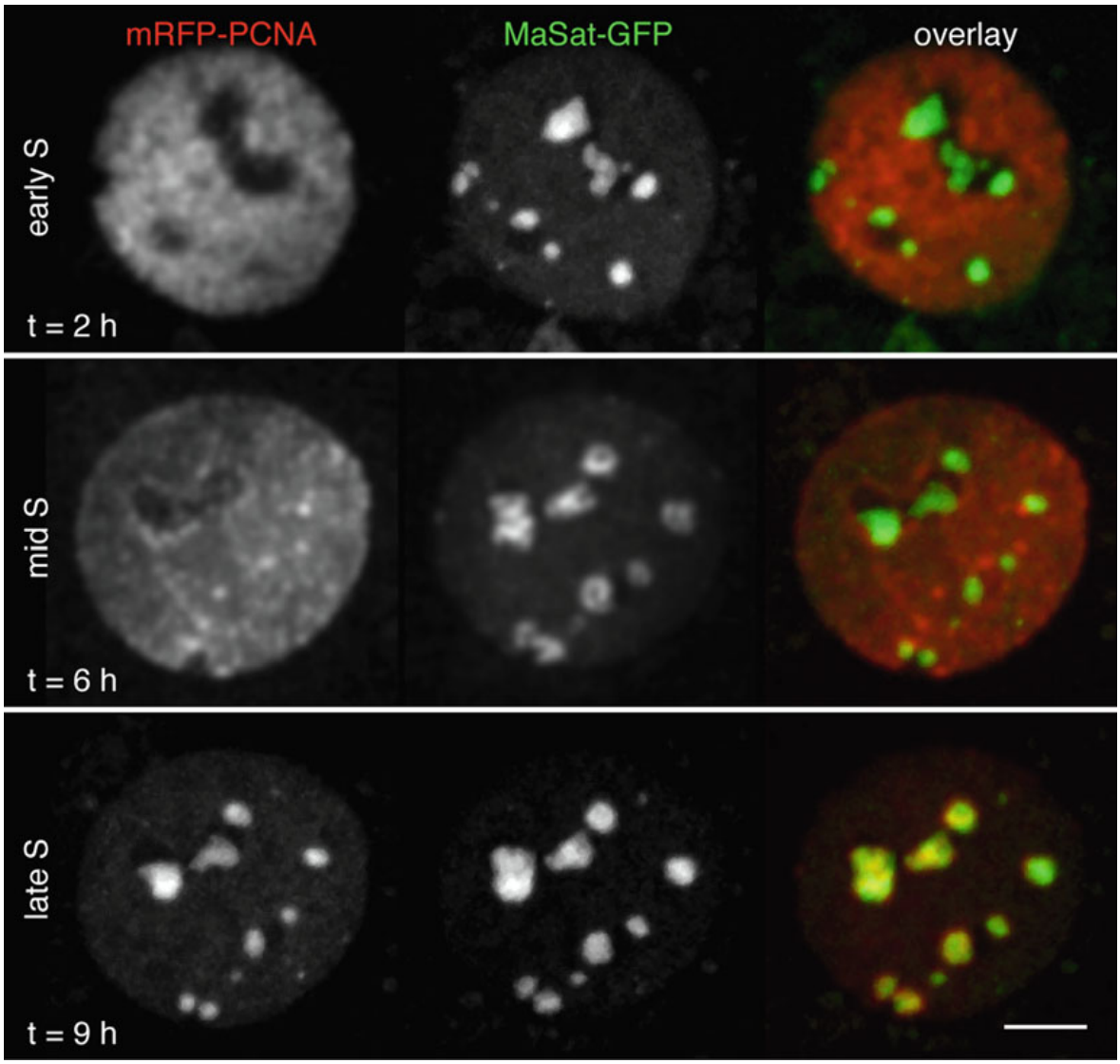

Fig. 1 Mouse embryonic fibroblast transiently co-expressing mRFP-PCNA, as a marker for sites of ongoing DNA replication and MaSat-GFP, as a marker for heterochromatin. Cells were imaged in a spinning disk microscope equipped with a climatization chamber so as to maintain constant temperature (37 °C), 5 % CO_2 and 60 % humidity. 3D confocal stacks were acquired at 1 h time intervals for a period of 12 h. Exemplary images of the same cell undergoing different S-phase stages and exhibiting the corresponding characteristic patterns. Scale bar: 5 μm

Different nuclear regions can be visualized specifically using various in vivo markers [23–25]. The protocol is adapted to image cells in a 35 mm glass-bottomed dish.

1. Pre-warm growing medium and PBS + EDTA to 37 °C and trypsin and nucleofection solution to room temperature. Prepare the dish where electroporated cells will be seeded by adding the final volume of growing medium (2 ml for a 35 mm dish) and keep it in an incubator so that the medium reaches 37 °C and CO_2 diffuses into it.
2. Use a $0.5–1 \times 10^6$ adherently growing cells (*see* **Note 6**) on, e.g., a 10 cm diameter plate. Remove growing medium and wash carefully with 5 ml PBS EDTA so as not to detach cells from the surface. Add 0.5 ml trypsin and incubate at 37 °C for 2–5 min. Monitor cell detachment under a microscope. When most cells have detached from the growing substrate and are now single cells, stop the reaction by addition of 4.5 ml growing medium. If cells clump, carefully pipette the cell suspension up and down a couple of times before stopping the trypsin reaction. Centrifuge the cells for 7 min at $300 \times g$.
3. Prepare 100 µl of nucleofection solution with 2 µg total plasmid DNA.
4. Once the cells are pelleted, discard the supernatant and carefully resuspend them in 100 µl nucleofection solution with plasmid DNA. Transfer the cell suspension into an appropriate cuvette avoiding air bubbles. Immediately perform the electroporation using the appropriate program for your cells (*see* **Note 7**). Take the previously prepared dish from the incubator, pipette approximately 500 µl medium from the dish into the cuvette, and carefully resuspend the cells. Transfer cell suspension into the dish with the rest of the medium; carefully shake the dish and return it to the incubator. Incubate overnight.
5. On the next day, remove the medium, carefully wash once or twice with pre-warmed medium to remove dead cells and debris, and add new medium.
6. Before bringing the cells to the microscope, make sure that the incubation chamber is already at 37 °C, 5 % CO_2, and >40 % humidity level.
7. Place the dish with the transfected cells on the microscope. Allow the dish to acclimatize to the new conditions for some minutes before starting imaging. Slight changes in temperature can affect the material in such a way that the focal plane can change dramatically during the first 10–20 min.
8. Look for transfected cells using the longest wavelength possible and short exposure times to minimize phototoxicity (i.e., in the case of co-expression of GFP and mRFP tagged proteins,

look for transfected cells using the red channel and only quickly check to see whether the cells also express the GFP-tagged construct). Select cells (*see* **Note 8**) that express the minimal amount of fluorescent protein that can be imaged properly. Too high expression levels can lower the chances that transfected cells will pass normally through S-phase. Extreme overexpression can also cause apoptosis. In case the lid is to be removed/replaced, do so before selecting the cells for imaging, since the dish might otherwise be shifted (*see* **Note 9**).

9. Set up the imaging conditions finding a compromise between phototoxicity and undersampling. The ideal conditions depend strongly on the cell line, since some cells are more sensitive to transfection and phototoxicity. In general, acquiring *z*-stacks at a time interval of 10–30 min is usually enough to follow changes in replication patterns. The minimal time to acquire an entire S-phase/cell cycle depends on how fast the cells divide. Under optimal conditions, cells can be kept on the stage and imaged for over 2 days (*see* **Note 10**).

3.2 Polytemporal DNA Replication Staining

Here, we present the detailed protocol for imaging multiple replication time points in mammalian cells (*see* Fig. 2). Proliferating cells are supplied with thymidine analogs, which are incorporated in the replicating genomic DNA for the duration of the pulse. Incorporation of modified nucleotides is stopped by chasing with excess unlabeled thymidine (*see* **Note 11**). The protocol is adapted for multiple 16 mm diameter coverslips in a 60 mm cell culture dish. Pulse-chase length needs to be adapted to doubling time and S-phase duration of the respective cell line, as well as to the purpose of the experiment. In principle, any replicating, cultured cells can be used for this approach.

1. Replication pulse labeling with thymidine analogs (IdU, EdU, and CldU).

   Label, e.g., 20 min with a final concentration of 10 μM IdU in growth medium at 37 °C, rinse twice with pre-warmed growth medium, and incubate cells for, e.g., 60 min with 200 μM thymidine in growth medium at 37 °C. Rinse again twice to remove thymidine from growth medium.

   Label 20 min with a final concentration of 10 μM EdU in growth medium at 37 °C, rinse two times with growth medium, and incubate cells for 60 min with 200 μM thymidine in growth medium at 37 °C. Rinse again twice to remove thymidine from growth medium.

   Label 20 min with a final concentration of 10 μM CldU in growth medium at 37 °C, rinse two times with growth medium, and incubate cells for 60 min with 200 μM thymidine in growth medium at 37 °C (*see* **Note 12**).

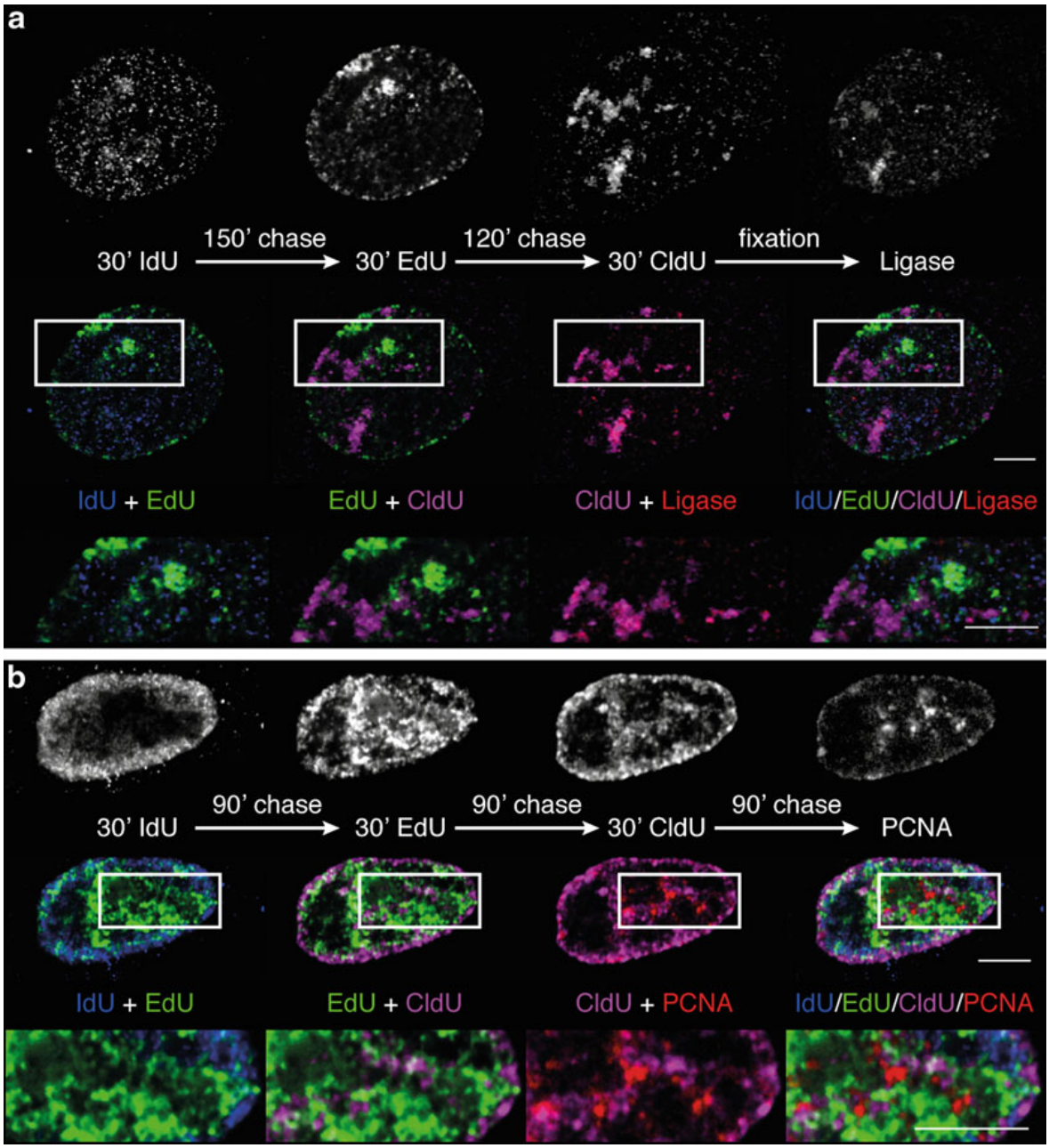

Fig. 2 Quadruple replication labeling in mammalian cells. Mid optical section of confocal images. (**a**) Six hour multiple pulse-chase replication staining in *M. cabrerae* fibroblast with immediate fixation after the CldU pulse. IdU pulse in *blue*, EdU pulse in *green*, CldU pulse in *magenta,* and DNA Ligase 1 in *red*, pulse and chase times as given in the image. (**b**) Six hour multiple pulse-chase replication staining in HeLa cells expressing mCherry-PCNA with fixation following CldU pulse and chase. IdU pulse in *blue*, EdU pulse in *green*, CldU pulse in *magenta,* and PCNA in *red*, pulse and chase times as given in the image. *Top row*: single replication stainings. *Middle row*: overlaid images of two sequential pulses followed by an overlay of all four pulses. *Bottom row*: selected ROI from the *middle row*. Scale bars: 5 μm

2. Fixation.
   Rinse cells once with PBS at room temperature to remove growth medium before fixing with 3.7 % formaldehyde in PBS for 10 min.
   Remove fixative and rinse two to three times with PBST.
   Cells can be stored at this point in PBS with 0.02 % Na-azide at 4 °C for several days.
3. Staining chamber.
   Prepare a lightproof chamber with a wet filter paper to maintain a humid environment and place parafilm on top of the filter [26]. Transfer coverslips to the chamber (*see* **Note 13**).
4. Permeabilization.
   To allow antibody penetration, permeabilize the cells with 0.5 % Triton X-100 in PBS for 10–20 min at room temperature. Wash the cells three times in PBST for 0, 5, and 10 min (hereafter referred to as triple wash) to remove the permeabilization reagent (*see* **Note 14**).
5. Detection of replication labeling (*see* **Note 15**).
   Use the ClickiT-EdU kit according to manufacturer's protocol to detect incorporated EdU followed by a triple wash (*see* **Note 16**).
   Block with 0.2 % fish skin in PBS for 45 min at room temperature.
   Mix 0.25 µl rat anti-BrdU Gentaur antibody solution (CldU detection) with 12.5 µl 2× DNase buffer and 12.5 µl 4 % BSA in PBS. Add 1 U DNaseI and incubate at 37 °C for 1 h, followed by a triple wash with PBSTE (*see* **Notes 17** and **18**).
   Mix 6.25 µl mouse anti-BrdU Becton Dickinson antibody solution (IdU detection) with 0.25 µl rabbit anti-DNA Ligase 1 antibody and 23.5 µl 4 % BSA in PBS and incubate at room temperature for 60 min, followed by a triple wash.
   Mix 0.06 µl anti-mouse IgG CF405M, 0.3 µl anti-rat IgG Cy5, 0.5 µl anti-rabbit IgG Cy3, and 24 µl 4 % BSA in PBS to perform secondary antibody incubation at room temperature for 60 min, followed by a triple wash.
6. Mounting.
   Rinse with ddH_2O to remove salts. Mount coverslips on microscope glass slide with Vectashield and seal with nail polish or mount with Moviol (*see* **Note 19**).

4 Notes

1. Factors to consider when choosing a cell line to perform live-cell microscopy include:
   - How well the cells can be transfected (transfection and expression rate)
   - How well the cells tolerate imaging-derived phototoxicity

- How much the cells move
- How fast they divide

2. While a good transfection rate is a factor to consider when choosing a transfection method, when following cell cycle progression at a single cell level, it is more important to achieve a moderate expression level. We recommend the nucleofection system from Amaxa (Lonza), although other methods can also be used.
3. Usually, the lid of microscopy dishes is of a thick plastic, which prevents good contrast images. For short-term imaging, it is possible to simply remove the lid.
4. If it is not possible to regulate the CO_2 and humidity levels, an alternative is to add 10 mM HEPES buffer to phenol-free medium and seal the dish with, for instance, paraffin to avoid evaporation of the medium.
5. Secondary antibodies indicated here can be substituted with your own favorite antibodies, as long as they are cross-absorbed to avoid cross-reaction with the other antibodies and the fluorophores conjugated provide enough spectral separation to be imaged by your microscope.
6. Cell density is a key factor for live-cell imaging of DNA replication. While a too high density can result in cell contact inhibition and therefore prevent cells from cycling, a too low density can result in cells moving more freely along the growing surface, making it extremely hard to keep them in frame over several hours. The optimal cell density depends on the cell line used: mouse fibroblasts and myoblasts tend to move, and therefore, a rather high density is recommended. On the other hand, HeLa cells, for instance, are less mobile and can therefore be plated at a lower density.
7. The program B-032 gives good results for mouse embryonic fibroblasts, C2C12 mouse myoblasts, HeLa cells, and *M. cabrerae* fibroblasts.
8. If the acquisition software allows the possibility of multipoint and mosaic imaging (stitching), the decision should be made depending on both the transfection rate and the mobility of the cell line used: a high transfection rate and cells that move fast are better imaged using the mosaic function, while sparsely transfected cells, or cells that barely move, are better imaged selecting separate points across the dish.
9. For time-lapse imaging over several hours, removing the lid would result in evaporation of the medium and possibly contamination of the sample. Therefore, in such cases it is better to replace the lid by a glass coverslip or keep the plastic lid.
10. In an asynchronous population at any given time point, the user will observe cells undergoing all of the different cell cycle substages.

Mitotic cells are easily recognized using phase contrast or DIC by their spherical morphology. At this stage of the cell cycle, PCNA diffuses throughout the cytoplasm. During G1 and G2, PCNA is exclusively nuclear but distributed homogenously. As S-phase begins, PCNA distribution becomes focal. During early S-phase the replication foci labeled by PCNA are distributed throughout the nucleus with the exception of the nuclear and nucleolar periphery. As cells progress into mid S-phase, the replication foci relocalize to these peripheral regions. During the second half, or late, S-phase, replication foci cluster at heterochromatic regions, giving the impression, at the confocal microscopy level, of fewer but larger foci (Fig. 1 and Movie S1).

11. With this pulse-chase-pulse labeling protocol, sequentially replicated regions of the genome are marked with differently modified nucleotides and visualized simultaneously within single cells. This protocol allows following the spatiotemporal dynamics of DNA replication progression in situ (Fig. 2).
12. We chose this specific chronological labeling order to facilitate visualization of potential cross-reaction between IdU and CldU antibodies. The additional intermediate EdU labeling time point allows a clear discrimination between both IdU and CldU labeling patterns. A high colocalization between both IdU and CldU antibodies signals indicates spurious cross-reaction of the primary antibodies with both nucleotides.
13. To reduce the required amount of antibodies, we use a "cell down protocol." A 25 µl drop of staining reagent for each 16 mm diameter coverslip was placed on the parafilm in the humidified chamber. The coverslips were placed with cells facing downward onto the reagent carefully avoiding any air bubbles. If conventional methods are used instead of the cell down protocol, the respective amounts of reagents have to be adapted.
14. For PCNA detection, incubate cells for 10 min in ice-cold methanol and air-dry coverslips. Cell shape is usually affected by MeOH incubation and air-drying.
15. Nucleotide labeling and fluorescently coupled proteins are readily combinable with other (immuno) fluorescent labeling methods. Chromosome painting, methylation labeling, and chromocenter labeling are only a few among many possible permutations.
16. We observed intensity decrease in other fluorochromes when the ClickiT-EdU kit was applied as the final detection step.
17. Primary antibodies rat anti-BrdU Gentaur and mouse anti-BrdU Becton Dickinson were detected sequentially to minimize cross-reaction. A high salt wash in between is not essential but improves the quality of the staining by decreasing cross-reactions.

18. Alternatively to DNaseI treatment, acid denaturation can be performed after permeabilization and before the first detection step to expose the modified nucleotides for antibody recognition. For acid denaturation, incubate with 4 N HCl solution (*see* Subheading 2) for 10 min at room temperature. While acid denaturation can cause artifacts and partially damage protein epitopes, such as the ones recognized by the anti-DNA Ligase 1 antibodies, nucleotide recognition is generally improved.
19. Each mounting agent has different advantages. Vectashield allows later unmounting and restaining, whereas Moviol is a permanent mounting agent.

Acknowledgements

We thank Juan Alberto Marchal (University of Jaen, Spain) for the *Microtus cabrerae* fibroblasts and all present and past members of the laboratory for their contributions over the years. The laboratory of M. Cristina Cardoso is supported by grants of the German Research Foundation (DFG) and the Federal Ministry of Education and Research (BMBF).

References

1. Berezney R, Dubey DD, Huberman JA (2000) Heterogeneity of eukaryotic replicons, replicon clusters, and replication foci. Chromosoma 108:471–484
2. Nakamura H, Morita T, Sato C (1986) Structural organizations of replicon domains during DNA synthetic phase in the mammalian nucleus. Exp Cell Res 165:291–297
3. Nakayasu H, Berezney R (1989) Mapping replicational sites in the eucaryotic cell nucleus. J Cell Biol 108:1–11
4. O'Keefe RT, Henderson SC, Spector DL (1992) Dynamic organization of DNA replication in mammalian cell nuclei: spatially and temporally defined replication of chromosome-specific alpha-satellite DNA sequences. J Cell Biol 116:1095–1110
5. Huberman JA, Riggs AD (1966) Autoradiography of chromosomal DNA fibers from Chinese hamster cells. Proc Natl Acad Sci USA 55:599–606
6. Huberman JA, Tsai A, Deich RA (1973) DNA replication sites within nuclei of mammalian cells. Nature 241:32–36
7. Gratzner HG (1982) Monoclonal antibody to 5-bromo- and 5-iododeoxyuridine: a new reagent for detection of DNA replication. Science 218:474–475
8. Bravo R, Macdonald-Bravo H (1985) Changes in the nuclear distribution of cyclin (PCNA) but not its synthesis depend on DNA replication. EMBO J 4:655–661
9. Cardoso MC, Leonhardt H, Nadal-Ginard B (1993) Reversal of terminal differentiation and control of DNA replication: cyclin A and Cdk2 specifically localize at subnuclear sites of DNA replication. Cell 74:979–992
10. Aten JA, Bakker PJ, Stap J, Boschman GA, Veenhof CH (1992) DNA double labelling with IdUrd and CldUrd for spatial and temporal analysis of cell proliferation and DNA replication. Histochem J 24:251–259
11. Manders E, Stap J, Brakenhoff G, Van Driel R, Aten J (1992) Dynamics of three-dimensional replication patterns during the S-phase, analysed by double labelling of DNA and confocal microscopy. J Cell Sci 103:857–862
12. Schermelleh L, Solovei I, Zink D, Cremer T (2001) Two-color fluorescence labeling of early and mid-to-late replicating chromatin in living cells. Chromosome Res 9:77–80
13. Chalfie M, Tu Y, Euskirchen G, Ward WW, Prasher DC (1994) Green fluorescent protein as a marker for gene expression. Science 263:802–805
14. Cardoso MC, Joseph C, Rahn HP, Reusch R, Nadal-Ginard B, Leonhardt H (1997) Mapping

and use of a sequence that targets DNA ligase I to sites of DNA replication in vivo. J Cell Biol 139:579–587
15. Leonhardt H, Rahn H, Weinzierl P, Sporbert A, Cremer T, Zink D, Cardoso M (2000) Dynamics of DNA replication factories in living cells. J Cell Biol 149:271–280
16. Sporbert A, Gahl A, Ankerhold R, Leonhardt H, Cardoso MC (2002) DNA polymerase clamp shows little turnover at established replication sites but sequential de novo assembly at adjacent origin clusters. Mol Cell 10:1355–1365
17. Chagin VO, Stear JH, Cardoso MC (2010) Organization of DNA Replication. Cold Spring Harb Perspect Biol 2
18. Casas-Delucchi CS, Brero A, Rahn H-P, Solovei I, Wutz A, Cremer T, Leonhardt H, Cardoso MC (2011) Histone acetylation controls the inactive X chromosome replication dynamics. Nat commun 2:222
19. Heisenberg W (1927) Über den anschaulichen Inhalt der quantentheoretischen Kinematik und Mechanik. Zeitschrift für Physik 43:172–198
20. Shaner NC, Steinbach PA, Tsien RY (2005) A guide to choosing fluorescent proteins. Nat Methods 2:905–909
21. Sporbert A, Domaing P, Leonhardt H, Cardoso MC (2005) PCNA acts as a stationary loading platform for transiently interacting Okazaki fragment maturation proteins. Nucleic Acids Res 33:3521–3528
22. Bullejos M, Burgos M, Jimenez R, Sanchez A (1996) Distribution of sister-chromatid exchanges in different types of chromatin in the X-chromosome of Microtus cabrerae. Experientia 52:511–515
23. Lindhout BI, Fransz P, Tessadori F, Meckel T, Hooykaas PJJ, van der Zaal BJ (2007) Live cell imaging of repetitive DNA sequences via GFP-tagged polydactyl zinc finger proteins. Nucleic Acids Res 35:e107
24. Casas-Delucchi CS, van Bemmel JG, Haase S, Herce HD, Nowak D, Meilinger D, Stear JH, Leonhardt H, Cardoso MC (2012) Histone hypoacetylation is required to maintain late replication timing of constitutive heterochromatin. Nucleic Acids Res 40:159–169
25. Weidtkamp-Peters S, Rahn H-P, Cardoso MC, Hemmerich P (2006) Replication of centromeric heterochromatin in mouse fibroblasts takes place in early, middle, and late S phase. Histochem Cell Biol 125:91–102
26. Cardoso MC, Leonhardt H (1995). Immunofluorescence techniques in cell cycle studies. In: Pagano, M (ed) Cell cycle: materials and methods. Heidelberg, Springer-Verlag, pp 15–28

4 High-Resolution analysis of mammalian DNA replication units

4.1 Aims of "High-Resolution analysis of mammalian DNA replication units"

After establishing a multi-replication labeling (see Chapter 3 [134]) to achieve higher spatio-temporal resolution of DNA replication in fixed cells, I aimed to develop a tool to quantify DNA replication foci imaged by confocal and super-resolution microscopy free of observer bias.

Therefore, I designed a computer-guided approach to quantify thousands of DNA replication foci in hundred of cells with a minimal amount of operator interaction, which is presented in this chapter. As recognition and segmentation of images in regions of interest highly depends on thresholding parameters and image noise, consistent selections of the analysis parameters is of the upmost importance to implement an objective and bias free quantification. The computer-guided quantification relays on intrinsic image parameters, the threshold, for example, is calculated based on the intensity histogram. This algorithm based approach is therefore a robust tool during experimental replicates to remove observer bias and achieve consistent quantifications during biological and technical replicates.

4.2 Contributions

- M. Reinhart developed the protocol for "3D-SIM Images" and prepared Figure 1 and 4.
- M. Reinhart cowrote the manuscript.

4.3 Publication

Chapter 3

High-Resolution Analysis of Mammalian DNA Replication Units

Vadim O. Chagin*, Marius Reinhart*, and M. Cristina Cardoso

Abstract

Genomic DNA of a eukaryotic cell is replicated once during the S-phase of the cell cycle to precisely maintain the complete genetic information. In the course of S-phase, semiconservative DNA synthesis is sequentially initiated and performed at thousands of discrete patches of the DNA helix termed replicons. At any given moment of S-phase, multiple replicons are active in parallel in different parts of the genome. In the last decades, tools and methods to visualize DNA synthesis inside cells have been developed. Pulse labeling with nucleotides as well as detecting components of the replication machinery yielded an overall picture of multiple discrete sites of active DNA synthesis termed replication foci (RFi) and forming spatio-temporal patterns within the cell nucleus. Recent advances in fluorescence microscopy and digital imaging in combination with computational image analysis allow a comprehensive quantitative analysis of RFi and provide valuable insights into the organization of the genomic DNA replication process and also of the genome itself. In this chapter, we describe in detail protocols for the visualization and quantification of RFi at different levels of optical and physical resolution.

Key words 3D-SIM, Confocal microscopy, DNA replication, Fluorescent protein, High-resolution fluorescence microscopy, Immunofluorescence staining, Nucleotide incorporation, Replication foci

1 Introduction

Precise and complete duplication of genome is essential for normal proliferation of cells. Eukaryotic cells duplicate their genome in the course of S-phase of the cell cycle by sequential initiation of DNA synthesis in multiple genomic locations. Stretches of DNA that are replicated from a single initiation event are termed replicons ([1]; reviewed in [2]). At any given moment of S-phase, many replicons are synthesized in multiple locations in parallel.

In addition to labeling and detecting the protein components of the DNA replication machinery, the high processivity of the replicative DNA polymerases allows visualization of the synthesized DNA by incorporation of nucleotide analogs [3–5].

*Vadim O. Chagin and Marius Reinhart have contributed equally to this work

Sonya Vengrova and Jacob Dalgaard (eds.), *DNA Replication: Methods and Protocols*, Methods in Molecular Biology, vol. 1300, DOI 10.1007/978-1-4939-2596-4_3, © Springer Science+Business Media New York 2015

At the cellular level, active sites of ongoing DNA synthesis are manifested by focal incorporation of the nucleotides and accumulation of the replication machinery proteins and referred to as replication foci—RFi [3, 6, 7]. Quantification and analysis of RFi characteristics have been widely used in DNA replication studies (*see* Fig. 1 and references therein [3, 8–12, 4, 13–20]). From such studies, it was established that genome replication follows a series of subnuclear spatial RFi patterns, which roughly trail the chromatin epistate, with the condensed constitutive heterochromatin replicating in the second half of S-phase [21, 8, 9, 7].

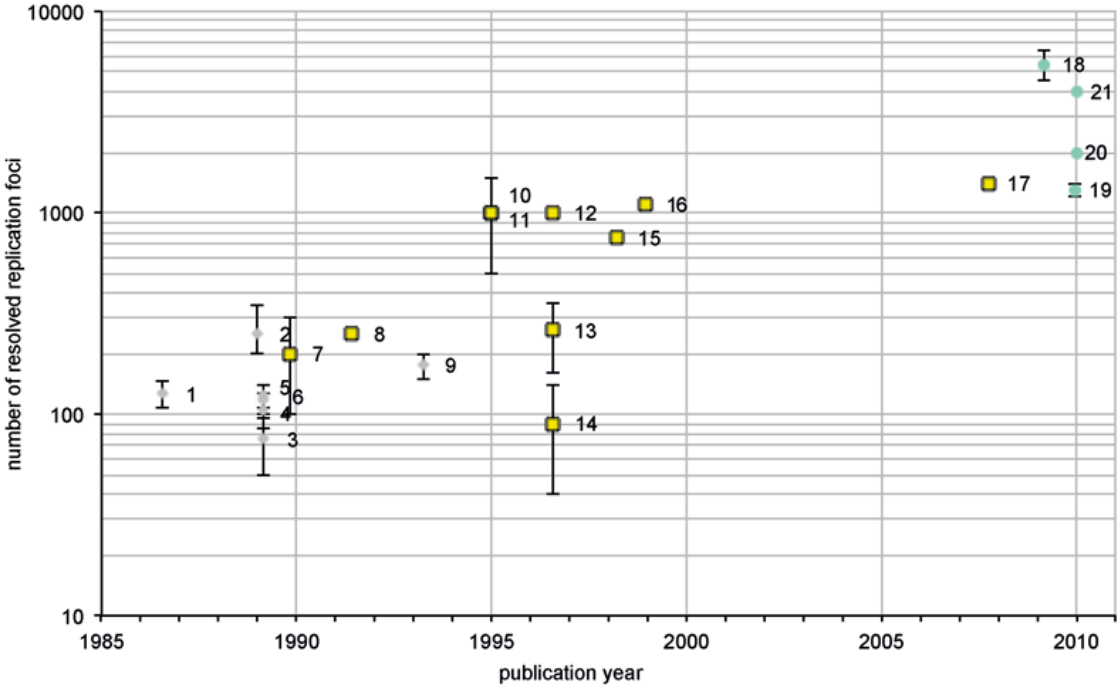

#	replication foci numbers	year, month	cell line name	cell line origin/description	reference	imaging method
1	126+-18,8	1986, Aug	3Y1-B (IMR-90|100T)	rat embryonic fibroblast	Nakamura et al.	wide field
2	150-300 (~250)	1989, Jan	3T3	mouse fibroblast cells	Nakayasu and Berezney	wide field
3	<100 (S5)	1989, Mar	MCF-7 | cov362c14 | cov86044 (S5)	human cancer cell	van Dierendonck et al.	wide field
4	85-127 (S1)	1989, Mar	MCF-7 (S1)	human cancer cell	van Dierendonck et al.	wide field
5	107-141 (S1)	1989, Mar	cov362c14 (S1)	human cancer cell	van Dierendonck et al.	wide field
6	96-138 (S1)	1989, Mar	cov86044 (S1)	human cancer cell	van Dierendonck et al.	wide field
7	100-300	1989, Nov	Xenopus (sperm nuclei in egg extract)	in vitro fertilized Xenopus eggs	Mills et al.	CLSM
8	250	1991, Jun	3T3 (S1)	mouse fibroblast cells	Fox et al.	CLSM
9	150-200	1993, Apr	HeLa	human cervical cancer cell	Hozák et al.	wide field
10	500-1500	1995, Jan	K562	human myelogenous leukemia	Tomilin et al.	CLSM
11	500-1500	1995, Jan	MCF-7	human breast cancer	Tomilin et al.	CLSM
12	>1000	1996, Aug	3T3	mouse fibroblast cells	Berezney et al.	CLSM
13	160-360 (SE)	1996, Aug	V79 (SE)	chinese hamster fibroblasts	Manders et al.	CLSM
14	40-140 (SL)	1996, Aug	V79 (SL)	chinese hamster fibroblasts	Manders et al.	CLSM
15	750	1998, Mar	HeLa	human cervical cancer cell	Jackson and Pombo	CLSM
16	1100	1998, Dec	3T3	mouse fibroblast cells	Ma et al.	CLSM
17	1400	2007, Oct	GM05389	human fetal lung fibroblasts	Gotoh	CLSM
18	5460 ± 923	2009, Mar	HeLa	human cervical cancer cell	Ligasová et al.	EM
19	~1200-1400 (SE)	2009, Dec	MRC5	normal human fetal lung fibroblast	Cseresnyes et al.	STED
20	~2000 (SL)	2010, Jan	C2C12 (SL)	mouse myoblast cells	Baddeley et al.	SMI
21	4000 (SL)	2010, Jan	C2C12 (SL)	mouse myoblast cells	Baddeley et al.	3D-SIM

Fig. 1 Historical progress in DNA replication foci quantification

Attempts to quantify RFi numbers in cells and to relate them with estimations of total replicons per genome by DNA fiber analysis ([22]; reviewed in [23]) were initiated in the mid-1980s and are summarized chronologically in Fig. 1. With the advent of laser scanning confocal microscopy as well as digital imaging and image analysis in the mid-1990s, the numbers of RFi increased severalfold. In the last years, the development of super-resolution fluorescence microscopy has once again boosted the numbers of RFi (Fig. 1). The precision of RFi numbers analysis can be improved by (1) changing physical resolution of the cellular preparations [24], (2) increasing optical resolution of the cellular images [20], and (3) improving accuracy of RFi quantification [16]. In general, advances in each of those aspects of RFi analysis have led to higher numbers of RFi identified (Fig. 1). At the highest precision of quantification, RFi numbers were comparable with the theoretical estimated numbers of active replicons [20]. Quantification of RFi, therefore, can provide detailed information regarding organization of genome duplication at a molecular level.

In this chapter, we describe in detail approaches for labeling and for statistically sound quantification of DNA replication units at different levels of optical and/or physical resolution. Sequential labeling with different nucleotide analogs or direct analysis of RFi in live cells expressing fluorescent replication factors [25] and/or after incorporation of fluorescent nucleotide analogs can be used to elucidate dynamic aspects of the DNA replication process. Depending on the particular question to be addressed, the researcher can select an optimal combination of steps of the protocols presented to quantitatively analyze DNA replication units with the necessary level of accuracy, while minimizing experimental material and time. The protocols presented can be adapted and used in the analysis of intracellular distribution of a variety of biomolecules involved in localized molecular processes, e.g., DNA repair or transcription.

2 Materials

2.1 (A)Synchronously Growing Cell Cultures

1. Standard cell culture equipment.

2.2 RFi Labeling by Cell-Permeable Nucleotide Incorporation

1. 1,000× stock solution of halogenated nucleotide analog, e.g., BrdU (5-bromo-2′-deoxyuridine): 10 mM BrdU in ddH_2O, filter sterilized, aliquoted, and stored at −20 °C; *or* 1,000× stock solution of alkyne labeled nucleotide, e.g., EdU (5-ethynyl-2′-deoxyuridine): 10 mM EdU in DMSO (*see* **Note 1** for advantages and disadvantages of different nucleotide analogs).
2. Standard cell culture media and supplements.

2.3 RFi Labeling by Cell-Impermeable Nucleotide Incorporation

1. Borosilicate coverslips, round or square, 0.152 mm thick.
2. Standard cell culture media and supplements.
3. Parafilm.
4. "Humid chamber": Petri dish diameter 150 mm wrapped with aluminum foil and having a piece of wet absorbent paper inside [29].
5. Nucleotides: 10 mM stock solution of fluorescently labeled nucleotide, e.g., Cy3-dUTP.
6. A hypodermic needle.
7. Forceps.
8. Inverted microscope.

2.4 3D-Preserved Cell Preparations

1. PBS, 1×: (8 g NaCl , 0.2 g KCl_2, 17 g $Na_2HPO_4 \times 7H_2O$, 0.2 gKH_2PO_4 per liter of ddH_2O, pH ~ 6.8, prepare from autoclaved 10× stock solution).
2. 0.05–0.1 % Triton X-100 solution in PBS.
3. CSK buffer: 10 mM PIPES-KOH, pH 7.0, 100 mM NaCl, 300 mM sucrose, 3 mM $MgCl_2$.
4. 0.1 % TritonX-100 solution in CSK buffer.
5. 36.5–38 % formaldehyde in H_2O.
6. PBST: 1× PBS, 0.01 % Tween.

2.5 Hypotonically Resolved RFi

2.5.1 Harvesting Cells

1. PBST: 0.01 % Tween in 1× PBS.
2. Trypsin/EDTA solution: 0.025 Trypsin, 0.01 % EDTA in PBS.
3. Cell culture medium or fetal calf serum.
4. 15 ml conical tube.

2.5.2 Hypotonic Treatment

1. Hypotonic solution: 50–75 mM KCl in ddH_2O. Prepare fresh.
2. 99.8 % methanol.
3. ≥99.7 % acetic acid.

2.5.3 Fixation

1. MeAA solution: three volumes of cold methanol and one volume of acetic acid.

2.5.4 Slide Preparation

1. Pre-cleaned microscope slides.
2. MeAA solution (Subheading 2.5.3, **item 1**).
3. Pasteur pipette.
4. Water bath heated to 60–75 °C.
5. Heating table with regulated temperature or Bunsen burner or alcohol lamp.

2.6 RFi Detection

2.6.1 RFi Detection by Tagged Replication Factors

Protein components of the replication machinery can be labeled by expressing fluorescently tagged proteins, e.g., GFP-PCNA using:

(a) Transient expression: Corresponding expression construct (vector) and conventional (PEI, $CaPO_4$) or commercially available transfection protocols/kits for introducing vectors into cells.

(b) Stable expression: A number of mammalian cell lines stably expressing replication proteins have been reported [7, 26].

2.6.2 RFi Detection of Native (Untagged) Replication Proteins

1. Borosilicate coverslips, round or square, 0.152 mm thick.
2. Standard cell culture media and supplements.
3. Parafilm.
4. "Humid chamber": Petri dish diameter 150 mm wrapped with aluminum foil and having a piece of wet absorbent paper inside [29].
5. 0.1 % Triton X-100 solution in PBS (*see* Subheading 2.4, **item 2**).
6. 1 % BSA or 0.2 % fish skin gelatin in PBS.
7. PBST: 1× PBS, 0.01 % Tween.
8. Primary antibodies against the protein, e.g., anti-PCNA monoclonal antibody [27, 28] or anti-DNA ligase I rabbit polyclonal antibody [6].
9. Secondary fluorochrome-conjugated antibodies specific to the Ig of the primary antibodies *or* primary or secondary antibodies tagged to biotin and (strept)avidin conjugated to a fluorescent moiety (*see* **Note 2**).

2.6.3 RFi Detection of Cell-Permeable Nucleotide Analogs

1. Borosilicate coverslips, round or square, 0.152 mm thick.
2. Standard cell culture media and supplements.
3. Parafilm.
4. "Humid chamber": Petri dish diameter 150 mm wrapped with aluminum foil and having a piece of wet absorbent paper inside [29].
5. 0.1 % Triton X-100 solution in PBS (*see* Subheading 2.4, **item 2**).
6. 1 % BSA or 0.2 % fish skin gelatin in PBS.
7. PBST (*see* Subheading 2.6.2, **item 7**).
8. 1,000× DNaseI: 1 mg/ml DNaseI in 50 % glycerol. Stored at −20 °C and 2× denaturation buffer: 60 mM Tris–HCl (pH 8.1), 0.66 mM $MgCl_2$, 1 mM mercaptoethanol in ddH_2O (enzymatic denaturation); *or* 4 N HCl (acidic denaturation). These reagents are not necessary for click chemistry-based detection.

9. *BrdU*: mouse anti-BrdU antibody (BD, clone B44, Cat no: 347580, or clone IU-4, CALTAG Labs) and secondary anti-mouse Ig antibodies conjugated with Alexa dyes of appropriate emission wavelength; *or EdU*: click reagents labeled with Alexa dyes of appropriate emission wavelength (Baseclick or Invitrogen).

2.6.4 DNA Counterstaining

1. PBST (Subheading 2.6.2, **item 7**).
2. 1,000× DNA counterstaining stock solution: 1 mg/ml Hoechst 33258 in ddH_2O (350/461 nm excitation/emission maxima, respectively) *or* 1 mg/ml 4′,6-diamidino-2-phenylindole dihydrochloride (DAPI) (350/461 nm) in ddH_2O *or* 1 mM solution Molecular Probes TO-PRO®-3 Iodide (642/661 nm) in DMSO. Aliquot and store frozen.

2.7 Mounting

1. Pre-cleaned microscope slides.
2. Mounting medium: nonhardening antifadents, AF, Citifluor Ltd. CFM, Vector Laboratories Inc. Vectashield®; *or* hardening antifadents, Moviol [25], Molecular Probes ProLong® Gold.
3. Absorbent paper (lint-free).
4. Pigment-free nail polish.

2.8 Fluorescence Microscopy

1. Microscopy setup (*see* Subheading 3.8).

2.9 RFi Quantification

2.9.1 Confocal or Wide-Field Images: Segmentation of Replication Foci

1. ImageJ software, version 1.43 or later.

2.9.2 3D-SIM Images

1. ImageJ and Perkin Elmer Volocity 5 software.

3 Methods

Procedures with live cells are carried out in a tissue culture room equipped with a laminar flow biosafety cabinet and CO_2 incubator. All procedures with coverslips utilizing small volumes of solutions are carried out on a piece of Parafilm in the "humid chamber." (Bio)material disposal regulations should be diligently followed.

3.1 (A)Synchronously Growing Cell Cultures

Having an actively proliferating culture is a prerequisite for all protocols of replication sites detection. Generally, cells should be no more than 80 % confluent. Asynchronously growing cell cultures,

where cells in all stages of the cell cycle and, importantly, S-phase are present, can be obtained by regularly subculturing the cells to a lower density. For primary adherent cultures, enrichment of cells in particular periods of S-phase can be achieved by splitting the cultures after they become contact inhibited and obtaining samples at specific time points (typically starting 8–12 h after the cells are split). Alternatively, a chemical synchronization protocol can be applied [30, 31], though this may alter cellular metabolism [32].

Visually inspect the cells. An actively growing culture will be characterized by a sufficient number of mitotic cells and low amount of cell debris in the medium.

3.2 RFi Labeling by Cell-Permeable Nucleotide Incorporation

1. If cells are supposed to be grown further after the labeling (e.g., in pulse-chase-pulse experiments), take half of the conditioned medium from the dish with the cells and keep it in the incubator. Absence of differences in the medium characteristics will ensure unaltered S-phase dynamics.
2. Add nucleotide to the cell culture medium to a final concentration of 10 μM (*see* **Notes 3** and **4**).
3. Place the cells back into the CO_2 incubator and incubate for the desired period of time (*see* **Note 5**).
4. If further in vivo procedures are planned:
   (a) Collect and discard the medium containing the nucleotide.
   (b) Wash the cells with pre-warmed medium and discard wash medium.
   (c) Add standard volume of pre-warmed and conditioned culture medium.

3.3 RFi Labeling by Cell-Impermeable Nucleotide Incorporation [5]

1. Grow cells on coverslips to the highest density at which the cells still proliferate. A Petri dish containing several coverslips can be used.
2. Prepare the labeled nucleotide solution in pre-warmed cell culture medium (10–20 μl per 18–24 mm coverslips, final concentration 10 μM of the labeled nucleotide).
3. Prepare a hypodermic needle.
4. Using forceps, take a coverslip with the cells out of the Petri dish.
5. Remove the extra medium by touching the side of the Petri dish with the edge of the coverslip.
6. Place the coverslip into a new Petri dish of a size suitable to accommodate the coverslip.
7. Press the coverslip to the dish using the needle and add 10–20 μl of the labeled nucleotide solution.

8. While observing the cells on an inverted microscope, make a series of parallel scratches with the tip of the needle. Touching the cells with the needle will cause transient plasma membrane disruption and penetration of the diluted nucleotide into the cell's cytoplasm.
9. Put the Petri dish with the coverslip into the CO_2 incubator for 1–3 min.
10. Cover the coverslip with 1–2 ml of the warm conditioned cell culture medium taken from the "parent" Petri dish.
11. Incubate for the desired period of time (*see* **Note 6**).
12. Proceed for further treatments or fixation.

3.4 3D-Preserved Cell Preparations

1. Remove culture medium avoiding drying at any stages (*see* **Note 7**).
2. Wash the coverslips with the cells with PBS (*see* **Note 8**). Alternatively, coverslips with the cells can be placed into a new Petri dish with the PBS solution.
3. To reduce the background staining/signal from the non-bound fraction of the replication proteins, the following pre-treatment procedures can be used prior to fixation. If this step is not required, proceed directly to **step 6**.
4. (Optional) Extraction before fixation: incubate coverslip in 0.05–0.1 % Triton X-100 solution in PBS for 3 min at RT or incubate coverslip in 0.1 % TritonX-100 solution in CSK buffer [33] (*see* **Note 9**) 1–5 min at RT. This extraction can also be performed on ice, which is useful not to loose cells that detach easily.
5. Aspirate the pre-extraction solution.
6. Wash coverslips with PBS.
7. Remove the wash buffer.
8. Cover the cells with freshly prepared 3.7 % formaldehyde solution (*see* **Note 10**).
9. Incubate for 10–15 min at RT protected from light.
10. Remove formaldehyde and wash thoroughly with PBST at least twice (*see* **Note 11**).
11. Proceed to RFi staining (Subheading 3.6, *see* **Note 12**).

3.5 Hypotonically Resolved RFi

Hypotonic treatment leads to swelling of the cells (*see* **Note 13**). The consequent fixation with the mixture of methanol and acetic acid leads to extraction of many cellular proteins including histones. Drying the resulting cells/nuclei preparations on the glass slides leads to considerable flattening of the nuclei and enhanced physical resolution of the DNA replication foci (Fig. 2).

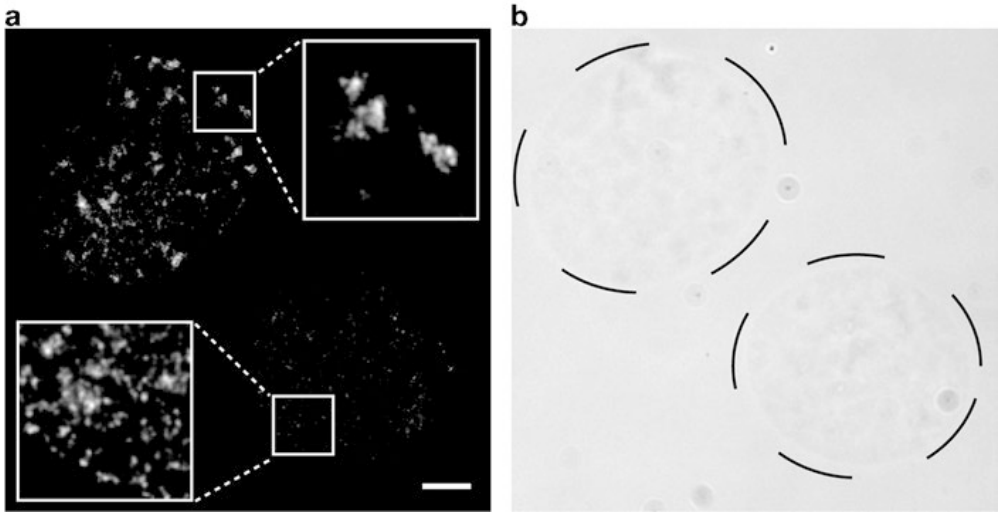

Fig. 2 Hypotonically resolved DNA replication foci. Mouse myoblasts growing at 70 % confluency were incubated with 10 μM BrdU for 15 min and processed as described under Subheadings 3.5–3.8. (**a**) Late S-phase (*upper*) and early S-phase (*lower*) RFi distribution patterns are presented with corresponding phase contrast images (**b**). Scale bar: 5 μm

3.5.1 Harvesting Cells

1. Replace culture medium with cold PBST. Wash twice.
2. Add pre-warmed trypsin/EDTA solution (0.4–0.5 ml per 25 cm^2) and incubate for 3–5 min at 37 °C.
3. Observe cells at the microscope.
4. When most of the cells become round, bump at the side of dish with your palm.
5. Check that the cells have detached and are floating.
6. Add a small amount of the cell culture medium or fetal calf serum to stop the trypsin action.
7. Collect cell suspension and place it into a 15 ml conical tube.
8. Spin down the cells at ~300 × *g* for 5 min at 4 °C.
9. Remove supernatant as completely as possible, leaving about 20–50 μl of the medium.
10. Resuspend the cells by gently tapping against the tube.

3.5.2 Hypotonic Treatment

1. Add 1–3 ml of pre-warmed hypotonic solution (*see* **Note 14**).
2. Incubate in a water bath at 37 °C for 15–30 min.
3. While incubating in the hypotonic solution, mix three volumes of cold methanol and one volume of acetic acid (3:1 MeAA solution, Carnoy's fixative) and place it into the fridge until use.
4. Centrifuge the cells at ~300 × *g* for 5 min at 4 °C (*see* **Note 15**).
5. Remove supernatant as completely as possible.
6. Resuspend cells in the remaining volume (20–50 μl) by gently tapping the tube. Do NOT resuspend the cells by pipetting.

3.5.3 Fixation

1. *Slowly* add several drops of freshly prepared ice-cold MeAA solution (*see* **Note 16**).
2. Incubate for 5 min at RT.
3. Add 0.5 ml more of MeAA solution and incubate for 10 min at RT.
4. Centrifuge at ~300 × *g* for 5 min at 4 °C.
5. Replace the solution with excess volume (1–2 ml) of fresh ice-cold MeAA.
6. Incubate for at least 30 min at 4 °C.
7. Centrifuge at ~300 × *g* for 5 min at 4 °C and replace the solution with excess volume (1–2 ml) of fresh ice-cold MeAA. Keep it at −20 °C for up to several weeks or proceed to the next step.
8. Centrifuge at ~300 × *g* for 5 min at 4 °C and resuspend the cells in a smaller volume (300–500 μl) of MeAA to get the desired concentration. The cells are preferably resuspended by tapping the tube against the table. Only very slow pipetting is acceptable.

3.5.4 Slide Preparation

1. Use pre-cleaned microscope slides or wash the slides thoroughly with mild detergent, rinse several times with ddH_2O, and air dry.
2. Immerse pre-cleaned slides in MeAA at least 15 min prior to use, and wipe slides dry with a lint-free tissue.
3. Drop 1–2 small (~15–20 μl) drops of cell suspension from Subheading 3.5.3, **step 8** above onto slide surface with a Pasteur pipette.
4. Allow the drops to spread.
5. Pass the slide through vapor of a water bath heated to 60–75 °C.
6. Dry it at RT or at 40 °C on the heated table or pass the slide through a flame or put the slide on a slightly tilted surface and let it air dry at RT.
7. Inspect the slide for the flatness of the nuclei.
8. The slides can be kept dry at 4 °C for several days before staining.

3.6 RFi Detection

It is recommended to use fluorescent groups with increased photostability, e.g., Alexa or Atto dyes. Signal from GFP-tagged protein can be additionally enhanced using anti-GFP antibodies [34]. For cells with RFi labeled by fluorescently tagged (e.g., GFP-tagged) proteins or by fluorescently tagged nucleotide incorporation, proceed directly to DNA counterstaining (Subheading 3.6.4).

3.6.1 RFi Detection by Tagged Replication Factors

Protein components of the replication units can be visualized by expressing fluorescently tagged replication proteins. For transient transfection with fluorescent replication factors, transfect the cells by following the steps of an optimal protocol for the cell type in question or following the manufacturer's instructions (*see* **Note 17**). Alternatively, cells stably expressing fluorescent replication at a level, which does not interfere with replication dynamics, can be used (*see* **Note 18**).

3.6.2 RFi Detection of Native (Untagged) Replication Proteins

1. Permeabilize cells by incubating in 0.1 % Triton X-100 solution for 10–20 min at RT (*see* **Note 19**).
2. Wash twice with PBS.
3. To block, incubate with 1 % BSA or 0.2 % fish skin gelatin in PBS for 20 min at RT.
4. Incubate with primary antibodies specific to the replication protein for an hour at RT.
5. Wash coverslip with PBST three times.
6. Incubate with secondary antibodies tagged to a fluorescent group.

3.6.3 RFi Detection of Incorporated Cell-Permeable Nucleotide Analogs

In case of halogenated nucleotide analogs, cells must be permeabilized and DNA denatured prior to incubation with primary antibodies (**steps 1–4** below). EdU detection requires only permeabilization of the cells (**steps 1, 2, 3** (optional), and 7, below). Detailed protocols for nonfluorescently tagged nucleotides detection are presented in [25].

The outline of the procedure is as follows:

1. Permeabilize cells by incubating in 0.1 % Triton X-100 solution for 10–20 min at RT (*see* **Note 19**).
2. Wash twice with PBS.
3. To block, incubate with 1 % BSA or 0.2 % fish skin gelatin in PBS for 20 min at RT.
4. (Skip this step in case of EDU detection and proceed directly to **step 7**)

   Perform acidic denaturation of DNA by incubation with 4 N HCl 30 min at RT, wash the cells thrice with PBST, and then incubate with primary antibodies specific to the incorporated nucleotide for 30–60 min at RT *or* enzymatically expose and detect the epitope by incubation in a 1× DNase buffer solution containing DNase I (20 U/ml) and anti-BrdU mouse monoclonal antibody for 30–60 min at 37 °C.
5. Wash coverslip with PBST three times.
6. Incubate with secondary antibodies tagged to a fluorescent group.

7. Detect the incorporated EdU by incubation with a fluorescent azide in the presence of Cu(I) according to the manufacturer's instructions.

3.6.4 DNA Counterstaining

1. Rinse coverslips with PBST.
2. Add 20–50 μl of 1× DNA counterstaining solution and incubate for 5 min at RT.

3.7 Mounting

1. Put a small drop of the mounting medium (*see* **Note 20**) on the microscope slide (for coverslip-grown cells).
2. If cells were grown and/or stained on a slide, proceed to (Subheading 3.7, **step 5**).
3. Wash salts away by dipping coverslips briefly in ddH_2O.
4. Remove excess water by touching absorbent paper with the edge of the coverslip.
5. Place the coverslip over the drop of mounting medium with the cells facing the mounting medium (*see* **Note 21**).
6. When mounting with hardening medium, let it solidify by incubating in the dark overnight at RT.
7. For liquid mounting medium, carefully put slides with coverslip down on a paper towel and wait for 5 min for excess media to be absorbed.
8. Seal coverslip with nail polish all-around.
9. Proceed for imaging.

3.8 Fluorescence Microscopy

Imaging of the labeled RFi can be performed using commercially available or custom-made microscopy setups (*see* **Note 22**). DNA replication foci in 3D-preserved nuclei can be imaged using confocal systems (laser scanning confocal systems or spinning (Nipkow) disk-based microscopes) or super-resolution setups, which allow 3D imaging. Using live-cell RFi labeling and confocal high temporal resolution microscopy or pulse-chase-pulse labeling approach [25] and multicolor super-resolution microscopy allows temporal analysis of DNA replication (*see* **Note 23**). Multicolor structured illumination microscopy (3D-SIM) [35] is the most promising multicolor super-resolution imaging approach, which has been successfully applied to RFi analysis [20, 36]. Due to their utmost flatness, RFi on the hypotonically treated nuclei preparations can be analyzed by the whole spectrum of microscopy techniques, including wide-field microscopy, confocal microscopy (*see* **Note 24**), and 2D super-resolution microscopy techniques [20, 37].

3.9 RFi Quantification

There are two major steps in object-counting procedures: first, the images are processed and/or segmented to discriminate between signal and background pixels, and, then, individual objects in the signal segment of the image are identified and counted. The different steps are summarized in Figs. 3 and 4.

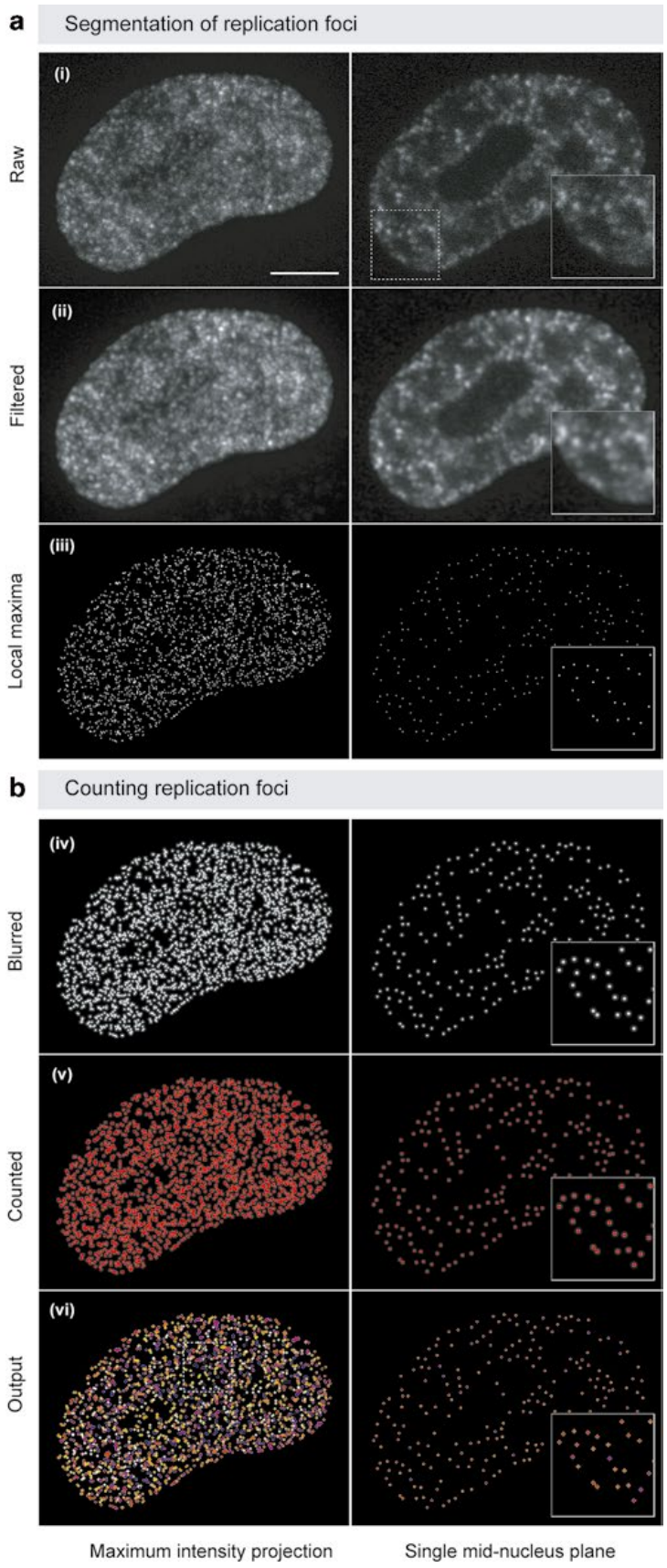

Fig. 3 Quantification of replication sites on conventional fluorescent microscopy images. An overview of the intermediate results of RFi quantification on 3D stacks of confocal images (**a**, **b**) described in Subheading 3.9.1. To quantify RFi in hypotonically flattened nuclei, the steps of part (**a**) suffice. Scale bar: 5 μm

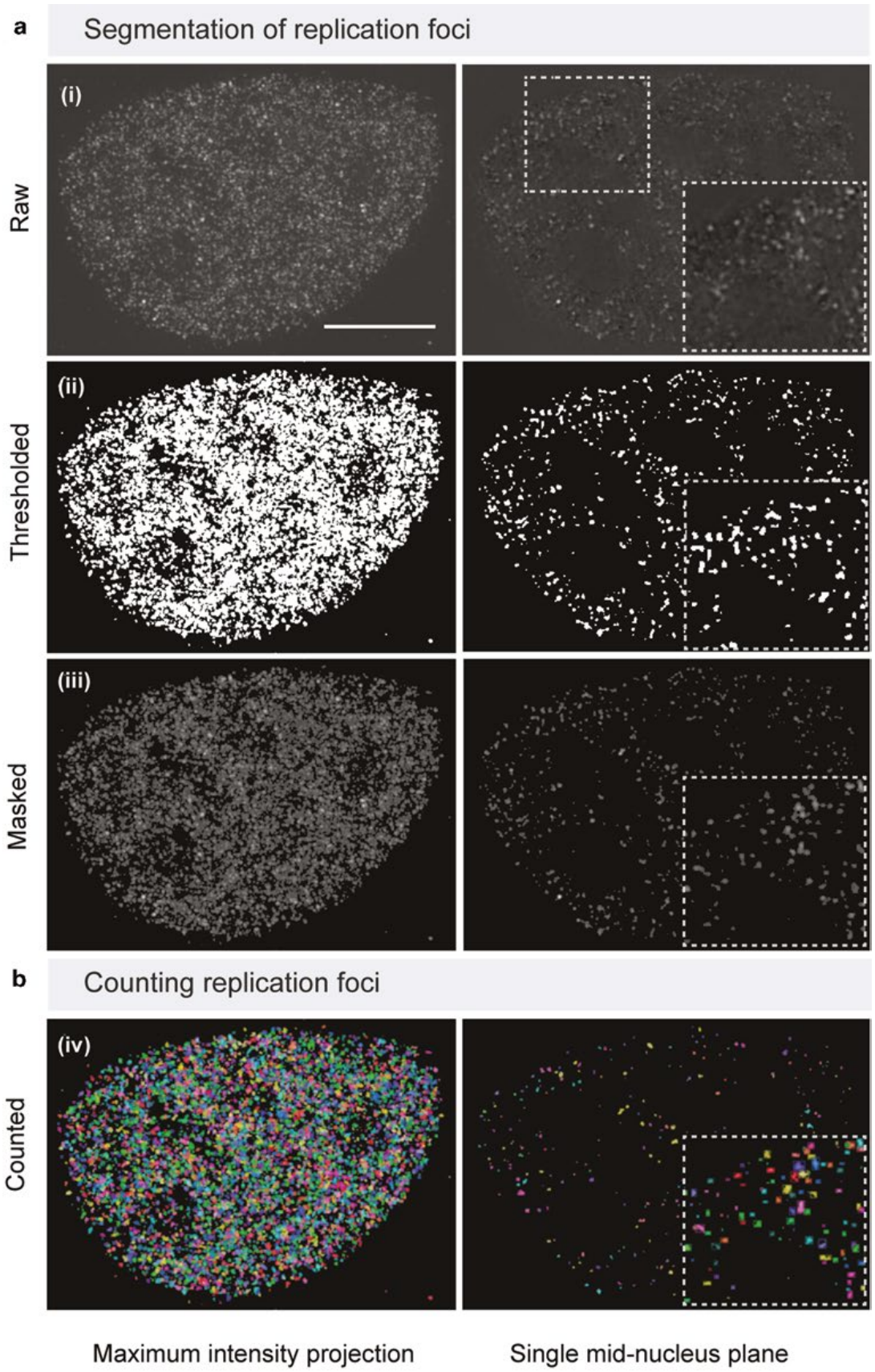

Fig. 4 Quantification of replication sites on super-resolution fluorescent microscopy images. An overview of the intermediate results of RFi quantification on 3D stacks of 3D-SIM images (**a**, **b**) described in Subheading 3.9.2. Scale bar: 5 μm

3.9.1 Confocal or Wide-Field Images

The procedure presented (Fig. 3) relies on the identification of local maxima of intensity. Accordingly, the influence of random noise, which is represented as 1 pixel spikes in intensities, on local maxima identification should be reduced. For that a smoothing filter is used having the kernel size of 1–2 pixels. Larger kernel sizes will lead to considerable reduction in image contrast and failure to identify closely located maxima as separate ones.

Segmentation of Replication Foci

1. Open the image stack in ImageJ. Remove slices without signal or having unfocused image of the nucleus (Fig. 3a (i)).
2. To filter one pixel noise, go to "Process" menu>Filter and select a smoothing filter. For the selected filter, e.g., "Mean" set the kernel size. Run the filter to process all images in the stack. Smoothing the images shifts the image histogram to the region of lower intensities. For standard threshold detection during further steps of image processing, images are normalized.
3. To normalize image histogram, go to "Process" menu>Enhance contrast. Choose linear stretching of the histogram: select "Normalize" and process all slices. Use stack histogram during the normalization and avoid introducing saturated pixels (Fig. 3a (ii)).
4. For identification of local maxima, go to "Process" menu>Find maxima and select "Preview point selection." Identified local maxima will be shown by small crosses.
5. Choose noise tolerance setting to exclude background signal from the analysis. The particular value of noise tolerance (threshold) will depend on many factors, including bit range, signal-to-noise ratio, and image quality. Use one of the central sections of the nucleus. Change noise tolerance stepwise and follow the changes in pixels being selected. Correct setting will be manifested by only a few maxima identified outside the nucleus area and, e.g., inside nucleoli. The number of identified maxima will be shown. For single plane images, calculate RFi inside nucleus using the region of interest (ROI) and skip further steps.
6. Write down or remember the selected noise tolerance.
7. To identify local maxima in 3D, run "Find Stack Maxima" macros (http://imagej.nih.gov/ij/macros/FindStackMaxima.txt) with the selected noise tolerance setting, and select "single points" as the procedure output (Fig. 3a (iii)).
8. Save the output stack.

Counting of replication foci

Local maxima are identified and marked in the output binary image as single white pixels. Counting of such single-pixel objects on the stack of images (in 3D) will lead to an overestimation of the number of objects (*see* **Note 25**). To get a conservative estimate of

the RFi number and account for RFi present in more than one slice in the image stack, replace the identified local maxima with objects of standard size by blurring the output stack using convolution with Gaussian kernel.

9. Go to "Process" menu>Filter and select "Gaussian blur."
10. Set the kernel size of 1–2 pixels and process all slices (*see* **Note 26**).
11. Normalize the processed stack (*see* Subheading 3.9.1 **step 2** and **3**) (Fig. 3b (iv)).
12. Save the resulting image stack.
13. To estimate the number of objects in 3D, run "3D object counter" plug-in (http://rsbweb.nih.gov/ij/plugins/track/objects.html).
14. Set "Threshold" in the plug-in menu to 21 (*see* **Note 27**) (Fig. 3b (v)).
15. For the output of the data analysis, select "Maps to show" = "objects" and "Results tables to show" = "Statistics" and "Summary." In addition to the numbers of RFi identified, the plug-in will return a stack with color-coded individual objects (Fig. 3b (vi)).

3.9.2 3D-SIM Images

For the two step approach used in analysis of 3D-SIM images (Fig. 4), the first step consists of the segmentation of the nuclei in ImageJ [38], and the final step uses the commercial software Volocity 5 (Perkin Elmer) and performs further segmentation of touching objects and automated counting. An intensity-based object recognition is followed by a proprietary watershed algorithm for the separation of touching objects.

Segmentation of replication foci

1. Open the image in ImageJ and crop the nuclei of interest ("Image" menu>"Crop") (*see* **Note 28**).
2. Duplicate the cropped image stack with the "Image" menu>"Duplicate">"Duplicate Stack" option (*see* **Note 29**) (Fig. 4a (i)).
3. With the duplicated image, adjust with the "Image" menu>"Adjust">"Autothreshold function."
4. Choose the "Triangle Method" (*see* **Note 30**) and following options: "Ignore black," "White objects on black background," "Stack," and "Use stack histogram." During this step, an automatic thresholding, the triangle method, is used to differentiate between background noise and replication foci based on the shape of the histogram (Fig. 4a (ii)).
5. To recombine both images, go to the "Process" menu, and select "image calculator" with the following options:

(a) Image1: Choose thresholded image.

(b) Specify method: "Min."

(c) Image2: Choose cropped original image.

(d) Select "Create New Window."

(e) Process all images from this stack.

6. Save resulting masked image as TIFF (Fig. 4a (iii)).

Separation and counting of replication foci (*see* **Note 31**).

7. Import masked image to Volocity 5 (Perkin Elmer), and generate a 3D stack by using the "Tools" menu>"Make Volumes" (*see* **Note 32**) command (*see* **Note 33**).
8. To quantify the replication foci, choose "Measurements" tab, and drag following objects to the measurement:
   (a) "Find objects," select the wheel in top right corner to specify intensities and specify "Lower" = 1.
   (b) Drag also task "Separate touching objects" to measurement window.
   (c) At this stage, a measurement will be performed by Volocity window (*see* **Note 34**) (Fig. 4b (iv)).
9. To save the measurement, go to "Measurements" menu>"Make Measurement Item" and name the item accordingly.
10. Select the Measurement item and select "File" menu> "Export">"As Comma separated Value" and save to a convenient location (*see* **Note 35**).

4 Notes

1. DNA labeling using each of the nucleotides has its own advantages and/or drawbacks. Halogenated nucleotide analogs provide for very efficient DNA labeling, but require denaturing treatment of the preparations, which may affect detection of other epitopes. Fluorescently labeled nucleotides can be used for in vivo microscopy studies but they are cell impermeable and require sophisticated procedures for their delivery into the cell. Alkyne nucleotides are easy to detect, but rely on chemical reactions for their detection and may be affected by particular, e.g., acidic treatments. EdU can also trigger DNA damage response and affect cell cycle progression in the long term [39].
2. Signal from GFP-tagged replication proteins can be further enhanced using:
   (a) anti-GFP primary antibodies
   (b) GFP enhancing nanobodies [34]

3. Reducing the volume of cell culture medium prior to nucleotide addition may be advisable when expensive or not readily available nucleotide analogs are used.
4. Best working EdU or BrdU concentrations are cell line specific. For these reasons and also to increase the intensity of RFi labeling, it may be advisable to use higher concentrations of the nucleotide.
5. Longer nucleotide incorporation times will result in brighter signal and better signal-to-noise ratio. However, increasing the time of labeling can lead to labeling of adjacent or newly activated replicons thus decreasing spatial resolution of the method. To get a snapshot of simultaneously active replicons in a particular cell, we suggest using times of incubation below characteristic replicon's "lifetime." Typically 10–20 min of incorporation with nucleotide for mouse or human cells works well (*see* **Note 4**).
6. Live cell imaging is compromised immediately after labeling due to very bright background signal from the labeled nucleotide, which has entered the cell during the scratching procedure. At about 30–60 min after labeling, the background staining drops, and cells displaying typical replication patterns can be observed live. The pattern is stably inherited to the daughter cells and the labeled RFi can be followed for several cell cycles as partially labeled segregating chromosome territories [40].
7. To avoid detachment of poorly adherent cells, coverslips can be slightly dried (until "granular" appearance of the surface), placed on Parafilm and a small volume (50–100 μl) of the Triton X-100 solution carefully placed over the coverslip.
8. Using cold PBS wash can help precisely control nucleotide incorporation time, which is especially important with short labeling times.
9. The CSK buffer is hypertonic and provides for efficient extraction of many nuclear proteins, which is, e.g., essential to detect MCM proteins bound to chromatin. However, chromatin structure and nuclear morphology are affected by this treatment.
10. To avoid detachment of poorly adherent cells, cells can be prefixed using mild formaldehyde solution (0.1 % in PBS). Using such prefixation prior to 3.7 % formaldehyde solution is also helpful when analyzing weakly bound factors.
11. Labeled cells can be stored in PBS at 4 °C up to several days prior to staining. Sealing the Petri dish with Parafilm and adding NaN_3 extends that period.
12. Some antibodies (e.g., anti-PCNA mouse and rat monoclonal antibodies) require methanol treatment of the cells. With such antibodies, the cells can be first formaldehyde fixed for better

preservation of the nuclear morphology and then methanol treated (postfixed) for the sake of efficient antibody detection of the epitopes of interest.

13. The hypotonic protocol cannot be combined with expression of GFP-tagged proteins because the strong acidic treatment destroys GFP fluorescence.
14. The choice of the hypotonic solution and minimal time of the hypotonic treatment is cell type and species specific. The best working solution and exact time should be experimentally selected for each cell line. In our hands, 15 min of 50 mM KCl incubation is sufficient for most cells. For rodent cells, 20–25 min incubation and 75 mM KCl/1 % $Na_2HCitrate$ give sometimes better results.
15. Successful hypotonic treatment is manifested by an increase in the pellet size as compared to the initial pellet size. We include time of centrifugation into the time of hypotonic treatment.
16. Slow and homogeneous increase in MeAA concentration is important. To obtain this, we add MeAA dropwise to the walls of the tube and flick the tube after each drop. Alternatively, the tube can be placed on a slowly rotating shaker and MeAA added dropwise.
17. Make sure that the transfection is performed one or two cell cycles before the time of observation or experiment (*see* also **Note 2**) and select cells with low to mid fluorescent protein level.
18. We suggest GFP-PCNA or GFP-DNA ligase I, which represents essential components of the replication fork [2]. For super-resolution microscopy (e.g., 3D-SIM imaging, which requires 45 times more illumination compared to conventional imaging techniques), enhancement and stabilization of GFP fluorescence are required and can be achieved using additional immunostaining (*see* **Note 2**).
19. All procedures can be carried out on a piece of Parafilm in the Petri dish covered with foil and containing a piece of wet filter paper or wet tissue, "humid chamber" [29].
20. For super-resolution microscopy, it is important to match the refractive indices of the mounting medium, coverslip, and microscope immersion as closely as possible. Nonhardening antifadents are recommended to preserve 3D structure of the cells.
21. To avoid changing cellular morphology due to excessive drying of the hardening antifading solution, it is recommended to seal the sides of the coverslip using nail polish.
22. For higher signal-to-noise ratio of the images, high numerical aperture (used commonly for total internal reflection fluorescence microscopy) objectives can be used.

23. As the energy of illumination is inversely proportional to the wavelength, when multiple fluorochromes are used to optimize the signal-to-noise ratio and minimize photobleaching, sequential acquisition of images of individual channels and starting with the longer wavelength are advisable.
24. In this case, confocal microscopy does not provide an additional advantage due to better z-resolution and elimination of the out-of-focus light. However, because of the localized sample illumination, confocal imaging leads to a sharper point spread function giving a higher x,y contrast (theoretical resolution is ~1.4-fold better) and better signal-to-noise ratio.
25. The accuracy of maxima identification is influenced by image noise, which can lead to 1–2 pixel shifts in maxima positions even after smoothing the image. The same DNA replication focus can be represented as focal signals in the neighboring stack slices, for which spatially separated local maxima can be identified. As a result, the same 3D continuous DNA replication focus will be accounted as several individual RFi in consecutive image slices.
26. A fluorescent point object will be imaged as a bell-shaped distribution of signal of a particular radius (*see*, e.g., [41]). Accordingly, there will be a minimal size of the objects in the image. Parameters of both steps (Subheading 3.9.1, **steps 2** and **6**) should be selected with account to the minimal size. The parameters applied by us can be used for 63× objectives with NA>1.4 (pixel size <~100 nm) and emission wavelengths ~500–600 nm.
27. Operations of **steps 9–11** under Subheading 3.9.1 replace local maxima marked by single pixels with standard objects representing normalized Gaussian distributions. Setting nonzero threshold in the plug-in sets the size of the objects to be counted in the stack. Importantly, the threshold also determines how many signals will overlap in the adjacent slices and, hence, attributed as belonging to the same objects (RFi) continued in 3D.
28. It is easier to make a z-max projection ("Image" menu> "Stacks">"Z-Project," select "all slices," and "Max Intensity"); select the nuclei there and transfer the mask via the ROI Manager ("Tools" menu>"ROI Manager," you can even name the ROI).
29. **Steps 2–6** can be automatized by writing a macro.
30. An implementation of this method is described in detail by Zack, Rogers, and Latt in "Automatic measurement of sister chromatid exchange frequency" [42]. Gabriel Landini has implemented the method in the "Autothreshold" ImageJ plug-in.

31. Changing the order of the protocol steps may result in a different outcome of measurements.
32. Volocity uses "Volume" as a synonym for a 3D image stack.
33. Do not forget to set the pixel size via "Edit" menu>"Properties." In most scenarios, the pixel size will otherwise be lost.
34. Batch processing of many images is possible using "Make Measurement" item.
35. A modification of the protocol can be used for RFi segmentation in very early/late S-phase cells (small number of objects over a noisy background) and/or really noisy datasets. Subheading 3.9.2 separation and counting of replication foci is performed using the complete image intensity range for thresholding (e.g., for every 8-bit images, all 255 values are chosen as individual thresholds). The number of identified objects over threshold is plotted, and an exponential curve is fitted to the graph. The best estimate threshold corresponds to the point where the first derivative of the fitted exponent curve is −1. This method is advisable only for low contrast or very dim images as it is an immensely (computational) time-intensive task, getting worse with increased bit depth.

Acknowledgements

We thank all present and past members of the laboratory for their contributions over the years. Vadim O. Chagin was supported by grants of the Russian Foundation for Basic Research (## 12-04-01489a, 13-04-00442a). The laboratory of M. Cristina Cardoso is supported by grants of the German Research Foundation (DFG CA 198/9) and the Federal Ministry of Education and Research (BMBF).

References

1. Edenberg HJ, Huberman JA (1975) Eukaryotic chromosome replication. Ann Rev Genet 9:245–284
2. Chagin VO, Stear JH, Cardoso MC (2010) Organization of DNA replication. In: Misteli T (ed) The nucleus. Cold Spring Harbor, New York
3. Nakamura H, Morita T, Sato C (1986) Structural organizations of replicon domains during DNA synthetic phase in the mammalian nucleus. Exp Cell Res 165:291–297
4. Tomilin N, Solovjeva L, Krutilina R, Chamberland C, Hancock R, Vig B (1995) Visualization of elementary DNA replication units in human nuclei corresponding in size to DNA loop domains. Chromosome Res 3: 32–40
5. Schermelleh L, Solovei I, Zink D, Cremer T (2001) Two-color fluorescence labeling of early and mid-to-late replicating chromatin in living cells. Chromosome Res 9:77–80
6. Cardoso MC, Joseph C, Rahn HP, Reusch R, Nadal-Ginard B, Leonhardt H (1997) Mapping and use of a sequence that targets DNA ligase I to sites of DNA replication in vivo. J Cell Biol 139:579–587
7. Leonhardt H, Rahn HP, Weinzierl P, Sporbert A, Cremer T, Zink D, Cardoso MC (2000) Dynamics of DNA replication factories in living cells. J Cell Biol 149:271–280

8. Nakayasu H, Berezney R (1989) Mapping replicational sites in the eucaryotic cell nucleus. J Cell Biol 108:1–11
9. van Dierendonck JH, Keyzer R, van de Velde CJ, Cornelisse CJ (1989) Subdivision of S-phase by analysis of nuclear 5-bromodeoxyuridine staining patterns. Cytometry 10:143–150
10. Mills AD, Blow JJ, White JG, Amos WB, Wilcock D, Laskey RA (1989) Replication occurs at discrete foci spaced throughout nuclei replicating in vitro. J Cell Sci 94: 471–477
11. Fox MH, Arndt-Jovin DJ, Jovin TM, Baumann PH, Robert-Nicoud M (1991) Spatial and temporal distribution of DNA replication sites localized by immunofluorescence and confocal microscopy in mouse fibroblasts. J Cell Sci 99:247–253
12. Hozak P, Hassan AB, Jackson DA, Cook PR (1993) Visualization of replication factories attached to nucleoskeleton. Cell 73:361–373
13. Berezney R, Mortillaro M, Ma H, Meng C, Samarabandu J, Wei X, Somanathan S, Liou WS, Pan SJ, Cheng PC (1996) Connecting nuclear architecture and genomic function. J Cell Biochem 62:223–226
14. Manders EM, Stap J, Strackee J, van Driel R, Aten JA (1996) Dynamic behavior of DNA replication domains. Exp Cell Res 226:328–335
15. Jackson DA, Pombo A (1998) Replicon clusters are stable units of chromosome structure: evidence that nuclear organization contributes to the efficient activation and propagation of S phase in human cells. J Cell Biol 140:1285–1295
16. Ma H, Samarabandu J, Devdhar RS, Acharya R, Cheng P, Meng C, Berezney R (1998) Spatial and temporal dynamics of DNA replication sites in mammalian cells. J Cell Biol 143:1415–1425
17. Gotoh E (2007) Visualizing the dynamics of chromosome structure formation coupled with DNA replication. Chromosoma 116: 453–462
18. Ligasova A, Raska I, Koberna K (2009) Organization of human replicon: singles or zipping couples? J. Struct Biol 165:204–213
19. Cseresnyes Z, Schwarz U, Green CM (2009) Analysis of replication factories in human cells by super-resolution light microscopy. BMC Cell Biol 10:88
20. Baddeley D, Chagin V, Schermelleh L, Martin S, Pombo A, Gahl A, Domaing P, Birk U, Leonhardt H, Cremer H, Cardoso MC (2010) Measurement of replication structures at the nanometer scale using super-resolution light microscopy. Nucleic Acid Res 38:e8
21. Lima-de-Faria A, Jaworska H (1968) Late DNA synthesis in heterochromatin. Nature 217:138–142
22. Huberman JA, Riggs AD (1968) On the mechanism of DNA replication in mammalian chromosomes. J Mol Biol 32:327–341
23. Berezney R, Dubey DD, Huberman JA (2000) Heterogeneity of eukaryotic replicons, replicon clusters, and replication foci. Chromosoma 108:471–484
24. Chagin VO, Rozanov Iu M, Solov'eva LV, Tomilin NV (2004) High resolution analysis of replication foci by conventional fluorescent microscopy. I A study of complexity and DNA content of the foci. Tsitologiia 46:229–243
25. Reinhart M, Casas-Delucchi CS, Cardoso MC (2013) Spatiotemporal visualization of DNA replication dynamics. Methods Mol Biol 1042:213–225
26. Ersoy I, Bunyak F, Chagin V, Cardoso MC, Palaniappan K (2009) Segmentation and classification of cell cycle phases in fluorescence imaging. Lect Notes Comput Sci 5762: 617–624
27. Waseem NH, Lane DP (1990) Monoclonal antibody analysis of the proliferating cell nuclear antigen (PCNA). Structural conservation and the detection of a nucleolar form. J Cell Sci 96:121–129
28. Rottach A, Kremmer E, Nowak D, Boisguerin P, Volkmer R, Cardoso MC, Leonhardt H, Rothbauer U (2008) Generation and characterization of a rat monoclonal antibody specific for PCNA. Hybridoma (Larchmt) 27:91–98
29. Cardoso MC, Leonhardt H (1995) Immunofluorescence techniques in cell cycle studies. In: Pagano M (ed) Cell cycle: materials and methods. Springer-Verlag, Heidelberg, pp 15–28
30. Jackson DA (1995) S-phase progression in synchronized human cells. Exp Cell Res 220:62–70
31. Yerly-Motta V, Pavy JJ, Herve P (1999) Screening of five specific cell cycle inhibitors using a T cell lymphoma cell line synchrony/release assay. Biotech Histochem 74:119–128
32. Anglana M, Apiou F, Bensimon A, Debatisse M (2003) Dynamics of DNA replication in mammalian somatic cells: nucleotide pool modulates origin choice and interorigin spacing. Cell 114:385–394
33. Masata M, Juda P, Raska O, Cardoso MC, Raska I (2011) A fraction of MCM 2 proteins remain associated with replication foci during a major part of S phase. Folia Biol 57:3–11
34. Kirchhofer A, Helma J, Schmidthals K, Frauer C, Cui S, Karcher A, Pellis M, Muyldermans S, Casas-Delucchi CS, Cardoso MC, Leonhardt H, Hopfner KP, Rothbauer U (2010)

Modulation of protein properties in living cells using nanobodies. Nat Struct Mol Biol 17: 133–138

35. Schermelleh L, Carlton PM, Haase S, Shao L, Winoto L, Kner P, Burke B, Cardoso MC, Agard DA, Gustafsson MG, Leonhardt H, Sedat JW (2008) Subdiffraction multicolor imaging of the nuclear periphery with 3D structured illumination microscopy. Science 320:1332–1336
36. Markaki Y, Smeets D, Cremer M, Schermelleh L (2013) Fluorescence in situ hybridization applications for super-resolution 3D structured illumination microscopy. Methods Mol Biol 950:43–64
37. Martin S, Failla AV, Spori U, Cremer C, Pombo A (2004) Measuring the size of biological nanostructures with Spatially Modulated Illumination Microscopy. Mol Biol Cell 15:2449–2455
38. Rasband WS (1997–2014) ImageJ, http://imagej.nih.gov/ij/. U S National Institutes of Health, Bethesda, Maryland, USA
39. Kohlmeier F, Maya-Mendoza A, Jackson DA (2013) EdU induces DNA damage response and cell death in mESC in culture. Chromosome Res 21:87–100
40. Walter J, Schermelleh L, Cremer M, Tashiro S, Cremer T (2003) Chromosome order in HeLa cells changes during mitosis and early G1, but is stably maintained during subsequent interphase stages. J Cell Biol 160:685–697
41. Stelzer EHK (1998) Contrast, resolution, pixelation, dynamic range and signal-to-noise ratio: fundamental limits to resolution in fluorescence light microscopy. J Microsc 189:15–24
42. Zack GW, Rogers WE, Latt SA (1977) Automatic measurement of sister chromatid exchange frequency. J Histochem Cytochem 25:741–753

5 4D Visualization of replication foci in mammalian cells corresponding to individual replicons

5.1 Aims of "4D Visualization of replication foci in mammalian cells corresponding to individual replicons"

The results obtained by multi-replication labelings and the bias free computer-guided foci quantification method were applied in the following two Nature Communication publications.

In this chapter I applied the newly developed foci recognition toolkit to label, image and quantify more than 300 cells to achieve a statistically significant and unbiased outcome in two different mammalian cell lines. With the described methods in Chapter 3 and 4, I was finally able to lift the veil from wide field and even confocal imaging and resolve and quantify DNA replication foci. The DNA replication foci analysis matched beautifully with the calculated 50,000 replisomes necessity to replicate the whole genome during a single S-Phase[71,113]. The number of measured DNA replication foci were completed by comparative fiber measurements and genome size analysis.

3D visualization and *in situ* quantification of single replicons throughout S-Phase of mammalian cells was finally obtained.

5.2 Contributions

- M. Reinhart performed experiments for the quantification of RFi, replication fork speed, inter origin distances and S-Phase duration.
- M. Reinhart analyzed the data and generated Figure 1.
- M. Reinhart analyzed the data and generated Figure 2.
- M. Reinhart analyzed the data and generated Figure 3.
- M. Reinhart analyzed the data for Figure 4b and contributed to Figure 4.
- M. Reinhart contributed to Supplementary Figure 2.
- M. Reinhart generated Supplementary Figure 3.
- M. Reinhart analyzed the data and generated Supplementary Figure 5.
- M. Reinhart analyzed the data and generated Supplementary Figure 7.
- M. Reinhart analyzed the data and generated Table 1
- M. Reinhart analyzed the data and generated Table 3
- M. Reinhart analyzed the data and generated Table 4
- M. Reinhart analyzed the data and generated Table 5
- M. Reinhart analyzed the data and generated Supplementary Table 1
- M. Reinhart developed the image analysis protocol for *in situ* quantification of replication foci.
- M. Reinhart cowrote the manuscript.

5.3 Publication

nature COMMUNICATIONS

ARTICLE

Received 16 Apr 2015 | Accepted 3 Mar 2016 | Published 7 Apr 2016

DOI: 10.1038/ncomms11231 OPEN

4D Visualization of replication foci in mammalian cells corresponding to individual replicons

V.O. Chagin[1,2], C.S. Casas-Delucchi[1,3,*], M. Reinhart[1,*], L. Schermelleh[4,5], Y. Markaki[5], A. Maiser[5], J.J. Bolius[1], A. Bensimon[6], M. Fillies[7,8], P. Domaing[7], Y.M. Rozanov[2], H. Leonhardt[5] & M.C. Cardoso[1]

Since the pioneering proposal of the replicon model of DNA replication 50 years ago, the predicted replicons have not been identified and quantified at the cellular level. Here, we combine conventional and super-resolution microscopy of replication sites in live and fixed cells with computational image analysis. We complement these data with genome size measurements, comprehensive analysis of S-phase dynamics and quantification of replication fork speed and replicon size in human and mouse cells. These multidimensional analyses demonstrate that replication foci (RFi) in three-dimensional (3D) preserved somatic mammalian cells can be optically resolved down to single replicons throughout S-phase. This challenges the conventional interpretation of nuclear RFi as replication factories, that is, the complex entities that process multiple clustered replicons. Accordingly, 3D genome organization and duplication can be now followed within the chromatin context at the level of individual replicons.

[1] Department of Biology, Technische Universitaet Darmstadt, Darmstadt 64287, Germany. [2] Laboratory of chromosome stability, Institute of Cytology, St. Petersburg 194064, Russia. [3] Cancer Research UK London Research Institute, Clare Hall Laboratories, South Mimms EN6 3LD, UK. [4] Micron Advanced Bioimaging Unit, Department of Biochemistry, University of Oxford, OX1 3QU Oxford, UK. [5] Center for Integrated Protein Science at the Department of Biology, Ludwig Maximilians University Munich, Planegg-Martinsried 82152, Germany. [6] Genomic Vision, Bagneux 92220, France. [7] Max Delbrueck Center for Molecular Medicine, Berlin 13125, Germany. [8] Charité—Universitaetsmedizin, 13353 Berlin, Germany. * These authors contributed equally to this work. Correspondence and requests for materials should be addressed to M.C.C. (email: cardoso@bio.tu-darmstadt.de)

Genomic DNA is duplicated during the S-phase of the eukaryotic cell cycle. At the chromatin fibre level, DNA replication can be characterized by the location on the DNA molecule where the DNA synthetic complexes (replisomes) are assembled and replication is initiated (the so-called origin of replication) and by the actual positions where DNA synthesis occurs at any given moment, termed replication forks[1]. Only a subset of potential origins of replication will be activated in the individual cell in a given cell cycle[2–4]. Each activated origin of replication normally gives rise to two replication forks that drift apart along the template DNA. Initiation of DNA synthesis at a particular origin of replication provides a functional definition of replicon as a chromosome segment replicated as a result of a single initiation event in a particular cell cycle. To duplicate the whole genome in a reasonable time, multiple replicons must operate in parallel at any given time point during S-phase. Data regarding replicon arrangement, size and the rate of replication fork movement, were originally obtained from pattern analysis of tritiated thymidine-labelled tracks of replication forks on extended DNA molecules[5–7]. These DNA autoradiography findings suggested that the genome replicates via clusters of small (50–300 kbp) synchronously activated replicons[8,9]. The total number of replicons activated during S-phase was indirectly estimated as 20,000–50,000 (refs 10–12).

At the cell nucleus level, focal sites of DNA synthesis, hereafter called replication foci (RFi) can be visualized by either labelling replisome components or by detecting sites of nucleotide incorporation upon pulse labelling[13]. The spatial pattern of subnuclear distribution of RFi undergoes dynamic changes during S-phase progression and is characteristic for the different S-phase sub-stages[10,13,14]. General principles of DNA replication were studied using the analysis of various RFi characteristics, such as their number, brightness, size, lifetime and their intranuclear distribution[10–18]. Up to six distinct patterns of RFi could be distinguished in cycling somatic cells[10,19], although more commonly S-phase was subdivided into early, middle and late stages: Se, Sm and Sl, respectively[20–22].

Notably, the number of RFi that was observed in each S-phase pattern with conventional microscopic techniques[13,23] was much smaller than the estimated number of active replicons leading to the conclusion that each RF contained multiple replicons[11–16,21,23]. The stability of RFi over several cell cycles and characteristics of their brightness suggested a relation of nuclear RFi to tandem clusters of synchronously activated replicons described on DNA fibres[12].

In parallel, the concept of 'replication factories' arose from electron microscopy observations of localized incorporation of replication label and accumulation of replication proteins in ~150 nuclear sites[24], which were similar to the reported numbers of RFi and followed the dynamics of RFi patterns during S-phase[25]. As a result, it was suggested that genome duplication occurred by sliding the template DNA of multiple replicons through composite polymerizing sites of each factory immobilized at the nuclear matrix[25].

On the basis of these initial studies, RFi were for decades considered as complex functional–structural units of chromatin that contained multiple replicons[26,27].

Studies using fluorescence halo technique revealed a dynamic relationship between replicon size and the size of chromatin loops[28–30] providing a link between the organization of DNA replication and the structural organization of chromatin. As a result it has been hypothesized that metazoan genome is duplicated by synchronous processing of multiple loops within chromatin domains organized around replication factories[31].

A comprehensive three-dimensional (3D) analysis of elementary replication units throughout different S-phase stages in mammalian cells was compromised by the limited resolution of optical microscopy. Electron microscopy studies, although less limited in resolution, relied on precarious calculations to estimate the total number of nuclear RFi on the basis of data obtained from partial sections of nuclei[32,33]. Accordingly, development of new approaches was essential to close the gap between the data obtained in conventional microscopic and DNA fibre studies on genome replication in higher eukaryotes. Recent advances in super-resolution microscopy provided tools for detailed optical analysis of replication structures in 3D-preserved nuclei[34,35]. Although, various high-resolution microscopy techniques led to an increase in the observed numbers of RFi[34,36], 3D-structured illumination microscopy (3D-SIM) proved to be the most suitable approach allowing multicolour 3D detection of replication sites in spatially preserved nuclei[34]. Importantly, the corresponding eightfold increase in 3D resolution posed additional challenges since high throughput analysis and quantification of nuclei containing thousands of RFi was impossible without developing and validating computer-assisted automated approaches.

To re-evaluate the above replication factory concept and test the hypothesis that replicons and not replicon clusters may in fact represent the *in situ* elementary units of DNA replication; in this study, we perform a comprehensive super-resolution analysis of RFi in somatic human and mouse cells. RFi are visualized both by labelling newly synthesized DNA and PCNA as a crucial replisome component. We complement the RFi analysis with quantifications of genome size, S-phase duration and measurements of molecular replicon characteristics of the same cells to overcome inaccuracy through indirect estimates. Using newly developed protocols for robust RFi quantification, we demonstrate that comparable numbers of several thousands of RFi are active throughout all S-phase stages. The combined consideration of the experimental data show that conventionally observed RFi can be optically resolved down to single replicons in all S-phase sub-stages. Our findings imply that S-phase dynamics is primarily dictated by chromatin folding and individual synthetic complexes independently 'read' and 'copy' the underlying chromatin units[37].

Results

Kinetic analysis of cell cycle characteristics. To overcome the inaccuracy that arises from indirect estimates we performed direct live-cell analysis of the cell cycle parameters for the newly generated human cell lines (Supplementary Fig. 1 and Supplementary Note 1), as well as for the previously characterized mouse cell line[21]. To measure the duration of all cell cycle stages, we obtained time-lapse series of confocal images from live cells every 15–20 min for at least one complete cell cycle. The absence of phototoxicity-derived effects was supported by two lines of evidence: first, cells commonly entered into mitosis after being illuminated for the whole-cell cycle (Fig. 1a and Supplementary Movie 1); and second, the cell cycle duration (22.6 h) measured from microscopic images of live cells and the time needed for the culture to double in the absence of illumination were essentially the same (Fig. 1b and Table 1). The different cell cycle stages were classified on the basis of sequential appearance of characteristic PCNA distributions (Fig. 1a). Cells with uniformly distributed nuclear PCNA foci were classified as being in early S-phase (Se), perinucleolar foci rings were used as main marker of mid S-phase cells (Sm) and bright RFi clusters were used to distinguish cells in late S-phase. The onset of mitosis was manifested by the dilution of PCNA signal and changes in the shape of the cell that were also evident in phase contrast images. (Fig. 1a and Supplementary

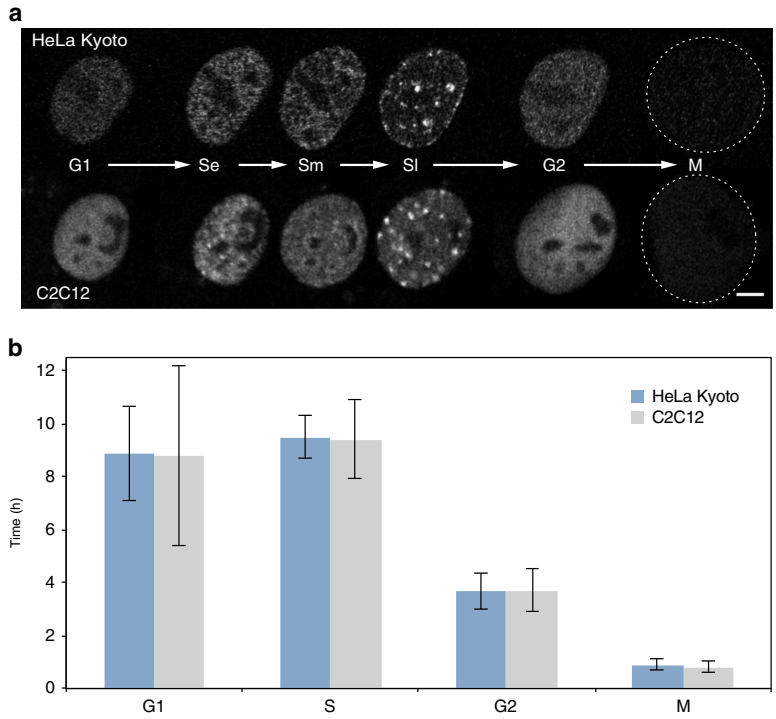

Figure 1 | Direct measurement of cell cycle kinetics. (**a**) Patterns of PCNA distribution in all cell cycle stages imaged with live-cell time-lapse microscopy of human HeLa Kyoto (top) and mouse C2C12 cells (bottom). S-phase stages are further subdivided into early (Se) mid (Sm) and late (Sl). (**b**) Duration of the cell cycle phases (mean ± s.d.; additional data in Table 1) measured from time-lapse microscopy analysis as shown in **a** (see also Supplementary Movie 1). Error bars represent s.d., number of replicates for human cells G1: 31, S: 30, G2: 27, M: 26; mouse cell replicates, G1: 20, S: 16, G2: 5, M: 10. Scale bar, 5 µm.

Table 1 | Cell cycle (stage) duration measurements.

Cell cycle (stage)	HeLa Kyoto (h)				C2C12 (h)			
	Mean	s.d.	s.e.m.	*n*	Mean	s.d.	s.e.m.	*n*
G1	8.9	1.8	0.3	31	8.8	3.4	0.7	20
S-phase	9.5	0.8	0.2	30	9.4	1.5	0.4	16
G2	3.7	0.7	0.1	27	3.7	0.8	0.3	5
Mitosis	0.9	0.2	0.0	26	0.8	0.2	0.1	10
Doubling time	22.6	2.3	0.4		22.6	2.5	1.0	

n, Number of cells.

Movie 1). We used the information on the preceding or the following cell cycle stage to classify nuclei with homogeneous PCNA distribution as G1 or G2 stage.

Despite differences in their karyotypes, the human and mouse cells had comparable cell cycle and S-phase (9.5 h) durations (Fig. 1b and Table 1).

Genome size measurements. A cell line represents a lineage of cells capable of unlimited proliferation cycles in culture. Transformation of these cells can often lead to changes in chromosome numbers and/or genome size. Accordingly, it was necessary to determine the amount of genomic DNA for each cell line using normal diploid mouse cells as a reference (Fig. 2a). All cell lines had non-diploid karyotypes. The HeLa Kyoto cell lines expressing GFP-PCNA or mCherry-PCNA had very close genome sizes of 9.7 and 9.8 Gbp, respectively (Fig. 2a and Table 2). In view of their common origin and close similarity, these cell lines were used interchangeably in further experiments. C2C12 cells expressing GFP-PCNA were quasi-tetraploid[38], with 11.4 Gbp genome size (Fig. 2a and Table 2).

Quantification of molecular characteristics of replicons. The time needed to duplicate a genome is primarily determined by: (i) the average spacing of active replication origins; and (ii) the rate of DNA synthesis. To measure both, inter-origin distances (IODs) and the rate of chain elongation (replication fork speed, RFS), we performed labelling of the cells by consecutive incubation with two thymidine analogues—IdU and CldU (Supplementary Fig. 2) and took advantage of the DNA combing procedure that led to uniform stretching of DNA fibres[39]. This procedure produces on average stretched DNA fibres of 250–500 kbp in length[39], with a fibre length of at least ~200 kbp essential for relevant RFS and IOD experimental estimates[40]. The average IOD was comparable in mouse and human cells (189 and 162 kbp for HeLa Kyoto and C2C12, respectively; Fig. 2b and Tables 3 and 4). On the other hand, the average RFS was very different with 1.65 kbp min^{-1} in human cells and 2.46 kbp min^{-1} in mouse cells (Fig. 2b and Tables 3 and 4). The consistency and statistical relevance of the sample size was verified by a sliding average test (Supplementary Fig. 2C and Supplementary Note 2).

Visualization of DNA replication sites in cells using 3D-SIM. Next, we visualized the replication sites *in situ* throughout S-phase in both human and mouse cells at different light-microscopy resolution levels. Samples for 3D-SIM

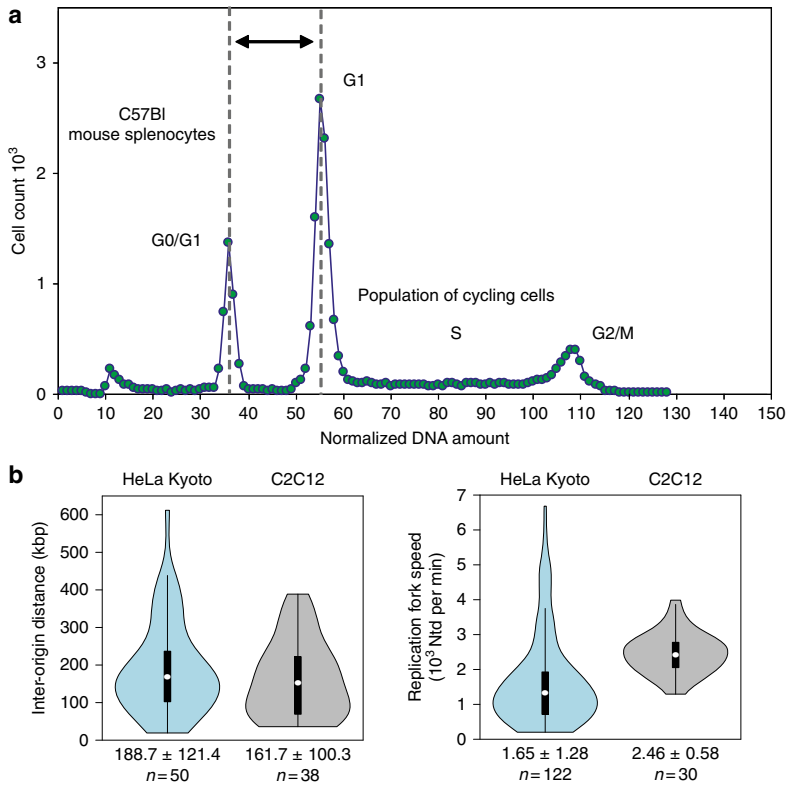

Figure 2 | Genomic DNA content and DNA fibre analysis of replicons. (**a**) DNA flow cytometry histogram of ethidium bromide/olivomycin stained HeLa Kyoto mCherry-PCNA expressing cells admixed with C57Bl mouse splenocytes is shown. The peak at channels 34–38 corresponds to the G1/G0 peak of non-cycling splenocytes. HeLa Kyoto cell cycle distribution is represented by a typical DNA flow cytometry histogram consisting of G1, S-phase and G2/M populations. To calculate the amount of genomic DNA in the cycling cell line, G1/G0 peak of mouse splenocytes and G1 peak of the cell line were approximated with Gaussian distributions and the relative position of the G1 peak was calculated (for details see methods and Table 2). (**b**) Cells were pulse labelled with IdU for 30 min, followed by a 30 min CldU pulse. Whole-genome DNA was extracted under gentle conditions and single DNA fibres were stretched with the constant factor of 2 kbp per μm. Incorporated nucleotides were immunostained and signals acquired in a wide-field microscope. Fluorescent tracks were measured by hand and used to calculate mean IOD and RFS. For details see methods; Supplementary Fig. 2 and Tables 3 and 4.

Table 2 | Genome size measurements.

Cell line	Relative DNA amount*	Genomic DNA (pg)	Genome Size (10^3 Mbp)	*n*
HeLa Kyoto GFP-PCNA	1.527	9.899	9.682 ± 0.002	9
HeLa Kyoto mCherry-PCNA	1.544	10.007	9.786 ± 0.006	8
C2C12 GFP-PCNA	1.798	11.676	11.419 ± 0.006	4

*represents the ratio between the DNA amounts of the indicated cells in G1 and the DNA amount of G0/G1 C57Bl mouse splenocytes. All values are given as Mean ± s.e.m.; *n* represents number of independent measurements.

Table 3 | Statistics of the IOD measurements.

IOD (kbp)	HeLa Kyoto	C2C12
Mean	188.7	161.7
s.d.	121.4	100.3
s.e.m.	17.2	16.3
95% CI	33.6	31.9
n	50	38

CI, confidence interval; IOD, inter-origin distance; *n*, number of tracks.

Table 4 | Statistics of the RFS measurements.

RFS (10^3Ntd per min)	HeLa Kyoto	C2C12
Mean	1.65	2.46
s.d.	1.28	0.58
s.e.m.	0.12	0.11
95% CI	0.23	0.21
n	122	30

CI, confidence interval; *n*, number of tracks; RFS, replication fork speed.

super-resolution imaging with RFi labelled by nucleotide incorporation were prepared by growing proliferating cultures of mouse and human cells in the presence of different cell permeable thymidine analogues (EdU or BrdU). In addition, RFi labelled by fluorescent PCNA to highlight replisomes were imaged in the same cells. The moderate expression levels of fluorescent PCNA in the stable cell lines essential to ensure unaltered cell cycle dynamics, were not strong enough to utilize the full potential of the 3D-SIM method[34,35,41]. Hence, an additional staining with anti-PCNA antibodies was performed to enhance the PCNA signal. To cover all optical resolution levels, we also acquired laser scanning confocal microscopy images and generated conventional wide-field epifluorescence images from the raw data sets obtained at the 3D-SIM system as well as the respective deconvolved images. In most cases, not only fixed and stained cell images but also live-cell images were acquired, as shown in Fig. 3. All characteristic S-phase patterns described in conventional wide-field and confocal microscopy could be identified in super-resolution images.

Pan S-phase quantification of replication foci numbers. Using newly developed computational approaches for RFi quantification (Supplementary Note 3, Supplementary Fig. 3 and ref. 42), we next counted the numbers of RFi (nucleotide and protein labelling) for every major S-phase stage at the different optical resolution levels (Fig. 3 and Supplementary Table 1).

Application of the counting protocol[42] to Z-stacks of confocal images led to the identification of on average 1,096 and 811 RFi per human and mouse cell in early S-phase comparable to previous reports. Mid S-phase cells yielded moderately higher RFi numbers, whereas this number decreased in late S-phase when the characteristic pattern of bigger and brighter RFi appeared (Fig. 3a). Similarly to confocal data, the number of RFi in deconvolved wide-field image stacks of early S-phase cells was 848 and 1,011 for human and mouse cells, respectively (Fig. 3b). Some S-phase stage fluctuation in RFi numbers (from 4,000 to 6,003 and 3,687 to 5,462 for human and mouse cells, respectively) could be found in 3D-SIM image stacks with mid S-phase numbers higher in human cells and early S-phase numbers higher in mouse cells (Fig. 3c). This suggests cell type or species-specific differences in S-phase dynamics and stresses the importance of complementing the *in situ* RFi measurements with a thorough characterization of genome size, IOD and RFS in the same cells. In both, human and mouse cells, RFi numbers declined toward late S-phase, due to prominent clustering of a substantial portion of RFi compromising proper separation and identification of individual RFi (Supplementary Fig. 4 and Supplementary Note 4) as well as decaying number of replicons towards the end of S-phase. To obtain an estimate of maximum number of RFi, we therefore excluded late S-phase cells from further calculations and averaged RFi numbers observed in early and mid segments of S-phase. With PCNA (replisome) labelling we detected on average slightly higher numbers of RFi for both mouse and human cell lines as compared with nucleotide labelling (Supplementary Fig. 5 and Supplementary Note 4). In addition, we acquired 3D-SIM time-lapse images of RFi in live cells labelled with GFP-PCNA (Fig. 3d). The RFi counted from the live super-resolution analysis yielded numbers close to the fixed-cell analysis albeit, in view of the rapid signal degradation as a consequence of GFP photobleaching, generally lower. We further observed inherent variability in RFi numbers between individual cells. Such variability may be a unique feature uncovered by high-resolution imaging of replication structures, which previously, at lower resolution, was manifested as variability in intensity of RFi[12,21,43]. Independently from the variability in individual replicon characteristics and in RFi numbers per cell, genome duplication must be completed within a normal S-phase length of 9.5 h.

As the 3D-SIM system, in addition to reconstructed super-resolved image stacks, allows to simultaneously generate the corresponding wide-field (and optionally deconvolved) image stacks, we were able to directly compare the total per cell RFi from different imaging-resolution conditions of the very same set of cells. We calculated both the ratios of RFi within every single cell or pooled the data from many cells together and calculated the population RFi ratio. Both ratios (Fig. 3e) perfectly agreed and indicated that on average a RFi detected at conventional light-microscopy resolution corresponds to 5.2 and 5.5 (nano)RFi at super-resolution imaging for human and mouse respectively. Moreover, these numbers varied between 4.5 and 6.3, with the higher values in mid S-phase of human cells.

Genome duplication parameters reveals single replicons. Finally, we integrated the numbers of all experimentally determined parameters for mouse and human cells to evaluate the relation of 3D-SIM-resolved RFi to elementary replication units (Fig. 4 and Table 5).

We used unsynchronized cells to measure distance between adjacent origins (IOD) activated at different moments of S-phase. The total number of replicons (equivalent to origins that become active) during S-phase equals to the genome size divided by the average IOD (used as an approximation for replicon size). This results on 51,404 and 70,501 replicons needed in total to duplicate the human and mouse cell genome, respectively, which is compatible with reported estimates[10–12]. The subset of simultaneously active replicons at any given time is proposed to be determined by the number of available limiting factor molecules[3,4]. The total duration of DNA synthesis of an average bidirectional replicon (replicon 'lifetime') was calculated by dividing IOD by two times the RFS, resulting in $\sim$57 min in human cells and $\sim$33 min in mouse cells, which corresponds to the period of time each limiting factor is occupied. The number of times each limiting factor molecule is reused can be estimated as the duration of S-phase divided by the average replicon lifetime. The latter results in 10 and 17 cycles for each limiting factor molecule during the complete S-phase in HeLa and C2C12 cells, respectively.

Since IOD measurements can be more affected by DNA fibre length than RFS measurements[40], we used primarily RFS data to estimate the number of replicons needed to replicate the whole genome. The number of replication forks that need to operate in parallel during S-phase can be calculated by dividing the time needed to duplicate the whole genome by a single replication fork (genome size divided by the average RFS) by the measured S-phase duration. This calculation showed that $\sim$10,000 (human cells) and 8,000 (mouse cells) forks or half as many bidirectional replicons ($\sim$5,000 and $\sim$4,000) operated in parallel in human and mouse cells, respectively (Table 5). The numbers of RFi counted by super-resolution microscopy (5,583 and 5,314 for human and mouse cells, respectively) can now be directly compared with the predicted numbers of simultaneously active replicons (5,149 and 4,108 for human and mouse cells, respectively). The outcome is a quotient of calculated simultaneously active replicons to the measured average number of RFi in 3D-SIM images for both mouse and human cells (Table 5). The robustness of our calculation is verified by a calculated mean squared error (MSE, Table 5) using a simplified version of the Gaussian error formula (see, equation 3 in the Materials and methods). The quotient in human cells of 0.92 is accompanied by a MSE of 0.2 and the quotient in mouse cells of

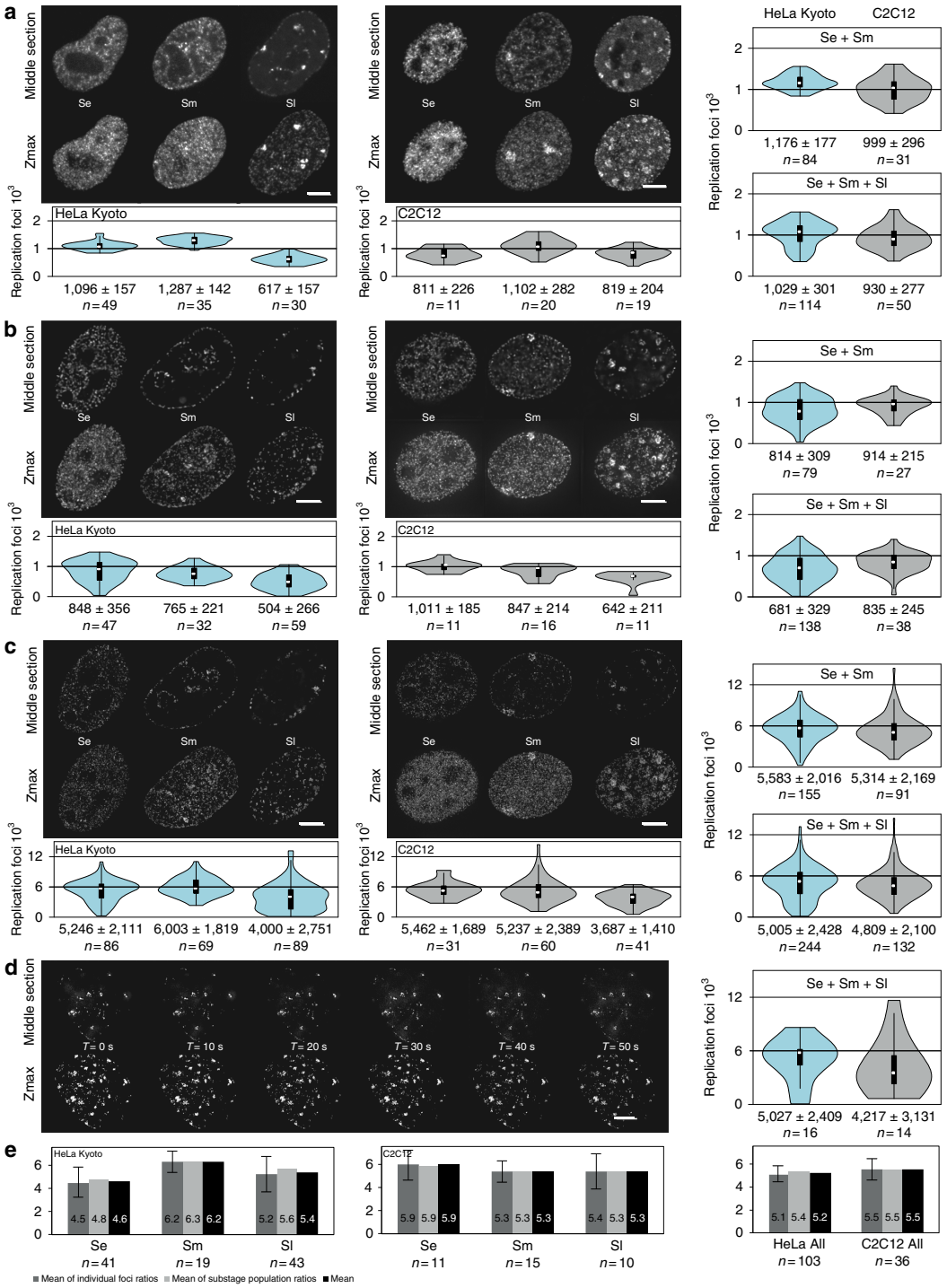

Figure 3 | 3D quantification of RFi numbers throughout S-phase. (**a**) Mid sections and maximum intensity z-projections (Zmax) of spinning disk confocal microscopy images of human (HeLa Kyoto) and mouse (C2C12) cells as indicated representative of the three major S-phase patterns—early (Se), mid (Sm) and late (Sl)—are shown. Scale bar, 5 μm. Numbers (mean ± s.d.; summary of the data in Supplementary Fig. 5 and Supplementary Table 1) of nuclear RFi quantified as described in Supplementary Fig. 3 are plotted separately for each of the three major S-phase patterns as well as the pooled data for Se and Sm and the whole S-phase. N indicates the number of cells analysed. (**b**) As in **a** representative images from wide-field deconvolution microscopy and corresponding RFi numbers. Scale bar, 5 μm. (**c**) As in **a** representative images from 3D-SIM and corresponding RFi numbers. Scale bar, 5 μm. (**d**) Time series (see also Supplementary Movie 2) of live mouse cells imaged using 3D-SIM and corresponding RFi numbers for mouse and also for human cells. Scale bar, 5 μm. (**e**) Histogram of RFi ratios from super-resolution versus conventional microscopy. Ratios were calculated either per individual cell (dark grey) or from all cells pooled (light grey). In addition, both data sets were combined (black). Given error bars represent the s.d.

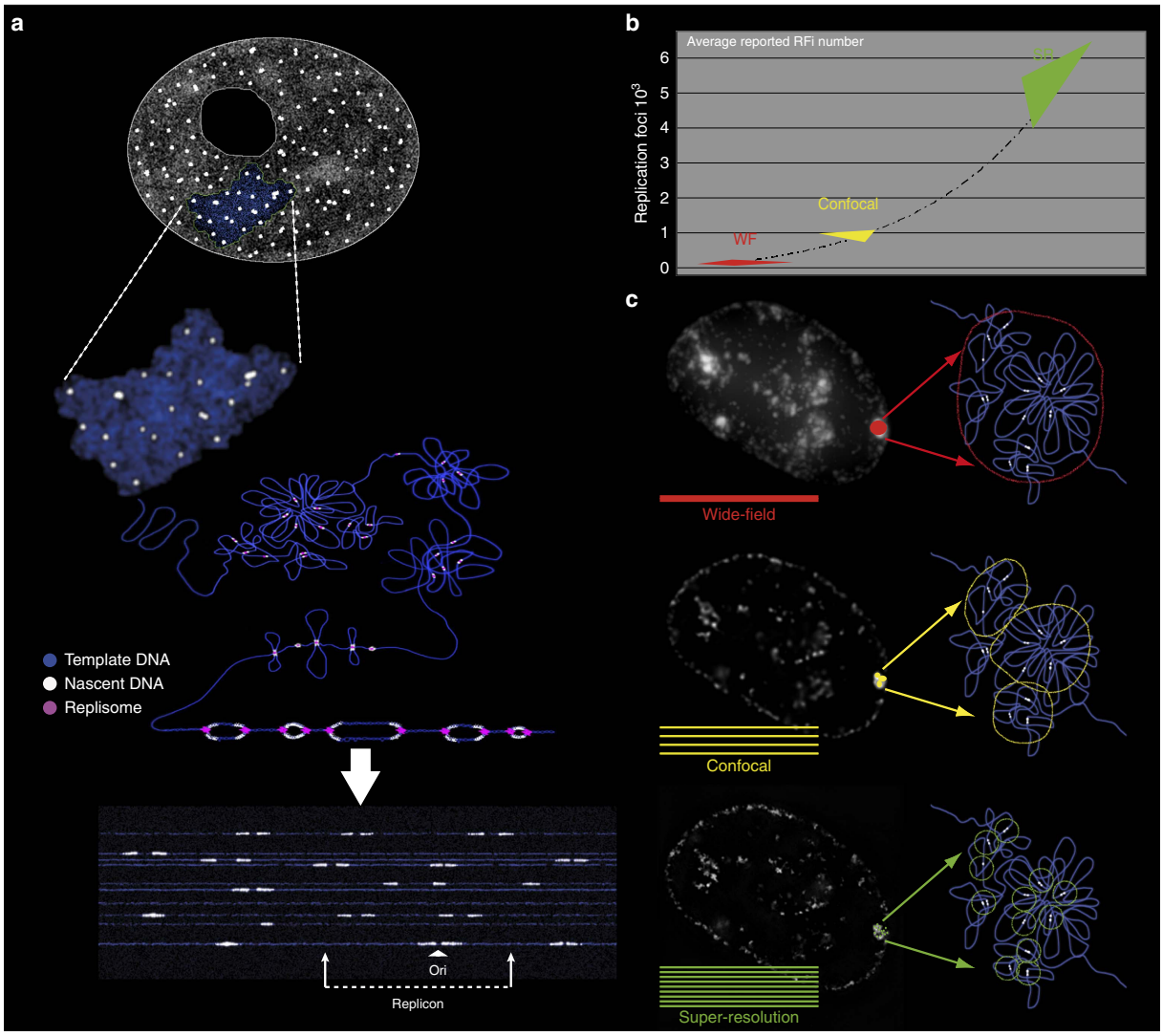

Figure 4 | Replication sites dissected by super-resolution microscopy in the mammalian nucleus correspond to individual replicons. (**a**) A cartoon showing how replication sites/units can be seen at different levels of chromatin compaction from the extended DNA fibres to the 3D-preserved whole-cell (nucleus) level. (**b**) Increase in RFi numbers driven by resolution improvements in microscopy during the past three decades[42]. WF: wide field; SR: super-resolution microscopy. (**c**) Microscopic images and corresponding cartoon interpretation of replication sites in the mammalian nucleus imaged at different levels of resolution. For summary of experimental numbers and calculations see Table 5.

0.77 has a MSE of 0.3 respectively. Those MSE take into account the variances of the measured genome size (Table 2), the measured fork speed (Table 3) and the measured S-phase length (Table 1). The difference of the average number of replicons per single RF between human (0.92) and mouse (0.77) cells, likely arise from differential clustering of replication forks in particular cell types and/or S-phase sub-periods when some RFi can contain individual replication forks.

All in all, we conclude that, for all S-phase patterns, the majority of nuclear replication sites were resolved down to the level of single replicons with a portion of spatially separated single replication forks.

Discussion

In this study, we present a comprehensive examination of DNA replication in mammalian cells including various resolution levels of optical microscopy. Special effort was made to control for all inaccuracies that could affect the outcome of the analysis and characterization of RFi in super-resolution images.

First, we took advantage of mammalian cell lines stably expressing fluorescent replication factors and performed confocal live-cell microscopy to directly characterize the temporal S-phase dynamics in these cells. We further measured genome size for each cell line used in our experiments and analysed the molecular characteristics of replicons in the same cells. To quantify RFi numbers in super-resolution images, we developed and verified user-independent protocols for 3D RFi segmentation and counting. We compared RFi quantifications results with respect with the other parameters measured for identical cells.

In both cell lines we detected on average five thousands RFi at any S-phase sub-stage using super-resolution imaging (Fig. 3). Combining all the experimental data together, we concluded that the majority of RFi represent single replicons at 3D-SIM

Table 5 | Calculation of the number of replicons per replication focus from the experimental data.

Experimental data	Human HeLa Kyoto (Mean ± s.e.m.)	Mouse C2C12 (Mean ± s.e.m.)
RFS, 10^3 Ntd per min	1.65 ± 0.12	2.46 ± 0.11
IOD, kbp	188.7 ± 17.2	161.7 ± 16.3
GS, 10^3 Mbp	9.7 ± 0.002	11.4 ± 0.006
Active RFi at any given time point	5,583 ± 162	5,314 ± 227
Total S-phase duration, minutes	570 ± 9	564 ± 23
Calculations	**Human HeLa Kyoto (Mean ± MSE)**	**Mouse C2C12 (Mean ± MSE)**
Time to replicate the genome with one fork (GS/RFS), hours	97,662 ± 1.95 × 10^{-5}	77,230 ± 1.19*10^{-5}
Replication forks active in parallel (GS/RFS/S-phase duration)	10,298 ± 1	8,216 ± 0.0
Replicons active in parallel (active forks/2)	5,149	4,108
Replicons per RFi (calculated replicons active in parallel/counted RFi)	**0.92 ± 0.2**	**0.77 ± 0.3**

GS, Genome size; IOD, Inter-origin distance; MSE, mean squared error; RFi, replication foci; RFS, replication fork speed.
See equation (3) in Materials and methods.

resolution with a number of optically resolved single replication forks.

According to the limiting factor concept, the number of active replicons at any given S-phase time-point is determined by the pool of available limiting factors. If for these replicons it is assumed that the corresponding origins of replication are activated during a short-time window of S-phase, the time of synthesis of the whole subset will roughly correspond to the lifetime of an average replicon, which we estimated as 57 min for human and 33 min for mouse cells. S-phase progression can be modelled as sequential activation of subsets of origins and DNA synthesis in the corresponding pluralities of replicons. It is unlikely, however, that there are distinct classes of origins, which are initiated strictly one after the other. A more realistic scenario is that origin firing of adjacent replicons in the next subset starts before replicons from the previous subset complete DNA synthesis, leading to replicons from multiple subsets being active in parallel[2,44]. Both sequential synchronous and asynchronous modes of origin firing would nonetheless lead to identical average numbers of simultaneously active replicons (Supplementary Fig. 6). Similarly, the subdivision of S-phase into three major discrete sub-stages (Se, Sm and Sl) is an oversimplification of real RFi dynamics, which very likely represents a continuous spreading of replication onto non-replicated chromosome segments and corresponding gradual changes in RFi patterns. DNA flow cytometry histograms (Supplementary Fig. 6 as well as accompanying study[37]) demonstrate the absence of substantial differences in cumulative DNA synthesis intensity throughout S-phase. Therefore, the average estimates of RFi numbers used in our calculations represented a reasonable simplification.

The empirical differences between Se, Sm and Sl RFi numbers may illustrate variations in degree of clustering of replication forks during individual S-phase stages. For example, the portion of RFi containing single-replication forks may be higher than average during early S-phase in mouse C2C12 and during middle S-phase in HeLa Kyoto cells. In the latter cases, 3D-SIM may still not completely resolve all RFi leading to their underestimation (Fig. 3c and Supplementary Fig. 4). We also observed cell-to-cell variability in RFi numbers and S-phase duration, as well as average spacing of origins and RFS[45]. Differences in RFi numbers in Se, Sm and Sl may also be associated with corresponding changes in RFS and IOD. Nonetheless, the mouse myoblasts having a larger genome size but the same S-phase duration (time to duplicate the whole genome) did not compensate by increasing the average number of simultaneously active replicons but rather mainly by tweaking up the DNA synthesis speed. The latter has interesting metabolic implications regarding nucleotide pool availability.

While the intra-S-phase variations of all these parameters are worthy of a separate study, such a detailed analysis will not affect our main conclusions since, despite the reported variability of the above parameters, genome duplication is completed by the end of S-phase.

The observation of spatially separated replication machineries corresponding to individual replicons and replication forks in (live) 3D-preserved cells contradicts the model of S-phase progression based on replication factories as common synthetic centres that process multiple tandem replicons. The term 'replication factories' was initially coined based on the combined consideration of: (i) small number of RFi, which were nuclease resistant and contained nascent DNA and replication proteins; and (ii) DNA fibre data on organization of replicons in clusters; which taken together suggested that each replication focus 'was a 'factory' containing many polymerizing machines' that synchronously processes aggregates of multiple tandem replicons[24,26]. The reported clustering of multiple tandem replicons may be a consequence of the inhibitor treatments used in the original DNA fibre and autoradiography studies leading to dormant origin activation[7,12,27]. Our data show that individual replicons or even single forks can be optically resolved. Therefore, these data suggest that the basics of the replication factories concept are not supported by the improved resolution of imaging and RFi can no longer be considered as complex entities, that is, factories. Accordingly, our data suggest that, at the nuclear level, the process of DNA replication is unlikely to involve assembly of multiple origins of replication at specific aggregate synthesis centres, but the replication machinery rather reads structural aspects of chromatin organization. Chromatin separation into individual replication units may correlate with its organization into topologically associated stable domains[12,46] however not much is known of what determines chromosome organization into TADs.

The idea that chromatin organization can dictate the spatial organization of DNA replication is supported by the data on *de-novo* assembly of new replisomes by a domino effect-like mechanism *in cis*[21,44,47]. In this scenario, further elaborated in the accompanying study[37], the sites of assembly, the pattern and dynamics of nuclear RFi will be dictated by the intranuclear folding of the chromatin fibre itself. Accordingly, in physiological conditions (that is, in the absence of replicative stress) replication-related reorganization of chromatin will be limited to local changes of chromatin condensation state, which will be more prominent in compacted heterochromatin. The above model of S-phase progression is also compatible with the reported influence of DNA replication fork movement on the chromatin loop size organization and origin choice in the following cell cycle[29].

Resolving conventional nuclear RFi down to sites containing single replicons or replication forks implies a modified interpretation of the RFi characteristics that are traditionally analysed in studies of spatio-temporal organization of DNA replication. In this respect, the original meaning of the term 'replication factory' as a macromolecular complex performing simultaneous synthesis of multiple replicons, needs to be reduced to smaller replisome complexes or even single replisomes, which are assembled on DNA spatially organized within the nucleus.

An inherent component of the replication factory model were clusters of 30 nm chromatin loops arranged at each factory[26], which were assumed to form rosette-like chromatin sub-compartments. Analysis of chromatin interactions using 3C-based technologies[48] has suggested that, above 11 nm nucleosomal string, there can exist not only canonical 30 nm fibre[49] but also various higher-level compaction states of interphase chromatin[50,51]. Our data and the ensuing model[37] are compatible with the view that interphase chromatin fibres are organized by complex and dynamic topological looping interactions[52], which provide a structural framework for DNA metabolism. Based on our comparison of numbers of RFi from conventional and super-resolution microscopy, an average of five replicons correspond to one conventional replication focus (Fig. 3e). This analysis suggests a spatial association of replicons within one Mbp chromatin segment, which likely reflects the spatial chromatin organization of the segment. Nonetheless, genetic continuity would not be mandatory for such an association. As proposed in our accompanying study[37], the induced domino-like replication origin activation, would implicitly lead to the temporal grouping of active replicons within a chromatin fibre. Further experimental analyses of dynamic relationships between neighbouring RFi will be needed.

Finally, the results presented in this study also suggest that 3D-SIM microscopy is a first-choice approach for multicolour 3D analysis of elementary replication units in eukaryotic cells. Based on 3D-SIM microscopy and multicolour 3D analysis, further experiments need to be designed to address the 3D arrangement of replicons in relation to epigenetic chromatin signatures and other aspects of functional chromatin organization. Our findings and ongoing development of higher spatio-temporal resolution 3D-SIM live systems[53–55] create a basis for *in vivo* genome duplication analysis in 3D at a single-replicon resolution. Importantly, we present evidence that individual replicons within the chromatin context and not replicon clusters represent the main players of DNA replication. We propose that beyond the 150–200 bp nucleosomal DNA unit, a subsequent order of functional chromatin organization is constituted by the a thousand times larger (150–200 kbp) genome unit functioning as individual replicons during S-phase. Fifty years after the introduction of the replicon concept[56] individual replicons are again in focus backed by our vastly improved knowledge of chromatin structure and function.

Methods

Cell culture. HeLa Kyoto cells[57] (a kind gift from Jan Ellenberg) were grown in DMEM medium supplemented with 10% FCS, L-glutamine and antibiotics at 37 °C in a humidified atmosphere of 5% CO_2. Mouse C2C12 myoblasts expressing fluorescently tagged PCNA[21] were grown in DMEM medium supplemented with 20% FCS, L-glutamine and antibiotics at 37 °C in a humidified atmosphere of 5% CO_2.

Generation of cell lines stably expressing fluorescent PCNA. HeLa Kyoto cell lines expressing fluorescent PCNA variants were obtained using the Flp-In system (Invitrogen) based on the Flp site-specific recombinase. Briefly, cells were first transfected with a plasmid bearing a FRT site and the Zeocin resistance gene fused to the *LacZ* gene (pFRT-lacZeo) using PEI transfection[58]. Cells where the plasmid integrated into a chromosome were selected throughout a week on the basis of the newly acquired Zeocin resistance (75 μg ml^{-1}) and eight clones with integrated FRT sites were isolated. Beta-galactosidase activity of HeLa Kyoto LacZ stable clones was then verified using X-gal and ONPG (*o*-nitrophenyl-β-D-galactosidase) assays.

HeLa Kyoto FRTLacZ clones with low and high β-galactosidase activity were selected for further transfection with pFRT-B-GPCNA (encoding GFP-PCNA) and pFRT-B-CPCNA (encoding mCherry-PCNA) plasmids and cotransfected with pOG44 Flp-recombinase using Transfectin (BioRad) (Supplementary Fig. 1A). Four hours after transfection the cell culture medium was exchanged and cells were grown for 48 h and selected with 2.5 μg ml^{-1} Blasticidin (Invitrogen).

Characterization of cell lines expressing fluorescent PCNA. Absence of cell cycle effects was verified by propidium iodide (PI) staining and flow cytometry analysis (Supplementary Fig. 1C). For cell cycle analysis with PI staining, cells were trypsinized, washed with PBS, pelleted and fixed with ice-cold methanol (1–4 h incubated at 4 °C). After fixation, cells were pelleted and resuspended in PBS then treated with RNAseA (Sigma, working concentration: 50 μg ml^{-1}) and incubated with PI solution (final concentration 50 μg ml^{-1}, 30 min at 4 °C). Samples were run on a BD FACSVantage flow cytometer and the data were analysed using FlowJo software (Tree Star Inc.).

Expression and characteristic S-phase distributions of fluorescent PCNA were verified visually. Colocalization of GFP-PCNA and mCherry-PCNA with active sites of active nuclear replication was confirmed using BrdU labelling and detection that was performed as follows: BrdU (BD Biosciences) was added to the cell culture medium to the final concentration of 100 μM for 30 min, the cells were then washed with PBS and then fixed with 3.7% formaldehyde for 10 min at room temperature; DNA was denatured by DNAseI treatment, anti-BrdU primary mouse antibody (1:5, BD Biosciences, catalog # 347580) and donkey anti-mouse IgG Texas Red (1:200, Jackson Immuno Research Laboratories, catalog # 715-075-151) or goat anti-mouse IgG Alexa Fluor 488 (1:400, ThermoFisher Scientific, catalog # 11001) secondary antibodies; and nuclear DNA was stained with DAPI (0.5 μg ml^{-1}), 5 min at room temperature.

Counting of BrdU positive S-phase cells versus non-S-phase cells showed that 34.9% of cells were in S-phase. This number was comparable to the flow cytometry estimates.

For immunoblot analysis (Supplementary Fig. 1B) of the ectopic fusion proteins and the relative amount of the endogenous PCNA, whole-cell lysates were analysed by SDS–polyacrylamide gel electrophoresis, transferred to nitrocellulose membranes and incubated with rat anti-PCNA monoclonal antibodies 16D10 (ref. 59) followed by donkey anti-rat IgG Cy5 (1:200, Jackson Immuno Research Laboratories, catalog # 712-175-153) and detection using a fluorescence scanning imaging system (STORM, GE Healthcare).

Genome size measurements. To measure the amount of genomic DNA the cells were washed twice with PBS/EDTA buffer, trypsinized and resuspended in Versene solution (0.2 g l^{-1} EDTA(Na4) in PBS). Before staining, cells were counted and mixed with a comparable number of male C57Bl mice splenocytes. For DNA staining, the cellular suspension was supplemented with Triton X-100 (Sigma) to the final concentration of 0.1%, ethidium bromide (Calbiochem) to the final concentration 20 mg ml^{-1} and olivomycin A (MZM) to the final concentration 40 mg ml^{-1} and $MgCl_2$ to the final concentration 15 mM, and incubated for 24 h at 4 °C. Measurements were performed using a self-built high-resolution cytometer setup based on a fluorescence microscope and laminar flow chamber[60]. At least three DNA histograms were obtained for each probe. For C57Bl mouse splenocytes used as a standard object, the variation coefficient of DNA histograms was $<2.0\%$. To calculate the average DNA content in a cell population, positions of the peak in the histogram corresponding to the mouse splenocytes and G1 peak of the cell population were determined (Fig. 2a). The error of measurement of the G1 peak position was $\leq 0.2\%$. The relative amount of the genomic DNA in each cell line was corrected for human/mouse genome size and female/male differences (factors of 1.06 and 1.016, respectively). The size of genomic DNA in base pairs was calculated based on the estimated amount of DNA in a diploid human genome—7 pg (ref. 61)—with the following formula:

$$\mathrm{DNA(base\,pairs)} = \mathrm{DNA(pg)} \times 0.978 \times 10^9$$

DNA fibre experiments. Replication labelling and preparation of DNA fibres: Cells were pulse labelled with 100 μM IdU for 30 min, washed two times with PBS, followed by a 30 min 100 μM CldU pulse. Cells were trypsinized, pelleted and resuspended in low-temperature melting agarose to form plugs of 200,000 cells each. Plugs were incubated over night at 50 °C in 0.25 mg ml^{-1} proteinase K in 10% sarcosyl/EDTA, washed in Tris-EDTA buffer twice for 30 min at room temperature. Agarose was digested at 42 °C by two units of β-agarase per plug. Fibres were combed using the Genomic Vision combing machine as follows: in short, a silanized coverslip was incubated in the sample for 5 min. The coverslip was removed at a constant speed of 300 μm s^{-1} with a resulting average fibre length between 250–500 kbp.

Staining: DNA fibres were dehydrated in a series of ethanol with increasing concentration and denatured in a 0.5 M NaOH/1 M NaCl solution. After washing with 0.05 M Tris/1 M NaCl and PBS, the incorporated nucleotides were detected with two to four layers of antibodies in 4% BSA/PBS for each 1 h at 37 °C. Primary

antibodies: mouse anti-BrdU (1:5, BD Biosciences, catalog # 347580); rat anti-BrdU (1:25, Harlan Sera-Lab, catalog # OBT0030). Secondary antibodies: goat anti-mouse IgG Alexa 488 (1:200, ThermoFisher Scientific, catalog # 11001); and donkey anti-rat IgG Cy3 (1:200, Jackson Immuno Research Laboratories, catalog # 712-165-153). Third antibody: horse anti-goat IgG biotin (1:200, Vector Laboratories, catalog # BA-9500). Fourth layer: Streptavidin-Alexa 488 (1:200, Invitrogen, catalog # S11223). Stained DNA fibres were mounted in Vectashield (Invitrogen).

Microscopy: Epifluorescence images were obtained using an Axiovert 200 microscope (Zeiss) with a $\times$40/1.4 NA Plan-Apochromat oil immersion objective lens (Zeiss) and a cooled 12-bit charge-coupled device camera (Sensicam).

Image analysis: The brightness and colour of each image was adjusted with ImageJ[62]. It should be considered that the several pictures of one fibre look equal in brightness and contrast. IdU was set to green, CldU to red. Alignment of the images of the same fibre was performed with Photoshop (function 'photomerge'). Brightness and contrast was set again to optimize analysis conditions. The aligned images were measured in ImageJ. The unit of length was set on'micrometre' and the pixel width on 0.168 under image properties. To measure the length of the several parts for IOD and fork speed, the selection tool and the function 'measure' was used.

To get the track length in kbp, for the IODs, the value was multiplied with 2 (stretching-factor). For the fork speed in kbp min^{-1}, the value was additionally divided by 30 (30 min nucleotide pulse).

Dynamic cell cycle analysis. C2C12 stably expressing GFP-PCNA or HeLa Kyoto cells stably expressing FP-PCNA were plated on chambered glass coverslips one day before microscopy.

3D stacks were obtained on a UltraVIEW VoX spinning disc confocal system (Perkin Elmer, UK) in a closed live-cell microscopy chamber (ACU control, Olympus, Japan) heated to 37 °C, with 5% CO_2 and 60% air humidity control, mounted on a Nikon Ti microscope (Nikon, Japan). Image acquisition was performed using a $\times$60/1.45 NA Planapochromat oil immersion objective lens. Images were obtained with a cooled 14-bit EMCCD camera (Hamamatsu) and had a voxel size of $104 \times 104 \times 500\,nm^3$.

Alternatively, image time series were acquired with a Zeiss LSM 510 Meta laser scanning confocal microscope equipped with a stage mounted incubation system maintaining a humidified atmosphere of 5% CO_2 at 37 °C (Okolab) using a 63 $\times$ /1.4 NA Plan-Apochromat oil immersion objective lens and the 488 nm laser line of an Argon ion laser at low power every 15 min (zoom = 1.0, field size: 1,024 $\times$ 1,024 pixels; pixel size: $200 \times 200\,nm^2$) over 174 frames.

Individual frames were processed and assembled using ImageJ.

Visual inspection and classification of PCNA patterns frame by frame was performed and cells were first classified as: non-replicating, early/mid/late S-phase and mitotic. Temporal information on the preceding/subsequent cell cycle stage was used to discriminate between G1 and G2 cells.

The duration of each cell cycle sub-stage was determined by multiplying the number of frames corresponding to each cell cycle sub-stage by 15 min.

Replication labelling and staining. For BrdU replication labelling, cells grown on cover glasses were incubated with 10–20 µM BrdU (BD Biosciences) for 5–30 min, fixed and stained as described above. Alternatively, cells grown on cover glasses were incubated with 10–20 µM EdU (Invitrogen) for the specified time, fixed and stained using the Click-iT assay (Invitrogen). Fluorophores conjugated to the secondary antibody or fluorescent azide were chosen to have sufficiently different emission spectra from the fluorescent group attached to FP-PCNA.

To enhance GFP-PCNA signal and increase signal-to-noise ratio before 3D-SIM imaging, C2C12 GFP-PCNA or HeLa Kyoto GFP-PCNA cells were processed as follows: cells were incubated with the CSK extraction buffer (10 mM Pipes-KOH, pH 7.0, 100 mM NaCl, 300 mM sucrose, 3 mM $MgCl_2$) before fixing them as described in ref. 63. Fixed cells were permeabilized with 0.5% Triton X-100 and PCNA was detected using mouse anti-PCNA monoclonal antibody (1:200, Santa Cruz, catalog # sc-56) followed by goat anti-mouse IgG Alexa 488 (1:400, ThermoFisher Scientific, catalog # 11001). Stained samples were mounted in Vectashield (Invitrogen).

Replication foci visualization and quantification. *Confocal microscopy*: Images were acquired with a Leica TCS SP5II confocal laser scanning microscope (Leica Microsystems, Wetzlar, Germany) equipped with an oil immersion Plan-Apochromat $\times$100/1.44 NA objective lens (pixel size in *XY* set to 50 nm, Z-step = 290 nm) and laser lines at 405, 488, 561 and 633 nm. Alternatively, the spinning disk microscope was used (see dynamic cell cycle analysis section above).

3D-SIM: Super-resolution imaging of fixed samples was performed on a OMX prototype system[35] or DeltaVision OMX V3 system (GE Healthcare) equipped with a $\times$100/1.40 NA PlanApo oil immersion objective (Olympus), Cascade II:512 EMCCD cameras (Photometrics) and 405, 488 and 593 nm diode lasers. Live-cell super-resolution imaging was performed with a DeltaVision OMX V3 Blaze system (GE Healthcare), equipped with a $\times$60/1.42 NA PlanApo oil objective and (Olympus) and sCMOS cameras (PCO) for high-speed stack acquisition. Both, fixed and live 3D-SIM was performed as previously described[64].

3D-SIM super-resolution images were reconstructed[41] by processing raw images using the API DeltaVision OMX softWoRx image processing software (version: 5.9.9 release 19).

For comparison, conventional wide-field image stacks were generated from 3D-SIM raw data by average projection of five consecutive phase-shifted images from each plane for the first rotation angle and subsequently subjected to an iterative 3D deconvolution using softWoRX 6.0. For direct comparison with 3D-SIM images, the pixel numbers were doubled in *x* and *y* using a bicubic interpolation in ImageJ to unify voxel sizes in all cases to $40 \times 40 \times 125$ nm.

Image analysis: Quantification of RFi in cells was performed as summarized in Supplementary Fig. 3 and detailed in ref. 42. Briefly, confocal microscopy images were smoothed using mean filter ($r = 1.5$) to reduce effects of noise on local maxima identification. Stacks were normalized and local maxima were identified and marked with single pixels having maximum intensity using 'Find stack maxima' Image J macros available from: http://rsbweb.nih.gov/ij/macros/FindStackMaxima.txt. The stack with the map of local maxima was convolved with a Gaussian filter ($r = 1.0$) to generate artificial focal objects around the identified maxima. Finally, the number of the objects corresponding to the local maxima was counted using a 3D object counting plug-in[65] available from:

http://imagejdocu.tudor.lu/doku.php?id=plugin:analysis:3d_object_counter:start.

3D-SIM images were cropped with ImageJ to one nucleus only and background was removed automatically by the triangle method[66]. Volocity v.5 3D image analysis software (Perkin Elmer) was used to separate and count touching RFi (see Supplementary Fig. 3 for image preprocessing details).

Statistical analysis representation. Statistical analyses were represented with violin plots (Supplementary Fig. 7; modified from ref. 29), a variation to the box plot with a kernel density plot on each side to display the distribution of the data at different values. Similar to a box plot it includes a marker for the median, a box indicating the inter-quartile range and whiskers for the upper and lower adjacent values.

Error calculations. Error calculations were performed in R-Project (http://www.R-project.org).

S.d. for a single variable were computed via equation 1.

$$\tilde{\sigma} = \sqrt{\sum_{i=1}^{n} \frac{v_i^2}{n-1}} = \sqrt{\sum_{i=1}^{n} \frac{(x_i - \bar{x})^2}{n-1}} \quad (1)$$

S.e.m. of the mean were calculated with equation 2.

$$\tilde{\sigma} = \sqrt{\sum_{i=1}^{n} \frac{v_i^2}{n(n-1)}} = \frac{\tilde{\sigma}}{\sqrt{n}} \quad (2)$$

To calculate errors for diverse factors, for example, independent variables, the simplified version of the Gaussian error formula (the variance formula), as shown in equation 3, was used. Those errors were marked as 'MSE'.

$$\tilde{\sigma}_f = \sqrt{\sum_{j=1}^{k} \left(\tilde{\sigma}_{x_j} \frac{\partial f}{\partial x_j} \right)^2} \quad (3)$$

References

1. Chagin, V. O., Stear, J. H. & Cardoso, M. C. Organization of DNA replication. *Cold Spring Harb. Perspect. Biol.* **2,** a000737 (2010).
2. Shermoen, A. W., McCleland, M. L. & O'Farrell, P. H. Developmental control of late replication and S phase length. *Curr. Biol.* **20,** 2067–2077 (2010).
3. Goldar, A., Labit, H., Marheineke, K. & Hyrien, O. A dynamic stochastic model for DNA replication initiation in early embryos. *PloS ONE* **3,** e2919 (2008).
4. Rhind, N. DNA replication timing: random thoughts about origin firing. *Nat. Cell. Biol.* **8,** 1313–1316 (2006).
5. Cairns, J. Autoradiography of HeLa cell DNA. *J. Mol. Biol.* **15,** 372–373 (1966).
6. Hand, R. DNA replication in mammalian cells. Altered patterns of initiation during inhibition of protein synthesis. *J. Cell Biol.* **67,** 761–773 (1975).
7. Huberman, J. A. & Riggs, A. D. On the mechanism of DNA replication in mammalian chromosomes. *J. Mol. Biol.* **32,** 327–341 (1968).
8. Edenberg, H. J. & Huberman, J. A. Eukaryotic chromosome replication. *Annu. Rev. Genet.* **9,** 245–284 (1975).
9. Hand, R. Eucaryotic DNA: organization of the genome for replication. *Cell* **15,** 317–325 (1978).
10. O'Keefe, R. T., Henderson, S. C. & Spector, D. L. Dynamic organization of DNA replication in mammalian cell nuclei: spatially and temporally defined replication of chromosome-specific alpha-satellite DNA sequences. *J. Cell Biol.* **116,** 1095–1110 (1992).
11. Ma, H. *et al.* Spatial and temporal dynamics of DNA replication sites in mammalian cells. *J. Cell Biol.* **143,** 1415–1425 (1998).
12. Jackson, D. A. & Pombo, A. Replicon clusters are stable units of chromosome structure: evidence that nuclear organization contributes to the efficient

activation and propagation of S phase in human cells. *J. Cell Biol.* **140,** 1285–1295 (1998).
13. Nakamura, H., Morita, T. & Sato, C. Structural organizations of replicon domains during DNA synthetic phase in the mammalian nucleus. *Exp. Cell Res.* **165,** 291–297 (1986).
14. Nakayasu, H. & Berezney, R. Mapping replicational sites in the eucaryotic cell nucleus. *J. Cell Biol.* **108,** 1–11 (1989).
15. Manders, E. M., Stap, J., Brakenhoff, G. J., van Driel, R. & Aten, J. A. Dynamics of three-dimensional replication patterns during the S-phase, analysed by double labelling of DNA and confocal microscopy. *J. Cell Sci.* **103,** 857–862 (1992).
16. Manders, E. M., Stap, J., Strackee, J., van Driel, R. & Aten, J. A. Dynamic behavior of DNA replication domains. *Exp. Cell. Res.* **226,** 328–335 (1996).
17. Tomilin, N. *et al.* Visualization of elementary DNA replication units in human nuclei corresponding in size to DNA loop domains. *Chromosome Res.* **3,** 32–40 (1995).
18. van Driel, R., Manders, E. M., de Jong, L., Stap, J. & Aten, J. A. Mapping of DNA replication sites in situ by fluorescence microscopy. *Methods Cell Biol.* **53,** 455–469 (1998).
19. Kennedy, B. K., Barbie, D. A., Classon, M., Dyson, N. & Harlow, E. Nuclear organization of DNA replication in primary mammalian cells. *Genes Dev.* **14,** 2855–2868 (2000).
20. Dimitrova, D. S. & Berezney, R. The spatio-temporal organization of DNA replication sites is identical in primary, immortalized and transformed mammalian cells. *J. Cell Sci.* **115,** 4037–4051 (2002).
21. Leonhardt, H. *et al.* Dynamics of DNA replication factories in living cells. *J. Cell Biol.* **149,** 271–280 (2000).
22. van Dierendonck, J. H., Keyzer, R., van de Velde, C. J. & Cornelisse, C. J. Subdivision of S-phase by analysis of nuclear 5-bromodeoxyuridine staining patterns. *Cytometry* **10,** 143–150 (1989).
23. Mills, A. D. *et al.* Replication occurs at discrete foci spaced throughout nuclei replicating *in vitro*. *J. Cell. Sci.* **94,** 471–477 (1989).
24. Hozak, P., Hassan, A. B., Jackson, D. A. & Cook, P. R. Visualization of replication factories attached to nucleoskeleton. *Cell* **73,** 361–373 (1993).
25. Hozak, P., Jackson, D. A. & Cook, P. R. Replication factories and nuclear bodies: the ultrastructural characterization of replication sites during the cell cycle. *J. Cell Sci.* **107,** 2191–2202 (1994).
26. Cook, P. R. The organization of replication and transcription. *Science* **284,** 1790–1795 (1999).
27. Ge, X. Q., Jackson, D. A. & Blow, J. J. Dormant origins licensed by excess Mcm2-7 are required for human cells to survive replicative stress. *Genes Dev.* **21,** 3331–3341 (2007).
28. Buongiorno-Nardelli, M., Micheli, G., Carri, M. T. & Marilley, M. A relationship between replicon size and supercoiled loop domains in the eukaryotic genome. *Nature* **298,** 100–102 (1982).
29. Hintze, J. L. & Nelson, R. D. Violin plots: a box plot-density trace synergism. *Am. Stat.* **52,** 181–184 (1998).
30. Rajan, M. *et al.* Generation of an alpaca-derived nanobody recognizing gamma-H2AX. *FEBS Open Bio* **5,** 779–788 (2015).
31. Cayrou, C., Coulombe, P. & Mechali, M. Programming DNA replication origins and chromosome organization. *Chromosome Res.* **18,** 137–145 (2010).
32. Koberna, K. *et al.* Electron microscopy of DNA replication in 3-D: evidence for similar-sized replication foci throughout S-phase. *J. Cell. Biochem.* **94,** 126–138 (2005).
33. Ligasova, A., Raska, I. & Koberna, K. Organization of human replicon: singles or zipping couples? *J. Struct. Biol.* **165,** 204–213 (2009).
34. Baddeley, D. *et al.* Measurement of replication structures at the nanometer scale using super-resolution light microscopy. *Nucleic Acids Res.* **38,** e8 (2010).
35. Schermelleh, L. *et al.* Subdiffraction multicolor imaging of the nuclear periphery with 3D structured illumination microscopy. *Science* **320,** 1332–1336 (2008).
36. Cseresnyes, Z., Schwarz, U. & Green, C. M. Analysis of replication factories in human cells by super-resolution light microscopy. *BMC Cell Biol.* **10,** 88 (2009).
37. Löb, D. *et al.* 3D replicon distributions arise from stochastic initiation and domino-like DNA replication progression. *Nat. Commun.* **7,** 11207 doi: 10.1038/ncomms11207 (2016).
38. Casas-Delucchi, C. S. *et al.* Histone acetylation controls the inactive X chromosome replication dynamics. *Nat. Commun.* **2,** 222 (2011).
39. Schurra, C. & Bensimon, A. Combing genomic DNA for structural and functional studies. *Methods Mol. Biol.* **464,** 71–90 (2009).
40. Techer, H. *et al.* Replication dynamics: biases and robustness of DNA fiber analysis. *J. Mol. Biol.* **425,** 4845–4855 (2013).
41. Schermelleh, L., Heintzmann, R. & Leonhardt, H. A guide to super-resolution fluorescence microscopy. *J. Cell Biol.* **190,** 165–175 (2010).
42. Chagin, V. O., Reinhart, M. & Cardoso, M. C. in *Methods Mol Biol* Vol. 1300 (eds Dalgaard, J. & Vengrova, S.) 43–65 (Springer Science + Business Media, New York, 2015).
43. Fox, M. H., Arndt-Jovin, D. J., Jovin, T. M., Baumann, P. H. & Robert-Nicoud, M. Spatial and temporal distribution of DNA replication sites localized by immunofluorescence and confocal microscopy in mouse fibroblasts. *J. Cell Sci.* **99,** 247–253 (1991).
44. Sporbert, A., Gahl, A., Ankerhold, R., Leonhardt, H. & Cardoso, M. C. DNA polymerase clamp shows little turnover at established replication sites but sequential *de novo* assembly at adjacent origin clusters. *Mol. Cell* **10,** 1355–1365 (2002).
45. Berezney, R., Dubey, D. D. & Huberman, J. A. Heterogeneity of eukaryotic replicons, replicon clusters, and replication foci. *Chromosoma* **108,** 471–484 (2000).
46. Pope, B. D. *et al.* Topologically associating domains are stable units of replication-timing regulation. *Nature* **515,** 402–405 (2014).
47. Maya-Mendoza, A., Olivares-Chauvet, P., Shaw, A. & Jackson, D. A. S phase progression in human cells is dictated by the genetic continuity of DNA foci. *PLoS Genet.* **6,** e1000900 (2010).
48. Fraser, J., Williamson, I., Bickmore, W. A. & Dostie, J. An overview of genome organization and how we got there: from FISH to Hi-C. *Microbiol. Mol. Biol. Rev.* **79,** 347–372 (2015).
49. McGhee, J. D., Rau, D. C., Charney, E. & Felsenfeld, G. Orientation of the nucleosome within the higher order structure of chromatin. *Cell* **22,** 87–96 (1980).
50. Bian, Q. & Belmont, A. S. Revisiting higher-order and large-scale chromatin organization. *Curr. Opin. Cell. Biol.* **24,** 359–366 (2012).
51. Razin, S. V. & Gavrilov, A. A. Chromatin without the 30-nm fiber: constrained disorder instead of hierarchical folding. *Epigenetics.* **9,** 653–657 (2014).
52. Mateos-Langerak, J. *et al.* Spatially confined folding of chromatin in the interphase nucleus. *Proc. Natl Acad. Sci. USA* **106,** 3812–3817 (2009).
53. Chen, B. C. *et al.* Lattice light-sheet microscopy: imaging molecules to embryos at high spatiotemporal resolution. *Science* **346,** 1257998 (2014).
54. Fiolka, R., Shao, L., Rego, E. H., Davidson, M. W. & Gustafsson, M. G. Time-lapse two-color 3D imaging of live cells with doubled resolution using structured illumination. *Proc. Natl Acad. Sci. USA* **109,** 5311–5315 (2012).
55. Shao, L., Kner, P., Rego, E. H. & Gustafsson, M. G. Super-resolution 3D microscopy of live whole cells using structured illumination. *Nat. Methods* **8,** 1044–1046 (2011).
56. Jacob, F., Brenner, S. & Cuzin, F. On the regulation of DNA replication in bacteria. *Cold Spring Harb. Symp. Quant. Biol.* **28,** 329–348 (1963).
57. Erfle, H. *et al.* Reverse transfection on cell arrays for high content screening microscopy. *Nat. Protoc.* **2,** 392–399 (2007).
58. Agarwal, N. *et al.* MeCP2 interacts with HP1 and modulates its heterochromatin association during myogenic differentiation. *Nucleic Acids Res.* **35,** 5402–5408 (2007).
59. Rottach, A. *et al.* Generation and characterization of a rat monoclonal antibody specific for PCNA. *Hybridoma* **27,** 91–98 (2008).
60. Chagin, V. O., Rozanov, Y. M. & Tomilin, N. V. Multiple deceleration of DNA synthesis during the S phase of cell cycle: study by flow cytometry method. *Dokl. Biochem. Biophys.* **394,** 11–14 (2004).
61. Gregory, T. R. *Animal Genome Size Database* <http://www.genomesize.com> (2012).
62. Rasband, W. S. *ImageJ, U.S. National Institutes of Health, Bethesda, Maryland, USA* <http://imagej.nih.gov/ij/> (1009-2012).
63. Masata, M., Juda, P., Raska, O., Cardoso, M. C. & Raska, I. A fraction of MCM 2 proteins remain associated with replication foci during a major part of S phase. *Folia Biol. (Praha)* **57,** 3–11 (2011).
64. Smeets, D. *et al.* Three-dimensional super-resolution microscopy of the inactive X chromosome territory reveals a collapse of its active nuclear compartment harboring distinct Xist RNA foci. *Epigenetics Chromatin* **7,** 8 (2014).
65. Bolte, S. & Cordelieres, F. P. A guided tour into subcellular colocalization analysis in light microscopy. *J. Microsc.* **224,** 213–232 (2006).
66. Zack, G. W., Rogers, W. E. & Latt, S. A. Automatic measurement of sister chromatid exchange frequency. *J. Histochem. Cytochem.* **25,** 741–753 (1977).

Acknowledgements

We thank Sebastian Haase for help in DNA fibre image analysis, Hans-Peter Rahn for assistance with flow cytometry and Danny Nowak and Anne Lehmkuhl for technical support. We are grateful to John Sedat and Pete Carlton for initial support with OMX experiments. This work was supported by grants of the German Research Foundation (DFG CA 198/9 to M.C.C., DFG SFB-TR5 to L.S., DFG SFB 1064 A17/Z05 to H.L. and Nanosystems Initiative Munich to H.L.) and a Wellcome Trust Strategic Award (091911) supporting Micron Oxford. C.S.C.-D. was supported in part by a Marie Curie long-term IEF fellowship.

Author contributions

A.B., M.F. and P.D generated/provided the materials. V.O.C., C.S.C.-D., M.R., L.S., Y.M., A.M., J.J.B. and Y.M.R. performed the experiments. V.O.C., C.S.C.-D., M.R., L.S. and Y.M. developed image analysis protocols. V.O.C., C.S.C.-D., M.R., L.S., Y.M. and Y.M.R.

analysed the data. V.O.C., H.L. and M.C.C. designed the project. V.O.C., C.S.C.-D., M.R. and M.C.C. wrote the manuscript. All authors commented on the manuscript.

Additional information

Supplementary Information accompanies this paper at http://www.nature.com/naturecommunications

Competing financial interests: The authors declare no competing financial interests.

Reprints and permission information is available online at http://npg.nature.com/reprintsandpermissions/

How to cite this article: Chagin, V. O. *et al.* 4D Visualization of replication foci in mammalian cells corresponding to individual replicons. *Nat. Commun.* 7:11231 doi: 10.1038/ncomms11231 (2016).

Supplementary Figure 1: Generation of HeLa Kyoto cell lines expressing PCNA tagged to fluorescent protein.

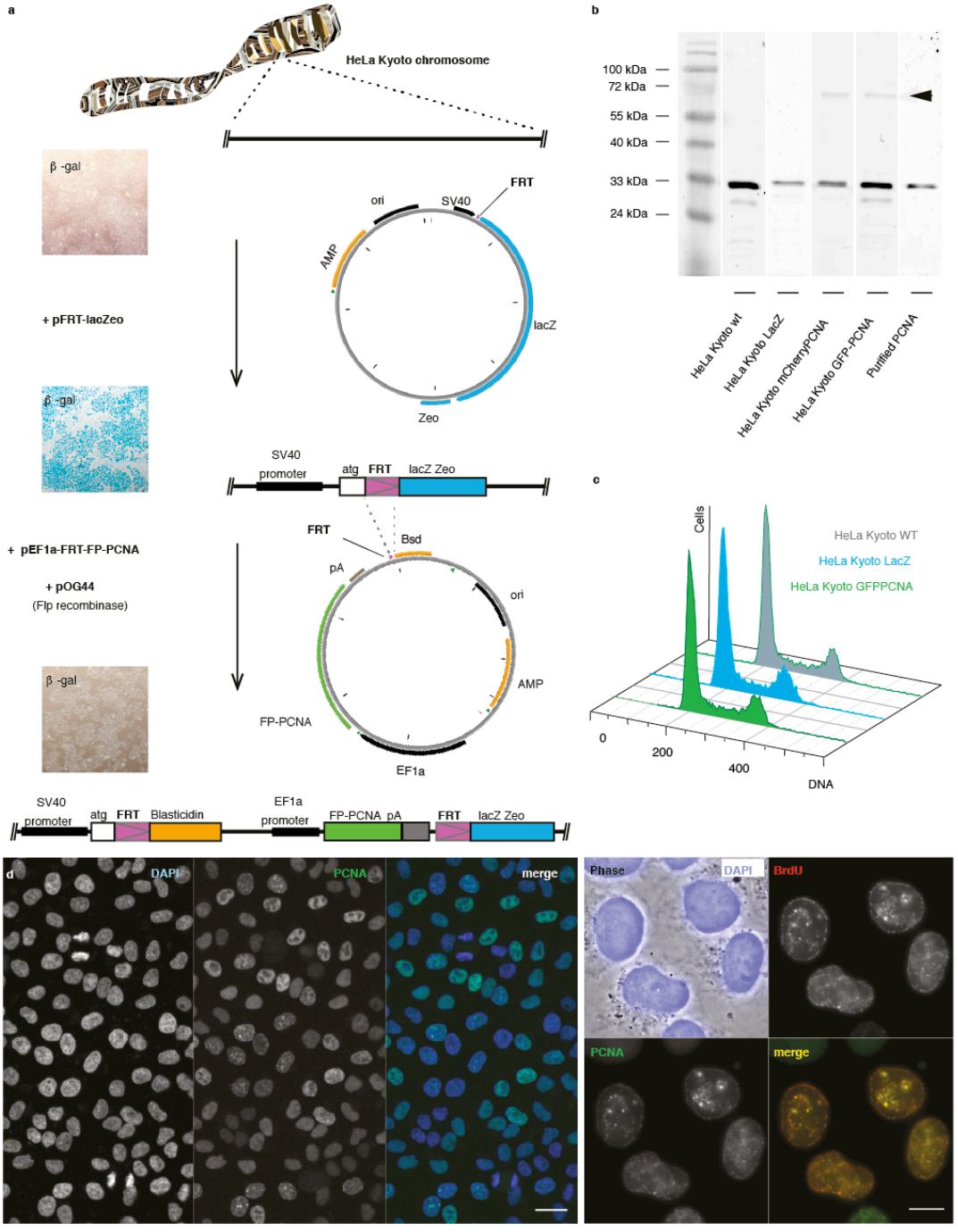

a. Schematic representation of the two-step protocol used to generate HeLa Kyoto cell lines stably expressing PCNA tagged to fluorescent protein – "FP-PCNA" (see Supplementary Note 1). HeLa Kyoto cell lines expressing mCherry-PCNA or GFP-PCNA proteins were generated by: First, introducing FRT site recognized by Flp recombinase together with LacZ and gene of Zeocin resistance. The cells where integration of the plasmid into a chromosome occurred were then selected on the basis of the acquired Zeocin resistance (eight days 75 µg/ml) and eight clones with integrated FRT sites were isolated. Beta-Galactosidase activity was assayed as an indicator of activity of SV40 promoter. Second, several HeLa-Kyoto-FRTLacZ-clones with low and high ß-galactosidase expression were selected for further co-transfection with FRT-GFP-PCNA or FRT-mCherry-PCNA containing plasmids with pOG44 plasmid containing gene of Flp-recombinase. Successful integration of FP-PCNA at the chromosomal FRT sites was verified based on acquired Blasticidin resistance and loss of LacZ activity. Scale bar: 50 micron. **b.** Immunoblot analysis of FP-PCNA expression levels in HeLa Kyoto cells at all stages of the protocol shown in (a). **c.** Flow cytometry histograms demonstrating the absence of alterations in the cell cycle dynamics. **d.** Left panel: microscopic images demonstrating the stability and uniformity of FP-PCNA expression. Scale bar: 10 micron. Right panel: colocalization of FP-PCNA with the nuclear sites of DNA synthesis. Scale bar: 5 micron.

Supplementary Figure 2: Criteria for inter-origin distance and replication fork speed sampling.

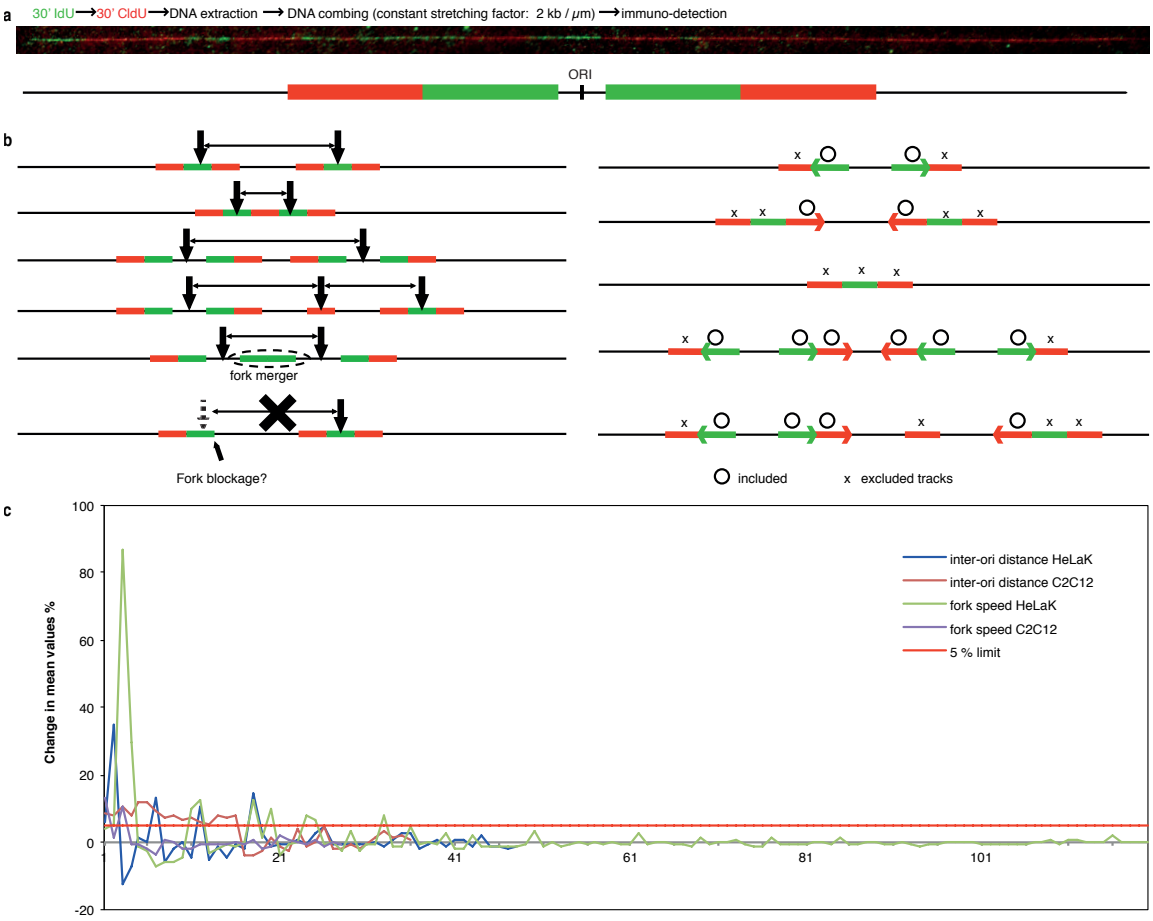

a. Schematic summary of the labeling, DNA fiber stretching and immunodetection steps. Exemplary image of stained DNA tracks acquired with a wide-field microscope. **b.** Fluorescent DNA fiber tracks were selected according to their pattern for calculations of inter-origin distances (IOD) and / or replication fork speed (RFS) as shown. Thick arrows indicate the positions considered as replication origins, thin arrows represent the IOD. Circles mark the tracks included into the calculations of RFS, crosses mark the tracks excluded from the calculations. **c.** The effect of increasing the sample size on the mean value of the indicated parameter is represented as a plot of the change in the average value of the sample "n" to the mean of "n-1" (See Supplementary Note 2).

Supplementary Figure 3: Protocols for *in situ* quantification of replication foci.

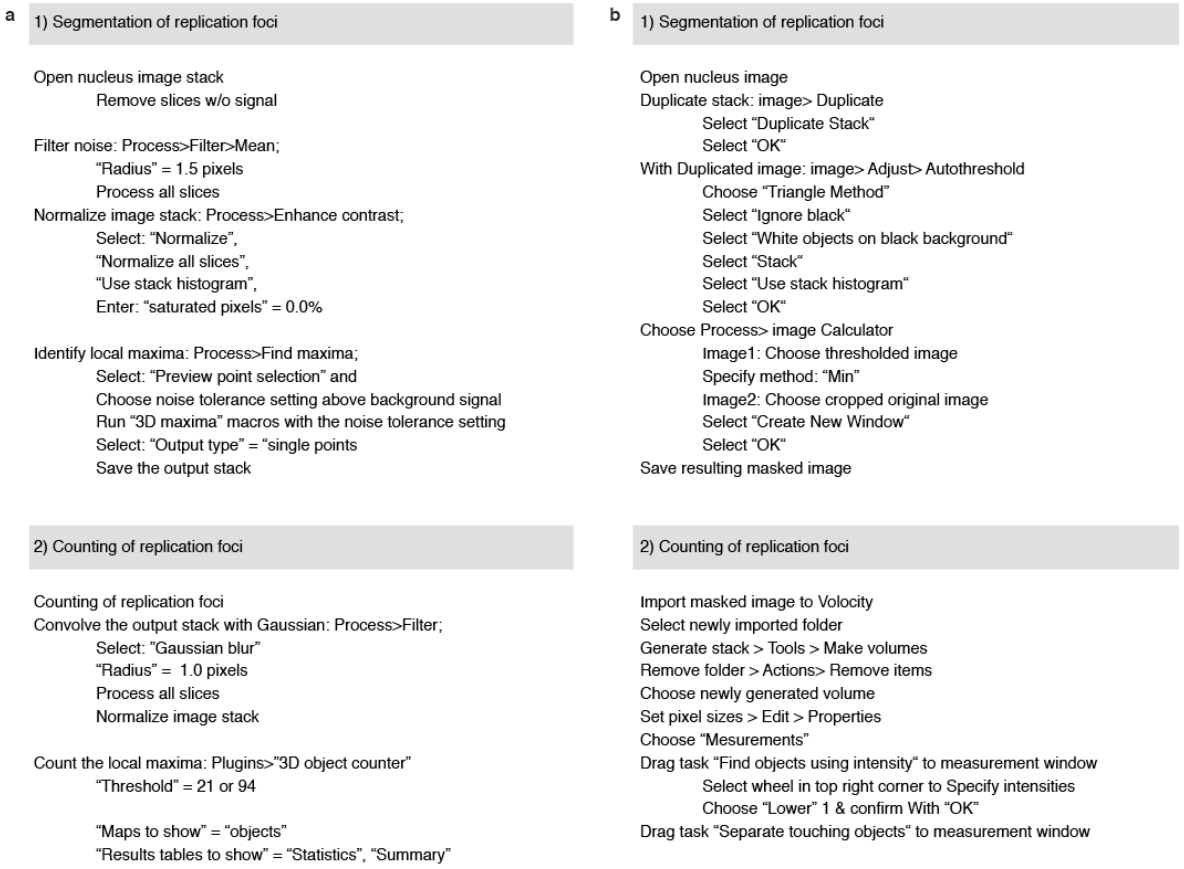

Step-by-step protocols for RFi identification and counting are summarized for: (**a**) confocal image stacks; (**b**) for 3D-SIM image stacks (See Supplementary Note 3).

Supplementary Figure 4: Replication foci clustering in late S-phase.

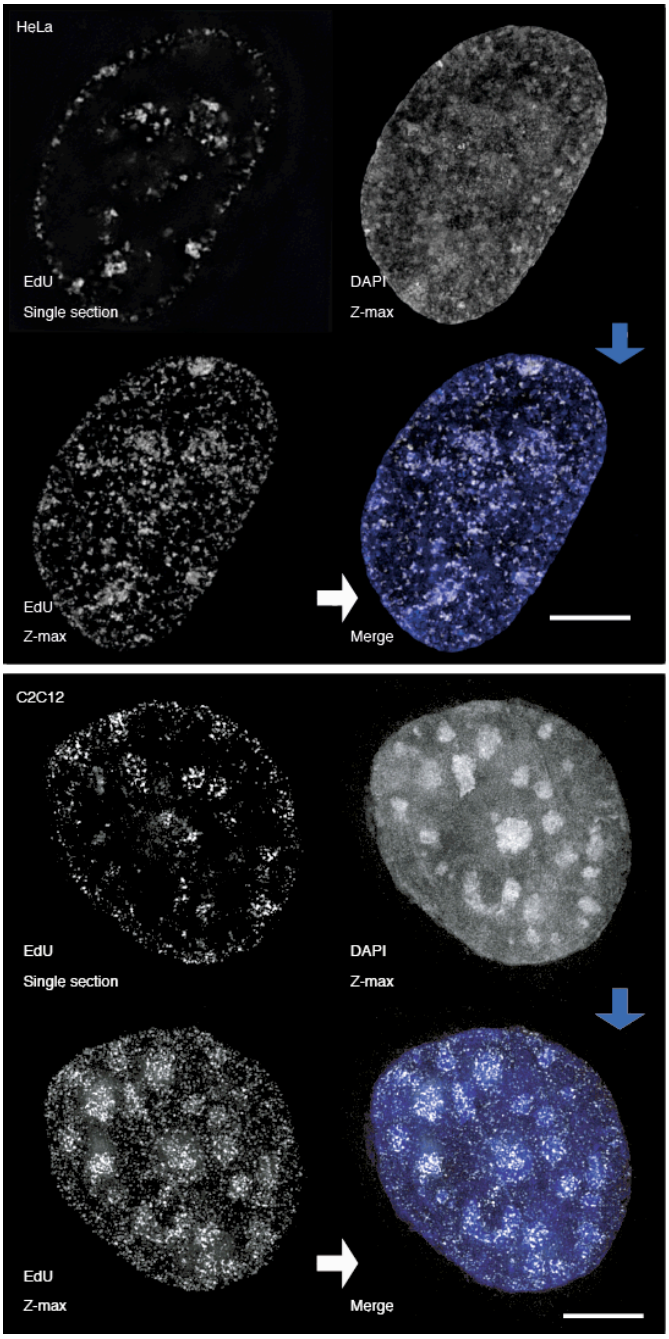

The degree of the observed heterochromatin associated clustering of EdU-labeled RFi in HeLa Kyoto cells (top panel). Replication foci labeled by demonstrate pronounced clustering during late S-phase in chromocenter regions of mouse C2C12 cells (bottom panel). See also Supplementary Note 4. Scale bar: 5 micron.

Supplementary Figure 5: Comparison of S-phase nucleotide (left) and protein (right) labeled replication foci numbers in HeLa Kyoto and C2C12 cells.

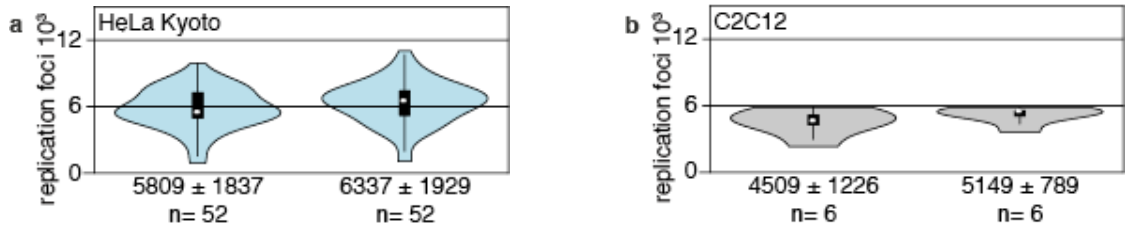

Details as in Figure 3. See also Supplementary Note 4.

Supplementary Figure 6: Schematic of different modes of replicon activation.

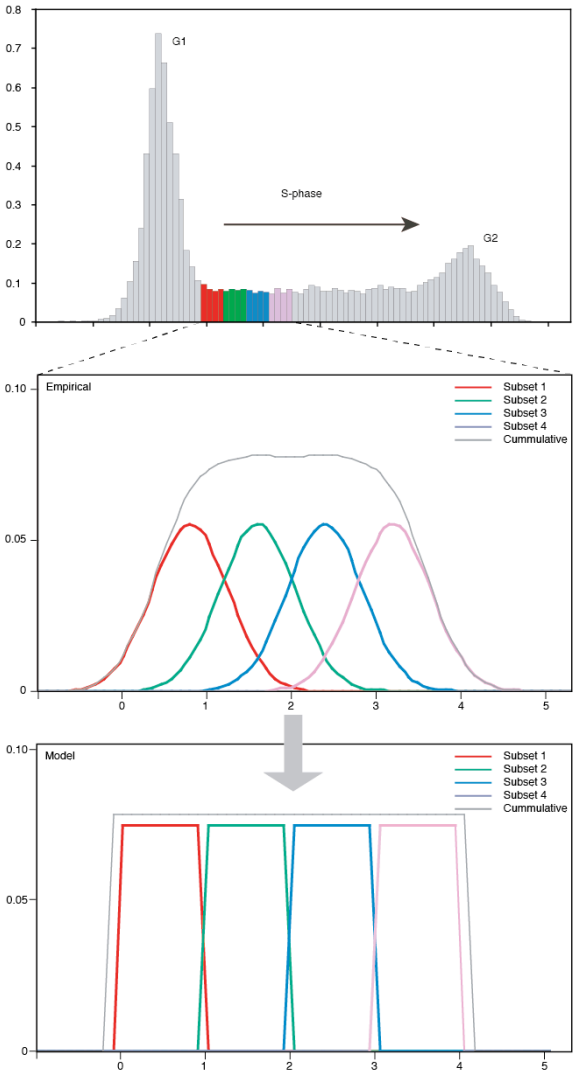

S-phase dynamics is represented as sequential activation of groups of replicons scattered over the genome. Each colored curve depicts combined intensity of DNA synthesis in a respective replicon subset. Cumulative DNA synthesis profile (S-phase part of DNA histogram, **top panel**) will be similar, if S-phase dynamics is modeled by asynchronous overlapping (Gaussian curves) mode of origin activation (**middle panel**), or as synchronized sequential (step-like curves) initiation of DNA synthesis (**bottom panel**) by the groups of replicons.

Supplementary Figure 7: Statistics representation using Violin plots.

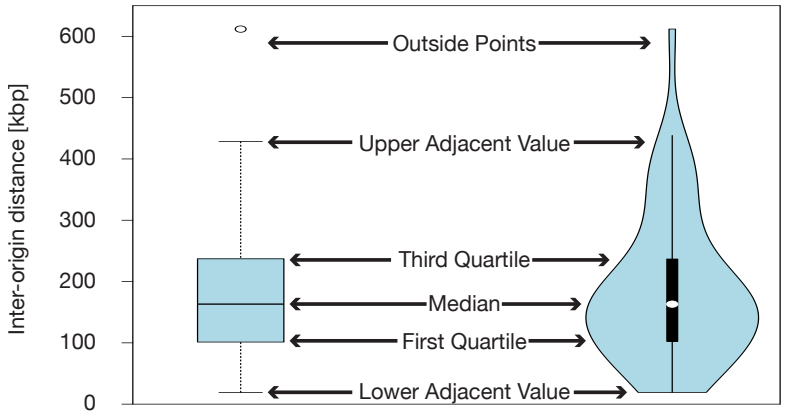

Supplementary Table 1: Summary of RFi measurements statistics.

S-phase stage	Cell line	Resolution	RFi mean	RFi median	SEM[1]	SD[2]	RFi min	RFi max	n[3]
early	HeLa Kyoto	confocal	1095.9	1072	22.4	157	839	1547	49
mid	HeLa Kyoto	confocal	1287.4	1301	23.9	141.6	941	1559	35
late	HeLa Kyoto	confocal	616.8	623	28.7	157.2	353	986	30
combined	HeLa Kyoto	confocal	1028.6	1081	28.2	300.9	353	1559	114
max	HeLa Kyoto	confocal	1175.7	1158	19.4	177.5	839	1559	84
early	C2C12	confocal	811	746	68	225.7	418	1162	11
mid	C2C12	confocal	1102	1072	63.1	282.3	517	1615	20
late	C2C12	confocal	818.5	857	46.8	203.9	366	1229	19
combined	C2C12	confocal	930.2	902	39.1	276.8	366	1615	50
max	C2C13	confocal	998.7	1035	53.1	295.7	418	1615	31
early	HeLa Kyoto	WFD	847.7	911	51.9	355.7	37	1476	47
mid	HeLa Kyoto	WFD	765	757.5	39.1	221	357	1269	32
late	HeLa Kyoto	WFD	503.8	488	34.6	265.6	16	1058	59
combined	HeLa Kyoto	WFD	681.5	703	28	328.8	16	1476	138
max	HeLa Kyoto	WFD	814.2	787	34.8	309.4	37	1476	79
early	C2C12	WFD	1011.5	1056	55.8	185	743	1398	11
mid	C2C12	WFD	847.1	937.5	53.4	213.5	437	1108	16
late	C2C12	WFD	642	689	63.5	210.7	49	840	11
combined	C2C12	WFD	835.3	848	39.8	245.2	49	1398	38
max	C2C13	WFD	914	964	41.4	215	437	1398	27
early	HeLa Kyoto	3D-SIM	5246	5703.5	227.6	2111	249	10976	86
mid	HeLa Kyoto	3D-SIM	6002.7	5699	218.9	1818.6	2326	11037	69
late	HeLa Kyoto	3D-SIM	3999.9	4059	291.6	2750.5	134	13178	89
combined	HeLa Kyoto	3D-SIM	5005.5	5206	155.5	2428.4	134	13178	244
max	HeLa Kyoto	3D-SIM	5582.8	5699	161.9	2015.5	249	11037	155
early	C2C12	3D-SIM	5462.4	5254	303.4	1689.2	2760	9279	31
mid	C2C12	3D-SIM	5236.9	4897.5	308.5	2389.5	1121	14394	60
late	C2C12	3D-SIM	3687.3	3987	220.1	1409.5	537	6436	41
combined	C2C12	3D-SIM	4808.5	4563	182.8	2100.1	537	14394	132
max	C2C13	3D-SIM	5313.7	5054	227.4	2169.3	1121	14394	91
combined	HeLa Kyoto	3D-SIM live	4216.7	3533	836.8	3131	652	11649	14
combined	C2C12	3D-SIM live	5026.8	5817.5	602.2	2408.9	61	8615	16

[1] standard error of mean

[2] standard deviation

[3] number of cells quantified

"max" values represent combined measurements from early and mid S-phases

Supplementary Note 1: Cell lines with stable expression of fluorescent DNA replication markers.

An important advantage of cell lines expressing fluorescent replication markers is the possibility of using them for live-cell analysis of the genome duplication process. Hence, in addition to our previously described mouse myoblast line expressing labeled GFP-tagged PCNA [1], we generated two human HeLa Kyoto cell lines variants expressing PCNA tagged to fluorescent proteins (FP-PCNA) by applying a two-step protocol of chromosomal integration based on Flp-mediated site-specific recombination (Supplementary Figure 1). By using different FP-PCNA constructs in the second step of the protocol, two cell lines were designed to express GFP-tagged PCNA and mCherry-tagged PCNA, respectively [1,2]. Both human cell lines revealed stable and uniform expression of fluorescently-tagged PCNA variants (Figure 1D, left panel) at about 12% of endogenous PCNA level, as measured by quantitative Western blot (Supplementary Figure 1B). We further verified by flow cytometry that the FP-PCNA proteins did not lead to cell cycle alterations (Supplementary Figure 1C). Similarly to native PCNA, recombinant FP-PCNA proteins localized in the nucleus and labeled sites of active DNA synthesis (Supplementary Figure 1D, right panel). Hence, we concluded that the generated HeLa Kyoto FP-PCNA cell lines exhibited unaltered replication dynamics [3,4] and represented an adequate model system for DNA replication in human cells.

Supplementary Note 2: Quantification of molecular replication parameters on combed DNA fibers.

The combination of double replication labeling and the fiber spreading protocol gave the possibility to discard fused or partially labeled replication fork tracks (Supplementary Figure 2) and provided increased precision for each measurement. At the same time, the number of tracks included into the quantifications was consequently reduced. Therefore, to ensure the relevance of our measurements we verified that the mean values of both measured parameters, RFS and IOD, were not affected by the sample size used. For that we varied the number of measurements used in the calculations and assessed the corresponding changes in the calculated mean values. For both parameters, individual measurements changed the mean values in less than 5% for the sample sizes used. Hence, we concluded that the number of replication fork tracks included in the calculations was sufficient for statistically significant measurements (Supplementary Figure 2C).

Supplementary Note 3: Development of computer-aided protocols for replication foci quantification.

Our initial tests revealed that very small threshold variations at the segmentation step could lead to substantial variations in the resulting RFi numbers. We therefore set out to develop approaches based on intrinsic image features that consequently would be as user-

independent as possible. Various algorithms for quantification of replication foci at the different resolution levels (confocal, wide field deconvolution and super-resolution 3D-SIM) were validated using parallel manual counting of RFi by independent persons. When assessing the outcome of RFi quantifications, preference was given to algorithms that resulted in fewer RFi (for a conservative estimate) than to algorithms that lead to overestimation of RFi numbers. The best correspondence between results of (semi)automatic RFi quantification and manual counting was obtained using the protocols described in Supplementary Figure 3 and in more detail in [5].

Supplementary Note 4: Influence of chromatin compaction and labeling mode on super-resolution imaging of replication foci.

Within highly compacted chromosomal regions perfect segmentation of foci even at super-resolution microscopy level is challenging (see Supplementary Figure 4). Hence, in particular in late S-phase mouse cells RFi numbers decreased. In addition, on average the number of RFi counted from PCNA labeling super-resolution images was slightly higher than the number of RFi labeled by nucleotide incorporation (Supplementary Figure 5). This difference could be due to an inefficient incorporation and/or detection of incorporated nucleotides. Alternatively, differences regarding dynamic behavior of DNA and PCNA components of RFi were revealed with super-resolution microscopy. It should be noted that during a 15-minute pulse of nucleotide incorporation an average replication fork labels about 25 kbp that correspond to eight microns of unpacked DNA. Therefore, up to certain condensation level the signal from the labeled nucleotide will be fuzzier than the focal signal from PCNA-containing replisomes. An underestimation of RFi numbers can be considered as a conservative estimate of actual RFi numbers and does not affect our further calculations and conclusions.

Supplementary References

1 Leonhardt, H. *et al.* Dynamics of DNA replication factories in living cells. *J Cell Biol* **149**, 271-280 (2000).

2 Rottach, A. *et al.* Generation and characterization of a rat monoclonal antibody specific for PCNA. *Hybridoma* **27**, 91-98 (2008).

3 Dimitrova, D. S. & Berezney, R. The spatio-temporal organization of DNA replication sites is identical in primary, immortalized and transformed mammalian cells. *J Cell Sci* **115**, 4037-4051 (2002).

4 Kennedy, B. K., Barbie, D. A., Classon, M., Dyson, N. & Harlow, E. Nuclear organization of DNA replication in primary mammalian cells. *Genes Dev* **14**, 2855-2868 (2000).

5 Chagin, V. O., Reinhart, M. & Cardoso, M. C. in *Methods Mol Biol* Vol. 1300 (eds J. Dalgaard & S. Vengrova) 43-65 (Springer Science+Business Media New York, 2015).

6 3D replicon distributions arise from stochastic initiation and domino-like DNA replication progression.

6.1 Aims of "3D replicon distributions arise from stochastic initiation and domino-like DNA replication progression."

The precise DNA replication data, acquired in two different mammalian cell lines (see Chapter 5), allowed us to create a computer model to simulate the highly dynamic DNA replication process. Following the KISS principle ("Keep it simple, stupid")[79] the aim of the computer model was to include as few parameters as possible.

My key idea was to correlate this 1D replication model with live cell microscopy data involved arranging the virtual chromatin in a virtual cell nucleus. Active DNA replication sites at different DNA replication time points are highlighted and used to generate a virtual *in silico* microscopy image. N. Lengert and D. Löw implemented this idea beautifully in the model, which is therefore able to generate virtual *in silico* replication images with a detail level comparable to super-resolution microscopy images of DNA replication. With euchromatin and heterochromatin as the only parameters that define the location and time point of replication, simulated images already gave insights into the mechanisms of DNA replication. As the first iterations of the model only had two chromatin types, the subsequent images resulted in only the two S-Phase replication patterns of early and late S-Phase. The simple addition of a third chromatin state, equivalent to facultative heterochromatin, resulted in the gain of the typical mid S-phase replication pattern, demonstrating the high accuracy of our simulation model.

6.2 Contributions

- M. Reinhart analyzed data for Figure 2
- M. Reinhart analyzed data for Figure 3
- M. Reinhart analyzed data for Figure 4
- M. Reinhart analyzed data for Supplementary Figure 3.
- M. Reinhart codesigned the model.
- M. Reinhart cowrote the manuscript.
- M. Reinhart provided the idea to visualize 1D replication in the context of a 3D nucleus and compare it with super-resolution microscopy images.

6.3 Publication

nature COMMUNICATIONS

ARTICLE

Received 16 Apr 2015 | Accepted 2 Mar 2016 | Published 7 Apr 2016

DOI: 10.1038/ncomms11207 OPEN

3D replicon distributions arise from stochastic initiation and domino-like DNA replication progression

D. Löb[1,*], N. Lengert[1,*], V.O. Chagin[2,3,*], M. Reinhart[3], C.S. Casas-Delucchi[3], M.C. Cardoso[3] & B. Drossel[1]

DNA replication dynamics in cells from higher eukaryotes follows very complex but highly efficient mechanisms. However, the principles behind initiation of potential replication origins and emergence of typical patterns of nuclear replication sites remain unclear. Here, we propose a comprehensive model of DNA replication in human cells that is based on stochastic, proximity-induced replication initiation. Critical model features are: spontaneous stochastic firing of individual origins in euchromatin and facultative heterochromatin, inhibition of firing at distances below the size of chromatin loops and a domino-like effect by which replication forks induce firing of nearby origins. The model reproduces the empirical temporal and chromatin-related properties of DNA replication in human cells. We advance the one-dimensional DNA replication model to a spatial model by taking into account chromatin folding in the nucleus, and we are able to reproduce the spatial and temporal characteristics of the replication foci distribution throughout S-phase.

[1] Department of Physics, Institute for Condensed Matter Physics, Technische Universität Darmstadt, 64289 Darmstadt, Germany. [2] Laboratory of Chromosome Stability, Institute of Cytology, St Petersburg 194064, Russia. [3] Department of Biology, Technische Universität Darmstadt, 64287 Darmstadt, Germany. * These authors contributed equally to this work. Correspondence and requests for materials should be addressed to N.L. (email: nicor@fkp.tu-darmstadt.de.).

When the genome of eukaryotic cells is duplicated during the S-phase of the cell cycle, it is essential that the entire karyotype is reliably and precisely reproduced. Importantly, this process must be able to cope with variations in S-phase duration[1], potential chromosomal abnormalities and ploidy variations. Before the actual replication start, pre-replicative complexes are assembled on the DNA, licensing the origins of replication initiation[2]. These origins are activated by specific proteins, which initiate DNA duplication by interacting with the DNA polymerase complex[3]. The sites of DNA synthesis are called replication forks, which normally emerge in bidirectional pairs from each activated origin and travel in opposite directions. The DNA segment duplicated by such a pair of replication forks is termed as 'replicon'[3,4]. The amount of time needed to duplicate a DNA molecule depends solely on the speed of replication fork movement and the sum and distribution of activated origins.

Metazoan genomes feature a higher order organizational structure, which is not present in the well-characterized yeast model organisms[5–7]. Contrary to yeast, the positions of replication origins in metazoan DNA do not appear to be determined by DNA sequence[8,9]. Positions and activation times of individual origins can be related to various chromatin features[3,10–14], and molecular analyses have shown that positions of active origins, inter-origin distances and the speed of replication fork movement can vary even within individual cells[15,16]. Biological analyses of replication progression throughout S-phase in mammalian cells led to a domino-like next-in-line model[17] where replication is triggered by replication of adjacent regions. Guilbaud *et al.*[18] described chromosomal regions in HeLa cells with sequentially activated origins that are neither clearly early nor clearly late replicating. The existence of a long-range control of otherwise stochastic or induced firing of origins in the presence of replication forks was subsequently suggested. Genome-scale mapping of DNA replication origins demonstrated general plasticity of active origin positions, which was interpreted as replicon size flexibility within a predetermined replicon cluster[19]. Accordingly, the replication programme in metazoans demonstrates a high level of plasticity, thus ensuring complete genome duplication in the face of developmental and environmental changes[1]. Models of genome duplication in metazoans, therefore, need to include stochastic mechanisms to account for origins initiated at non-predetermined sites[20] and a flexible spatio-temporal structure of S-phase[13,21]. Recently, a quantitative model of human genome replication was presented by Shaw *et al.*[22]. By introducing clusters of origins which are fired together spontaneously or by activation from a neighbouring cluster, and by implementing the observed temporal variation of fork speed[23], the authors reproduce S-phase dynamics and replication progression on a cluster scale. However, the formation of clusters is likely to emerge from more elementary processes. The interplay of deterministic and stochastic influences in these processes, which is yet unclear[24,25], needs to be motivated by more detailed experimental data. Besides, an adequate model of genome duplication in eukaryotes must reproduce not only the temporal dynamics, but also the spatial characteristics of DNA replication *in vivo*. Here, we use domino-like DNA replication progression and random loop folding of chromatin to present a minimal model of DNA replication in higher eukaryotes that is able to reproduce spatial dynamics of the replication foci (RFi) throughout S-phase without need for replicon clustering at common synthetic centres as shown in Chagin *et al.*[26]

Results

Correlated and limited firing of origins. Potential replication origins are distributed randomly on the DNA at distances down to a few kbp (refs 2,7,18,27) and are capable of firing spontaneously. Thus, in our model the location of potential origins along the DNA is determined randomly. The probability for spontaneous firing events is assumed to be higher in euchromatic regions than the probability of firing potential origins in facultative and constitutive heterochromatic regions. Further firing events are 'induced' events in the proximity of active replication forks[17].

Due to the induced firing process, the probability for very short distances between firing origins would be much higher than experimentally observed (Fig. 2b). Thus, we introduced a distance around active forks, where firing of potential origins is inhibited (the inhibition distance—d_i). A range of the d_i values from 7 to 120 kbp was selected based on the reported correlation of distances between preferentially activated origins[27–31] and average sizes of the chromatin loops in different functional chromatin organization models[14,32]. To find the most probable value for d_i we compared the experimental distribution of inter-origin distances (Fig. 2b) with the distribution obtained from simulations varying the d_i value (5 kbp steps) by calculating the χ^2 value as well as the Kullback–Leibler divergence. Both measures have a broad minimum for d_i values between 35 and 55 kb indicating the most probable range. In the simulations presented here, a value of 55 kb was used, because smaller values lead to an increasing total number of origins fired. Figure 1 shows a schematic of the induced firing process in the model. The range of induced firing is determined by the parameter σ, the s.d. of the Gaussian curve, which is used to set the induced firing probabilities of nearby potential origins. Induced firing probabilities below 0.1 are set to zero to avoid the infinite range of the Gaussian curve. Increasing the value of σ broadens the simulated distribution of inter-origin distances shifting the mean towards higher distances and decreasing σ enhances the peak of the distribution below 200 kb. In the range from 100 to 280 kb for the parameter σ there are only minor changes to the distribution of inter-origin distances, therefore it can not be determined more precisely from the given data.

The shape of the DNA flow cytometry histogram and equal replicon numbers throughout S-phase[26] suggest a rate of global DNA duplication approximately constant through most of S-phase. This is modelled by introducing a 'limiting factor', representing a necessary component of each active replication

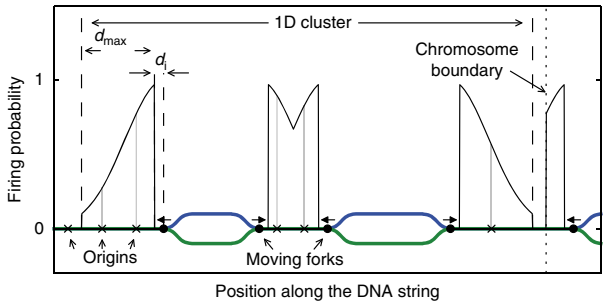

Figure 1 | Induced firing probability. The firing probability of origins that are close to forks follows a Gaussian probability density, indicated as shaded areas next to the forks. Firing at positions closer than $d_i = 55$ kbp to a fork is inhibited and the probability density is cutoff at values below 0.1. The relative probabilities of individual origins are indicated by dark grey bars. All four forks to the left of the chromosome boundary belong to a single 1D fork cluster (assuming that neighbouring forks are <1 Mbp apart). The chromosome boundary near the right edge of the image isolates chromatin belonging to different chromosomes and thus cuts off the induced firing range of the rightmost fork.

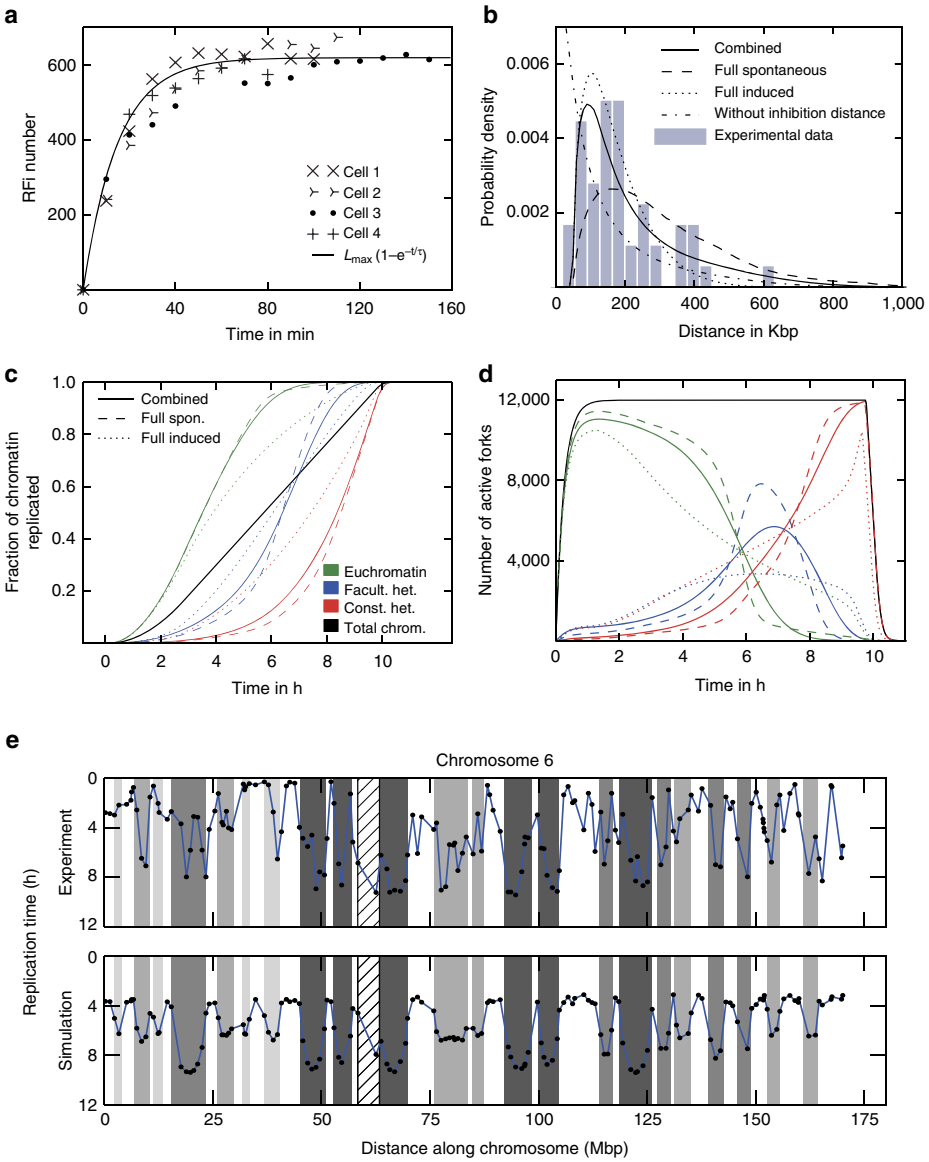

Figure 2 | Several simulated replication characteristics compared with experimental data. (**a**) Confocal RFi measurements were used to model the initial increase of the limiting factor with a mono-exponential fit $L(t) = L_{max}(1 - e^{-t/\tau})$ with timescale $\tau = 15$ min. (**b**) Distribution of distances between adjacent fired origins from DNA combing data for HeLa Kyoto cells. The distribution has a peak below 200 kbp and a heavy tail up to 600 kbp. The corresponding distribution, averaged over 100 simulations, displays similar features. (**c**) Fraction of replicated chromatin as a function of time. Colours are used to distinguish between the chromatin type specific and total replication. Dotted lines show the simulation results, when only induced firing events are allowed. Dashed lines display the other extreme case, where solely spontaneous firing was used. The combined model includes both firing events and the results are shown with solid lines. (**d**) Time-dependent number of forks in each chromatin type. (**e**) Comparison of our model with replication timing data for chromosome 6 from the ENCODE project[44] (cell type GM12878). Sampling positions are identical to the positions in the experimental data. For individual simulations, the euchromatic peaks start at time zero, but because of the specific sampling positions and averaging over 100 simulations, the displayed peaks are less extreme. The Pearson's correlation coefficient between the theoretical and experimental data shown here is 0.60. The Background indicates the Giemsa staining, where white regions are interpreted as euchromatin and shaded regions as facultative or constitutive heterochromatin. The centromere is indicated as a striped pattern. Analogous figures for other human chromosomes can be found in the Supplementary Figs 4–6.

fork, that limits the total number of active replication forks in the nucleus to the number of the limiting factor molecules. The concept of a limiting number of available forks was also used in models of metazoan DNA replication to obtain realistic origin activation profiles and synthesis rates[33–35]. We assume that the limiting factor moves nearly instantaneously through the nucleus[36,37], starts to become available once the cell enters S-phase, and that its number increases during the first hour until it reaches a maximum level that is maintained until the end of S-phase (Methods section and Fig. 2a). Our experimental data suggest that the number of simultaneously active replicons is between 4,000 and 6,000 (ref. 26), which is of a similar order of magnitude as previous DNA replication models suggested[33,34]. Hence, the maximum number of active replication forks is set to

$L_{max} = 12{,}000$. The total genome replication time of 10.3 h obtained in the computer simulation using this limiting factor concurs with the empirically found S-phase duration of 9.5 h ± 0.8 (s.d.)[26].

It is estimated that the total number of active origins involved in the replication of an entire mammalian genome lies in between 30,000 and 50,000 (refs 19,26,38), which includes the simulated value ranging from 43,800 to 44,500 (simulation parameters listed in Table 1). In simulations with smaller inhibition distances the total number of fired origins increases up to a value of 74,000 at $d_i = 0$. Thus our model predicts, that not more than one origin is activated per chromatin loop with a passive replication of other potential origins in the loop[28,30], which reproduces the known correlation between the replicon and chromatin loop sizes.

Slower replication in early S-phase. We directly measured the amount of genomic DNA synthesized in each S-phase sub-period corresponding to the three major S-phase patterns (for details see Fig. 3, Methods section and Supplementary Fig. 1). Nuclei with early S-phase patterns contained up to 15% more DNA as compared with G1 population, with the cells displaying mid S-phase containing up to 50% more DNA, whereas the cells with late S-phase patterns ranged from 50% more DNA to 100%, that is, duplicated genomic DNA content (Fig. 3b). Comparing the amount of genomic DNA synthesized by RFi in a particular S-phase sub-periods with their absolute durations revealed two-fold reduced global genome duplication rate in early S-phase, which lasts for 27% of S-phase (Fig. 3a–c). This observation was further supported by twofold reduced nucleotide incorporation in early S-phase pattern (Fig. 3d,e), indicating that a reduced fork speed causes the observed reduction in total DNA synthesis rate. The reduced DNA synthesis rate could be a consequence of nucleotide scarcity at the beginning of S-phase, or of the interplay between replication and transcription leading to a slower replication fork speed[39,40], both of which will have the same macroscopic manifestations. We modelled slower replication in early S-phase using a linear increase in fork speed during the first 2.8 h. After the initial increase the fork speed stays constant at a value of $v = 28\,\mathrm{bp\,s^{-1}}$ for the rest of S-phase as observed experimentally (Fig. 3a). The value was directly measured by Chagin *et al.*[26] and is consistent with the duration of S-phase. The initial increase in the simulations was adjusted to reproduce the measured fraction of 15% (1.6 Gbp) of replicated DNA during the first 2.8 h with reduced fork speed (Fig. 3b,c). The remaining 8.8 Gbp are replicated at the full speed in ~7.5 h, resulting in a total S-phase duration time of 10.3 h, similar to measured S-phase duration[26] (Fig. 3a–c).

Therefore, the combination of a limiting factor and an initial fork speed increase during the first third of S-phase followed by an approximately constant rate for the rest of S-phase[10], leads to a cell cycle profile consistent with our experimental data.

Occurrence of a distinct mid sub S-phase. To test whether both spontaneous and induced firing are required, we varied the parameters relating to the two types of firing. The results of the two extreme cases with only spontaneous or only induced firing events are shown as dashed and dotted lines, respectively, in Fig. 2c,d.

If firing of origins is solely simulated by spontaneous events, the average replication time of the chromatin types depends highly on the spontaneous firing probabilities p_{eu}, p_{fac} and p_{con} for euchromatin, facultative and constitutive heterochromatin, respectively. As seen in Fig. 2d a clear distinction between the subphases, in which a majority of replication forks can be found in one chromatin type, can be reproduced with probabilities satisfying $p_{eu} \gg p_{fac} \gg p_{const}$ (see Table 1 for values used). However, a full spontaneous model leads to longer average inter-origin distances than experimentally observed[26] (Fig. 2b). Increasing the differences beween the spontaneous firing probabilities does not lead to a noticeable lower average since intra chromatin zone firing still allows for very large distances shifting the distribution to larger values. To test whether the difference between the distributions is sufficient to reject the purely spontaneous model, we performed a bootstrap significance test, where the average over a subset of 50 simulated distances between fired origins was calculated. The subset was chosen randomly 10,000 times and the P value for the null hypothesis (no rejection) was determined from the smaller one of the fractions of simulated averages below/above the experimental average of 188 kbp. For the purely spontaneous model, after 10,000 repetitions not a single average distance greater than the experimental average was observed leading to a clear rejection with a P value $< 10^{-4}$.

In the case where only induced firing was allowed, the necessary initial firing was simulated by firing one origin in every euchromatic zone at the time $t = 0$. This leads to good agreement

Table 1 | Model parameters.

Parameter	Value	Underlying experimental data and consistency arguments
Genome size	$l \approx 10$ Gbp	Directly measured by Chagin *et al.*[26]
Number of eu-, facultative and constitutive heterochromatin zones	$N_{eu} = 1{,}380$ $N_{fac} = 702$ $N_{con} = 627$	Giemsa band data from the UCSC database (hg19)[55]
Number of potential origins	$N_O = 500{,}000$	Distances between MCM complexes[2,7] and origins density in mouse cells[19]
Limiting factor	$L_{max} = 12{,}000$	Double the number of replicons[26], consistency with fork speed and duration of S-phase
Initial limiting factor growth timescale	$\tau = 15$ min	Taken from replication foci number growth (Fig. 2a)
Maximum fork speed	$v = 28\,\mathrm{bp\,s^{-1}}$	Directly measured by Chagin *et al.*[26], consistency with limiting factor and duration of S-phase
Distance parameter of induced firing	$\sigma = 240$ kbp	Distances between fired origins (Fig. 2b)
Distance parameter of firing inhibition	$d_i = 55$ kbp	Distances between fired origins (Fig. 2b), consistency with known size of looped domains[63,65]
Spontaneous firing probabilities	$p_{eu} = 0.8$ $p_{fac} = 0.05$ $p_{con} = 0.0$	Determined by the visibility of a distinct mid S-phase pattern produced by the simulations.

All the parameters of our computer model. For each parameter, the known/measured quantities from which its value is determined are listed. With the exception of σ, d_i, p_{eu}, p_{fac} and p_{con} the experimental values for all parameters were inserted into the model *a priori*.

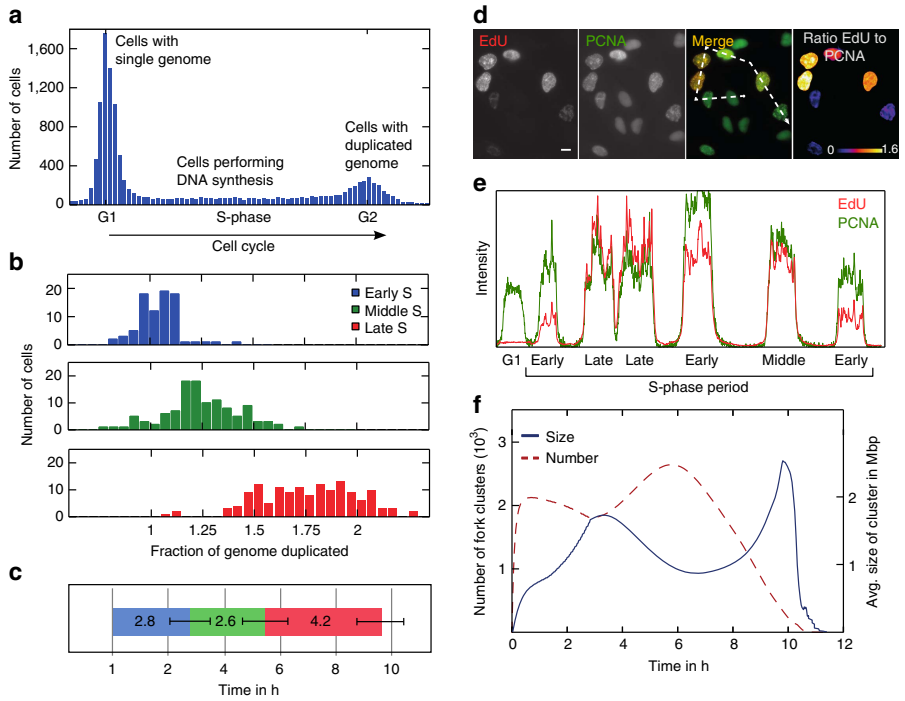

Figure 3 | Replication subphase analysis and simulated fork clusters. (**a**) DNA content frequency throughout the cell cycle. Cells are binned by DNA content (DAPI signal), with the abscissa showing the DNA content of the bins in arbitrary units. The distribution remains at an approximately constant value throughout S-phase, that is, between the G1 and G2 peaks, meaning that the overall rate of replication is constant. (**b**) Frequency of specific DNA content intervals in an ensemble of 840 HeLa Kyoto cells from five separate slide areas dependent on their cell cycle position. Through inspection of the PCNA signal, the cells were sorted into early, middle and late S-phase. It is notable that the number of early S-phase cells drops off steeply at 15% of the DNA replicated. (**c**): The observed subphase durations, where the error bars indicate the s.d. Subphase durations were obtained using live cell microscopy as described in the accompanying manuscript Chagin *et al.*[26] modified from Reinhart *et al.*[69] (**d**) HeLa Kyoto cells stably expressing mCherry-PCNA were labelled with modified nucleotides (20 μm EdU) for 15 min before fixation. Wide-field images of cells going through different S-phase stages show that, while the overall level of PCNA is rather constant, the total amount of incorporated nucleotides is clearly lower in cells going through early S-phase, indicating a lower synthesis rate. From left to right: single channel images, overlay of EdU (red) and PCNA (green) signals, representation of the ratio of EdU to PCNA signal intensity. LUT as indicated. Scale bar, 10 μm. (**e**) Line profile from the overlaid EdU (red) and PCNA (green) image over six cells going through different S-phase sub-stages as indicated. (**f**) Number and size of replication clusters over time. EdU, 5-Ethynyl-2′-deoxyuridine; LUT, Lookup Tables; MCM, Minichromosome maintenance protein complex; UCSC, University of California, Santa Cruz.

with experimental data (Fig. 2b) regarding distribution of distances between fired origins (*P* value 0.20), but this scenario does not produce a visible peak of active forks in facultative heterochromatin during mid S-phase (Fig. 2d).

Thus, only a model which uses a combination of both spontaneous and induced firing reproduces correctly the distribution of distances between fired origins and a distinct middle S-phase during which mainly facultative heterochromatin is replicated. The fraction of total spontaneous firing events in the combined model is 20%, of which 92% occur in euchromatic zones. The average over a subset of 50 simulated distances between fired origins, which can be directly compared with the experimental mean value of 188 kbp (Fig. 2b), ranges from 140 to 300 kbp, depending on the predominant chromatin type. The *P* value of 0.12 obtained from the same bootstrap significance test described above is too high to reject the null hypothesis.

Development of 1D clusters. Induced firing events in the vicinity of active forks lead to clusters of active forks on the one-dimensional (1D) DNA string, which expand outwards. As the 1D cluster increases in size, the probability that the next firing event will occur in it or close to it increases also. Clustered replication is maintained in our model through individual firing and annihilation events. We consider two adjacent forks to belong to the same cluster if their distance is <1 Mbp, which is consistent with the distance over which induced firing can occur in our model and the characteristic size of chromatin domains[41,42]. Clusters can therefore split into two parts that move in opposing directions when large stretches of DNA within them have been replicated. Figure 3f show the number and size of clusters during S-phase using the combined model. Spontaneous firing is dominant in euchromatin and the number of clusters increases rapidly during the initial phase (Fig. 3f) due to an increasing limiting factor and the random placement of origins over long distances. As long as the fork speed increases (until 2.8 h) the probability for neighbouring clusters to merge rises leading to a reduced cluster number. During mid S-phase clusters start splitting into two and thus the number increases again.

Measurements of the cluster size during early S-phase report a typical size of 1 Mbp (ref. 43). In our simulations the average size of replication clusters is comparable (Fig. 3f), but varies during S-phase. There is a transient increase in cluster size between 2 and 5 h caused by the spreading of early replication clusters followed by a decrease due to splitting of clusters. Since the combined model includes a very low spontaneous firing probability for origins in heterochromatic zones, most heterochromatin has to be replicated by fronts of clusters entering from adjacent zones.

As the replication of smaller zones is completed the size of the remaining clusters increases because the total fork number stays constant.

Replication front progression. We performed an evaluation of replication timing at the chromosome scale in our simulations and compared it with the microarray data from Woodfine *et al.*[10] as well as data from the ENCODE project[44]. To mimic those experiments, we extracted the replication times of DNA corresponding to experimental sampling positions. Figure 2e shows the resemblance of our results to the experimental data. Both theoretical and experimental replication timing profiles exhibit distinctive peaks due to early replication in the euchromatic zones, including the smallest euchromatin zones. The presence of these peaks in the experiment indicates that indeed there are early firing events in all euchromatic zones, corresponding to a high spontaneous firing probability.

While our curves are averaged over 100 simulations and are therefore smooth compared with the averages of four experimental measurements, the simulated patterns still correspond to the empirical data. The centres of euchromatic regions are on average replicated first and the centres of heterochromatic regions are replicated last with distinctive transition zones in between. The model further shows groups of contiguous chromatin zones collectively replicating earlier or later than others similar to the experimental data (Fig. 2e, between 25 and 45 Mbp). On the scale of chromatin zones the replication timing profile and the number of 1D replication clusters was not sensitive to small variations in parameters, and the distribution of chromatin zone sizes as long as both firing types were enabled the majority of zone sizes was between 1 and 6 Mbp (Supplementary Fig. 2).

The correlations between simulation and experiment are comparable to the lowest correlations measured between different experiments (Supplementary Note 1 and Supplementary Table 1). We suggest that these differences are due to the given resolution of chromatin zones and the difference in specific facultative heterochromatin composition and karyotype as all experiments are based on cancer cell lines with non-diploid genomes. A more accurate agreement with empirical replication timing patterns can be achieved when local firing probabilities along the entire DNA are based on the concentration of DNase hypersensitive sites[34], and not merely on the chromatin type.

Our model also explains how induced firing at the cluster front leads to a much higher front progression speed compared with the measured speed of single forks[26]. We obtain a cluster front speed of 100 bp s^{-1} (see Methods section for calculation), which matches the slopes of replication timing measurements reported in the literature[10,45].

Emergence of 3D replication patterns from replicon dynamics. It is known from fluorescence microscopy in fixed[21,26,46–48] and living cells[49,50] that each of the sub-periods of S-phase is characterized by distinct patterns in the three-dimensional (3D) nuclear arrangement as well as by different clustering of RFi. To compare the dynamics of the 1D replication clusters in our model with the experimentally observed 3D characteristics of RFi, we generated in silico microscopy images of our model results (Fig. 4). To this purpose, we created a Monte Carlo simulation based on the random loop model for long polymers by Bohn *et al.*[51], which has already been successfully used to describe folding of chromatin in human cells[52].

Under the assumption of different chromatin compaction for particular chromatin types[11,53,54], a combination of higher spring constants in heterochromatin with truly random linking results in chromosomes with dense heterochromatic regions and a wider nuclear region containing primarily euchromatin. We extended the random loop model to include the experimentally observed accumulation of facultative heterochromatin at the nuclear and nucleolar periphery by simulating a cell with two nucleoli, inaccessible for the polymer chain. A pseudo gravitational potential was used to attract facultative heterochromatin to the nuclear and nucleolar periphery and the same force with reverse sign also causes the distribution of constitutive heterochromatin in the bulk of the nucleus. Additionally, a small repulsive force was introduced into the model to minimize the overlap of chromosome territories.

Microscopy images of early S-phase show a large number of small and evenly distributed RFi in the entire nuclear volume except nucleoli. During early S-phase in our simulations most forks as well as 1D fork clusters are within euchromatin. The decreased compaction of euchromatin together with the considerable size of 1D clusters gives the fork distribution a seemingly random pattern resembling early S-phase microscopy images as described above. The arrangement of foci at the nuclear and nucleolar periphery observed during middle S-phase in the

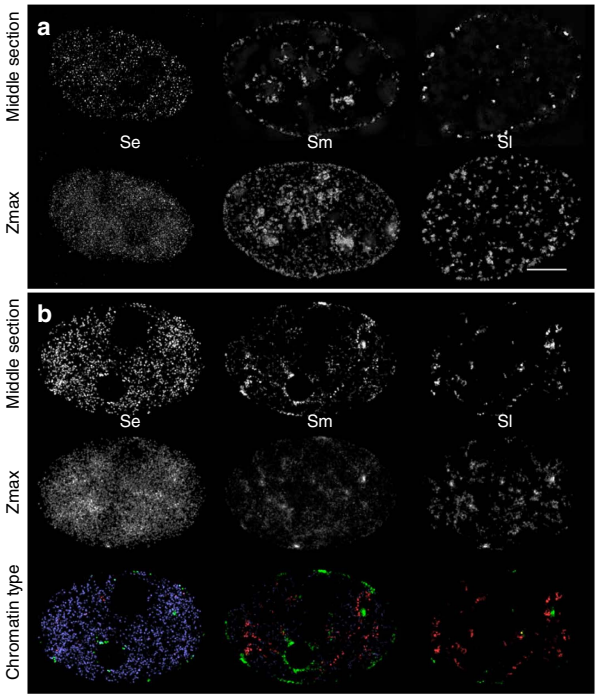

Figure 4 | Comparison between the microscopy pattern during replication in experiment and model. (**a**) Experimental maximum intensity z-projections and middle section images of green fluorescent protein (GFP)-tagged PCNA in HeLa cells during replication (as described by Chagin *et al.*[26] scale bar, 5 μm). (**b**) The corresponding patterns of the replication model results from a 3D DNA conformation calculated using the random loop model. The fork positions in the simulations were accumulated over 15 min similar to the experimental staining time. A Gaussian blur was applied to imitate the limited experimental voxel sizes of 40 × 40 × 125 nm. In the last row the simulated fork positions are marked depending on the chromatin type (blue, euchromatin; green, facultative heterochromatin; red, constitutive heterochromatin). Images for different parameters and chromatin distributions can be created online at http://sim.bio.tu-darmstadt.de. See also Supplementary Movies 1–3 for a visualization of the fork movement within the nucleus.

experiment is also reproduced by our model. In this subphase the simulation places most of the active replication forks in facultative heterochromatic zones followed by a gradually increasing number of active forks in constitutive heterochromatin. Hence, the mid S-phase pattern is generated by a superposition of both the facultative and the constitutive heterochromatic patterns in the 3D DNA conformation. Replication of facultative heterochromatin, especially inactive X chromosome replication, occurred during mid S-phase in a shorter time interval compared with the other chromosomes in agreement with experimental findings[11]. In our replication model, forks during late S-phase are located primarily in heterochromatin, which in the random loop model is constrained to a small volume for each chromosome. When the 1D replication clusters are therefore concentrated in the heterochromatin zones of a chromosome, 3D clusters characteristic for the empirical late S-phase patterns are formed. The high density of replication forks within 1D clusters during late S-phase amplifies this effect further. While we observe a steady increase in the size of replication clusters, these results demonstrate that 3D RFi distribution is primarily determined by their localization in particular chromatin types (Fig. 4b).

The simulations can be performed online at http://sim.bio.tu-darmstadt.de with a custom set of parameters and various chromatin type distributions. Graphs for visualization of the results as well as 3D in silico microscopy images are created online. Also, videos of the fork movement inside the whole nucleus (similar to Supplementary Movies 1–3) and of the fork progression on a single chromosome are available online.

Discussion

We have demonstrated that a stochastic model of domino-like DNA replication progression reproduces the spatio-temporal characteristics of replication dynamics in human cells. The model involves a minimalistic set of parameters, derived from experimental data in HeLa cells, and independently includes the rules for DNA replication initiation, the distribution of chromatin zone sizes[55] (Supplementary Fig. 2) and a random loop higher order chromatin organization[51,52]. Our model is minimal also in the sense that it reproduces S-phase dynamics in four-dimension on the basis of initiation rules for individual replicons and spatial chromatin arrangement independent from any common synthetic centres such as replication factories as shown in Chagin *et al.*[26]

A central mechanism of our model is the domino-like effect of firing of origins occurring in the proximity of active replication forks[17]. The inhibition distances of 55 kb was selected within the range of known sizes of chromatin loops involved in DNA replication[14,28,30,31] and fits already described evidence regarding preselection of origins to be activated. In Jun *et al.*[14], the origin spacing and initiation rate has been linked to chromatin loop formation probability determined by persistence length of the chromatin. The process of DNA replication in Xenopus early embryo was modelled within the paradigm of chromatin loops fluctuating around replication factories, where the probability of particular origin initiation depended on the distance to the two left and right approaching forks[14]. We do not use the concept of replication factories in our simulations, but rely on chromatin looping in determining the inhibition distance that corresponds to 'origin exclusion zone' discussed earlier[56]. Biological effects behind inhibition of firing ahead of active replication forks can include topological constraints preventing DNA unwinding at proximal origins and/or mechanisms preventing replication machinery assembly at the sites, which are not at the bases of chromatin loops. In the first scenario the size of these replication-related loops will be mainly determined by stiffness of the chromatin fiber around the active replication forks, while the second scenario implies that looping pattern of chromatin can be predetermined in G1. Thus, our model incorporates assembly of replication initiation factors at chromatin loop bases, but spatial and temporal dynamics of genome duplication is reproduced without the concept of multiloop aggregates assembled around replication factories and corresponding clusters of synchronously activated replicons.

Further to replication-related chromatin loops, which are indirectly comprised by our model via the inhibition distance d_i, the model also includes chromatin loops from the random loop model approximation of nuclear chromatin folding[52]. The size of chromatin loops originating from the random loop model (at least 2 Mbp)[52] is much bigger than the size of the replication-related chromatin loops which corresponds to the view that chromatin loops are formed both as a result of polymer properties of chromatin fiber and involvement of DNA into nuclear processes[14,32,57]. Accordingly, similarly to other models of nuclear chromatin organization (Random walk/giant loop scales in the model by Sachs *et al.*[58]; multiloop subcompartments and giant loop domains in Munkel and Langowsky[32]) our model is based on different scales of chromatin looping, where the loops arise from both physical and functional properties of chromatin fibres[57].

Another important ingredient of our model is the presence of a limiting factor that restricts the total number of replication forks active at any given time during S-phase. Other authors[22,59] already established that a limiting factor is needed to obtain realistic origin activation profiles and synthesis rates in models of mammalian DNA replication. After an initial mono-exponential increase during the first hour, the limiting factor was kept at the constant value 12,000, which agrees with our count of 4,000–6,000 replicons[26]. We arrive at the same number of available limiting factors when calculating the total number of replication forks based on the duration of S-phase, the size of the genome and the fork speed obtained from our experimental characterization of HeLa cells[26]. This means that the limiting factor is fixed by two consistent experimental measurements. Using a constant limiting factor has the advantage that it is simpler than other approaches, which require a growing limiting factor[33,59] or a time-dependent firing rate[60,61] to control the replication rate.

Unlike previous models[14,59,60], we explicitly used the specific chromatin layout on the scale of chromatin zones (euchromatin, facultative and constitutive heterochromatin) of human cells by modeling each HeLa chromosome like the corresponding human chromosome. We found that on the scale of chromatin zones not all details matter for the replication timing and the number of 1D replication clusters, as long as both firing types are enabled and the distribution of chromatin zone sizes has most of its weight between 1 and 6 Mbp (Supplementary Fig. 2). However, a more detailed probability map for initiation events as used by Gindin *et al.*[34] enhances the correlation with experimental replication timing.

While on average euchromatic regions are replicated during early and heterochromatic regions during late S-phase, the exact time at which a specific site is replicated varies between individual simulations in our model, in agreement with the empirical observation that it varies in otherwise identical cells *in vivo*[19,62]. Cayrou *et al.*[19] explained this observation with the 'flexible replicon' model, which involves spontaneous firing and silencing of origins in the vicinity of firing events similarly to our model, but postulates preexisting clusters of origins, which our model does not require. Instead, clusters of replication forks are a result of the domino-like replication progression.

To relate the results of our 1D replication model to the characteristic foci patterns observed in fluorescence microscopy, we represented the fork positions derived from the replication model on a 3D chromatin conformation[51,52]. The simulated 'in silico microscopy' images reproduce three major S-phase patterns observed in fluorescent microscopy[26] (Fig. 4): the homogenous distribution of early RFi, the characteristic mid S-phase RFi at the nuclear and nucleolar periphery, where the facultative heterochromatin is located, and the clustered foci of late S-phase.

Higher compaction of facultative and constitutive heterochromatin were accounted for by introducing bigger values of spring constants into the model. More compact state of heterochromatin and accumulation of 1D replication fork clusters in heterochromatin was sufficient to reproduce characteristic complex RFi of late S-phase. Recent studies by high-resolution chromosome conformation capture confirm association between open and closed 3D chromatin structures with early and late replicating DNA[42].

After stochastic activation of origins in euchromatic regions at the onset of S-phase, transition between early and late replication is observed within our model as the mid S-phase pattern, likely corresponding to replication timing of transition regions described by Pope *et al.*[42].

The 3D RFi dynamics was generally reproduced using the same values for replication fork speed and distance parameters for induced firing and firing inhibition for the whole genome. The above parameters can potentially vary between individual genomic locations. When the corresponding data on chromatin organization and DNA replication dynamics is available for particular genomic segments, this information can be included into the model to better reproduce DNA replication dynamics in these parts of genome.

Similarly, parameters of our model can be adapted for a potential use in embryonic replication. There are several distinctive features of DNA replication in metazoan embryos including very fast (ca 20 min) S-phase, small replicon and chromatin loops sizes[14]. Therefore in case of embryonic replication the inhibition distance and limiting factor values should be changed and slower early S-phase should be excluded from the model.

To conclude, the experimentally observed spatio-temporal characteristics of DNA replication in somatic cells can be reproduced by a combination of 1D replication initiation/progression rules and random folding of DNA in the nucleus. Our model provides a minimal theoretical framework for a comprehensive description of S-phase dynamics in four-dimension including the complete genome duplication, overall S-phase duration, constant synthesis intensity, the timing profiles and the 3D patterns of individual replicons spatially similar to those observed experimentally[26].

Methods

All simulations underlying this publication were performed using the two simulation packages 'replication' and 'dna_metropolis', which were created by one of the authors. They are written in the C++11 standard of the C++ programming language and can be built and compiled using the GNU toolchain. Both packages, complete with source code (GPLv3 license) and installation instructions are available online at https://github.com/nleng/DNA-replication. Additionally, for illustrative purposes, the simulations can be performed online at http://sim.bio.tu-darmstadt.de together with an evaluation of the results.

Simulation package 'replication'. For the implementation of our replication model, we translated our algorithm into search, insertion and deletion operations on sorted lists. Unlike the algorithm proposed by Jun *et al.*[60], who use two lists for the length of replicated and unreplicated regions, in our algorithm ordered lists are maintained for barriers, potential origins, left-going forks and right-going forks. The central data structure in the system is the event heap which is a binary heap data structure that at any given time contains all future collision events between the objects that are currently in the system (forks, chromosome barriers and chromatin zone transitions), sorted by time of occurrence. Thus the root element in the heap always holds the next event in the system. In each simulation step, the root element of the heap is removed and time is advanced to its time of occurrence.

If the removal triggers a chromatin zone boundary crossing or a firing event (because a limiting factor has been freed), then the addition and removal of future collision events becomes necessary. To keep such operations efficient, ordered lists are maintained for barriers, potential origins, left-going forks and right-going forks. These lists are implemented using a special red-black tree that, in addition to standard red-black tree behaviour, allows indexed element access scaling $O(\ln N)$ with the number of elements N (all nodes keep track of the number of their children).

For instance, if it is determined that an origin has to be fired, a random origin is picked from the available origins and checked if it has been passively replicated by the active forks. If not, its relative firing probability (a value between 0 and 1) is determined by the maximum of the spontaneous and induced firing probabilities and a random number between 0 and 1 is drawn. Should the random number be lower than the probability, the origin is fired, otherwise the process is repeated. If the origins lies inside the inhibition distance of an active fork, its firing probability is set to zero. Firing of the origin means that two forks, one in each direction, will be created, which have to be inserted into the fork lists, and for which collision events have to be calculated.

Experimental data suggest that the total number of replicons is between 4,000 and 6,000 (ref. 26). We consider a replicon to consist of two forks, meaning that the number of active replication forks is $\sim$12,000. Accordingly, in our model, the maximum value of the number of replication forks is set to $L_{\max} = 12{,}000$. With this value, the total genome replication time obtained in the computer simulation agrees with the empirically found S-phase duration[26]. To model the increase of the limiting factor $L(t)$ in the beginning of S-phase, we used the function

$$L(t) = L_{\max}\left(1 - e^{-t/\tau}\right) \quad (1)$$

with $\tau = 15$ min, as obtained from the dynamics of RFi numbers measured in live HeLa Kyoto cells in the beginning of S-phase. The function as well as the experimental data is shown in Fig. 2a. A model with a linearly increasing number of limiting factors as proposed before[33,35] would not fit the data as well as the exponential relaxation used in our model.

A fork moves along the DNA until it collides with another fork that 'moves' in the opposite direction, whereupon both forks annihilate. As both the activation of an origin as well as annihilation require two forks, they do not only appear in pairs but are also removed in pairs, freeing two limiting factors. We assume that forks travel freely from one chromatin type into another, but are stopped at the boundaries between chromosomes, setting one limiting factor free.

Package 'dna_metropolis'. In the random loop model, a polymer (that is, the DNA) is approximated as a chain of beads with harmonic springs between adjacent beads without volume exclusion (Gaussian chain). Non-adjacent beads are linked randomly, such that loops are generated at an average incidence of 5 loops per 10 Mbp. Because this random linking generates loops on all size scales (that is, possibly connecting any two positions on a chromosome), they serve to restrict chromosomes to the limited volume. Movement of beads is restricted to an oblate ellipsoid with two horizontal semi-axes of $r_x = 7.5\,\mu$m and $r_y = 5\,\mu$m and a vertical semiaxis of $r_z = 3.5\,\mu$m, which models the volume of an average nucleus.

When we laid out the rationale for origin firing inhibition, we based our argument on looped domains on a $d_l = 55$ kbp, which equals the lower estimate for the domain scale[63–65]. Since the inter-bead distance used in our random loop model simulations is 100 kbp, these domains are not resolved in the Monte Carlo model results and should not be confused with the loops of the random loop model. These latter loops, which have an average size of 2 Mbp, participate in the higher order chromatin organization.

In a previous study of human DNA by Mateos-Langerak *et al.*[52], different linking probabilities were used to model differences in displacement for transcriptionally active and inactive regions. However, in using such linking probability variations for euochromatin, facultative heterochromatin and constitutive heterochromatin, we noticed that beside from the uneven distribution on the scale of the whole cell, there was no discernible difference in the micro arrangement of the three chromatin types and thus no formation of distinct 3D RFi (Supplementary Fig. 3). We, therefore, used different spring constants for the three chromatin types and random linking instead to reflect the different degrees of compaction of the three types of chromatin.

HeLa karyotype data were used to generate the bead chains for all chromosomes. One necessary extension of the random loop model is the inclusion of the experimentally observed accumulation of facultative heterochromatin at the nuclear and nucleolar periphery. Thus the cell was simulated with two nucleoli, wherein the polymer chain is not allowed to enter, and the attraction of facultative heterochromatin was implemented as a pseudo gravitational potential. Additionally, a small repulsive force was introduced into the model to minimize the overlap of chromosome territories.

The potential for a Gaussian chain with N_{beads} beads with position $\mathbf{x}_i$ is:

$$U_{\text{Gauss}} = \sum_{i=1}^{N_{\text{beads}}-1} \frac{\kappa_i}{2} \|\mathbf{x}_i - \mathbf{x}_{i+1}\|^2, \quad (2)$$

with the spring constant κ_i in our case being 1×10^{-8} for euchromatin, 5×10^{-7} for facultative and 3×10^{-6} for constitutive heterochromatin. The order of magnitude of these spring constants determines how compact the chromatin is structured. Therefore, the visibility of S-phase patterns in the in silico microscopy images, such as a homogenous distribution in early and RFi in late S-phase, is sensitive to changes in these parameters. N_{beads} varies between the chromosomes with a total number of 103,634 beads for the whole genome (one bead per 100 kbp). Connections between beads of different chromosomes are skipped. Random loop connections within chromosomes give an additional potential term:

$$U_{\text{Loop}} = \sum_{\substack{i=1 \\ k_i, j_i \in [0, N_{\text{beads}}]}}^{5{,}000} \frac{\kappa_{\text{L}}}{2} \|\mathbf{x}_{k_i} - \mathbf{x}_{j_i}\|^2, \quad (3)$$

where the total number of 5,000 connections is based on a comparison of random loop model results with experimental genomic distance data by Mateos-Langerak *et al.*[52]. We chose an average loop size of 2 Mbp, which is towards the low end of their loop size estimate. The spring constant here is $\kappa_{\text{L}} = 5 \times 10^{-7}$.

In our model, cellular scaffolding and membrane interactions are implemented as two pseudo gravitational forces. First to ensure that each chromosome has its own nuclear territory, it is necessary to implement a small repulsive force (reversed gravity) between chromosomes. This effect was achieved in a previous model by defining local 'effective temperatures' resulting from non-equilibrium activities such as gene transcription[66]. But as the chromosomal overlap is not a central aspect of our model, we pursue a simple approach with the following repulsive potential:

$$U_{\text{Rep}} = \sum_{\substack{\forall m \neq n \\ m, n \in \text{ chromosomes}}} \kappa_{\text{R}} \frac{W_m \cdot W_n}{\sqrt{\|\mathbf{x}_{\mathbf{m}} - \mathbf{x}_{\mathbf{n}}\|^2}} \quad (4)$$

Here, vectors $\mathbf{x}_m$ and $\mathbf{x}_n$ are the centre positions of chromosomes m and n, W_m and W_n are the chromosome weights (that is, number of beads). In all simulations presented here, $\kappa_{\text{R}} = 10^{-4}$ was used, which means that the per-bead contribution of the repulsive potential is significantly smaller than the contribution of the bead connection potential. Because a Gaussian chain without volume exclusion is used for each chromosome, the repulsive force is needed to avoid all chromosomes being distributed on top of each other.

Second, to generate the experimentally observed distribution of facultative heterochromatin at the nuclear and nucleolar periphery, a gravitational force between beads belonging to facultative heterochromatic zones and the nuclear membrane or the nucleolar membrane has been implemented. This additional potential is important for the visibility of a distinct mid S-phase pattern.

$$U_{\text{Nuc}} = \sum_{i \in \text{fac}} \sum_{j=1}^{2} - \frac{\kappa_{\text{N}}}{\sqrt{\|\mathbf{x}_i - \mathbf{x}_{\text{nuc}_j}\|^2}} - \sum_{i \in \text{fac}} \frac{\kappa_{\text{N}}}{r_{\text{nuc}} + r_{\text{eff}} \cdot \left(1 - \sqrt{\frac{x_i^2}{r_x^2} + \frac{y_i^2}{r_y^2} + \frac{z_i^2}{r_z^2}}\right)}, \quad (5)$$

where $\mathbf{x}_i = (x_i, y_i, z_i)$ is the position of the ith bead, $\mathbf{x}_{\text{nuc}_j}$ the position of the nuclei, $r_{\text{eff}} = \sqrt[3]{r_x r_y r_z}$ the effective ellipsoid radius and $r_{\text{nuc}} = 1.0\,\mu\text{m}$ has a value close to the nucleolar radii (1.2–1.5 μm) to prevent the potential from having infinite values and to generate a similar strength for both the nuclear and nucleolar periphery. Additionally, the same force was used for constitutive heterochromatin, but with reversed sign and lowered strength ($\kappa_{\text{N}} = 30.0$ for facultative and $\kappa_{\text{N}} = 15.0$ for constitutive heterochromatin).

For the total potential, the four terms are added together:

$$U = U_{\text{Gauss}} + U_{\text{Loop}} + U_{\text{Rep}} + U_{\text{Nuc}}. \quad (6)$$

We use the standard Metropolis algorithm to let the beads relax into equilibrium with a temperature reservoir at 290 K. Replication fork positions from our replication model are then mapped onto the chromatin, thus generating a coordinate in 3D's for each fork.

Cluster front speed. The slope of the replication timing curves is determined by the progression of induced firing and can be estimated by the following considerations. After the initial spontaneous firing event, a 1D replication cluster starts expanding. Once the limiting factor has reached its stationary value of $L_{\text{max}} = 12{,}000$, the average amount of DNA replicated within each cluster per unit time is given by $vL_{\text{max}}/N_{\text{c}}$, with N_{c} being the number of clusters. As long as the cluster consists of two fronts (early S-phase) 'wave speed' of each front can be estimated as follows:

$$v_{\text{w}} = \frac{v \cdot L_{\text{max}}}{2N_{\text{c}}}. \quad (7)$$

At the end of early S-phase (2.8 h), when the fork speed has reached its final value of $v = 28\,\text{bp}\,\text{s}^{-1}$, v_{w} has a value of $\sim 100\,\text{bp}\,\text{s}^{-1}$, which matches the slopes of replication timing measurements reported in the literature[10,45]. It progressively increases as the number of 1D clusters declines.

Image acquisition. HeLa Kyoto Cells (see Chagin *et al.*[26]) were grown on square coverslips to 60–80% confluence, washed and fixed with 3.7% freshly prepared formaldehyde solution. Immunofluorescence stainings were performed as described by Chagin *et al.*[26]. After rinsing with PBS the coverslips were stained with 100 ng ml^{-1} 4,6-diamidino-2-phenylindole (DAPI; Sigma). Samples were mounted in Vectashield (Vector Laboratories).

Single section 16-bit images of DAPI, green fluorescent protein/mCherry-PCNA fluorescence for several arbitrary fields were acquired using a Leica SP5 confocal microscope equipped with HCX PL APO lambda blue 40.0 · 1.25 OIL UV objective. Excitation of DAPI, green fluorescent protein or mCherry was performed with 405 nm (diode laser), 488 nm (Argon laser) or 543 nm (He-Ne laser) laser lines, respectively. The parameters of the system were adjusted to avoid saturation. Settings used were: 2,048 × 2,048 pixels (387.5 × 387.5 μm^2) frame size, 8 airy unit pinhole diameter; 200 Hz scan speed.

3DSIM images (Fig. 4a and Supplementary Fig. 3a) were acquired and reconstructed as described in Chagin *et al.*[26]

Image quantification. Integral DAPI intensities of individual nuclei in single images were quantified using the ImageJ 'Analyze particle' command. The background signal was excluded by setting threshold at the level of intensity of the signal outside the nuclei.

The command generated a table containing integrated intensities of DAPI signal in the individual nuclei and returned the image of the outlines of the measured nuclei with the assigned numbers (Supplementary Fig. 1a).

That image was used as complementary data to the table with information on cell cycle stage of the cells: First, each of the nuclei was classified as early, middle or late S-phase or non-S-phase based on visual inspection of the proliferating cell nuclear antigen (PCNA) pattern (Supplementary Fig. 1b). The non-S-phase cells were separated into G1 and G2 subgroups based on stepwise increase in the DAPI signal (Supplementary Fig. 1c).

Average intensity of G1 and G2 nuclei was calculated and all measured values were normalized using:

$$I_{norm} = 1 + \frac{I - I_{G1}}{I_{G2} - I_{G1}}, \quad (8)$$

where I is integral intensity of an individual nucleus in an image, I_{G1} and I_{G2} are average intensities of G1 and G2 nuclei in the image, respectively, and I_{norm} is the normalized integral intensity of the nucleus. As a result of the normalization, the centres of the peaks for G1 and G2 nuclei were assigned to 1 and 2, respectively. This procedure was repeated for each field and the resulting normalized data were pooled and presented as a histogram with bin size 0.05. A total of 840 cells in five separate slide areas were analysed.

Chromatin zone classification. An important feature of experimental DNA replication data is that early replication occurs preferentially in euchromatin (R-bands), whereas later replication occurs mostly in heterochromatin (G-bands). For this reason, a replication model must include the patterning of DNA into zones of different chromatin type[67]. In our model the DNA is conceived as a 1D string with a length of about 10^{10} base pairs, which is characteristic of the HeLa aneuploid genome[26]. Positions on the DNA are represented by a continuous variable.

Partitioning of the DNA into chromosomes is implemented by dividing the string into sections separated by barriers, which cannot be overcome by replication forks and block induced firing events. In contrast, replication forks can move through boundaries between eu- and heterochromatin zones. Therefore, the zones only differ with respect to their accessibility at the beginning of S-phase.

The sizes, positions and types of the chromatin zones were derived from human genome (hg19) Giemsa band data of the UCSC Genome Browser project (863 entries)[55], because the staining values indicate the compaction of the local chromatin structure. Chromatin zones with zero Giemsa staining (gneg) were classified as euchromatin. Those with light staining (gpos25 or gpos50) as facultative heterochromatin. All other staining values (gpos75, gpos100, acen, gvar and stalk) were interpreted as constitutive heterochromatin. As an exception, the inactive X chromosome was simulated as 100% facultative heterochromatin to include experimental observations[68]. To adjust the model to HeLa cells, we added extra copies of those chromosomes that are contained more than twice in HeLa cells resulting in a total number of 76 chromosomes. The exact number for each chromosome is shown in Supplementary Table 2. Abnormal chromosomes were replaced by unaltered copies of their ancestral human chromosome. This resulted in 1,380 zones of euchromatin, 702 zones of facultative and 627 of constitutive heterochromatin. Due to differences in the average zone size the corresponding fractions of the total chromatin content are 42, 22 and 36%, respectively. The size distribution of the three chromatin zone types is shown in Supplementary Fig. 2.

Data availability. The simulation source code (GPLv3 license) and installation instructions are available online at https://github.com/nleng/DNA-replication. Additionally the simulations can be performed online at http://sim.bio.tu-darmstadt.de.

References

1. Gilbert, D. M. Replication origin plasticity, Taylor-made: inhibition versus recruitment of origins under conditions of replication stress. *Chromosoma* **116,** 341–347 (2007).
2. Blow, J. J. & Dutta, A. Preventing re-replication of chromosomal DNA. *Nat. Rev. Mol. Cell Biol.* **6,** 476–486 (2005).
3. Chagin, V. O., Stear, J. H. & Cardoso, M. C. Organization of DNA replication. *Cold Spring Harb Perspect Biol* **2,** a000737 (2010).
4. Jacob, F., Brenner, S. & Cuzin, F. On the regulation of DNA replication in bacteria. *Cold Spring Harbor Symposia on Quantitative Biology* **28,** 329–348 (1963).
5. Lygeros, J. *et al.* Stochastic hybrid modeling of DNA replication across a complete genome. *Proc. Natl Acad. Sci. USA* **105,** 12295–12300 (2008).
6. Spiesser, T. W., Klipp, E. & Barberis, M. A model for the spatiotemporal organization of DNA replication in Saccharomyces cerevisiae. *Mol. Genet. Genomics* **282,** 25–35 (2009).
7. Hyrien, O., Marheineke, K. & Goldar, A. Paradoxes of eukaryotic DNA replication: MCM proteins and the random completion problem. *Bioessays* **25,** 116–125 (2003).
8. Machida, Y. J., Hamlin, J. L. & Dutta, A. Right place, right time, and only once: replication initiation in metazoans. *Cell* **123,** 13–24 (2005).
9. Mechali, M. Eukaryotic DNA replication origins: many choices for appropriate answers. *Nat. Rev. Mol. Cell Biol.* **11,** 728–738 (2010).
10. Woodfine, K. *et al.* Replication timing of the human genome. *Hum. Mol. Genet.* **13,** 191–202 (2004).
11. Casas-Delucchi, C. S. *et al.* Histone acetylation controls the inactive X chromosome replication dynamics. *Nat. Commun.* **2,** 222 (2011).
12. Casas-Delucchi, C. S. *et al.* Histone hypoacetylation is required to maintain late replication timing of constitutive heterochromatin. *Nucleic Acids Res.* **40,** 159–169 (2012).
13. Hiratani, I. *et al.* Global reorganization of replication domains during embryonic stem cell differentiation. *PLoS Biol.* **6,** e245 (2008).
14. Jun, S., Herrick, J., Bensimon, A. & Bechhoefer, J. Persistence length of chromatin determines origin spacing in Xenopus early-embryo DNA replication: quantitative comparisons between theory and experiment. *Cell Cycle* **3,** 211–217 (2004).
15. Berezney, R., Dubey, D. D. & Huberman, J. A. Heterogeneity of eukaryotic replicons, replicon clusters, and replication foci. *Chromosoma* **108,** 471–484 (2000).
16. Aladjem, M. I. & Fanning, E. The replicon revisited: an old model learns new tricks in metazoan chromosomes. *EMBO Rep.* **5,** 686–691 (2004).
17. Sporbert, A., Gahl, A., Ankerhold, R., Leonhardt, H. & Cardoso, M. C. DNA polymerase clamp shows little turnover at established replication sites but sequential *de novo* assembly at adjacent origin clusters. *Mol. Cell* **10,** 1355–1365 (2002).
18. Guilbaud, G. *et al.* Evidence for sequential and increasing activation of replication origins along replication timing gradients in the human genome. *PLoS Comput. Biol.* **7,** e1002322 (2011).
19. Cayrou, C. *et al.* Genome-scale analysis of metazoan replication origins reveals their organization in specific but flexible sites defined by conserved features. *Genome Res.* **21,** 1438–1449 (2011).
20. DePamphilis, M. L. Replication origins in metazoan chromosomes: fact or fiction? *Bioessays* **21,** 5–16 (1999).
21. O'Keefe, R. T., Henderson, S. C. & Spector, D. L. Dynamic organization of DNA replication in mammalian cell nuclei: spatially and temporally defined replication of chromosome-specific alpha-satellite DNA sequences. *J. Cell Biol.* **116,** 1095–1110 (1992).
22. Shaw, A., Olivares-Chauvet, P., Maya-Mendoza, A. & Jackson, D. A. S-phase progression in mammalian cells: modelling the influence of nuclear organization. *Chromosome Res.* **18,** 163–178 (2010).
23. Takebayashi, S.-I. *et al.* Regulation of replication at the R/G chromosomal band boundary and pericentromeric heterochromatin of mammalian cells. *Exp. Cell Res.* **304,** 162–174 (2005).
24. Rhind, N. DNA replication timing: random thoughts about origin firing. *Nat. Cell Biol.* **8,** 1313–1316 (2006).
25. Lebofsky, R., Heilig, R., Sonnleitner, M., Weissenbach, J. & Bensimon, A. DNA replication origin interference increases the spacing between initiation events in human cells. *Mol. Biol. Cell* **17,** 5337–5345 (2006).
26. Chagin, V. O. *et al.* 4D Visualization of replication foci in mammalian cells corresponding to individual replicons. *Nat. Commun.* **7,** 11231 (2016).
27. Blow, J. J., Gillespie, P. J., Francis, D. & Jackson, D. A. Replication origins in xenopus egg extract are 5–15 kilobases apart and are activated in clusters that fire at different times. *J. Cell Biol.* **152,** 15–26 (2001).
28. Buongiorno-Nardelli, M., Micheli, G., Carri, M. T. & Marilley, M. A relationship between replicon size and supercoiled loop domains in the eukaryotic genome. *Nature* **298,** 100–102 (1982).
29. Walter, J. & Newport, J. W. Regulation of replicon size in Xenopus egg extracts. *Science* **275,** 993–995 (1997).
30. Courbet, S. *et al.* Replication fork movement sets chromatin loop size and origin choice in mammalian cells. *Nature* **455,** 557–560 (2008).
31. Guillou, E. *et al.* Cohesin organizes chromatin loops at DNA replication factories. *Genes Dev.* **24,** 2812–2822 (2010).
32. Münkel, C. & Langowski, J. Chromosome structure predicted by a polymer model. *Phys. Rev. E* **57,** 5888 (1998).
33. Goldar, A., Labit, H., Marheineke, K. & Hyrien, O. A dynamic stochastic model for DNA replication initiation in early embryos. *PLoS One* **3,** e2919 (2008).
34. Gindin, Y., Valenzuela, M. S., Aladjem, M. I., Meltzer, P. S. & Bilke, S. A chromatin structure-based model accurately predicts DNA replication timing in human cells. *Mol. Syst. Biol.* **10,** 722 (2014).
35. Yang, S. C.-H. *et al.* How Xenopus laevis embryos replicate reliably: investigating the random-completion problem. *Phys. Rev. E* **78,** 041917 (2008).
36. Grünwald, D. *et al.* Probing intranuclear environments at the single-molecule level. *Biophys. J.* **94,** 2847–2858 (2008).
37. Dross, N. *et al.* Mapping eGFP oligomer mobility in living cell nuclei. *PLoS One* **4,** e5041 (2009).
38. Huberman, J. A. & Riggs, A. D. Autoradiography of chromosomal DNA fibers from Chinese hamster cells. *Proc. Natl Acad. Sci. USA* **55,** 599–606 (1966).
39. Dewar, J. M. & Walter, J. C. Chromosome biology: conflict management for replication and transcription. *Curr. Biol.* **23,** R200–R202 (2013).
40. Pomerantz, R. T. & O'Donnell, M. What happens when replication and transcription complexes collide? *Cell Cycle* **9,** 2537–2543 (2010).
41. Cremer, T. & Cremer, C. Chromosome territories, nuclear architecture and gene regulation in mammalian cells. *Nat. Rev. Genet.* **2,** 292–301 (2001).
42. Pope, B. D. *et al.* Topologically associating domains are stable units of replication-timing regulation. *Nature* **515,** 402–405 (2014).
43. Jackson, D. A. & Pombo, A. Replicon clusters are stable units of chromosome structure: evidence that nuclear organization contributes to the efficient activation and propagation of S phase in human cells. *J. Cell Biol.* **140,** 1285–1295 (1998).
44. Consortium, E. P. *et al.* An integrated encyclopedia of DNA elements in the human genome. *Nature* **489,** 57–74 (2012).
45. Watanabe, Y. *et al.* Chromosome-wide assessment of replication timing for human chromosomes 11q and 21q: disease-related genes in timing-switch regions. *Hum. Mol. Genet.* **11,** 13–21 (2002).
46. Manders, E. M., Stap, J., Brakenhoff, G. J., van Driel, R. & Aten, J. A. Dynamics of three-dimensional replication patterns during the S-phase, analysed by double labelling of DNA and confocal microscopy. *J. Cell Sci.* **103**(Pt 3): 857–862 (1992).
47. Nakamura, H., Morita, T. & Sato, C. Structural organizations of replicon domains during DNA synthetic phase in the mammalian nucleus. *Exp. Cell Res.* **165,** 291–297 (1986).
48. Nakayasu, H. & Berezney, R. Mapping replicational sites in the eucaryotic cell nucleus. *J. Cell Biol.* **108,** 1–11 (1989).
49. Cardoso, M. C., Leonhardt, H. & Nadal-Ginard, B. Reversal of terminal differentiation and control of DNA replication: cyclin A and Cdk2 specifically localize at subnuclear sites of DNA replication. *Cell* **74,** 979–992 (1993).
50. Leonhardt, H. *et al.* Dynamics of DNA replication factories in living cells. *J. Cell Biol.* **149,** 271–280 (2000).
51. Bohn, M., Heermann, D. W. & van Driel, R. Random loop model for long polymers. *Phys. Rev. E Stat. Nonlin. Soft Matter Phys.* **76,** 051805 (2007).
52. Mateos-Langerak, J. *et al.* Spatially confined folding of chromatin in the interphase nucleus. *Proc. Natl Acad. Sci. USA* **106,** 3812–3817 (2009).
53. Parada, L. & Misteli, T. Chromosome positioning in the interphase nucleus. *Trends Cell Biol.* **12,** 425–432 (2002).
54. Bolzer, A. *et al.* Three-dimensional maps of all chromosomes in human male fibroblast nuclei and prometaphase rosettes. *PLoS Biol.* **3,** e157 (2005).
55. Dreszer, T. R. *et al.* The UCSC Genome Browser database: extensions and updates 2011. *Nucleic Acids Res.* **40,** D918–D923 (2012).
56. Lucas, I., Chevrier-Miller, M., Sogo, J. M. & Hyrien, O. Mechanisms ensuring rapid and complete DNA replication despite random initiation in Xenopus early embryos. *J. Mol. Biol.* **296,** 769–786 (2000).
57. Duan, Z. & Blau, C. A. The genome in space and time: does form always follow function? *Bioessays* **34,** 800–810 (2012).
58. Sachs, R., Van Den Engh, G., Trask, B., Yokota, H. & Hearst, J. A random-walk/giant-loop model for interphase chromosomes. *Proc. Natl Acad. Sci. USA* **92,** 2710–2714 (1995).
59. Goldar, A., Marsolier-Kergoat, M.-C. & Hyrien, O. Universal temporal profile of replication origin activation in eukaryotes. *PLoS One* **4,** e5899 (2009).
60. Jun, S., Zhang, H. & Bechhoefer, J. Nucleation and growth in one dimension. I. The generalized Kolmogorov-Johnson-Mehl-Avrami model. *Phys. Rev. E* **71,** 011908 (2005).
61. Bechhoefer, J. & Marshall, B. How Xenopus laevis replicates DNA reliably even though its origins of replication are located and initiated stochastically. *Phys. Rev. Lett.* **98,** 098105 (2007).

62. Bickmore, W. A. & Carothers, A. D. Factors affecting the timing and imprinting of replication on a mammalian chromosome. *J. Cell Sci.* **108**(Pt 8): 2801–2809 (1995).
63. Earnshaw, W. C. & Laemmli, U. K. Architecture of metaphase chromosomes and chromosome scaffolds. *J. Cell Biol.* **96,** 84–93 (1983).
64. Paulson, J. R. & Laemmli, U. The structure of histone-depleted metaphase chromosomes. *Cell* **12,** 817–828 (1977).
65. Jackson, D., Dickinson, P. & Cook, P. The size of chromatin loops in HeLa cells. *EMBO J.* **9,** 567 (1990).
66. Ganai, N., Sengupta, S. & Menon, G. I. Chromosome positioning from activity-based segregation. *Nucleic Acids Res.* **42,** 4145–4159 (2014).
67. Drouin, R., Lemieux, N. & Richer, C. L. Analysis of DNA replication during S-phase by means of dynamic chromosome banding at high resolution. *Chromosoma* **99,** 273–280 (1990).
68. Rego, A., Sinclair, P. B., Tao, W., Kireev, I. & Belmont, A. S. The facultative heterochromatin of the inactive X chromosome has a distinctive condensed ultrastructure. *J. Cell Sci.* **121,** 1119–1127 (2008).
69. Reinhart, M., Casas-Delucchi, C. S. & Cardoso, M. C. Spatiotemporal visualization of DNA replication dynamics. *Imaging Gene Expr.* **1042,** 213–225 (2013).

Acknowledgements

We thank Agnes Szejka for contributing to the foundations of our replication model and Dr Yuriy M. Rozanov, who helped with the analysis of S-phase dynamics presented in Fig. 3. This work was supported by grants from the German Research Council (DFG CA 198/9 and Graduate college 1,657) and the Helmholtz Graduate School for Hadron and Ion Research. The funders had no role in study design, data collection and analysis, decision to publish or preparation of the manuscript.

Author contributions

V.O.C., C.S.C.D. and M.R. performed the experiments. V.O.C., C.S.C.D., M.R., D.L., N.L. and B.D. analysed the data. D.L., B.D., N.L., V.O.C. and M.R. designed the model. D.L., N.L. and B.D. provided model algorithm and implementation. M.C.C., B.D., D.L. and V.O.C. designed the project. D.L., N.L., V.O.C., M.R., M.C.C. and B.D. wrote the manuscript. Website and videos by N.L. All authors commented on the manuscript.

Additional information

Supplementary Information accompanies this paper at http://www.nature.com/naturecommunications

Competing financial interests: The authors declare no competing financial interests.

Reprints and permission information is available online at http://npg.nature.com/reprintsandpermissions/

How to cite this article: Löb, D. *et al.* 3D replicon distributions arise from stochastic initiation and domino-like DNA replication progression. *Nat. Commun.* 7:11207 doi: 10.1038/ncomms11207 (2016).

Supplementary Figures

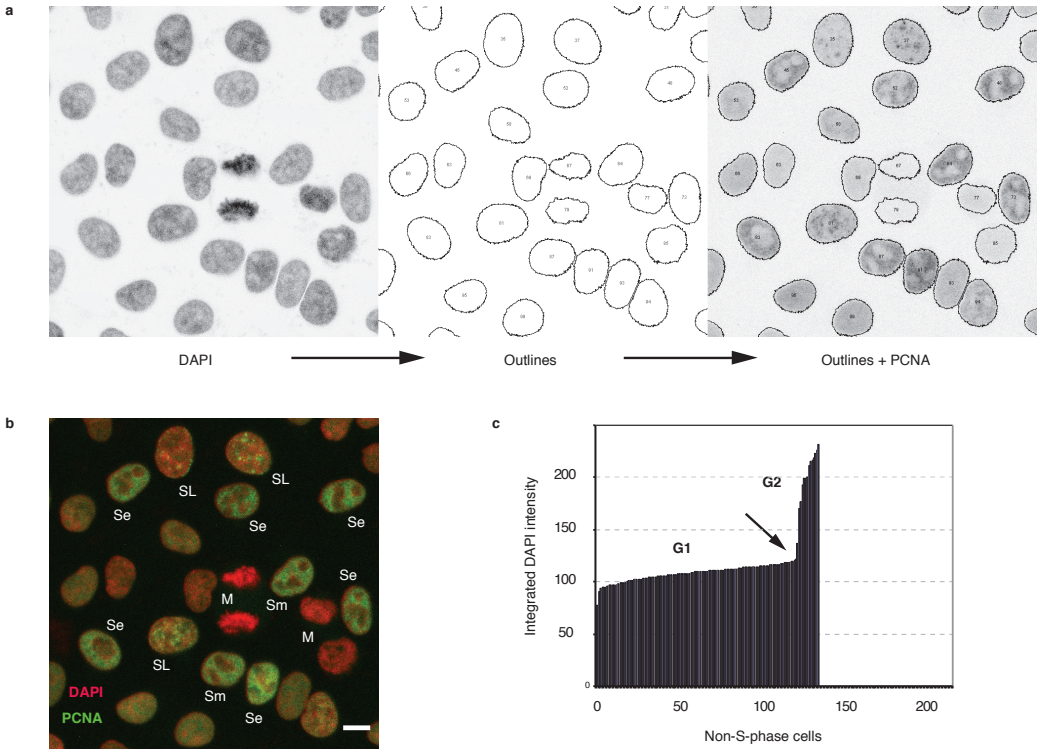

Supplementary Figure 1. Quantification of DNA content corresponding to the three major S-phase patterns. Nuclei of HeLa Kyoto mCherryPCNA cells were stained with DAPI. A total of 840 cells in 5 separate slide areas were analyzed. **(a)** Procedure for assigning DNA contents of individual cells with S-phase patterns. **(b)** Cells in early, middle and late S-phase were classified based on characteristic features of the PCNA distribution: uniform nucleoplasmic foci, perinucleoar foci rings and bright foci clusters, respectively. Note the relatively high DAPI intensity and absence of PCNA signal in mitotic nuclei. **(c)** Classification of non-S-phase cells into G1 and G2 populations based on the sharp increase in DAPI intensity. **(a)** and **(b)** show a small area of the field used for the analysis in **(c)**. The scale bar is 10 μm, this data was also used to estimate the nuclear sizes and shapes for the 3D model.

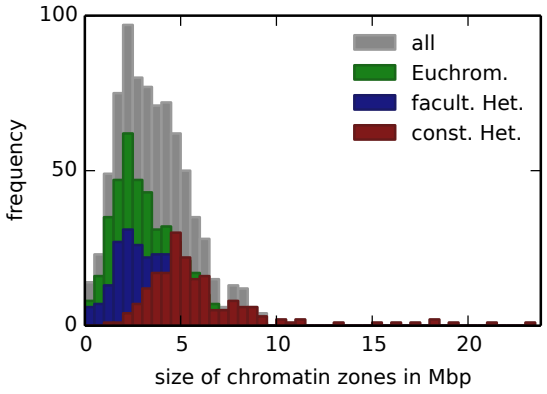

Supplementary Figure 2. Size distribution of chromatin zones. Human genome Giemsa and data of the UCSC Genome Browser project[1] was used to determine the sizes, positions and types of the chromatin zones. Zero staining was interpreted as euchromatin, light staining as facultative heterochromatin and dark staining as constitutive heterochromatin. The average chromatin zone sizes are 3.1 Mbp for euchromatin, 3.3 Mbp for facultative and 5.9 Mbp for constitutive heterochromatin respectively.

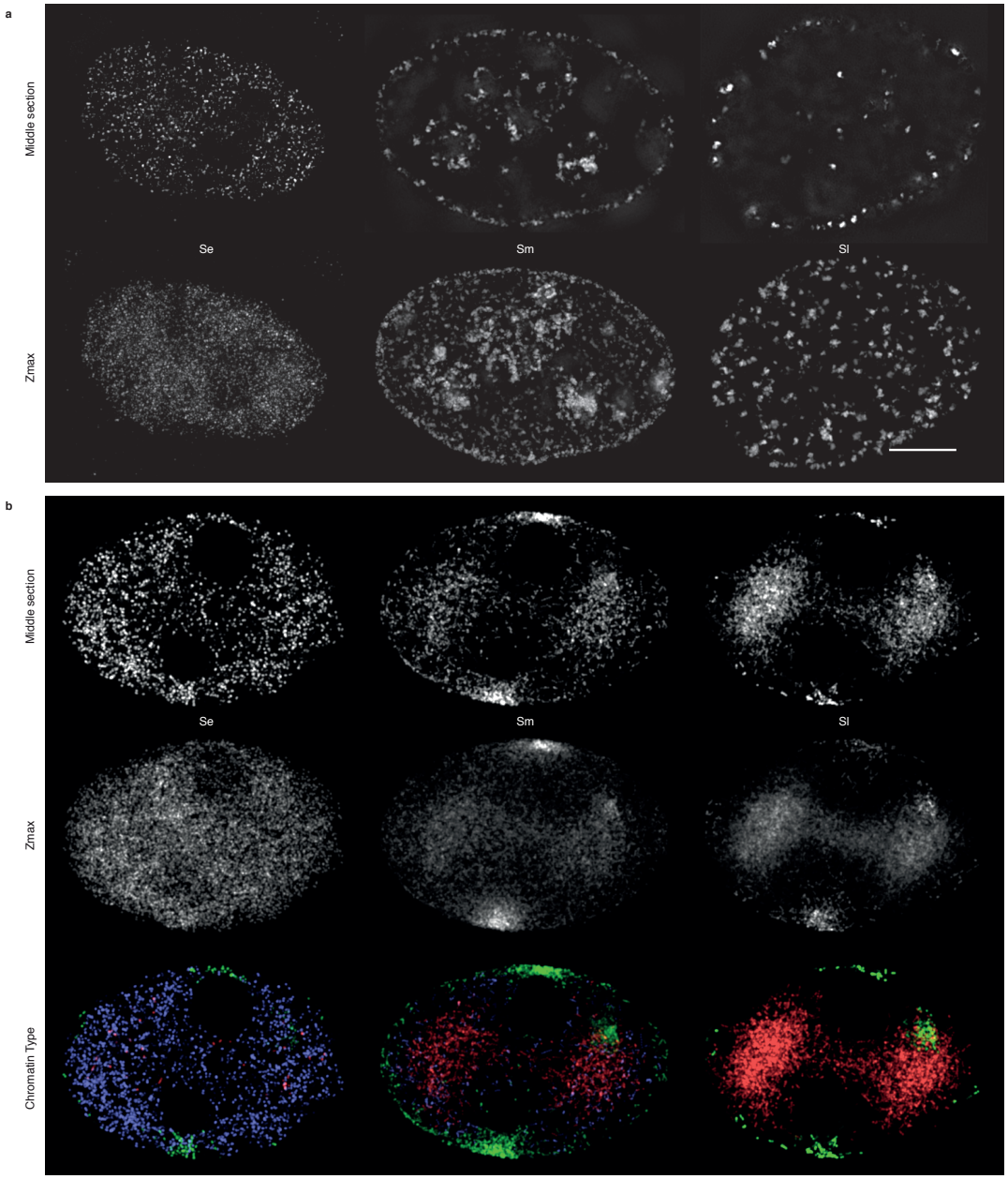

Supplementary Figure 3. Microscopy-like Images. 3D projection for the random loop model parameters used by Mateos-Langerak.[2] Both chromatin types have the same spring constant but the number of connections within them is different. Consistent with that publication, the total number of connections is 5,000, and the relative connection portions are 7/16 for constitutive Heterochromatin, 5/16 for facultative Heterochromatin, 3/16 for Euchromatin and 1/16 for inter-chromatin connections. Using these parameters, no clearly discernible formation of 3D foci is observed. **(a)** Experimental maximum intensity z-projections and middle section images of GFP-tagged PCNA inHeLa cells during early, middle and late S-phase (as described by Chagin et al.,[3] scale bar: 5 μm). **(b)** Corresponding "in silico microscopy" images. In the last row the simulated fork positions are marked depending on the chromatin type (blue: euchromatin, green: facultative heterochromatin, red: constitutive heterochromatin). Images for different parameters and chromatin distributions can be created online at http://sim.bio.tu-darmstadt.de. See also Supplementary Movies 1-3 for a visualization of the fork movement within the nucleus.

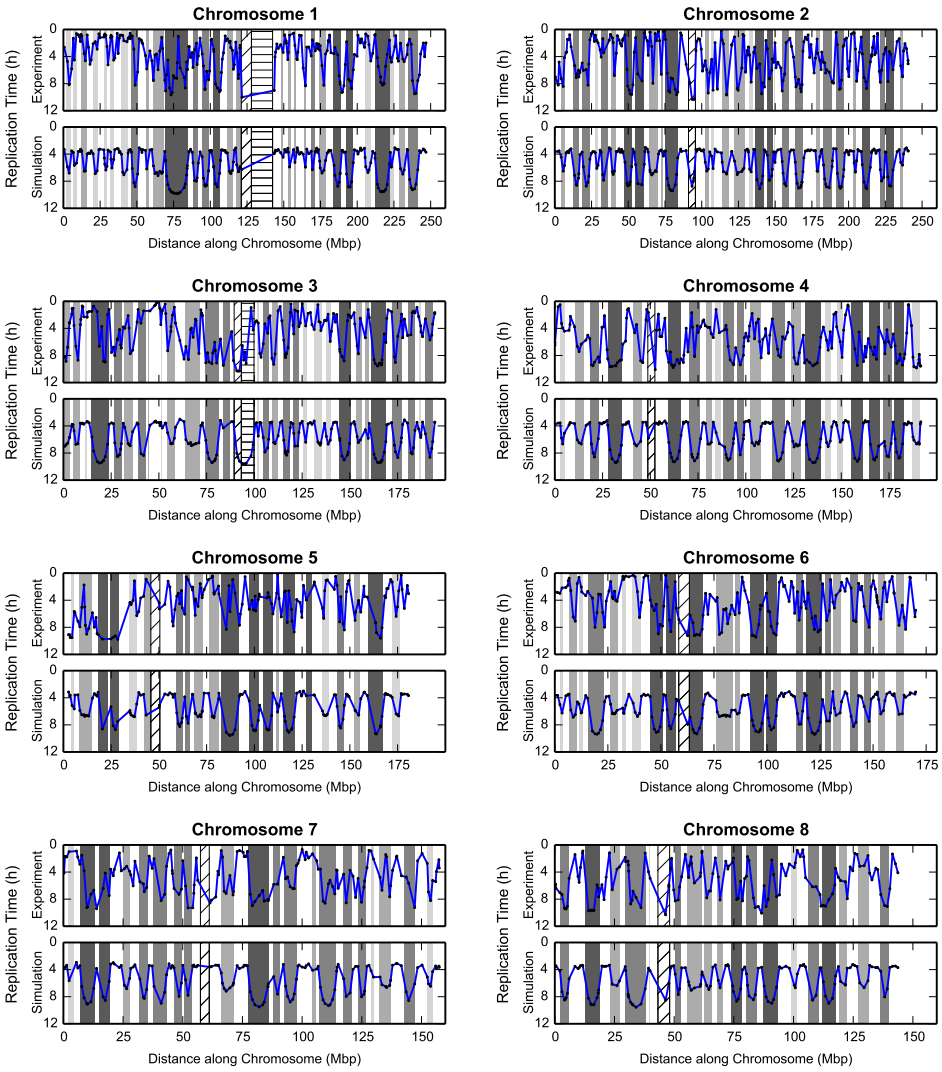

Supplementary Figure 4. Replication timing. Comparison of the replication timing of our model with data from the ENCODE project[4] (cell type GM12878) for chromosomes 1-8. Sampling positions are identical to the positions in the experimental data. For individual simulations, the euchromatic peaks start at time zero, but because of the specific sampling positions and averaging over 100 simulations, the displayed peaks are less extreme. The Background indicates the Giemsa staining, where white regions are interpreted as euchromatin and shaded regions as facultative or constitutive heterochromatin. The centromere is indicated as a striped pattern.

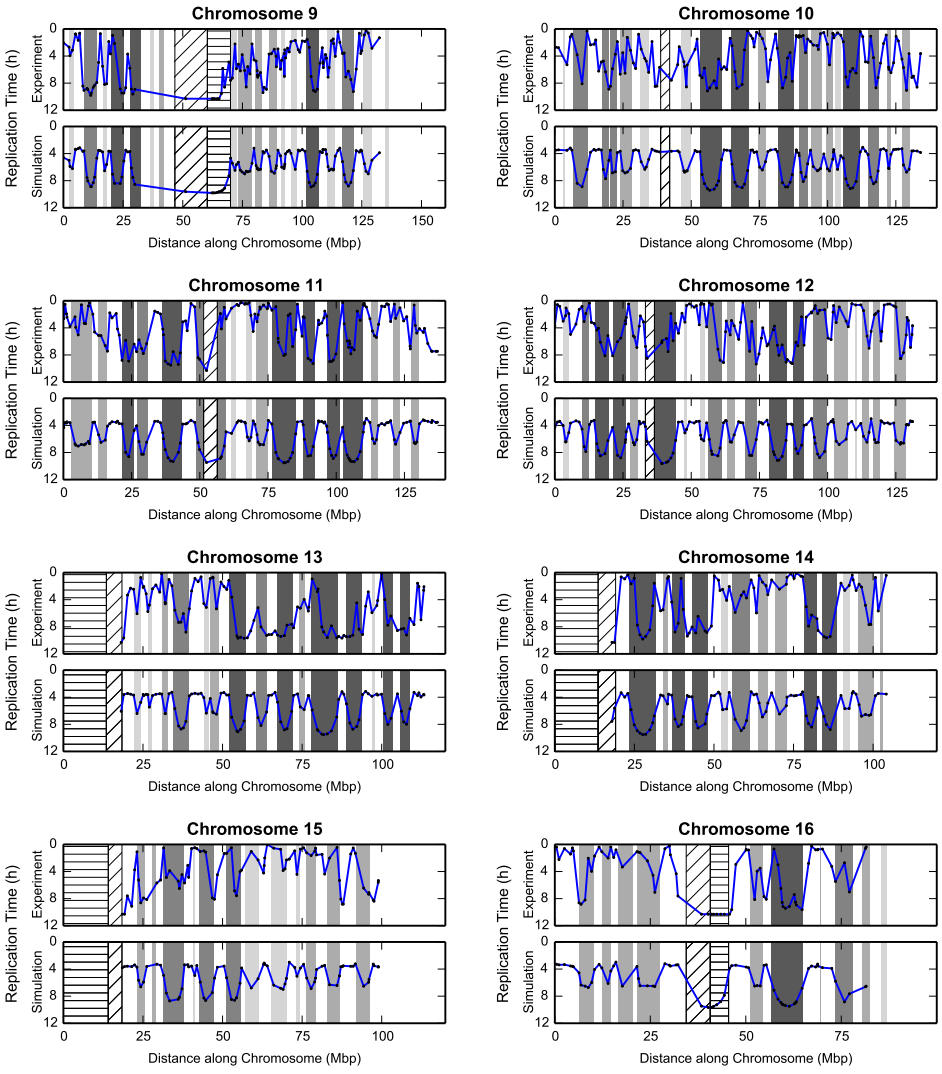

Supplementary Figure 5. Replication timing comparison for chromosomes 9-16.

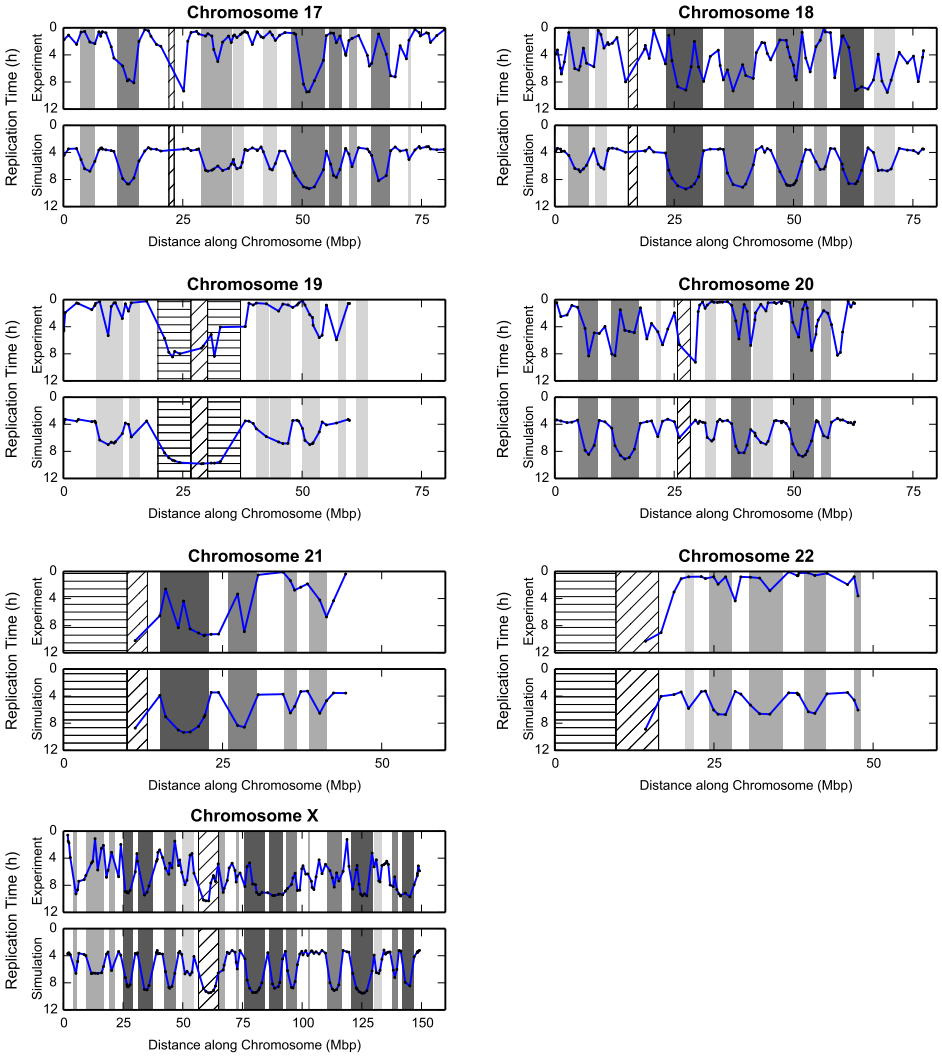

Supplementary Figure 6. Replication timing comparison for chromosomes 17-22 and the X chromosome.

Supplementary Tables

Supplementary Table 1. Average correlation coefficients for simulations and experimental data.

data type	Simulation	Woodfine	GM12878	Helas3	K562
Simulation	1.0	0.29	0.41	0.32	0.40
Woodfine		1.0	0.47	0.34	0.42
GM12878			1.0	0.74	0.83
Helas3				1.0	0.72
K562					1.0

Average over 23 chromosomes of the Pearson's correlation coefficients between the timing of sample positions in the model and in replication timing measurements from various sources (ENCODE project[4] and Woodfine et al.[5]). For all experiments the same chromosomal positions were used as by Woodfine et al.[5] (1 Mbp resolution).

Supplementary Table 2. Correlation coefficients for all chromosomes.

Chromosome	Duplicates	Correlation Coefficient
1	5	0.50
2	3	0.55
3	3	0.54
4	2	0.46
5	6	0.15
6	3	0.60
7	5	0.56
8	3	0.50
9	5	0.52
10	3	0.38
11	3	0.49
12	3	0.19
13	3	0.43
14	3	0.52
15	3	-0.05
16	3	0.63
17	4	0.43
18	2	0.21
19	3	0.65
20	3	0.16
21	3	0.44
22	3	0.27
23	2	0.41

Second column: Chromosomal duplicates used to model HeLa cells with a total number of 76 chromosomes.[6] Third column: Pearson's correlation coefficients between the timing of sample positions in the model and in measurements from the ENCODE project[4] for 23 human chromosomes with a resolution of 1 Mbp. The theoretical values used were averaged over 100 simulations.

Supplementary Note 1

We repeated the comparison of replication timing data from the ENCODE project[4] (cell type GM12878) and our model for 23 human chromosomes. The same level of agreement as for chromosome 6 was found for all chromosomes except chromosomes 9, 16 and the X chromosome. In chromosomes 9 and 16, the experimental data shows early replication of larger heterochromatic regions, whereas in the X chromosome data, the overall differences in replication timing for euchromatin and heterochromatin are much less pronounced. Possible reasons for this could be either epigenetic modifications regulating the replication of these chromosomes or the experiment statistics. The Pearson's correlation coefficients for all chromosomes and figures analogous to Figure 3e for all chromosomes are shown in Supplementary Table 2 and the comparisons are shown in Supplementary Figures 4-6.

We also compared the replication timing data of our simulation to data from three cell types measured in the ENCODE project[4] as well as data from Woodfine et al.[5] As shown in Supplementary Table 1 the correlation coefficients between experimental replication timing data (at the resolution of the Woodfine data[5]) varies between 0.34 and 0.83. The correlation between the averaged over 100 simulations and experimental data is lower (between 0.29 and 0.41). We ascribe this to the randomness of the simulated processes and the limited resolution of chromatin zones.

References

1. Dreszer, T. R. *et al.* The UCSC Genome Browser database: extensions and updates 2011. *Nucleic Acids Res* **40**, D918–D923 (2012).

2. Mateos-Langerak, J. *et al.* Spatially confined folding of chromatin in the interphase nucleus. *Proc Natl Acad Sci U S A* **106**, 3812–3817 (2009).

3. Chagin, V. O. *et al.* 4D Visualization of Replication Foci in Mammalian Cells Corresponding to Individual Replicons. *Manuscript co-submitted* .

4. Consortium, E. P. *et al.* An integrated encyclopedia of DNA elements in the human genome. *Nature* **489**, 57–74 (2012).

5. Woodfine, K. *et al.* Replication timing of the human genome. *Human Molecular Genetics* **13**, 191–202 (2004).

6. Macville, M. *et al.* Comprehensive and Definitive Molecular Cytogenetic Characterization of HeLa Cells by Spectral Karyotyping. *Cancer Research* **59**, 141–150 (1999).

7 Predictions from the model

7.1 Intro

In bacteria DNA replication typically starts at a single origin of replication (ori) on each circular chromosome. This replication ori is defined by consensus sequence, a specific DNA sequence [19,91]. Duplication of larger linear chromosomes requires replication forks at multiple locations. These locations have been mapped for mouse and human cells, but a consensus sequence of mammalian DNA replication origins is still missing. I reviewed the relevant literature, which contains information on DNA origin positions in human and mouse cells (see Table 7.1). In addition, I summarized a comparative analysis of ori mapping methods and corresponding overlap within the same cell type (see Table 7.1). The numbers of origins mapped in the literature is on the order of a quarter of one million per genome. Noteworthy, the ori positions reported in these publications overlap only between 9 % [128] and 70 % [74], depending on whether the same cell line and method of measurement was used (see Table 7.1). Origin mapping has been performed averaging billions of cells and it is well known in the literature that at each single cell and cell cycle only a fraction of the origins will fire [25]. Microscopy analysis corresponds only to snap shots in time and even with the quadruple replication labelling, each snap shot gives us ~10 % (5,000 RFi in over 50,000 total RFi) of all active replicons in a single cell cycle. The difficulty to correlation of DNA replication origins through colocalization analysis is increasing exponentially with increases in resolution, making the detection of specific DNA replication origins at the needed super-resolution level a "needle-in-a-haystack" type of pursuit. Even a conventional microscopy resolution study obtained a maximum of 30 % partially overlapping and labeled RFi in consecutive cell cycles [140]. To circumvent those limitations we will apply our *in silico* DNA replication model in the search for the DNA replication origin consensus motif.

Table 7.1: Summary of origin features reported in mammalian genome-wide mapping studies

Study	Cell Type	Origin number	Origin purification	Detection
Human				
Lucas et al., 2007 [98]	11365	32	SSS	Microarray
Cadoret et al., 2008 [18]	HeLa	283	lambda-SNS	Microarray
Karnani et al., 2010 [81]	HeLa	150	lambda-SNS / BrdU-SNS	Microarray
Mesner et al., 2011 [110]	early S HeLa	111 (646)	Bubble trap	Microarray
Mesner et al., 2011 [110]	HeLa	128 (657)	Bubble trap	Microarray
Mesner et al., 2011 [110]	GMO6990	177 (988)	Bubble trap	Microarray
Valenzuela et al., 2011 [172]	MCF-7	8281	SSS, lambda-SNS / lambda-SNS	Microarray sequencing
Valenzuela et al., 2011 [172]	BT474	8281	SSS, lambda-SNS / lambda-SNS	Microarray sequencing
Valenzuela et al., 2011 [172]	H520/MCF-7	8281	SSS, lambda-SNS / lambda-SNS	Microarray sequencing
Martin et al., 2011 [100]	K562	NR	lambda-SNS	Sequencing
Martin et al., 2011 [100]	MCF-7	NR	lambda-SNS	Sequencing
Besnard et al., 2012 [10]	HeLa	233545	lambda-SNS	Sequencing
Besnard et al., 2012 [10]	IMR-90	256990	lambda-SNS	Sequencing
Besnard et al., 2012 [10]	iPSCs from IMR-90	246866	lambda-SNS	Sequencing
Besnard et al., 2012 [10]	hESC H9	208520	lambda-SNS	Sequencing
Mesner et al., 2013 [109]	GM06990	72812 (123264)	Bubble trap	Sequencing
Dellino et al., 2013 [40]	HeLa	13,600	ORC1-ChIP	Sequencing
Picard et al., 2014 [128]	K562	59,185	lambda-SNS	Sequencing
Picard et al., 2014 [128]	HeLa	90,073	lambda-SNS	Sequencing reanalysis
Picard et al., 2014 [128]	IMR-90	89,889	lambda-SNS	Sequencing reanalysis
Picard et al., 2014 [128]	iPSCs from IMR-90	93,896	lambda-SNS	Sequencing
Picard et al., 2014 [128]	hESC H9	79,556	lambda-SNS	Sequencing reanalysis of Besnard et al., 2012 [10]
Mukhopadhyay et al., 2014 [117]	Pri. erythroblastsbasophilic	100000	lambda-SNS / BrdU-SNS	Sequencing
Mouse				
Sequeira-Mendes et al., 2009 [146]	mESC	97	lambda-SNS	Microarray
Sequeira-Mendes et al., 2009 [146]	PGK12	97	lambda-SNS	Microarray
Sequeira-Mendes et al., 2009 [146]	MEFs	97	lambda-SNS	Microarray
Sequeira-Mendes et al., 2009 [146]	NIH-3T3	97	lambda-SNS	Microarray
Cayrou et al., 2011 [25]	mESC GCR8	2748/6184	lambda-SNS	Microarray

Table 7.2: A comparative analysis of ori mapping methods and corresponding overlap within the same cell type

Study	Cell Type	Origin number	% genome covered	compared detection methods	compared detection methods
SNS-sole				**sole in scan**	**scan in sole**
Besnard et al., 2012 [10]	HeLa	233545	6	71	59
Besnard et al., 2012 [10]	IMR-90	256990	6	70	59
Besnard et al., 2012 [10]	iPSCs from IMR-90	246866	6	68	56
Besnard et al., 2012 [10]	hESC H9	208520	6	73	57
clusteres sns-sole				**clustered sole in scan**	**scan in clustered sole**
Besnard et al., 2012 [10]	HeLa	156952	17	71	63
Besnard et al., 2012 [10]	IMR-90	169195	18	70	64
Besnard et al., 2012 [10]	iPSCs from IMR-90	165905	18	69	62
Besnard et al., 2012 [10]	hESC H9	144904	15	7	62
sns vs. Bubble					
SNS-sole				**bubble in sns**	**SNS in Bubble**
Besnard et al., 2012 [10]	HeLa	233545	6	46	37
Besnard et al., 2012 [10]	IMR-90	256990	6	45	37
Besnard et al., 2012 [10]	iPSCs from IMR-90	246866	6	46	37
Besnard et al., 2012 [10]	hESC H9	208520	6	46	33
clustered sns-sole				**clustered sole in scan**	**scan in clustered sole**
Besnard et al., 2012 [10]	HeLa	134141	29	51	40
Besnard et al., 2012 [10]	IMR-90	144811	31	50	40
Besnard et al., 2012 [10]	iPSCs from IMR-90	141514	30	51	40
Besnard et al., 2012 [10]	hESC H9	125951	25	50	36
sns-scan					
Besnard et al., 2012 [10]	HeLa	90073	12	46	37
Besnard et al., 2012 [10]	IMR-90	89889	13	45	37
Besnard et al., 2012 [10]	iPSCs from IMR-90	93896	12	45	37
Besnard et al., 2012 [10]	hESC H9	79556	10	45	32
clustered sns-scan					
Besnard et al., 2012 [10]	HeLa	66270	15	67	45
Besnard et al., 2012 [10]	IMR-90	66679	16	65	45
Besnard et al., 2012 [10]	iPSCs from IMR-90	69396	15	65	46
Besnard et al., 2012 [10]	hESC H9	61454	13	63	40

7.1.1 "The greatest ideas are the simplest." W. Golding - the simplistic DNA replication model

The previous chapters left us with tools to go from microscopy to nanoscopy and visualize DNA replication structures and machineries beyond the diffraction limit. It culminated in an *in silico* DNA replication model to understand the theories of the finest DNA replication details. As with every model, it was designed to represent facts we measured in biological experiments. It was carefully designed to follow the KISS principle ("Keep it simple, stupid"), and removed or discarded all possible parameter, which were not essential for the model. The reduced input yielded a simplistic but still exceptional model to simulate the complex DNA replication process on a level comparable to experimental data.

7.2 Methods

All simulations were performed using the simulation packages "replication" and "dna_metropolis" as described in Löb et al.. All genomic data (human genome (hg19)) was acquired through the ENCODE/ UCSC Genome Browser project [89]. Eu- and heterochromatin zones only differ with respect to their accessibility at the beginning of S-phase [46,96]. Positions on the DNA are represented by a continuous variable. Position data was transcribed into a nucleotide sequence with hg19 and respective copy numbers of individual chromosomes in the HeLa Kyoto cell line (see Figure 7.1). Nucleotide frequencies were analyzed with seqLogo: Sequence logos for DNA sequence alignments [6]. Genome data was also acquired through the UCSC Genome Browser and correlated to 1 Mbp replication start domains.

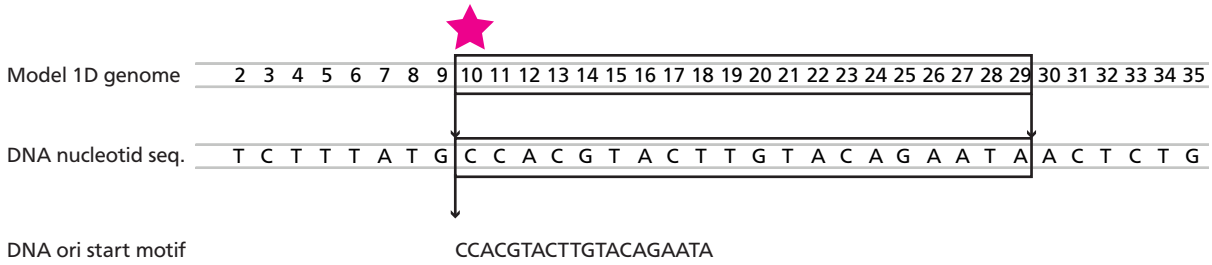

Figure 7.1: From a sequence free *in silico* model to the DNA replication origin sequence motif.
Alignment of sequence free 1D *in silico* DNA strand; middle) corresponding nucleotide frequency by comparable analysis and resulting DNA origin motif, the star indicates the beginning of the origin sequence.

7.3 The quest for the Holy Grail of mammalian DNA replication: the elusive DNA replication origin

In our quest for the elusive DNA replication origin motif in mammalian cells, I correlated the genome free simulated 1D replication data with human genome sequence data[89]. Replication origins activated due to the random initiation rate (see Figure 7.2) were discarded before the analysis as it would skew the outcome to random sequences. For this analysis only the earliest **induced** replication sites were evaluated.

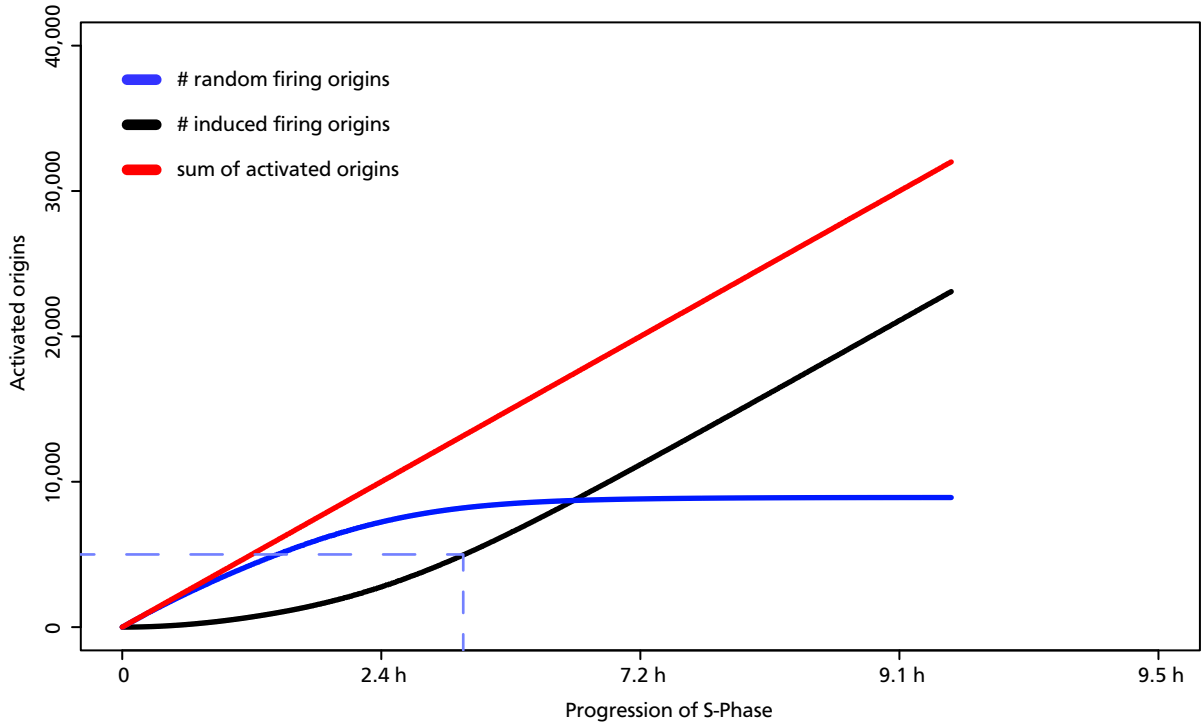

Figure 7.2: Temporal progression of DNA replication activation: random vs. induced.
The number of DNA replication foci, randomly activated (blue), induced (black) or in sum (red) during a S-Phase is plotted over time. The first origins are mostly represented by random firing origins according to the initial randomized activation. The number of activated induced DNA replication origins is accelerating during the first hours of S-Phase. In a domino-like manner, random activated origins and induced origins activate adjacent origins, increasing the number of involved origins.

I was able to map each activated DNA replication origin to their associated DNA sequence by combining replication timing data from the *in silico* model and genomic data from the ENCODE project. The human genome data was adapted to the HeLa Kyoto genome and the HeLa Kyoto karyotype as described in Chapter 6. This analysis was performed for

the earliest 5,000 induced replication origin sites on a whole genome scale and acquired over 100 simulated replicates resulting in 500,000 1k̇b sequences for the hole data set. For the five copy numbers of human Chromosome 1 in HeLa Kyoto (~12.8 % of the whole genome), presented in Figure 7.3 and 7.4, more than 59,000 DNA sequences were acquired and analyzed. Through this analysis I discovered a cyclic A/T rich DNA motif (see Figure 7.5 A and B) in the mostly C/G rich euchromatic regions. The unexpected A/T richness of the early S-Phase start regions hinted at an elusive mammalian DNA replication origin motif. To rule out technical or methodological errors, I performed an identical analysis with two different randomized sample sets. Sample set 1 featured a complete randomization of DNA replication origins, while sample set 2 inherited initiation sites arranged along the genome which were spaced multiples of thousand nucleotides pares apart. In detail, start sides from the sample set 1 can appear at any point along the genome where start sites for sample set 2 are at nucleotide positions $n * 1000$ e.g. 5,000; 227,000; 24,342,000. This $n * 1000$ spacing of origins is consistent with potential *in silico* DNA replication origins. Both control experiments had an equal random distribution of nucleotides throughout the analyzed DNA sequence (see Figure 7.5 C and D) with no reoccurring sequence motif.
This implies a periodic A/T rich DNA motif in DNA replication origins activated during early S-Phase. We expect sequence analysis further downstream to reveal C/G rich regions typical for euchromatin and highly active DNA regions [132]. Further, I made preliminary analyses of gene densities at the first 5,000 initiated sites (see Figure 7.4) at 1 Mbp scale, and correlated genes with the first induced DNA replication sites (see Figure 7.4). The poor DNA sequence resolution led to blurred results as the combined mega base pair domains represented more than 25 % of observed chromatin negating the search for specific genes. The next steps are further simulations to gain more simulation data and achieve a higher resolution for the gene density analysis and to statistically confirm the preliminary DNA origin motif data sets .

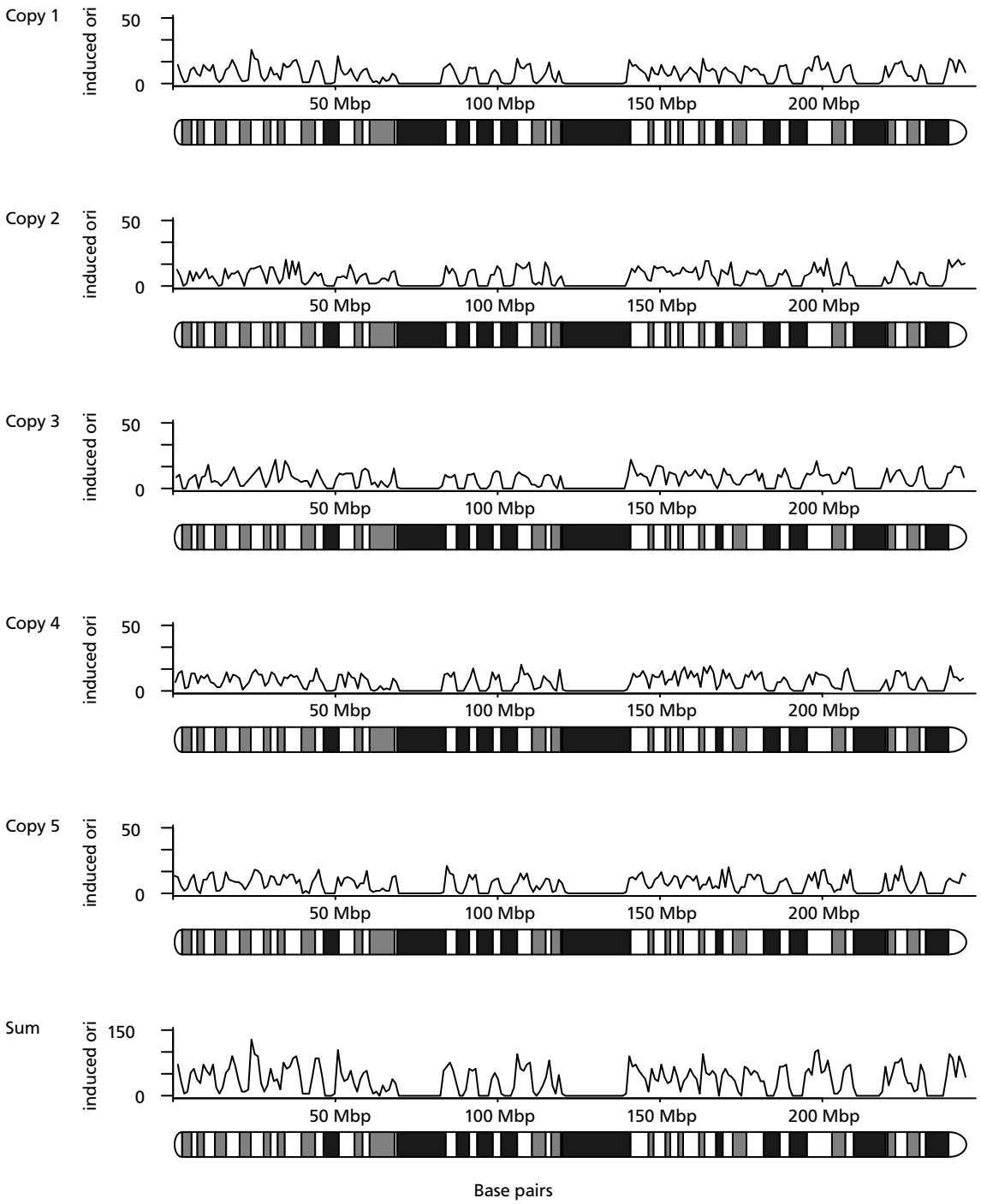

Figure 7.3: Ideogram and activated replication origins during the first 5,000 activations.
Five copies numbers of the HeLa Kyoto karyotype human Chromosome 1 are depicted with the accumulation of all active replication sites in the bottom graph. White areas in the ideogram represent euchromatic regions, light grey illustrates facultative and dark grey constitutive heterochromatin. The first 5,000 induced origins mostly correspond to euchromatic regions of Chromosome 1.

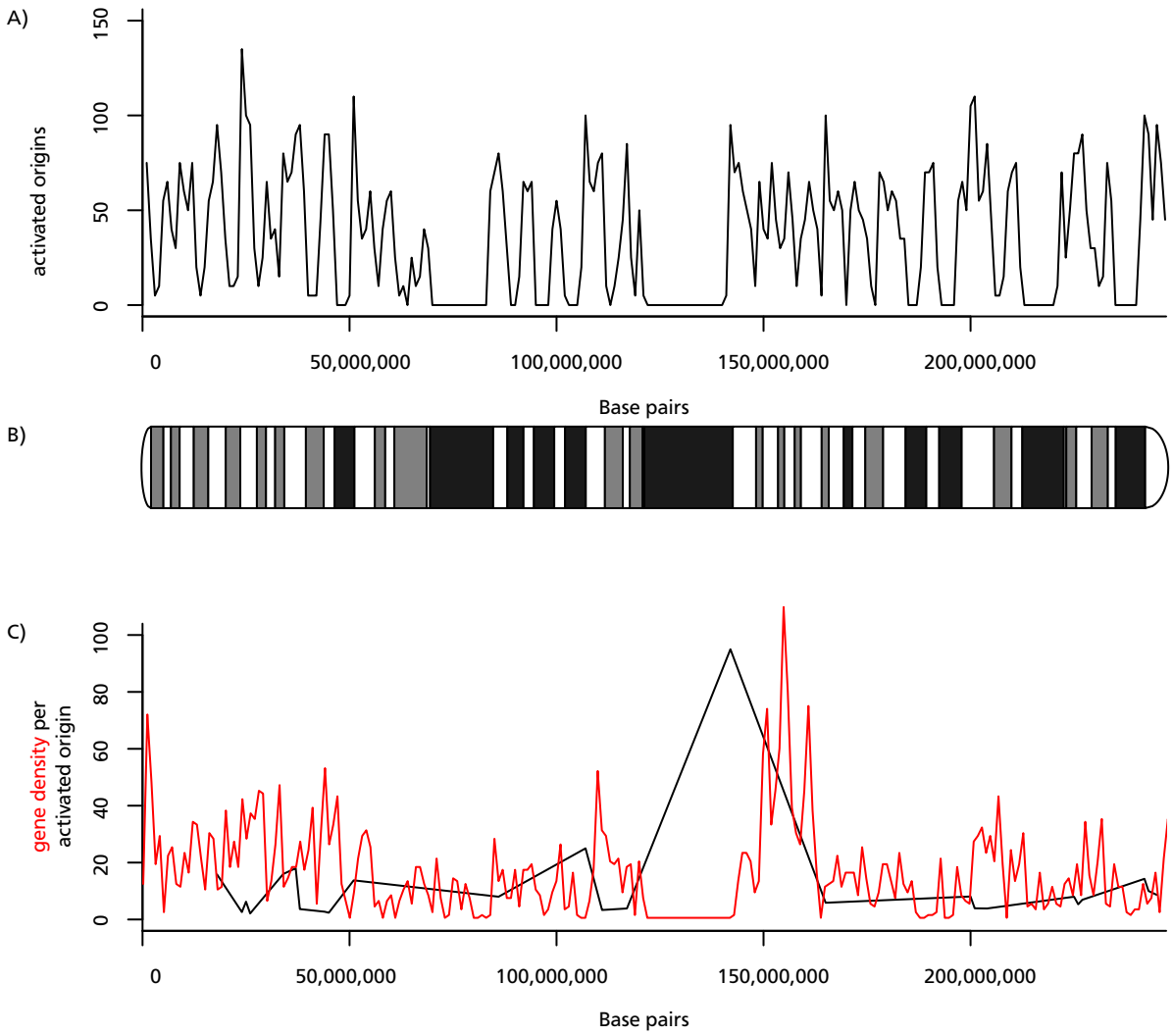

Figure 7.4: A) Frequency plot of the first 5,000 induced origins, mostly correspond to euchromatic regions of human Chromosome 1. B) Ideogram of human Chromosome 1, white areas in the ideogram represent euchromatic regions, light grey illustrates facultative and dark grey constitutive heterochromatin. C) Correlation of activated early DNA origins in 1 Mbp sized domains to the number of genes in those domains (black). Displayed in red, the count of genes per 1 Mbp cluster.

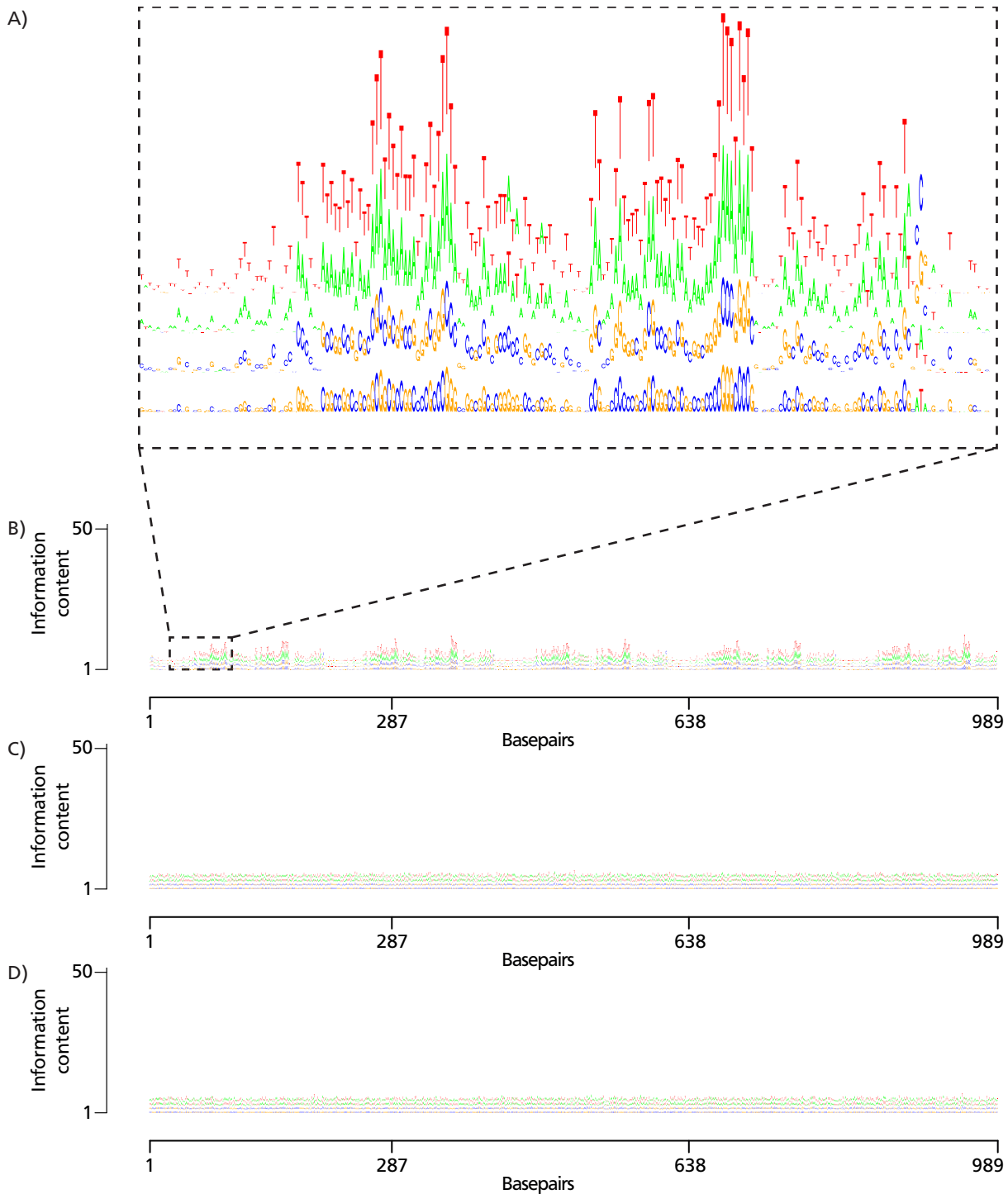

Figure 7.5: Potential DNA replication origin consensus motif in mammalian cells.
A) a magnification of the sequence analysis, thymine (T) in red, adenine (A) in green, cytosine (C) blue and guanine (G) yellow, B) 1,000 nucleotide strand with repetitive sequences. C) Randomized *in silico* experiments with completely randomized origin selection. D) Randomized *in silico* experiments with random origin selection as a 100 nucleotide sequence. Length = 1,000 nucleotides, he combined height of the letters correspondents to the information at each position.

8 Conclusion

8.1 Observation of complex biological assembly lines

Fifty years after the discovery of the replicon[19], individual replicons are in focus again and can be resolved in clarity never seen before (see Fig 8.1, and Table 8.1). When generations before us have resolved DNA replication as hundreds of foci clusters per cell[50,71,113,119,120,175], improvements already came with advancements in microscopic technique[34,60,77,99], but came up short of the calculated DNA replication sites[71,113]. High temporal resolution, combined with high spatial resolution and live cell imaging, finally gave the perfect opportunity to gain insights into the depth of DNA replication and the possibility to follow DNA replication foci within the chromatin context at the level of individual replicons.

8.2 Historical context with new insights

The inconsistencies between resolvable and calculated replisome numbers implied that each imaged/resolved DNA replication foci (RFi) must contain multiple active replication machineries. Observations of nuclease resistancy of those RFi clusters, the spatial organization of DNA fibers and chromatin loops led to the postulation that multiple replication machineries (∼5) must be linked to each other as "replication factories"[54,73,77].

8.3 Box of shiny new toys

Before my improvements in cell labeling (see Chapter 3[134]), high temporal resolution was achievable only by live cell microscopy, trading spatial resolution for temporal resolution and photobleaching. Multi-replication staining, especially the described quadruple staining, offers a combination of high temporal and high spatial resolution in a single 3D conserved cell. This method prevents extensive photobleaching and uncontrolled cell death through phytotoxicity intrinsic for super-resolution and even confocal live cell microscopy where high light intensities and long exposure times are necessary to image cells in 4D.

Multi-replication stained cells are even imageable on super-resolution microscopes, for example on 3D-SIM systems. With increased resolution and accompanying increase of raw data, the need for an analysis tool arose, especially for a tool capable of preventing (inadvertent) data manipulation by the research scientist, freeing the outcome of observer bias and increasing efficiency, by requiring minimal user interaction while performing automated repetitive analysis tasks (Chapter 4[28]).

8.4 Resolution or "seeing is believing"

Previously, confocal laser scanning microscope already allowed to dissect ∼1,000 DNA replication sites[34,60,77,99], an substantial increase over wide field microscopy[50,71,113,119,120,175] (Figure 8.1 and Table 8.1), but still failed to resolve the expected ∼50,000 individual DNA replication sites active during the complete S-Phase[71,113]. As shown in Chapter 5[27], it is now possible to further resolve DNA replication foci as seen with wide field and laser scanning microscopy further by super-resolution microscopy. I was able to dissect, quantify and measure individual replisomes during different cell

cycle phases and correlate each individual "confocal level DNA replication foci" into approximately five super-resolution foci (see Chapter 4 part 3.9ff and Chapter 5 Figure 3 and 4).

I measured DNA replication fork speed (RFS), inter origin distances (IODs) and DNA replication timing of S-Phase. I quantified the number of DNA replication foci required to replicate a full genome within a single S-Phase in accordance with, but independent of historical calculations[71,113].

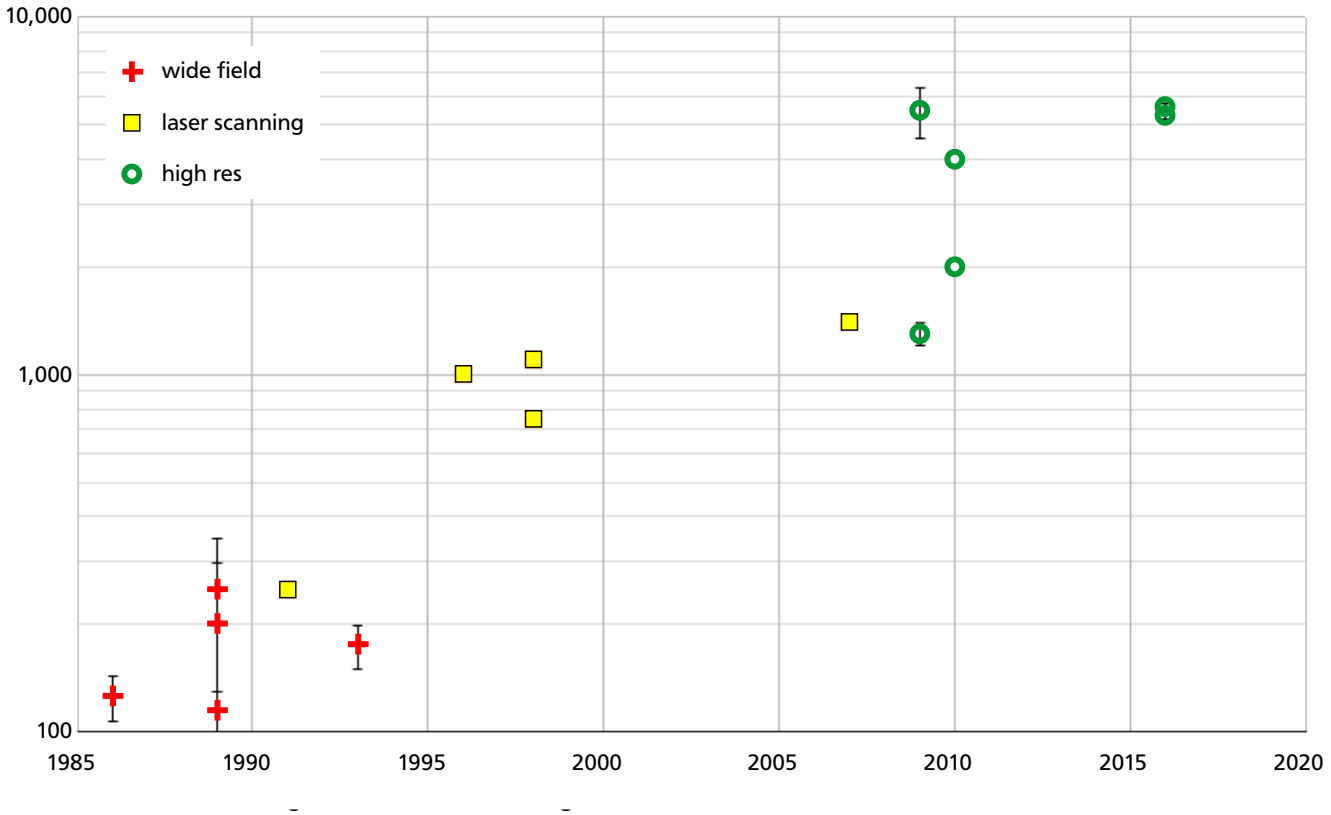

Figure 8.1: Number of reported DNA replication structures.
Increase in replication foci numbers driven by resolution improvements in microscopy during the last 30 years.

Table 8.1: Reported replication structures, Increase in replication foci numbers driven by resolution improvements in microscopy during the last 30 years.

RF Numbers	Year	cell line		Reference	imaging method
		name	origin/description		
126±18,8	1986	3Y1B (IMR-90|100T)	rat embryonic fibroblast	[119]	wide field
<100 (S1)	1989	MCF; cov362c14; cov86044	human cancer cell	[175]	wide field
100-130 (S5)	1989	MCF; cov362c14; cov86044	human cancer cell	[175]	wide field
100-300	1989	Xenopus sperm nuclei	Xenopus sperm	[113]	confocal LM
150-300 (~250)	1989	3T3	mouse fibroblast cells	[120]	wide field
250	1991	3T3	mouse fibroblast cells	[50]	CLSM
150-200	1993	HeLa	human cervical cancer cell	[71]	wide field
>1,000	1996	3T3	mouse fibroblast cells	[9]	CLSM
750	1998	HeLa	human cervical cancer cell	[77]	CLSM
1,100	1998	3T3	mouse fibroblast cells	[99]	CLSM
1,400	2007	GM05389	human fetal lung fibroblasts	[60]	CLSM
1,200-1,400	2009	MRC5	normal human fetal lung fibroblast	[34]	STED
5,460 ± 923	2009	HeLa	human cervical cancer cell	[93]	EM
4,000	2009	C2C12	mouse myoblast cells	[4]	3D-SIM
5,583	2016	HeLa Kyoto	human cervical cancer cell	[27]	3D-SIM
5,314	2016	C2C12	mouse myoblast cells	[27]	3D-SIM

The improved resolution and accompanying experiments suggest single replicons and do not involve an agglomeration of multiple DNA replication machineries at specific synthesis centers. This demonstrates that "replication factories" were just accumulations of multiple replisomes activating adjacent to an ongoing DNA synthesis. The activation of those adjacent DNA origins is described as a domino-like activation pattern of potential DNA replication origins adjacent to an ongoing DNA synthesis (see Chapter 6 Figure 1 [156]). The activation of those adjacent forks leads to naturally occurring DNA replication clusters without the need for higher order chromatin structure or linked replication machineries in "replication factories". The observed individual replicons and DNA replication forks in (live) 3D-preserved cells negate the idea of replication factories [27], instead the spatially organized replisomes throughout the nucleus arrived. This observation is further supported by the DNA replication computer model as explained in detail below.

The segmentation of conventional "laser scanning" RFi down to individual replicons and even to some single replication forks with this super-resolution approach imply:
The end of "replication factory" as a macromolecular complex.

8.5 Simulation of a beautiful system

The careful and extensive acquisition of experimental data on the complex DNA replication mechanism gave insights and ideas into the timeline and regulation of S-Phase. To dig even deeper into the very complex DNA replication mechanism, we developed a simplistic computer DNA replication model. In the spirit of Antoine de Saint-Exupery as "Perfection is Achieved Not When There Is Nothing More to Add, But When There Is Nothing Left to Take Away", we intentionally limited us to a simplistic simulation with the aim to include as few parameters as possible. Very few parameters were necessary to describe the replication model: it includes only spontaneous, stochastic firing of individual origins as a starting point for S-Phase and the domino-like activation, which fires origins close to active replication forks. Further, replication fork speed, the inhibition of firing at distances below the size of chromatin loops, an over all limiting factor and different chromatin types were added. Even with this little input the model was already comparable to experimental (see Chapter 5 and 6) and already published data [71,113,119,156]. The stochastic model with a domino-like origin activation reproduced not only the temporal characteristics of DNA replication but also the spatial replication characteristics typical for mammalian cells.
As described before, my key idea to compare the 1D replication model with live cell imaging and super-resolution microscopy images, was made possible through adaption of the whole 1D genome DNA replication model to represent 4D replication in a virtual nucleus implemented by N. Lengert and D. Löw. Replication-related chromatin loops linked to the inhibition distance, and chromatin loops from the random loop model (at least 2 Mbp) [103] approximate the distribution of chromatin fibers in the nucleus, while chromatin compaction is modeled by different spring rates for eu- and heterochromatin in the random loop model [103,133]. The different compaction states of chromatin and the accumulation of replication fork clusters in heterochromatin were already sufficient to reproduce characteristic complex RFi patterns throughout S-Phase.
Those simulated *in silico* images already gave insights into the mechanisms of DNA replication, as the first iterations of the model only had two chromatin types and the subsequent images showed only the two S-Phase replication patterns typical for early and late sub S-Phase. The simple addition of third chromatin state with a intermediate spring

/ compaction rate to the model, equivalent to facultative heterochromatin, gained the mid S-phase replication pattern, demonstrating the high accuracy of our theoretical predicted model. Predictions from the model could therefore already be validated by biological experiments. Exact DNA replication timing of individual replicons vary between individual simulations, but the majority of euchromatic regions will be replicated during early S-Phase, while most heterochromatin during late S-Phase. Those slight differences in the observed replication timing in the simulated data (Chapter 6 and in Figure 7.3) is congruent with the variations observed in live cell experiments by Cayrou et al.'s, the so called "flexible replicon" theory[25]. In conclusion, this DNA replication model produced 3D *in silico* microscopy images similar to 3D-SIM super-resolution images by combining 1D DNA replication initiation, progression and random DNA folding.

9 Outlook

9.1 Genome, transcriptome, proteome - Omics at the OMX

Live cell microscopy data from the 3D-SIM OMX blaze system was shown in Chapter 5, Figure 3. Temporal and spatial progression of individual DNA replication machineries were observed, unfortunately only with extensive photobleaching. The dynamic *in silico* images will be comparable with the super-resolution live cell images, and we will be able to follow individual replisomes during their synthesis from activation up to the annihilation and termination in 4D. Replisome assembly and even limiting factor distributions might become quantifiable by 3D-SIM or STED imaging as the basis for further insights into *in vitro*, *in vivo* and *in silico* genome replication.

9.2 Genome, transcriptome, proteome - *In silico* 'omics

Ongoing data analysis on the *in silico* DNA replication model guide us in the quest for the holy grail of mammalian DNA replication: the search for the elusive DNA replication origin motif. Preliminary data has already shown consensus motifs in the analyses of *in silico* DNA replication origins induced during early S-Phase (see Chapter 7). Further sequence analysis and a higher sample size are required to validate those preliminary findings. Those DNA replication origins will be matched to published data on potential DNA replication origins[10,18,25,40,81,98,100,109,110,117,128,146,172]. The sequence can be used further as a DNA FISH probe template to detect and validate the elusive DNA replication origins in real cells. The validated DNA sequence motif will be used to target, reposition and manipulate DNA replication origins comparable to yeast nucleus experiments by Taddei et al.[161].

With the help of Gene Ontology, a major bioinformatics initiative, we will clarify connections between DNA replication timing, active and inactive genes during S-Phase progression, and the preliminary findings of the DNA replication origin motifs. Gene ontology will also be used to correlate *in silico* data to transcriptomic and proteomic data sets.

9.3 How about stem cells?

To broaden the appeal of the replication model, we aim to adapt it to different cell lines. The flexibility of the DNA replication model will allow us to generate consistent data with only minimal input. It is easily adaptable to a wide range of cell types with minimal experiment data to establish the required DNA replication parameters. The parameters of the model can be fitted to different DNA replication parameters.

The primary aim is to predict DNA replication in embryonic stem cells. As there is only a minimalistic amount of data on replication in embryonic stem cells, we will adapt the model to simulate stem cell DNA replication and their distinctive DNA replication features. In this simulation, the focus will rest on the small replicons and differences in the chromatin loop sizes[80] compared to adult mammalian cells and most importantly to the very fast, only 20 min long, S-phase.

9.4 ... and chromatin organization?

The idea that DNA replication timing is not only dependent on chromatin types and active genes, but correlates with spatial organization and topologically associated stable domains[77,131], is already in the focus of another project. Heinz et

al. (unpublished data) correlated 3D arrangement of replicons in relation to epigenetic chromatin signatures as aspects of functional chromatin organization and demonstrate *de-novo* assembly of new replisomes in a domino-like manner not only in cis and but also in trans.

9.5 ... and further cell cycle processes?

As described in Section 9.2 the *in silico* model already "includes" DNA replication "unrelated" processes. So far, transcriptome analyses was performed on a preliminary basis. Future iterations of the model will include simulated gene transcription and interactions between the DNA replication machinery and the transcription machinery. The simulated interactions of the DNA replication machineries and the transcription machineries will lead to collisions between each other, stalled forks and finally DNA damage. Damage which hopefully can be repaired by an adapted DNA replication (and repair) model.

10 References

[1] **Astbury, W. A.** (**1947**). "Nucleic Acid." In "Symposia of the Society for Experimental Biology," .

[2] **Aten, J. A., Bakker, P. J., Stap, J., Boschman, G. A., and Veenhof, C. H.** (**1992**). "DNA double labelling with IdUrd and CldUrd for spatial and temporal analysis of cell proliferation and DNA replication." *The Histochemical journal*, 24(5): 251–259.

[3] **Bacon, R.** (**1267**). *Opus Majus*. Vatican Library, Vatican.

[4] **Baddeley, D., Chagin, V. O., Schermelleh, L., Martin, S., Pombo, A., Carlton, P. M., Gahl, A., Domaing, P., Birk, U. J., Leonhardt, H., Cremer, C., and Cardoso, M. C.** (**2010**). "Measurement of replication structures at the nanometer scale using super-resolution light microscopy." *Nucleic Acids Research*, 38(2): e8–e8.

[5] **Bailey, B., Farkas, D. L., Taylor, D. L., and Lanni, F.** (**1993**). "Enhancement of axial resolution in fluorescence microscopy by standing-wave excitation." *Nature*, 366(6450): 44–48.

[6] **Bembom, O.** (**2016**). *seqLogo: Sequence logos for DNA sequence alignments*. R package version 1.38.0.

[7] **Bensimon, A., Simon, A., Chiffaudel, A., Croquette, V., Heslot, F., and Bensimon, D.** (**1994**). "Alignment and sensitive detection of DNA by a moving interface." *Science*, 265(5181): 2096–2098.

[8] **Berezney, R., Dubey, D. D., and Huberman, J. A.** (**2000**). "Heterogeneity of eukaryotic replicons, replicon clusters, and replication foci." *Chromosoma*, 108(8): 471–484.

[9] **Berezney, R., Mortillaro, M., Ma, H., Meng, C., Samarabandu, J., Wei, X., Somanathan, S., Liou, W., Pan, S., and Cheng, P.** (**1996**). "Connecting nuclear architecture and genomic function." *Journal of Cellular Biochemistry*, 62(2): 223–226.

[10] **Besnard, E., Babled, A., Lapasset, L., Milhavet, O., Parrinello, H., Dantec, C., Marin, J.-M., and Lemaitre, J.-M.** (**2012**). "Unraveling cell type-specific and reprogrammable human replication origin signatures associated with G-quadruplex consensus motifs." *Nature structural & molecular biology*, 19(8): 837–844.

[11] **Bianco, J. N., Poli, J., Saksouk, J., Bacal, J., Silva, M. J., Yoshida, K., Lin, Y.-L., Tourrière, H., Lengronne, A., and Pasero, P.** (**2012**). "Analysis of DNA replication profiles in budding yeast and mammalian cells using DNA combing." *Methods*, 57(2): 149–157.

[12] **Blow, J. J. and Dutta, A.** (**2005**). "Preventing re-replication of chromosomal DNA." *Nature Reviews Molecular Cell Biology*, 6(6): 476–486.

[13] **Boos, D., Frigola, J., and Diffley, J. F. X.** (**2012**). "Activation of the replicative DNA helicase: breaking up is hard to do." *Current opinion in cell biology*, 24(3): 423–430.

[14] **Botchan, M. and Berger, J.** (**2010**). "DNA Replication: Making Two Forks from One Prereplication Complex." *Molecular cell*, 40(6): 860–861.

[15] **Boye, E. and Grallert, B.** (**2009**). "In DNA Replication, the Early Bird Catches the Worm." *Cell*, 136(5): 812–814.

[16] **Burhans, W. C., Vassilev, L. T., Caddle, M. S., Heintz, N. H., and DePamphills, M. L.** (**1990**). "Identification of an origin of bidirectional DNA replication in mammalian chromosomes." *Cell*, 62(5): 955–965.

[17] **Burhans, W. C., Vassilev, L. T., Wu, J., Sogo, J. M., Nallaseth, F. S., and DePamphilis, M. L.** (**1991**). "Emetine allows identification of origins of mammalian DNA replication by imbalanced DNA synthesis, not through conservative nucleosome segregation." *The EMBO journal*, 10(13): 4351–4360.

[18] **Cadoret, J.-C., Meisch, F., Hassan-Zadeh, V., Luyten, I., Guillet, C., Duret, L., Quesneville, H., and Prioleau, M.-N.** (**2008**). "Genome-wide studies highlight indirect links between human replication origins and gene regulation." *Proceedings of the National Academy of Sciences*, 105(41): 15 837–15 842.

[19] **Cairns, J.** (**1963**). "The bacterial chromosome and its manner of replication as seen by autoradiography." *Journal of molecular biology*, 6(3): 208–IN5.

[20] **Casas-Delucchi, C. S., Becker, A., Bolius, J. J., and Cardoso, M. C.** (**2012**). "Targeted manipulation of heterochromatin rescues MeCP2 Rett mutants and re-establishes higher order chromatin organization." *Nucleic Acids Research*, 40(22): e176–e176.

[21] **Casas-Delucchi, C. S. and Cardoso, M. C.** (**2014**). "Epigenetic control of DNA replication dynamics in mammals." *Nucleus (Austin, Tex.)*, 2(5): 370–382.

[22] **Casas-Delucchi, C. S., van Bemmel, J. G., Haase, S., Herce, H. D., Nowak, D., Meilinger, D., Stear, J. H., Leonhardt, H., and Cardoso, M. C.** (**2011**). "Histone hypoacetylation is required to maintain late replication timing of constitutive heterochromatin." *Nucleic Acids Research*, 40(1): 159–169.

[23] **Castillo Bosch, P., Segura-Bayona, S., Koole, W., van Heteren, J. T., Dewar, J. M., Tijsterman, M., and Knipscheer, P.** (**2014**). "FANCJ promotes DNA synthesis through G-quadruplex structures." *The EMBO journal*, 33(21): 2521–2533.

[24] **Cavalli, G. and Misteli, T.** (**2013**). "Functional implications of genome topology." *Nature structural & molecular biology*, 20(3): 290–299.

[25] **Cayrou, C., Coulombe, P., Vigneron, A., Stanojcik, S., Ganier, O., Peiffer, i., Rivals, E., Puy, A., Laurent-Chabalier, S., Desprat, R., and Méchali, M.** (**2011**). "Genome-scale analysis of metazoan replication origins reveals their organization in specific but flexible sites defined by conserved features." *Genome Research*, 21(9): gr.121 830.111–1449.

[26] **Cayrou, C., Grégoire, D., Coulombe, P., Danis, E., and Méchali, M.** (**2012**). "Genome-scale identification of active DNA replication origins." *Methods*, 57(2): 158–164.

[27] **Chagin, V. O., Casas-Delucchi, C. S., Reinhart, M., Schermelleh, L., Markaki, Y., Maiser, A., Bolius, J. J., Bensimon, A., Fillies, M., Domaing, P., Rozanov, Y. M., Leonhardt, H., and Cardoso, M. C.** (**2016**). "4D Visualization of replication foci in mammalian cells corresponding to individual replicons." *Nature communications*, 7: 11 231.

[28] **Chagin, V. O., Reinhart, M., and Cardoso, M. C.** (**2015**). "High-resolution analysis of Mammalian DNA replication units." *Methods in molecular biology (Clifton, N.J.)*, 1300: 43–65.

[29] **Chagin, V. O., Stear, J. H., and Cardoso, M. C.** (**2010**). "Organization of DNA Replication." *Cold Spring Harbor Perspectives in Biology*, 2(4): a000 737–a000 737.

[30] **Chalfie, M., Tu, Y., Euskirchen, G., Ward, W., and Prasher, D.** (**1994**). "Green fluorescent protein as a marker for gene expression." *Science*, 263(5148): 802–805. URL `http://science.sciencemag.org/content/263/5148/802`.

[31] **Champeris Tsaniras, S., Kanellakis, N., Symeonidou, I. E., Nikolopoulou, P., Lygerou, Z., and Taraviras, S.** (**2014**). "Licensing of DNA replication, cancer, pluripotency and differentiation: An interlinked world?" *Seminars in Cell and Developmental Biology*, 30: 174–180.

[32] **Chistol, G. and Walter, J. C.** (**2015**). "Single-Molecule Visualization of MCM2-7 DNA Loading: Seeing Is Believing." *Cell*, 161(3): 429–430.

[33] **Comoglio, F., Schlumpf, T., Schmid, V., Rohs, R., Beisel, C., and Paro, R.** (**2015**). "High-Resolution Profiling of Drosophila Replication Start Sites Reveals a DNA Shape and Chromatin Signature of Metazoan Origins." *Cell Reports*, 11(5): 821–834.

[34] **Cseresnyes, Z., Schwarz, U., and Green, C. M.** (**2009**). "Analysis of replication factories in human cells by super-resolution light microscopy." *BMC Cell Biology*, 10(1): 88.

[35] **Cvetic, C. and Walter, J. C.** (**2005**). "Eukaryotic origins of DNA replication: could you please be more specific?" *Seminars in Cell and Developmental Biology*, 16(3): 343–353.

[36] **Dahm, R.** (**2007**). "Discovering DNA: Friedrich Miescher and the early years of nucleic acid research." *Human Genetics*, 122(6): 565–581.

[37] **D'Angiolella, V., Donato, V., Vijayakumar, S., Saraf, A., Florens, L., Washburn, M. P., Dynlacht, B., and Pagano, M.** (**2010**). "SCF(Cyclin F) controls centrosome homeostasis and mitotic fidelity through CP110 degradation." *Nature*, 466(7302): 138–142.

[38] **Danna, K. J. and Nathans, D. (1972)**. "Bidirectional Replication of Simian Virus 40 DNA." *Proceedings of the National Academy of Sciences of the United States of America*, 69(11): 3097–3100.

[39] **Davey, M. J. and O'Donnell, M. (2000)**. "Mechanisms of DNA replication." *Current Opinion in Chemical Biology*, 4(5): 581–586.

[40] **Dellino, G. I., Cittaro, D., Piccioni, R., Luzi, L., Banfi, S., Segalla, S., Cesaroni, M., Mendoza-Maldonado, R., Giacca, M., and Pelicci, P. G. (2013)**. "Genome-wide mapping of human DNA-replication origins: Levels of transcription at ORC1 sites regulate origin selection and replication timing." *Genome Research*, 23(1): 1–11.

[41] **DePamphilis, M. L. (2003)**. "The 'ORC cycle': a novel pathway for regulating eukaryotic DNA replication." *Gene*.

[42] **DePamphilis, M. L., Blow, J. J., Ghosh, S., Saha, T., Noguchi, K., and Vassilev, A. (2006)**. "Regulating the licensing of DNA replication origins in metazoa." *Current opinion in cell biology*, 18(3): 231–239.

[43] **Di Antonio, M., Rodriguez, R., and Balasubramanian, S. (2012)**. "Experimental approaches to identify cellular G-quadruplex structures and functions." *Methods*, 57(1): 84–92.

[44] **Dimitrova, D. S. and Gilbert, D. M. (1999)**. "The Spatial Position and Replication Timing of Chromosomal Domains Are Both Established in Early G1 Phase." *Molecular cell*, 4(6): 983–993.

[45] **Douglas, M. E. and Diffley, J. F. X. (2012)**. "Replication Timing: The Early Bird Catches the Worm." *Current Biology*, 22(3): R81–R82.

[46] **Dreszer, T. R., Karolchik, D., Zweig, A. S., Hinrichs, A. S., Raney, B. J., Kuhn, R. M., Meyer, L. R., Wong, M., Sloan, C. A., Rosenbloom, K. R., Roe, G., Rhead, B., Pohl, A., Malladi, V. S., Li, C. H., Learned, K., Kirkup, V., Hsu, F., Harte, R. A., Guruvadoo, L., Goldman, M., Giardine, B. M., Fujita, P. A., Diekhans, M., Cline, M. S., Clawson, H., Barber, G. P., Haussler, D., and James Kent, W. (2012)**. "The UCSC Genome Browser database: extensions and updates 2011." *Nucleic Acids Research*, 40(Database issue): D918–23.

[47] **Duzdevich, D., Warner, M. D., Ticau, S., Ivica, N. A., Bell, S. P., and Greene, E. C. (2015)**. "The Dynamics of Eukaryotic Replication Initiation: Origin Specificity, Licensing, and Firing at the Single-Molecule Level." *Molecular cell*, 58(3): 483–494.

[48] **Egger, M. D. and Petran, M. (1967)**. "New Reflected-Light Microscope for Viewing Unstained Brain and Ganglion Cells." *Science*, 157(3786): 305–307.

[49] **Forterre, P. (2013)**. "Why are there so many diverse replication machineries?" *Journal of molecular biology*, 425(23): 4714–4726.

[50] **Fox, M. H., Arndt-Jovin, D. J., Jovin, T. M., Baumann, P. H., and Robert-Nicoud, M. (1991)**. "Spatial and temporal distribution of DNA replication sites localized by immunofluorescence and confocal microscopy in mouse fibroblasts." *Journal of Cell Science*, 99 (Pt 2): 247–253.

[51] **Fu, Y. V., Yardimci, H., Long, D. T., Guainazzi, A., Bermudez, V. P., Hurwitz, J., van Oijen, A., Schärer, O. D., and Walter, J. C. (2011)**. "Selective Bypass of a Lagging Strand Roadblock by the Eukaryotic Replicative DNA Helicase." *Cell*, 146(6): 931–941.

[52] **Galilei, G. (1610)**. Sidereus Nuncius. Thomas Baglioni, Republic of Venice.

[53] **Gao, F., Luo, H., and Zhang, C. T. (2012)**. "DeOri: a database of eukaryotic DNA replication origins." *Bioinformatics*, 28(11): 1551–1552.

[54] **Ge, X. Q., Jackson, D. A., and Blow, J. J. (2007)**. "Dormant origins licensed by excess Mcm2 7 are required for human cells to survive replicative stress." *Genes & Development*, 21(24): 3331–3341.

[55] **Gerbi, S. (2002)**. "Initiation of DNA replication in multicellular eukaryotes." *Journal of Structural Biology*, 140(1-3): 17–30.

[56] **Gerbi, S. A. and Bielinsky, A.-K. (2002)**. "DNA replication and chromatin." *Current Opinion in Genetics & Development*, 12(2): 243–248.

[57] **Gilbert, D. (2001)**. "Making sense of eukaryotic DNA replication origins." *Science*.

[58] **Gilbert, D. M. (2012)**. "Replication origins run (ultra) deep." *Nature structural & molecular biology*, 19(8): 740–742.

[59] **Gilbert, N. and Allan, J. (2014)**. "Supercoiling in DNA and chromatin." *Current Opinion in Genetics & Development*, 25: 15–21.

[60] **Gotoh, E. (2007)**. "Visualizing the dynamics of chromosome structure formation coupled with DNA replication." *Chromosoma*, 116(5): 453–462.

[61] **Gratzner, H. G. (1982)**. "Monoclonal antibody to 5-bromo- and 5-iododeoxyuridine: A new reagent for detection of DNA replication." *Science*, 218(4571): 474–475.

[62] **Gundersen, G. G. and Worman, H. J. (2013)**. "Nuclear Positioning." *Cell*, 152(6): 1376–1389.

[63] **Gustafsson, M. G. L., Shao, L., Carlton, P. M., Wang, C. J. R., Golubovskaya, I. N., Cande, W. Z., Agard, D. A., and Sedat, J. W. (2008)**. "Three-Dimensional Resolution Doubling in Wide-Field Fluorescence Microscopy by Structured Illumination." *Biophysical journal*, 94(12): 4957–4970.

[64] **Haeckel, E. (1866)**. *Generelle Morphologie der Organismen : allgemeine Grundzuge der organischen Formen-Wissenschaft, mechanisch begrundet durch die von Charles Darwin reformirte Descendenz-Theorie /*. Georg Reimer,, Berlin :.

[65] **Hamdan, S. M., Johnson, D. E., Tanner, N. A., Lee, J.-B., Qimron, U., Tabor, S., van Oijen, A. M., and Richardson, C. C. (2007)**. "Dynamic DNA Helicase-DNA Polymerase Interactions Assure Processive Replication Fork Movement." *Molecular cell*, 27(4): 539–549.

[66] **Hell, S. W. (2003)**. "Toward fluorescence nanoscopy." *Nature biotechnology*, 21(11): 1347–1355.

[67] **Hell, S. W., Stelzer, E. H. K., Lindek, S., and Cremer, C. (1994)**. "Confocal microscopy with an increased detection aperture: type-B 4Pi confocal microscopy." *Optics letters*, 19(3): 222.

[68] **Heller, R. C., Kang, S., Lam, W. M., Chen, S., Chan, C. S., and Bell, S. P. (2011)**. "Eukaryotic Origin-Dependent DNA Replication In Vitro Reveals Sequential Action of DDK and S-CDK Kinases." *Cell*, 146(1): 80–91.

[69] **Herrick, J. and Bensimon, A. (1999)**. "Single molecule analysis of DNA replication." *Biochimie*, 81(8-9): 859–871.

[70] **Hori, M., Shibuya, K., Sato, M., and Saito, Y. (2014)**. "Lethal effects of short-wavelength visible light on insects." *Scientific reports*, 4: 7383.

[71] **Hozák, P., Hozák, P., Hassan, A. B., Hassan, A. B., Jackson, D. A., Jackson, D. A., Cook, P. R., and Cook, P. R. (1993)**. "Visualization of replication factories attached to nucleoskeleton." *Cell*, 73(2): 361–373.

[72] **Huberman, J. A. and Riggs, A. D. (1966)**. "Autoradiography of chromosomal DNA fibers from Chinese hamster cells." In "Proceedings of the National Academy of . . . ," .

[73] **Huberman, J. A. and Riggs, A. D. (1968)**. "On the mechanism of DNA replication in mammalian chromosomes." *Journal of molecular biology*, 32(2): 327–341.

[74] **Hyrien, O. (2015)**. "Peaks cloaked in the mist: The landscape of mammalian replication origins." *The Journal of cell biology*, 208(2): 147–160.

[75] **Hyrien, O., Rappailles, A., Guilbaud, G., Baker, A., Chen, C.-L., Goldar, A., Petryk, N., Kahli, M., Ma, E., d'Aubenton Carafa, Y., Audit, B., Thermes, C., and Arneodo, A. (2013)**. "From Simple Bacterial and Archaeal Replicons to Replication N/U-Domains." *Journal of molecular biology*, 425(23): 4673–4689.

[76] **Jackson, D. A., Dolle, A., Robertson, G., and Cook, P. R. (1992)**. "The attachments of chromatin loops to the nucleoskeleton." *Cell biology international reports*, 16(8): 687–696.

[77] **Jackson, D. A. and Pombo, A. (1998)**. "Replicon clusters are stable units of chromosome structure: evidence that nuclear organization contributes to the efficient activation and propagation of S phase in human cells." *The Journal of cell biology*, 140(6): 1285–1295.

[78] **Jaunin, F., Visser, A. E., Cmarko, D., Aten, J. A., and Fakan, S. (1998)**. "A New Immunocytochemical Technique for Ultrastructural Analysis of DNA Replication in Proliferating Cells After Application of Two Halogenated Deoxyuridines." *The journal of histochemistry and cytochemistry : official journal of the Histochemistry Society*, 46(10): 1203–1209.

[79] **Johnson, C. L. K. (1995)**. *Biographical Memoirs*, volume 67 of *Clarence Leonard (Kelly) Johnson February 27, 1910–December 21, 1990*. National Academies Press, Washington, D.C.

[80] **Jun, S., Herrick, J., Bensimon, A., and Bechhoefer, J. (2004)**. "Persistence length of chromatin determines origin spacing in Xenopus early-embryo DNA replication: quantitative comparisons between theory and experiment." *Cell Cycle*, 3(2): 223–229.

[81] **Karnani, N., Taylor, C. M., Malhotra, A., and Dutta, A. (2010)**. "Genomic Study of Replication Initiation in Human Chromosomes Reveals the Influence of Transcription Regulation and Chromatin Structure on Origin Selection." *Molecular biology of the cell*, 21(3): 393–404.

[82] **Keck, J. L. and Berger, J. M. (2000)**. "DNA replication at high resolution." *Chemistry & Biology*, 7(3): R63–R71.

[83] **Kireev, I., Lakonishok, M., Liu, W., Joshi, V. N., Powell, R., and Belmont, A. S. (2008)**. "In vivo immunogold labeling confirms large-scale chromatin folding motifs." *Nature Methods*.

[84] **Knott, S., Peace, J. M., Ostrow, A. Z., Gan, Y., and Rex, A. E. (2012)**. "Forkhead transcription factors establish origin timing and long-range clustering in S. cerevisiae." *Cell*.

[85] **Koberna, K., Ligasov, A., Mal nsk, J., Pliss, A., Siegel, A. J., Cva kov, Z., Fidlerov, H., Ma ata, M., Fialov, M. t., Ra ka, I., and Berezney, R. (2004)**. "Electron microscopy of DNA replication in 3-D: Evidence for similar-sized replication foci throughout S-phase." *Journal of Cellular Biochemistry*, 94(1): 126–138.

[86] **Köhler, A. (1893)**. "Ein neues Beleuchtungsverfahren für mikrophotographische Zwecke." *Zeitschrift für wissenschaftliche Mikroskopie und für mikroskopische Technik*, 10(4): 433–440.

[87] **Kriegstein, H. and Hogness, D. (1974)**. "Mechanism of DNA replication in Drosophila chromosomes: structure of replication forks and evidence for bidirectionality." *Proceedings of the National Academy of Sciences*, 71(1): 135.

[88] **Kubota, T., Nishimura, K., Kanemaki, M. T., and Donaldson, A. D. (2013)**. "The Elg1 Replication Factor C-like Complex Functions in PCNA Unloading during DNA Replication." *Molecular cell*, 50(2): 273–280.

[89] **Lander, E. S., Linton, L. M., Birren, B., Nusbaum, C., Zody, M. C., Baldwin, J., Devon, K., Dewar, K., Doyle, M., FitzHugh, W., Funke, R., Gage, D., Harris, K., Heaford, A., Howland, J., Kann, L., Lehoczky, J., LeVine, R., McEwan, P., McKernan, K., Meldrim, J., Mesirov, J. P., Miranda, C., Morris, W., Naylor, J., Raymond, C., Rosetti, M., Santos, R., Sheridan, A., Sougnez, C., Stange-Thomann, Y., Stojanovic, N., Subramanian, A., Wyman, D., Rogers, J., Sulston, J., Ainscough, R., Beck, S., Bentley, D., Burton, J., Clee, C., Carter, N., Coulson, A., Deadman, R., Deloukas, P., Dunham, A., Dunham, I., Durbin, R., French, L., Grafham, D., Gregory, S., Hubbard, T., Humphray, S., Hunt, A., Jones, M., Lloyd, C., McMurray, A., Matthews, L., Mercer, S., Milne, S., Mullikin, J. C., Mungall, A., Plumb, R., Ross, M., Shownkeen, R., Sims, S., Waterston, R. H., Wilson, R. K., Hillier, L. W., McPherson, J. D., Marra, M. A., Mardis, E. R., Fulton, L. A., Chinwalla, A. T., Pepin, K. H., Gish, W. R., Chissoe, S. L., Wendl, M. C., Delehaunty, K. D., Miner, T. L., Delehaunty, A., Kramer, J. B., Cook, L. L., Fulton, R. S., Johnson, D. L., Minx, P. J., Clifton, S. W., Hawkins, T., Branscomb, E., Predki, P., Richardson, P., Wenning, S., Slezak, T., Doggett, N., Cheng, J. F., Olsen, A., Lucas, S., Elkin, C., Uberbacher, E., Frazier, M., Gibbs, R. A., Muzny, D. M., Scherer, S. E., Bouck, J. B., Sodergren, E. J., Worley, K. C., Rives, C. M., Gorrell, J. H., Metzker, M. L., Naylor, S. L., Kucherlapati, R. S., Nelson, D. L., Weinstock, G. M., Sakaki, Y., Fujiyama, A., Hattori, M., Yada, T., Toyoda, A., Itoh, T., Kawagoe, C., Watanabe, H., Totoki, Y., Taylor, T., Weissenbach, J., Heilig, R., Saurin, W., Artiguenave, F., Brottier, P., Bruls, T., Pelletier, E., Robert, C., Wincker, P., Smith, D. R., Doucette-Stamm, L., Rubenfield, M., Weinstock, K., Lee, H. M., Dubois, J., Rosenthal, A., Platzer, M., Nyakatura, G., Taudien, S., Rump, A., Yang, H., Yu, J., Wang, J., Huang, G., Gu, J., Hood, L., Rowen, L., Madan, A., Qin, S., Davis, R. W., Federspiel, N. A., Abola, A. P., Proctor, M. J., Myers, R. M., Schmutz, J., Dickson, M., Grimwood, J., Cox, D. R., Olson, M. V., Kaul, R., Raymond, C., Shimizu, N., Kawasaki, K., Minoshima, S., Evans, G. A., Athanasiou, M., Schultz, R., Roe, B. A., Chen, F., Pan, H., Ramser, J., Lehrach, H., Reinhardt, R., McCombie, W. R., de la Bastide, M., Dedhia, N., Blocker, H., Hornischer, K., Nordsiek, G., Agarwala, R., Aravind, L., Bailey, J. A., Bateman, A., Batzoglou, S., Birney, E., Bork, P., Brown, D. G., Burge, C. B., Cerutti, L., Chen, H. C., Church, D., Clamp, M., Copley, R. R., Doerks, T., Eddy, S. R., Eichler, E. E., Furey, T. S., Galagan, J., Gilbert, J. G., Harmon, C., Hayashizaki, Y., Haussler, D., Hermjakob, H., Hokamp, K., Jang, W., Johnson, L. S., Jones, T. A., Kasif, S., Kaspryzk, A., Kennedy, S., Kent, W. J., Kitts, P., Koonin, E. V., Korf, I., Kulp, D., Lancet, D., Lowe, T. M., McLysaght, A., Mikkelsen, T., Moran, J. V., Mulder, N., Pollara, V. J., Ponting, C. P., Schuler, G., Schultz, J., Slater, G., Smit, A. F., Stupka, E., Szustakowki, J., Thierry-Mieg, D., Thierry-Mieg, J., Wagner, L., Wallis, J., Wheeler, R., Williams, A., Wolf, Y. I., Wolfe, K. H., Yang, S. P., Yeh, R. F., Collins, F., Guyer, M. S., Peterson, J., Felsenfeld, A., Wetterstrand, K. A., Patrinos, A., Morgan, M. J., de Jong, P., Catanese, J. J., Osoegawa, K., Shizuya, H., Choi, S., Chen, Y. J., and Szustakowki, J. (2001)**. "Initial sequencing and analysis of the human genome." *Nature*, 409(6822): 860–921.

[90] **Langston, L. D. and O'Donnell, M. (2006)**. "DNA Replication: Keep Moving and Don't Mind the Gap." *Molecular cell*, 23(2): 155–160.

[91] **Leonard, A. C. and Méchali, M. (2013)**. "DNA replication origins." *Cold Spring Harbor Perspectives in Biology*, 5(10): a010 116.

[92] **Leonhardt, H., Rahn, H. P., Weinzierl, P., Sporbert, A., Cremer, T., Zink, D., and Cardoso, M. C. (2000)**. "Dynamics of DNA replication factories in living cells." *The Journal of cell biology*, 149(2): 271–280.

[93] **Ligasová, A., Raska, I., and Koberna, K. (2009)**. "Organization of human replicon: Singles or zipping couples?" *Journal of Structural Biology*, 165(3): 204–213.

[94] **Lippincott-Schwartz, J., Snapp, E., and Kenworthy, A. (2001)**. "Studying protein dynamics in living cells." *Nature Reviews Molecular Cell Biology*, 2(6): 444–456.

[95] **Lipps, H. J. and Rhodes, D. (2009)**. "G-quadruplex structures: in vivo evidence and function." *Trends in Cell Biology*, 19(8): 414–422.

[96] **Löb, D., Lengert, N., Chagin, V. O., Reinhart, M., Casas-Delucchi, C. S., Cardoso, M. C., and Drossel, B. (2016)**. "3D replicon distributions arise from stochastic initiation and domino-like DNA replication progression." *Nature communications*, 7: 11 207.

[97] **Lovett, S. T. (2007)**. "Polymerase Switching in DNA Replication." *Molecular cell*, 27(4): 523–526.

[98] **Lucas, I., Palakodeti, A., Jiang, Y., Young, D. J., Jiang, N., Fernald, A. A., and Le Beau, M. M. (2007)**. "High-throughput mapping of origins of replication in human cells." *EMBO reports*, 8(8): 770–777.

[99] **Ma, H. (1998)**. "Spatial and Temporal Dynamics of DNA Replication Sites in Mammalian Cells." *The Journal of Cell Biology*, 143(6): 1415–1425.

[100] **Martin, M. M., Ryan, M., Kim, R., Zakas, A. L., Fu, H., Lin, C. M., Reinhold, W. C., Davis, S. R., Bilke, S., Liu, H., Doroshow, J. H., Reimers, M. A., Valenzuela, M. S., Pommier, Y., Meltzer, P. S., and Aladjem, M. I. (2011)**. "Genome-wide depletion of replication initiation events in highly transcribed regions." *Genome Research*, 21(11): 1822–1832.

[101] **Masai, H. (2013)**. "A Personal Reflection on the Replicon Theory: From R1 Plasmid to Replication Timing Regulation in Human Cells." *Journal of molecular biology*, 425(23): 4663–4672.

[102] **Masai, H., Matsumoto, S., You, Z., Yoshizawa-Sugata, N., and Oda, M. (2010)**. "Eukaryotic Chromosome DNA Replication: Where, When, and How?" *Annual Review of Biochemistry*, 79(1): 89–130.

[103] **Mateos-Langerak, J., Bohn, M., de Leeuw, W., Giromus, O., Manders, E. M. M., Verschure, P. J., Indemans, M. H. G., Gierman, H. J., Heermann, D. W., van Driel, R., and Goetze, S. (2009)**. "Spatially confined folding of chromatin in the interphase nucleus." *Proceedings of the National Academy of Sciences*, 106(10): 3812–3817.

[104] **Mazzotti, G., Rizzoli, R., Galanzi, A., Papa, S., Vitale, M., Falconi, M., Neri, L. M., Zini, N., and Maraldi, N. M. (1990)**. "High-resolution detection of newly synthesized DNA by anti-bromodeoxyuridine antibodies identifies specific chromatin domains." *The journal of histochemistry and cytochemistry : official journal of the Histochemistry Society*, 38(1): 13–22.

[105] **McGuffee, S. R., Smith, D. J., and Whitehouse, I. (2013)**. "Quantitative, Genome-Wide Analysis of Eukaryotic Replication Initiation and Termination." *Molecular cell*, 50(1): 123–135.

[106] **McInerney, P., Johnson, A., Katz, F., and O'Donnell, M. (2007)**. "Characterization of a Triple DNA Polymerase Replisome." *Molecular cell*, 27(4): 527–538.

[107] **Mendel, G. (1866)**. *Versuche über Pflanzen-Hybriden /*. Im Verlage des Vereines„ Brünn :.

[108] **Meselson, M. and Stahl, F. W. (1958)**. "The replication of DNA in Escherichia coli." *Proceedings of the National Academy of Sciences of the United States of America*, 44(7): 671–682.

[109] **Mesner, L. D., Valsakumar, V., Cieslik, M., Pickin, R., Hamlin, J. L., and Bekiranov, S. (2013)**. "Bubble-seq analysis of the human genome reveals distinct chromatin-mediated mechanisms for regulating early- and late-firing origins." *Genome Research*, 23(11): 1774–1788.

[110] **Mesner, L. D., Valsakumar, V., Karnani, N., Dutta, A., Hamlin, J. L., and Bekiranov, S. (2011)**. "Bubble-chip analysis of human origin distributions demonstrates on a genomic scale significant clustering into zones and significant association with transcription." *Genome Research*, 21(3): 377–389.

[111] **Michalet, X., Ekong, R., Fougerousse, F., Rousseaux, S., Schurra, C., Hornigold, N., van Slegtenhorst, M., Wolfe, J., Povey, S., Beckmann, J. S., and Bensimon, A. (1997)**. "Dynamic molecular combing: stretching the whole human genome for high-resolution studies." *Science*, 277(5331): 1518–1523.

[112] **Miescher, F. (1871)**. *Ueber die chemische Zusammensetzung der Eiterzellen*, volume 4. Hoppe-Seyler's medicinisch-chemische Untersuchungen.

[113] **Mills, A., Blow, J. J., White, J., Amos, W. B., Wilcock, D., and Laskey, R. (1989)**. "Replication occurs at discrete foci spaced throughout nuclei replicating in vitro." *Journal of Cell Science*, 94: 471.

[114] **Minsky, M. (1961)**. "Microscopy Apparatus, US Patent 3,103,467. Washington, DC: U.S." US Patent Office.

[115] **Mojardín, L., Vázquez, E., and Antequera, F. (2013)**. "Specification of DNA Replication Origins and Genomic Base Composition in Fission Yeasts." *Journal of molecular biology*, 425(23): 4706–4713.

[116] **Morrison, A., Araki, H., Clark, A. B., Hamatake, R. K., and Sugino, A. (1990)**. "A third essential DNA polymerase in S. cerevisiae." *Cell*, 62(6): 1143–1151.

[117] **Mukhopadhyay, R., Lajugie, J., Fourel, N., Selzer, A., Schizas, M., Bartholdy, B., Mar, J., Lin, C. M., Martin, M. M., Ryan, M., Aladjem, M. I., and Bouhassira, E. E. (2014)**. "Allele-specific genome-wide profiling in human primary erythroblasts reveal replication program organization." *PLoS genetics*, 10(5): e1004 319.

[118] **Murat, P. and Balasubramanian, S. (2014)**. "Existence and consequences of G-quadruplex structures in DNA." *Current Opinion in Genetics & Development*, 25: 22–29.

[119] **Nakamura, H., Nakamura, H., Morita, T., Morita, T., Sato, C., and Sato, C. (1986)**. "Structural organizations of replicon domains during DNA synthetic phase in the mammalian nucleus." *Experimental cell research*, 165(2): 291–297.

[120] **Nakayasu, H. (1989)**. "Mapping replicational sites in the eucaryotic cell nucleus." *The Journal of cell biology*, 108(1): 1–11.

[121] **Nick McElhinny, S. A., Gordenin, D. A., Stith, C. M., Burgers, P. M. J., and Kunkel, T. A. (2008)**. "Division of Labor at the Eukaryotic Replication Fork." *Molecular cell*, 30(2): 137–144.

[122] **Norio, P. and Schildkraut, C. L. (2001)**. "Visualization of DNA Replication on Individual Epstein-Barr Virus Episomes." *Science*, 294(5550): 2361–2364.

[123] **Okazaki, R., Okazaki, T., Sakabe, K., Sugimoto, K., and Sugino, A. (1968)**. "Mechanism of DNA chain growth. I. Possible discontinuity and unusual secondary structure of newly synthesized chains." *Proceedings of the National Academy of Sciences of the United States of America*, 59(2): 598–605.

[124] **Okazaki, T. and Okazaki, R. (1969)**. "Mechanism of DNA chain growth. IV. Direction of synthesis of T4 short DNA chains as revealed by exonucleolytic degradation." *Proceedings of the National Academy of Sciences of the United States of America*, 64(4): 1242–1248.

[125] **O'Keefe, R. T. (1992)**. "Dynamic organization of DNA replication in mammalian cell nuclei: spatially and temporally defined replication of chromosome-specific alpha-satellite DNA sequences." *The Journal of cell biology*, 116(5): 1095–1110.

[126] **Ozeri-Galai, E., Lebofsky, R., Rahat, A., Bester, A. C., Bensimon, A., and Kerem, B. (2011)**. "Failure of origin activation in response to fork stalling leads to chromosomal instability at fragile sites." *Molecular cell*, 43(1): 122–131.

[127] **Patel, P. K. (2005)**. "DNA Replication Origins Fire Stochastically in Fission Yeast." *Molecular biology of the cell*, 17(1): 308–316.

[128] **Picard, F., Cadoret, J.-C., Audit, B., Arneodo, A., Alberti, A., Battail, C., Duret, L., and Prioleau, M.-N. (2014)**. "The Spatiotemporal Program of DNA Replication Is Associated with Specific Combinations of Chromatin Marks in Human Cells." *PLoS genetics*, 10(5): e1004 282.

[129] **Pomerantz, R. T. and O'Donnell, M. (2007)**. "Replisome mechanics: insights into a twin DNA polymerase machine." *Trends in microbiology*, 15(4): 156–164.

[130] **Pope, B. D. and Gilbert, D. M. (2013)**. "The Replication Domain Model: Regulating Replicon Firing in the Context of Large-Scale Chromosome Architecture." *Journal of molecular biology*, 425(23): 4690–4695.

[131] **Pope, B. D., Ryba, T., Dileep, V., Yue, F., Wu, W., Denas, O., Vera, D. L., Wang, Y., Hansen, R. S., Canfield, T. K., Thurman, R. E., Cheng, Y., Gülsoy, G., Dennis, J. H., Snyder, M. P., Stamatoyannopoulos, J. A., Taylor, J., Hardison, R. C., Kahveci, T., Ren, B., and Gilbert, D. M. (2014)**. "Topologically associating domains are stable units of replication-timing regulation." *Nature*, 515(7527): 402–405.

[132] **Pozzoli, U., Menozzi, G., Fumagalli, M., Cereda, M., Comi, G. P., Cagliani, R., Bresolin, N., and Sironi, M. (2008)**. "Both selective and neutral processes drive GC content evolution in the human genome." *BMC evolutionary biology*, 8: 99.

[133] **Razin, S. V. and Gavrilov, A. A. (2014)**. "Chromatin without the 30-nm fiber: constrained disorder instead of hierarchical folding." *Epigenetics : official journal of the DNA Methylation Society*, 9(5): 653–657.

[134] **Reinhart, M., Casas-Delucchi, C. S., and Cardoso, M. C. (2013)**. "Spatiotemporal visualization of DNA replication dynamics." *Methods in molecular biology (Clifton, N.J.)*, 1042(Chapter 15): 213–225.

[135] **Remus, D. and Diffley, J. F. (2009)**. "Eukaryotic DNA replication control: Lock and load, then fire." *Current opinion in cell biology*, 21(6): 771–777.

[136] **Renard-Guillet, C., Kanoh, Y., Shirahige, K., and Masai, H. (2014)**. "Temporal and spatial regulation of eukaryotic DNA replication: From regulated initiation to genome-scale timing program." *Seminars in Cell and Developmental Biology*, 30: 110–120.

[137] **Ritson, D. J. and Moses, J. E. (2012)**. "A fragment based click chemistry approach towards hybrid G-quadruplex ligands: design, synthesis and biophysical evaluation." *Tetrahedron*, 68(1): 197–203.

[138] **Rizzoli, R., Baratta, B., Maraldi, N. M., Falconi, M., Galanzi, A., Papa, S., Vitale, M., Rizzi, E., Manzoli, L., and Mazzotti, G. (1992)**. "DNA synthesis progression in 3T3 synchronized fibroblasts: a high resolution approach." *Histochemistry*, 97(2): 181–187.

[139] **Ruska, E. (1993)**. "Ernst Ruska - Autobiography."

[140] **Sadoni, N. (2004)**. "Stable chromosomal units determine the spatial and temporal organization of DNA replication." *Journal of Cell Science*, 117(22): 5353–5365.

[141] **Sancar, A., Lindsey-Boltz, L. A., Unsal-Kaçmaz, K., and Linn, S. (2004)**. "Molecular mechanism of mammalian DNA repair and the DNA Damage Checkpoints." *Annual Review of Biochemistry*, 73(1): 39–85.

[142] **Sansoni, V., Casas-Delucchi, C. S., Rajan, M., Schmidt, A., Bönisch, C., Thomae, A. W., Staege, M. S., Hake, S. B., Cardoso, M. C., and Imhof, A. (2014)**. "The histone variant H2A.Bbd is enriched at sites of DNA synthesis." *Nucleic Acids Research*, 42(10): 6405–6420.

[143] **Sasaki, T. and Gilbert, D. M. (2007)**. "The many faces of the origin recognition complex." *Current opinion in cell biology*, 19(3): 337–343.

[144] **Schmidt, R., Wurm, C. A., Jakobs, S., Engelhardt, J., Egner, A., and Hell, S. W. (2008)**. "Spherical nanosized focal spot unravels the interior of cells." *Nature Methods*, 5(6): 539–544.

[145] **Schneider, C. A., Rasband, W. S., and Eliceiri, K. W. (2012)**. "NIH Image to ImageJ: 25 years of image analysis." *Nature Methods*, 9(7): 671–675.

[146] **Sequeira-Mendes, J., Díaz-Uriarte, R., Apedaile, A., Huntley, D., Brockdorff, N., and Gómez, M. (2009)**. "Transcription Initiation Activity Sets Replication Origin Efficiency in Mammalian Cells." *PLoS genetics*, 5(4): e1000 446.

[147] **Shimomura, O., Johnson, F. H., and Saiga, Y. (1962)**. "Extraction, Purification and Properties of Aequorin, a Bioluminescent Protein from the Luminous Hydromedusan,Aequorea." *Journal of cellular and comparative physiology*, 59(3): 223–239.

[148] **Siddiqui-Jain, A., Bliesath, J., Macalino, D., Omori, M., Huser, N., Streiner, N., Ho, C. B., Anderes, K., Proffitt, C., O'Brien, S. E., Lim, J. K. C., Von Hoff, D. D., Ryckman, D. M., Rice, W. G., and Drygin, D. (2012)**. "CK2 inhibitor CX-4945 suppresses DNA repair response triggered by DNA-targeted anticancer drugs and augments efficacy: mechanistic rationale for drug combination therapy." *Molecular Cancer Therapeutics*, 11(4): 994–1005.

[149] **Siler, K., Lee, K., and Bero, L. (2015)**. "Measuring the effectiveness of scientific gatekeeping." *Proceedings of the National Academy of Sciences*, 112(2): 360–365.

[150] **Singer, C. (1914)**. "Notes on the Early History of Microscopy." *Proceedings of the Royal Society of Medicine*, 7(Sect Hist Med): 247–279.

[151] **Siow, C. C., Nieduszynska, S. R., Muller, C. A., and Nieduszynski, C. A.** (**2011**). "OriDB, the DNA replication origin database updated and extended." *Nucleic Acids Research*, 40(D1): D682–D686.

[152] **Somanathan, S., Suchyna, T., Siegel, A., and Berezney, R.** (**2001**). "Targeting of PCNA to sites of DNA replication in the mammalian cell nucleus*." *Journal of Cellular Biochemistry*, 81(1): 56–67.

[153] **Song, Y. and Brady, S. T.** (**2015**). "Post-translational modifications of tubulin: pathways to functional diversity of microtubules." *Trends in Cell Biology*, 25(3): 125–136.

[154] **Soyfer, V. N.** (**2001**). "The consequences of political dictatorship for Russian science." *Nature Reviews Genetics*, 2(9): 723–729.

[155] **Sporbert, A., Domaing, P., Leonhardt, H., and Cardoso, M. C.** (**2005**). "PCNA acts as a stationary loading platform for transiently interacting Okazaki fragment maturation proteins." *Nucleic Acids Research*, 33(11): 3521–3528.

[156] **Sporbert, A., Gahl, A., Ankerhold, R., Leonhardt, H., and Cardoso, M. C.** (**2002**). "DNA Polymerase Clamp Shows Little Turnover at Established Replication Sites but Sequential De Novo Assembly at Adjacent Origin Clusters." *Molecular cell*, 10(6): 1355–1365.

[157] **Stillman, B.** (**2008**). "DNA Polymerases at the Replication Fork in Eukaryotes." *Molecular cell*, 30(3): 259–260.

[158] **Sugimoto, K., Okazaki, T., Imae, Y., and Okazaki, R.** (**1969**). "Mechanism of DNA chain growth, III. Equal annealing of T4 nascent short DNA chains with the separated complementary strands of the phage DNA." *Proceedings of the National Academy of Sciences of the United States of America*, 63(4): 1343–1350.

[159] **Sugimoto, K., Okazaki, T., and Okazaki, R.** (**1968**). "Mechanism of DNA chain growth, II. Accumulation of newly synthesized short chains in E. coli infected with ligase-defective T4 phages." *Proceedings of the National Academy of Sciences of the United States of America*, 60(4): 1356–1362.

[160] **Tada, S., Li, A., Maiorano, D., Méchali, M., and Blow, J. J.** (**2001**). "Repression of origin assembly in metaphase depends on inhibition of RLF-B/Cdt1 by geminin." *Nature cell biology*, 3(2): 107–113.

[161] **Taddei, A., Schober, H., and Gasser, S. M.** (**2010**). "The budding yeast nucleus." *Cold Spring Harbor Perspectives in Biology*, 2(8): a000 612.

[162] **Tanaka, S., Nakato, R., Katou, Y., Shirahige, K., and Araki, H.** (**2011**). "Origin Association of Sld3, Sld7, and Cdc45 Proteins Is a Key Step for Determination of Origin-Firing Timing." *Current Biology*, 21(24): 2055–2063.

[163] **Tarsounas, M. and Tijsterman, M.** (**2013**). "Genomes and G-Quadruplexes: For Better or for Worse." *Journal of molecular biology*, 425(23): 4782–4789.

[164] **Taylor, J., Woods, P., and Hughes, W.** (**1957**). "The organization and duplication of chromosomes as revealed by autoradiographic studies using tritium-labeled thymidinee." *Proceedings of the National Academy of Sciences of the United States of America*, 43(1): 122.

[165] **Taylor, J. H.** (**1977**). "Increase in DNA replication sites in cells held at the beginning of S phase." *Chromosoma*, 62(4): 291–300.

[166] **Taylor, J. H. and Hozier, J. C.** (**1976**). "Evidence for a four micron replication unit in CHO cells." *Chromosoma*, 57(4): 341–350.

[167] **Técher, H., Koundrioukoff, S., Azar, D., Wilhelm, T., Carignon, S., Brison, O., Debatisse, M., and Le Tallec, B.** (**2013**). "Replication Dynamics: Biases and Robustness of DNA Fiber Analysis." *Journal of molecular biology*, 425(23): 4845–4855.

[168] **Ticau, S., Friedman, L. J., Ivica, N. A., Gelles, J., and Bell, S. P.** (**2015**). "Single-Molecule Studies of Origin Licensing Reveal Mechanisms Ensuring Bidirectional Helicase Loading." *Cell*, 161(3): 513–525.

[169] **Tsien, R. Y.** (**1998**). "The green fluorescent protein." *Annual Review of Biochemistry*, 67(1): 509–544.

[170] **Ulrich, H. D.** (**2013**). "New Insights into Replication Clamp Unloading." *Journal of molecular biology*, 425(23): 4727–4732.

[171] **Urban, J. M., Foulk, M. S., Casella, C., and Gerbi, S. A.** (**2015**). "The hunt for origins of DNA replication in multicellular eukaryotes." *F1000Prime Reports*, 7.

[172] **Valenzuela, M. S., Chen, Y., Davis, S., Yang, F., Walker, R. L., Bilke, S., Lueders, J., Martin, M. M., Aladjem, M. I., Massion, P. P., and Meltzer, P. S.** (**2011**). "Preferential Localization of Human Origins of DNA Replication at the 5´-Ends of Expressed Genes and at Evolutionarily Conserved DNA Sequences." *PLoS ONE*, 6(5): e17 308.

[173] **Valton, A. L., Hassan-Zadeh, V., Lema, I., Boggetto, N., Alberti, P., Saintome, C., Riou, J. F., and Prioleau, M. N.** (**2014**). "G4 motifs affect origin positioning and efficiency in two vertebrate replicators." *The EMBO journal*, 33(7): 732–746.

[174] **van der Aa, A. J.** (**1851**). Biografisch Woordenboek der Nederlanden. J. J. van Brederode.

[175] **Van Dierendonck, J. H., Keyzer, R., van De Velde, C. J. H., and Cornelisse, C. J.** (**1989**). "Subdivision of S-phase by analysis of nuclear 5-bromodeoxyuridine staining patterns." *Cytometry*, 10(2): 143–150.

[176] **Van Dilla, M. A., Trujillo, T., Mullaney, P. F., and Coultex, J. R.** (**1969**). "Cell microfluorometry: a method for rapid fluorescence measurement." *Science*, 163(3872): 1213.

[177] **Vashee, S.** (**2003**). "Sequence-independent DNA binding and replication initiation by the human origin recognition complex." *Genes & Development*, 17(15): 1894–1908.

[178] **Volle, C. and Dalal, Y.** (**2014**). "Histone variants: the tricksters of the chromatin world." *Current Opinion in Genetics & Development*, 25: 8–14.

[179] **Watson, J. D. and Crick, F. H. C.** (**1953**). "Molecular structure of nucleic acids; a structure for deoxyribose nucleic acid." *Nature*, 171(4356): 737–738.

[180] **Whitehouse, I. and Smith, D. J.** (**2013**). "Chromatin dynamics at the replication fork: there's more to life than histones." *Current Opinion in Genetics & Development*, 23(2): 140–146.

[181] **Wilson, B. and Wilson, B.** (**1975**). "DNA replication in the amphibia." *Chromosoma*, 51(3).

[182] **Wu, J. R. and Gilbert, D. M.** (**1997**). "The replication origin decision point is a mitogen-independent, 2-aminopurine-sensitive, G1-phase event that precedes restriction point control." *Molecular and Cellular Biology*, 17(8): 4312–4321.

[183] **Yamazaki, S., Hayano, M., Masai, H., and Masai, H.** (**2013**). "Replication timing regulation of eukaryotic replicons: Rif1 as a global regulator of replication timing." *TRENDS in Genetics*, 29(8): 449–460.

[184] **Yardimci, H., Loveland, A. B., Habuchi, S., van Oijen, A. M., and Walter, J. C.** (**2010**). "Uncoupling of Sister Replisomes during Eukaryotic DNA Replication." *Molecular cell*, 40(5): 834–840.

[185] **Yeeles, J. T. P., Deegan, T. D., Janska, A., Early, A., and Diffley, J. F. X.** (**2015**). "Regulated eukaryotic DNA replication origin firing with purified proteins." *Nature*, 519(7544): 431–435.

[186] **Yoshida, K., Poveda, A., and Pasero, P.** (**2013**). "Time to Be Versatile: Regulation of the Replication Timing Program in Budding Yeast." *Journal of molecular biology*, 425(23): 4696–4705.

[187] **Yurov, Y. B.** (**1977**). "DNA replication in human diploid cells of different origin." *Cell Differentiation*, 6(2): i–ii.

[188] **Yurov, Y. B.** (**1978**). "Replication of chromosomal DNA in cultured abnormal human cells." *Human Genetics*, 43(1): 47–52.

[189] **Yurov, Y. B.** (**1979**). "The rate of fork movement during DNA replication in mammalian cells." *Chromosoma*, 74(3): 347–353.

[190] **Yurov, Y. B. and Liapunova, N. A.** (**1977**). "The units of DNA replication in the mammalian chromosomes: Evidence for a large size of replication units." *Chromosoma*, 60(3): 253–267.

[191] **Zernike, F.** (**1955**). "How I Discovered Phase Contrast." *Science*, 121(3141): 345–349.

11 Annex

11.1 Abbreviations

Table 11.1: Abbreviations

1D	One dimensional
3D	Three dimensional
3D-SIM	3D structured illumination microscopy
4D	Three dimensional and time resolution
BrdU	Bromodeoxyuridine
ChIP	Chromatin immunoprecipitation
CldU	Chlorodeoxyuridine
DNA	Deoxyribonucleic acid
EdU	Ethynyldeoxyuridine
ENCODE	Encyclopedia of DNA elements
FISH	Fluorescence in situ hybridization
GFP	Green fluorescent protein
hg19	Human referenz genome version 19
IdU	Iododeoxyuridine
IOD	Inter origin distance
kbp	Kilo base pair
SNS	Short nacent strand
Mbp	Mega base pair
ORC1	Origin recognition complex subunit 1
ORC1-ChIP	Chromatin immunoprecipitation (ORC1 as target)
ori	Origin of replication
PCNA	Proliferating cell nuclear antigen
RF	Replication foci (singular)
RFi	Replication foci (plural)
RFS	Replication fork speed
RNA	Ribonucleic acid
S-Phase	Synthesis phase
STED	Stimulated emission depletion (microscopy)

11.2 Acknowledgements

First things first, I would like to thank my "Doktormutter" Dr. M. Cristina Cardoso for giving me the opportunity to extend my diploma studies in carry out my doctoral thesis in her lab. I would like to express my gratitude to her for all her time, her interest, her ideas, her excellent input and her patience with me for pursuing my doctoral studies and my company at the same time, and breaking bones in between.

I would also thank Professor Dr. Barbara Drossel for agreeing to be my second examiner.

I am also very grateful for my office roomies, especially Dr. Bianca Bertulat and Dr. Alex Rapp, thank you for your selfless support, the laughs we shared and your input into my work. Not to forget moving around office furniture, three coffee makers and a cubic meter of milk... in a single Tetrapak!

My thanks also belong to Dr. Vadim O. Chagin and Dr. Corella Casas Delucchi for introducing me to high resolution microscopy and doing an excellent job supervising me during my diploma which laid the foundation to this thesis.

Not breaking the first rule this time, I thank Stephanie and Manu for support with the restart of "you know what" and for being great friends. I am still disappointed of them always arriving unbefitting their social-professional status, despite their announcement to the contrary!

I like to thank Stephan for putting up with my sketchy sport schedule and awaiting our colleagues back any day now.

Standing ovations, now possible on paper, go to all the other members and former members of the Cardoso Lab, namely Anne, Anne, Annette, Annina, Cathia, Diana, Florian, Francesco, Henry, Katrin, Laurence, Malini, Nicola, Patrick, Peng and Wei.

Furthermore I would like to thank Professor Dr. Heinrich Leonhardt and his group at the Ludwig-Maximilian-Universität München for sharing their imaging facility and providing excellent ideas and support.

Big thanks are also in order for Giacomo and Peter form Ferrarese, without their facility, machines and the supply, my thesis would never be finished. If you need good coffee, they will hook you up with everything.

I thank Britta, Lena and Kathrin for providing a red thread for a color wise challenged PhD student when I went over to blue, green, pink and yellow threads, or even gone plaid.

I would not forget Kathrin's contributions, not only for reading and correcting my thesis without laughing out loud, but also for being a good friend.

I would also thank Lena, for everything, especially her endless support, her work and her valued friendship.

Special thanks go to Britta, for her support even when hungry, her valued input and her willingness to kick my butt when it needs kicking. Thank you for all and everything!

Last but not least, danke ich meinen Eltern, Marga und Willi und ihre endlose Unterstützung, ihre Hilfe und ihre Motivation. Hätten sie mich nicht schon immer neugierig gemacht auf die Welt, mir nicht schon frühzeitig Technik und Wissenschaft nahegebracht, und mich stundenlang in Technischen Museen ertragen, wäre ich sicherlich kein Wissenschaftler geworden. Für all das und alles andere, zu dem der Platz hier nicht ausreicht, schulde ich ihnen endlose Dankbarkeit.

11.3 Declaration - Ehrenwörtliche Erklärung

Ich erkläre hiermit ehrenwörtlich, dass ich die vorliegende Arbeit entsprechend den Regeln guter wissenschaftlicher Praxis selbstständig und ohne unzulässige Hilfe Dritter angefertigt habe.

Sämtliche aus fremden Quellen direkt oder indirekt übernommenen Gedanken sowie sämtliche von Anderen direkt oder indirekt übernommenen Daten, Techniken und Materialien sind als solche kenntlich gemacht. Die Arbeit wurde bisher bei keiner anderen Hochschule zu Prüfungszwecken eingereicht.

Darmstadt, den

_____

(Datum, Marius Armin Reinhart)

11.4 List of contributions

11.4.1 Chapter 1 - Introduction

M.R. wrote the text and prepared figures and tables with historical overviews (Figure 1.1 and Table 1.1). M.R. generated Figure 1.2 including adaptations from V.C. [27,29].

11.4.2 Chapter 3 - Spatio-temporal visualization of DNA replication dynamics.

M.R. wrote the introduction, developed and wrote the protocol for "Polytemporal DNA Replication Staining" and prepared Figure 2. C.D. developed and wrote the protocol for "Live-Cell Visualization of DNA Replication Dynamics" and prepared Figure 1. M.C.C. conceived and supervised the project and revised the manuscript.

11.4.3 Chapter 4 - High-Resolution analysis of mammalian DNA replication units.

M.R. developed the protocol for "3D-SIM Images" and prepared Figure 1 and 4. V.C. developed the protocol for "Hypotonically Resolved RFi", "Confocal or Wide-Field Images" and prepared Figures 2 and 3. M.R and V.C. cowrote the manuscript. M.C.C. conceived and supervised the project and revised the manuscript.

11.4.4 Chapter 5 - 4D Visualization of replication foci in mammalian cells corresponding to individual replicons.

A.B., M.F. and P.D generated/provided the materials. V.O.C., C.S.C.-D., M.R., L.S., Y.M., A.M., J.J.B. and Y.M.R. performed the experiments. V.O.C., C.S.C.-D., M.R., L.S. and Y.M. developed image analysis protocols. V.O.C., C.S.C.-D., M.R., L.S., Y.M. and Y.M.R. analysed the data. V.O.C., H.L. and M.C.C. designed the project. V.O.C., C.S.C.-D., M.R. and M.C.C. wrote the manuscript. All authors commented on the manuscript.

11.4.5 Chapter 6 - 3D replicon distributions arise from stochastic initiation and domino-like DNA replication progression.

V.O.C., C.S.C.D. and M.R. performed the experiments. V.O.C., C.S.C.D., M.R., D.L., N.L. and B.D. analysed the data. D.L., B.D., N.L., V.O.C. and M.R. designed the model. D.L., N.L. and B.D. provided model algorithm and implementation. M.C.C., B.D., D.L. and V.O.C. designed the project. D.L., N.L., V.O.C., M.R., M.C.C. and B.D. wrote the manuscript. Website and videos by N.L. All authors commented on the manuscript.

11.4.6 Chapter 7 - Predictions from the model

M.R. wrote the chapter, compiled the tables (Table 7.1 and Table 7.1 and the Figures 7.1, 7.2, 7.3, 7.4 and 7.5. Data for the analysis was provided by the model (see Chapter 6)

11.4.7 Chapter 8 - Conclusion

M.R. wrote the chapter and generated Figure 8.1 and Table 8.1

11.5 Curriculum vitæ

Personal Information	
Name:	Marius Armin Reinhart
Adress:	Schnittspahnstrasse 10, 64287 Darmstadt, Germany
Date of birth:	22. 7. 1980
Place of birth:	Frankfurt am Main

Education	
06/2012	**Diploma in Biology** grade: very good
	Technische Universität Darmstadt, Fachbereich Biologie
	Diploma thesis:
	Visualisation of single replicons in mammalian cells using super resolution light microscopy
	Study focus: molecular cell- and developmental biology, microbiology, ecology
10/2006 - 06/2012	**Diploma studies in biology**
	Technische Universität Darmstadt
	Majors: molecular cell- and developmental biology, microbiology, ecology
3/2001 - 09/2006	Diploma studies in physics
	Technische Universität Darmstadt
06/2000	**Abitur** (general university entrance qualification) grade 1,7
	Heinrich-Böll-Schule, Hattersheim am Main
	Leistungsfächer: Biologie, Geschichte

Work experience	
01/2013 - ongoing	**PhD student in the group for Cell Biology and Epigenetics**
	Technische Universität Darmstadt
	Studying replication in mammalian cells, regarding replication speed, replication timing and epigenetic modifications thereof
10/2012 - ongoing	**IT service provider** BTRONIX GmbH
	IT Support
	Supervising complex workgroup layouts, High Availability Server Platforms and 2nd level Support for hard- and software, CEO
09/2006 - 12/2012	**IT service provider** btronix
	IT Support
	Supervising complex workgroup layouts, High Availability Server Platforms and 2nd level Support for hard- and software
08/2012 - 12/2012	**Assistant in the group for Cell Biology and Epigenetics**
	Technische Universität Darmstadt
	Supervising practical courses for students and establishing a microscopy center

03/2009 - 12/2009	**Student assistant in the group for animal ecology** Technische Universität Darmstadt worked on functional response experiments assisted complex ecological micro- and mesocosm experiments with decomposer organisms of the soil
05/2003 - 08/2006	**Maconcept**, IT Support Installing and Support of Apple, Windows and Linux Systems
09/2001 - 04/2003	**CCF-AG**, IT Support Installing and Support of SUN Solaris (Unix) Systems

Publications

2016	**4D Visualization of replication foci in mammalian cells corresponding to individual replicons.** Chagin, V.O., Casas-Delucchi, C.S.*, Reinhart, M.*, Schermelleh, L., Markaki, Y., Maiser, A., Bolius, J.J., Bensimon, A., Fillies, M., Domaing, P., Rozanov, Y.M., Leonhardt, H., and Cardoso, M.C. Nat. Commun. 7, 11231.
2016	**3D replicon distributions arise from stochastic initiation and domino-like DNA replication progression.** Lob, D., Lengert, N., Chagin, V.O., Reinhart, M., Casas-Delucchi, C.S., Cardoso, M.C., and Drossel, B. Nat. Commun. 7, 11231.
2015	**High-resolution analysis of Mammalian DNA replication units.** Chagin, V.O.*, Reinhart, M.*, and Cardoso, M.C. Methods Mol. Biol. 1300, 43-65.
2013	**Spatio-temporal visualization of DNA replication dynamics** Reinhart, M.*, Casas-Delucchi, C.S.*, and Cardoso, M.C. Methods Mol. Biol. 1042, 213-225.
	*these authors contributed equally

Languages

German, native language

English, fluent

Latin, Latinum